frontiers | Research Topics

Recent advances in measuring and controlling synaptic communication

Edited by
Jacopo Lamanna, Mattia Ferro and Emanuele Cocucci

Published in
Frontiers in Cellular Neuroscience

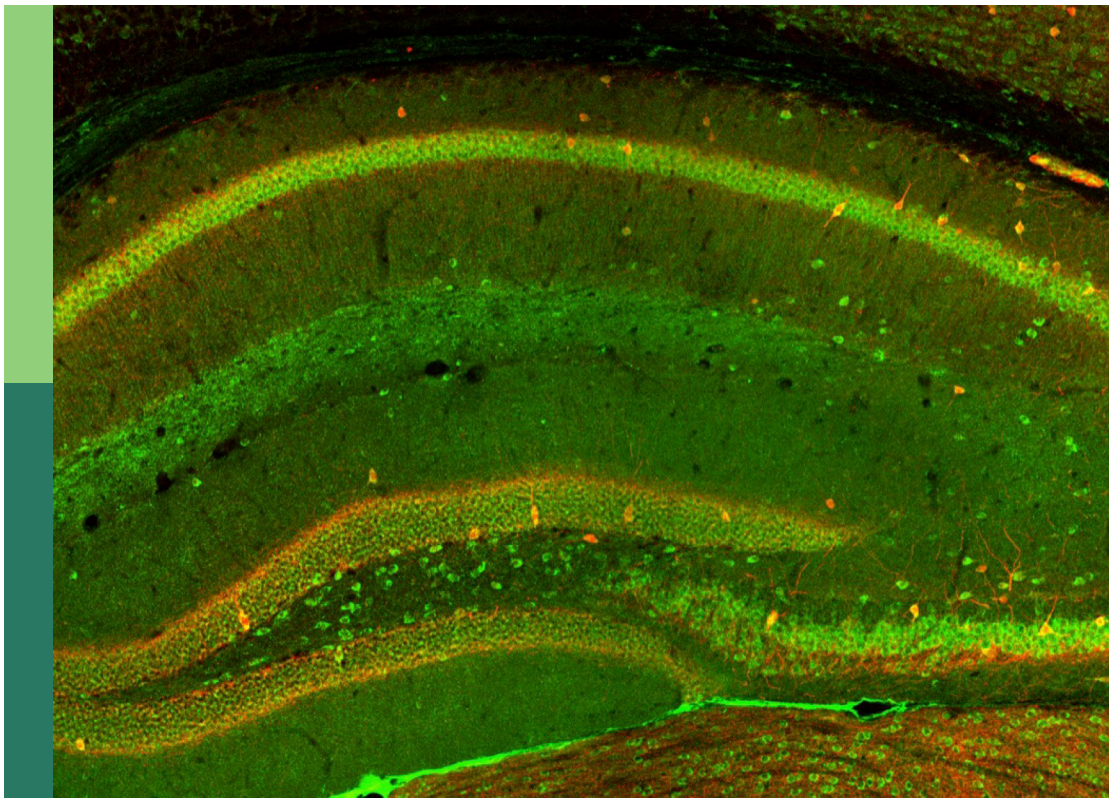

ISSN 1664-8714
ISBN 978-2-8325-3637-7
DOI 10.3389/978-2-8325-3637-7

About Frontiers

Frontiers is more than just an open access publisher of scholarly articles: it is a pioneering approach to the world of academia, radically improving the way scholarly research is managed. The grand vision of Frontiers is a world where all people have an equal opportunity to seek, share and generate knowledge. Frontiers provides immediate and permanent online open access to all its publications, but this alone is not enough to realize our grand goals.

Frontiers journal series

The Frontiers journal series is a multi-tier and interdisciplinary set of open-access, online journals, promising a paradigm shift from the current review, selection and dissemination processes in academic publishing. All Frontiers journals are driven by researchers for researchers; therefore, they constitute a service to the scholarly community. At the same time, the *Frontiers journal series* operates on a revolutionary invention, the tiered publishing system, initially addressing specific communities of scholars, and gradually climbing up to broader public understanding, thus serving the interests of the lay society, too.

Dedication to quality

Each Frontiers article is a landmark of the highest quality, thanks to genuinely collaborative interactions between authors and review editors, who include some of the world's best academicians. Research must be certified by peers before entering a stream of knowledge that may eventually reach the public - and shape society; therefore, Frontiers only applies the most rigorous and unbiased reviews. Frontiers revolutionizes research publishing by freely delivering the most outstanding research, evaluated with no bias from both the academic and social point of view. By applying the most advanced information technologies, Frontiers is catapulting scholarly publishing into a new generation.

What are Frontiers Research Topics?

Frontiers Research Topics are very popular trademarks of the *Frontiers journals series*: they are collections of at least ten articles, all centered on a particular subject. With their unique mix of varied contributions from Original Research to Review Articles, Frontiers Research Topics unify the most influential researchers, the latest key findings and historical advances in a hot research area.

Find out more on how to host your own Frontiers Research Topic or contribute to one as an author by contacting the Frontiers editorial office: frontiersin.org/about/contact

Recent advances in measuring and controlling synaptic communication

Topic editors

Jacopo Lamanna — Vita-Salute San Raffaele University, Italy

Mattia Ferro — Sigmund Freud University, Italy

Emanuele Cocucci — The Ohio State University, United States

Citation

Lamanna, J., Ferro, M., Cocucci, E., eds. (2023). *Recent advances in measuring and controlling synaptic communication*. Lausanne: Frontiers Media SA.

doi: 10.3389/978-2-8325-3637-7

Table of contents

04 Editorial: Recent advances in measuring and controlling synaptic communication
Jacopo Lamanna, Mattia Ferro and Emanuele Cocucci

07 Elucidating afferent-driven presynaptic inhibition of primary afferent input to spinal laminae I and X
Volodymyr Krotov, Kirill Agashkov, Sergii Romanenko, Oleh Halaidych, Yaroslav Andrianov, Boris V. Safronov, Pavel Belan and Nana Voitenko

20 Exploiting volume electron microscopy to investigate structural plasticity and stability of the postsynaptic compartment of central synapses
Greta Maiellano, Lucrezia Scandella and Maura Francolini

26 pOpsicle: An all-optical reporter system for synaptic vesicle recycling combining pH-sensitive fluorescent proteins with optogenetic manipulation of neuronal activity
Marius Seidenthal, Barbara Jánosi, Nils Rosenkranz, Noah Schuh, Nora Elvers, Miles Willoughby, Xinda Zhao and Alexander Gottschalk

42 Practical considerations in an era of multicolor optogenetics
Daniel J. Rindner and Gyorgy Lur

51 Alterations in synapses and mitochondria induced by acute or chronic intermittent hypoxia in the pre-Bötzinger complex of rats: an ultrastructural triple-labeling study with immunocytochemistry and histochemistry
Junjun Kang, Naining Lu, Shoujing Yang, Baolin Guo, Yuanyuan Zhu, Shengxi Wu, Xiaofeng Huang, Margaret T. T. Wong-Riley and Ying-Ying Liu

70 Different resting membrane potentials in posterior parietal cortex and prefrontal cortex in the view of recurrent synaptic strengths and neural network dynamics
Minsu Yoo, Yoon-Sil Yang, Jong-Cheol Rah and Joon Ho Choi

81 Variance analysis as a method to predict the locus of plasticity at populations of non-uniform synapses
Lucas B. Lumeij, Aile N. van Huijstee, Natalie L. M. Cappaert and Helmut W. Kessels

92 Detection of endogenous NPY release determined by novel GRAB sensor in cultured cortical neurons
Emma Kragelund Christensen, Ainoa Konomi-Pilkati, Joscha Rombach, Raquel Comaposada-Baro, Huan Wang, Yulong Li and Andreas Toft Sørensen

104 Assessing seizure liability *in vitro* with voltage-sensitive dye imaging in mouse hippocampal slices
Yuichi Utsumi, Makiko Taketoshi, Michiko Miwa, Yoko Tominaga and Takashi Tominaga

frontiers | Frontiers in Cellular Neuroscience

TYPE Editorial
PUBLISHED 21 September 2023
DOI 10.3389/fncel.2023.1289874

OPEN ACCESS

EDITED AND REVIEWED BY
Enrico Cherubini,
European Brain Research Institute, Italy

*CORRESPONDENCE
Jacopo Lamanna
✉ lamanna.jacopo@hsr.it

RECEIVED 06 September 2023
ACCEPTED 08 September 2023
PUBLISHED 21 September 2023

CITATION
Lamanna J, Ferro M and Cocucci E (2023) Editorial: Recent advances in measuring and controlling synaptic communication. *Front. Cell. Neurosci.* 17:1289874. doi: 10.3389/fncel.2023.1289874

Editorial: Recent advances in measuring and controlling synaptic communication

Jacopo Lamanna[1,2]*, Mattia Ferro[1,3] and Emanuele Cocucci[4]

[1]Center for Behavioral Neuroscience and Communication (BNC), Vita-Salute San Raffaele University, Milan, Italy, [2]Faculty of Psychology, Vita-Salute San Raffaele University, Milan, Italy, [3]Department of Psychology, Sigmund Freud University, Milan, Italy, [4]Division of Pharmaceutics and Pharmacology, College of Pharmacy, The Ohio State University, Columbus, OH, United States

KEYWORDS

synaptic transmission, synaptic plasticity, exo-endocytosis, neurotransmission, activity labeling, optogenetics, ultrastructural analysis, quantal analysis

Editorial on the Research Topic
Recent advances in measuring and controlling synaptic communication

Introduction

Synapses represent a unique neuronal compartment specialized in communication. The morpho-functional investigation of the synapse has always been hindered by its tiny size and high density of molecular elements, but specific technological and methodological advances helped us to reduce these limitations. As the matter of fact, in recent years, we have witnessed the continuous development of new methods allowing measuring and controlling synaptic activation both *in vitro* and *in vivo* (Lamanna et al., 2022). These include new genetically encoded sensors of synaptic exo-endocytosis (Ferro et al., 2017; Liu et al., 2021) and neurotransmitter release (Helassa et al., 2018; Patriarchi et al., 2018), but also engineered synaptic proteins able to control synaptic transmission (Won et al., 2021). Furthermore, new promising tools allow changing the functional properties of synapses in a plasticity-like manner (Goto et al., 2021).

All these methodological advances are likely to generate unprecedented knowledge about the dynamics of synaptic transmission and plasticity at several levels of the nervous system. Nevertheless, in most cases, the implementation of these new methods remains technically demanding, likely due to the high complexity of their operating principle (Glasgow et al., 2019; Lamanna et al., 2022). Hence, it would be worth refining and potentiating these tools to extend the range of experimental settings for their application. In addition, more classical and established approaches, such as electrophysiology, computational modeling and ultrastructural imaging, can be further implemented, e.g., by using alternative tools (Zhang et al., 2023) or advanced analysis approaches (Soares et al., 2019), to gather deeper insights into the physiology of neurotransmission.

In this Research Topic, we collected studies that validate, refine, or apply in an effective way advanced tools and approaches with the aim to investigate synaptic communication.

Development and refinement of novel sensors and actuators

To extend our capabilities of sensing and/or controlling synaptic activity, it is worth to improve more effective probes, either of chemical origin or genetically encoded, but

also to improve the experimental design and experimental setting to obtain more complete data and finally implement exhaustive pipelines for data analysis which often requires the development of dedicated software.

In this Research Topic, Seidenthal et al. describe the development and validation of the pOpsicle system, which combines recently developed variants of both pH-sensitive fluorescent proteins and channelrhodopsin, in order to simultaneously stimulate neuronal activity and measure exocytosis in the *Caenorhabditis elegans* using an all-optical approach.

Furthermore, Christensen et al. characterize a recently developed fluorescent reporter of neuropeptide Y (NPY) based on G-protein activation, evaluating its suitability to detect endogenous NPY release in primary neuronal cultures, as well as its technical limitations.

Utsumi et al. exploited voltage-sensitive dyes to characterize the electrophysiological response of seizure-inducing agents on *in vitro* hippocampal preparations; using this approach, the authors distinguish layer-specific activations as postsynaptic depolarizations or action potential activity, thus providing an effective tool for pharmacological testing of new compounds.

Finally, Rindner and Lur address the problem of cross-talk activation of opsins with scarcely-separated stimulation spectra in the same specimen and provide a method for estimating the acceptable range of stimulus intensity in multicolor optogenetics.

Extending the toolkit for the electrophysiological analysis of the synapse

Established electrophysiological techniques are routinely applied to either synapses, single neurons, or brain regions to investigate neuronal communication and brain connectivity. Nevertheless, addressing complex scientific questions or investigating specific circuits may require more advanced and tailored analytical approaches. In addition, computational modeling and *in silico* simulations are increasingly necessary to design new experiments and generalize the findings.

Krotov et al. exploited a recently developed electrophysiological approach based on anodal block of myelinated Aβ/δ-fibers to selectively activate C-afferents of the rodent spinal cord, aimed to investigate presynaptic inhibition driven by both types of afferents: they show differential characteristics in terms of segments involved and reciprocity of this phenomenon.

Yoo et al. developed a recurrent synaptic network computational model to assess the effects of the different resting membrane potential (RMP) levels they found in neurons from *in vitro* preparations of prefrontal and posterior parietal cortices. The authors provide evidence for a role of RMP in defining the differential activity regimes of these regions, with implications for cognitive functioning, and suggest a role of NMDA receptors in generating RMP differences.

Lumeij et al. extend the applicability of a combined variance analysis approach based on inverse square of coefficient-of-variation and variance-to-mean ratio of synaptic transmission. Based on both simulations and experimental characterization of β-amyloid-induced synaptic depression, they show that this approach is effective for identifying the locus of change of synaptic strength even when quantal parameters are not assumed as uniform.

Advances in ultrastructural imaging of the synapse

Due to the very limited size of the synaptic bouton, electron microscopy (EM) represents the best tool to morphologically characterize this compartment. Nevertheless, the simultaneous localization of multiple molecular and structural targets is technically challenging.

To address this issue, Kang et al. implemented a protocol for triple labeling of inhibitory and excitatory synapses in the pre-Bötzinger complex. They exploited, on the one hand, peroxidase and immunogold immunocytochemistry for targeting somatostatin and neurokinin 1, respectively, and, on the other, cytochrome oxidase histochemistry to characterize mitochondrial dynamics. Their investigation provides interesting insights about ultrastructural dynamics relevant to respiratory physiology.

Given the increasing number of approaches that exploit EM to study the synaptic function, Maiellano et al. discuss recent studies that exploited volume electronic microscopy, that can provide precise tomographic reconstruction of the synaptic bouton, and characterize the relationship between the geometry of postsynaptic compartments of central excitatory synapses and their functional state, in relation to synaptic plasticity phenomena.

Concluding remarks

In conclusion, this Research Topic is a collection of multifarious studies, where very different methodological approaches are developed, refined, or effectively applied to investigate neuronal communication and synaptic physiology. Importantly, these works show how both established and recently developed techniques can be further implemented and tailored to answer important questions in the space of neurophysiology. We believe that this Research Topic will contribute to future neuroscientific research by providing novel approaches and useful insights to generate new ideas.

Author contributions

JL: Writing—original draft, Writing—review and editing. MF: Writing—original draft, Writing—review and editing. EC: Writing—review and editing.

Conflict of interest

The authors declare that the research was conducted in the absence of any commercial or financial relationships that could be construed as a potential conflict of interest.

Publisher's note

References

Ferro, M., Lamanna, J., Ripamonti, M., Racchetti, G., Arena, A., Spadini, S., et al. (2017). Functional mapping of brain synapses by the enriching activity-marker SynaptoZip. *Nat. Commun.* 8, 1229. doi: 10.1038/s41467-017-01335-4

Glasgow, S. D., McPhedrain, R., Madranges, J. F., Kennedy, T. E., and Ruthazer, E. S. (2019). Approaches and limitations in the investigation of synaptic transmission and plasticity. *Front. Synaptic Neurosci.* 11, 1–16. doi: 10.3389/fnsyn.2019.00020

Goto, A., Bota, A., Miya, K., Wang, J., Tsukamoto, S., Jiang, X., et al. (2021). Stepwise synaptic plasticity events drive the early phase of memory consolidation. *Science* 374, 857–863. doi: 10.1126/science.abj9195

Helassa, N., Dürst, C. D., Coates, C., Kerruth, S., Arif, U., Schulze, C., et al. (2018). Ultrafast glutamate sensors resolve high-frequency release at Schaffer collateral synapses. *Proc. Natl. Acad. Sci. U. S. A.* 115, 5594–5599. doi: 10.1073/PNAS.1720648115

Lamanna, J., Ferro, M., Spadini, S., and Malgaroli, A. (2022). Exploiting the molecular diversity of the synapse to investigate neuronal communication: a guide through the current toolkit. *Eur. J. Neurosci.* 56, 6141–6161. doi: 10.1111/ejn.15848

Liu, A., Huang, X., He, W., Xue, F., Yang, Y., Liu, J., et al. (2021). pHmScarlet is a pH-sensitive red fluorescent protein to monitor exocytosis docking and fusion steps. *Nat. Commun.* 12, 1–12. doi: 10.1038/s41467-021-21666-7

Patriarchi, T., Cho, J. R., Merten, K., Howe, M. W., Marley, A., Xiong, W. H., et al. (2018). Ultrafast neuronal imaging of dopamine dynamics with designed genetically encoded sensors. *Science* 80, 360. doi: 10.1126./science.aat4422

Soares, C., Trotter, D., Longtin, A., Béïque, J. C., and Naud, R. (2019). Parsing out the variability of transmission at central synapses using optical quantal analysis. *Front. Synaptic Neurosci.* 11, 22. doi: 10.3389./fnsyn.2019.00022

Won, J., Pankratov, Y., Jang, M. W., Kim, S., Ju, Y. H., Lee, S., et al. (2021). Opto-vTrap, an optogenetic trap for reversible inhibition of vesicular release, synaptic transmission, and behavior. *Neuron* 110, 1–13. doi: 10.1016/j.neuron.11003

Zhang, A., Mandeville, E. T., Xu, L., Stary, C. M., Lo, E. H., Lieber, C. M., et al. (2023). Ultraflexible endovascular probes for brain recording through micrometer-scale vasculature. *Science* 381, 306–312. doi: 10.1126/science.adh3916

frontiers | Frontiers in Cellular Neuroscience

TYPE Original Research
PUBLISHED 11 January 2023
DOI 10.3389/fncel.2022.1029799

OPEN ACCESS

EDITED BY
Jacopo Lamanna,
Vita-Salute San Raffaele University, Italy

REVIEWED BY
Michael E. Hildebrand,
Carleton University, Canada
Sascha R. A. Alles,
University of New Mexico School of Medicine, United States

*CORRESPONDENCE
Volodymyr Krotov
✉ v.krotov@ucl.ac.uk

†PRESENT ADDRESS
Volodymyr Krotov,
Department of Neuroscience, Physiology and Pharmacology, University College London, London, United Kingdom

‡These authors have contributed equally to this work

SPECIALTY SECTION
This article was submitted to Cellular Neurophysiology, a section of the journal Frontiers in Cellular Neuroscience

RECEIVED 01 September 2022
ACCEPTED 14 December 2022
PUBLISHED 11 January 2023

CITATION
Krotov V, Agashkov K, Romanenko S, Halaidych O, Andrianov Y, Safronov BV, Belan P and Voitenko N (2023) Elucidating afferent-driven presynaptic inhibition of primary afferent input to spinal laminae I and X.
Front. Cell. Neurosci. 16:1029799.
doi: 10.3389/fncel.2022.1029799

Elucidating afferent-driven presynaptic inhibition of primary afferent input to spinal laminae I and X

Volodymyr Krotov[1,2*†], Kirill Agashkov[1‡], Sergii Romanenko[1‡], Oleh Halaidych[1‡], Yaroslav Andrianov[1‡], Boris V. Safronov[3,4], Pavel Belan[2,5] and Nana Voitenko[1,5,6]

[1]Department of Sensory Signaling, Bogomoletz Institute of Physiology, Kyiv, Ukraine, [2]Department of Molecular Biophysics, Bogomoletz Institute of Physiology, Kyiv, Ukraine, [3]i3S-Instituto de Investigação e Inovação em Saúde, Universidade do Porto, Porto, Portugal, [4]Neuronal Networks Group, Instituto de Biologia Molecular e Celular, Universidade do Porto, Porto, Portugal, [5]Department of Biomedicine and Neuroscience, Kyiv Academic University, Kyiv, Ukraine, [6]Dobrobut Academy Medical School, Kyiv, Ukraine

Although spinal processing of sensory information greatly relies on afferent-driven (AD) presynaptic inhibition (PI), our knowledge about how it shapes peripheral input to different types of nociceptive neurons remains insufficient. Here we examined the AD-PI of primary afferent input to spinal neurons in the marginal layer, lamina I, and the layer surrounding the central canal, lamina X; two nociceptive-processing regions with similar patterns of direct supply by Aδ- and C-afferents. Unmyelinated C-fibers were selectively activated by electrical stimuli of negative polarity that induced an anodal block of myelinated Aβ/δ-fibers. Combining this approach with the patch-clamp recording in an *ex vivo* spinal cord preparation, we found that attenuation of the AD-PI by the anodal block of Aβ/δ-fibers resulted in the appearance of new mono- and polysynaptic C-fiber-mediated excitatory postsynaptic current (EPSC) components. Such homosegmental Aβ/δ-AD-PI affected neurons in the segment of the dorsal root entrance as well as in the adjacent rostral segment. In their turn, C-fibers from the L5 dorsal root induced heterosegmental AD-PI of the inputs from the L4 Aδ- and C-afferents to the neurons in the L4 segment. The heterosegmental C-AD-PI was reciprocal since the L4 C-afferents inhibited the L5 Aδ- and C-fiber inputs, as well as some direct L5 Aβ-fiber inputs. Moreover, the C-AD-PI was found to control the spike discharge in spinal neurons. Given that the homosegmental Aβ/δ-AD-PI and heterosegmental C-AD-PI affected a substantial percentage of lamina I and X neurons, we suggest that these basic mechanisms are important for shaping primary afferent input to the neurons in the spinal nociceptive-processing network.

KEYWORDS

presynaptic inhibition, spinal cord, lamina I, lamina X, primary afferents, A-fibers, C-fibers

1. Introduction

Presynaptic inhibition (PI) of primary afferents is a fundamental mechanism shaping their input to the spinal cord. In the proprioceptive network, feedback inhibition ensures smoothness of locomotion (Fink et al., 2014), while PI of nociceptive afferents is critically important for processing pain signals (Melzack and Wall, 1965; Fernandes et al., 2020; Comitato and Bardoni, 2021; Ramírez-Morales et al., 2021; Krotov et al., 2022). PI can be induced by supraspinal descending fibers or segmental primary afferents and is mediated by GABA release at central terminals of primary afferents causing Cl^- efflux and primary afferent depolarization (PAD) (Guo and Hu, 2014; Comitato and Bardoni, 2021). PAD either prevents invasion of action potentials to the afferent terminal or reduces their amplitude, thus diminishing glutamate release to spinal neurons (Rudomin and Schmidt, 1999; Willis, 1999).

Despite its obvious physiological relevance, AD-PI and its effect on the afferent input to the spinal nociceptive neurons remain poorly understood. PI was mostly examined indirectly by morphological analysis of the axo-axonic synapses at primary afferent terminals, by recording the antidromic passive spread of PAD to the dorsal root [dorsal root potential (DRP)], or by analyzing changes in excitability of the intraspinal afferents by conditioning stimulation of cutaneous nerves (Hentall and Fields, 1979; Fitzgerald and Woolf, 1981; Calvillo et al., 1982). Recently developed methods that involve genetic manipulations to knock down $GABA_A$ receptor subunits at primary afferent terminals (Chen et al., 2014) or to express light-sensitive ChR2 receptors for activation of specific populations of GABAergic neurons (Fink et al., 2014; François et al., 2017) are time-consuming, sophisticated and expensive. Therefore, the development of simple approaches for investigating PI on a broad scale might greatly benefit spinal cord research. In the case of AD-PI, such method has recently been described (Fernandes et al., 2020). It relies on selective activation of C-fibers in the dorsal root through a suction electrode using electrical stimulus of inverted polarity. By applying this approach to the intact spinal cord preparations with several preserved dorsal roots, it was possible to reveal a homosegmental Aβ/δ-AD-PI and heterosegmental C-AD-PI of the C-fiber input to spinal lamina I neurons in the rat (Fernandes et al., 2020). In the present work, we used potential of this approach to further study the mechanisms of spinal processing of peripheral input.

The aim of this study was to examine AD-PI of peripheral inputs in rodent models, including the mouse, a species that nowadays is frequently used as a research model due to the abundance of its genetically modified strains. We did recordings from the neurons in the marginal zone, lamina I, and the area surrounding the central canal, lamina X, to examine effects for these two regions which are involved in spinal nociception and receive similar patterns of direct supply from cutaneous and visceral Aδ- and C-afferents (Light and Perl, 1979; Honda, 1985; Honda and Perl, 1985; Luz et al., 2015; Fernandes et al., 2016; Krotov et al., 2019). We have demonstrated that C-AD-PI is reciprocal for afferents from the L4 and L5 dorsal roots, controls the Aβ/δ- and C-fiber input and regulates spike discharge. We have also shown that primary afferent input to the nociceptive-processing spinal cord regions laminae I and X is similarly affected by AD-PI.

2. Materials and methods

2.1. Animals

In the present study, we used adult mice (2–3-month-old) and young rats (P11–13) of either sex. All experimental procedures were approved by the Animal Ethics Committee of the Bogomoletz Institute of Physiology (Kyiv, Ukraine) and performed in accordance with the European Commission Directive (86/609/EEC), ethical guidelines of the International Association for the Study of Pain, and the Society for Neuroscience Policies on the Use of Animals and Humans in Neuroscience Research.

2.2. *Ex vivo* spinal cord preparations

Lamina I neurons were studied in the isolated lumbosacral spinal cord preparations from adult mice using the approach described previously (Tadokoro et al., 2022). Briefly, a mouse was quickly decapitated, the vertebral column was cut out and immersed in oxygenated sucrose solution (20–22°C) containing (in mM): 200 sucrose, 2 KCl, 1.2 NaH_2PO_4, 0.5 $CaCl_2$, 7 $MgCl_2$, 26 $NaHCO_3$, 11 glucose (pH 7.4 when bubbled with 95% O_2 and 5% CO_2). The lumbosacral cord with preserved unilateral L5 or L5 and L4 dorsal roots was dissected, cleaned from the dura/pia mater, and glued to the metal plate to position the lateral lamina I on top.

Lamina X neurons were studied using young rats (Krotov et al., 2017, 2022). After removing from the vertebral column and peeling the dura mater, the spinal cord was hemisected along the midline, and the half containing roots was glued (medial side up) to a metal plate for the recordings.

2.3. Recordings

The experiments were performed at room temperature (20–22°C) in oxygenated solution containing (in mM): NaCl 125, KCl 2.5, $CaCl_2$ 2, $MgCl_2$ 1, NaH_2PO_4 1.25, $NaHCO_3$ 26 and glucose 10 (pH 7.4, 95% O_2 and 5% CO_2).

Dorsal root potentials and compound action potentials (CAPs) were recorded with a suction electrode from the L4 or L5

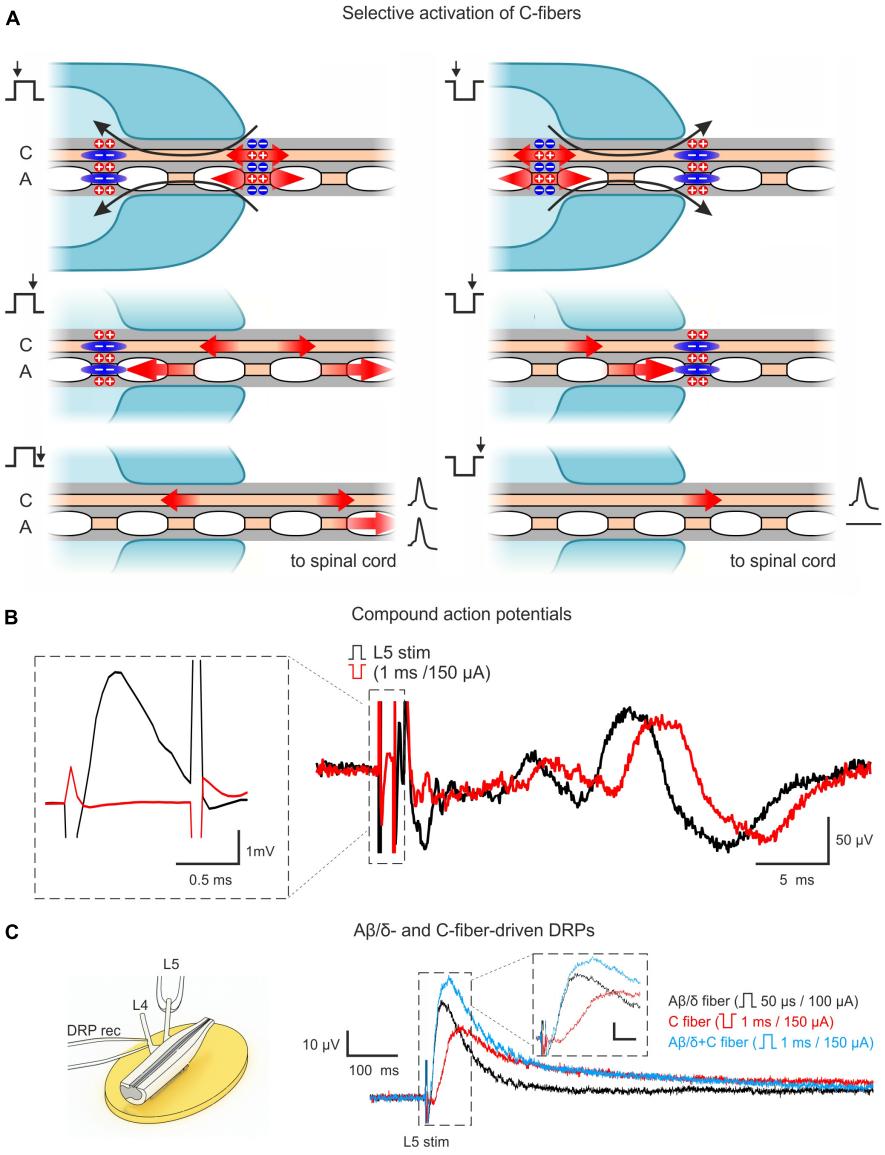

FIGURE 1
Approach for studying AD-PI in the spinal cord. **(A)** Technique for selective C-fiber activation by the inverted 1 ms pulse stimulation. Red arrows represent the spread of excitation. Blue zones represent regions of hyperpolarization-induced conduction block (anodal block). Given pipette lip geometry and difference in conduction velocities, Aβ/δ-fiber spikes produced by the negative stimuli at the internal end of the pipette lips are blocked at the external end, while C-fiber spikes can propagate to the spinal cord. A detailed description is given in the text. **(B)** C-fiber components of compound action potentials (CAPs) elicited by stimuli of normal (+150 μA × 1 ms, black) and inverted polarity (−150 μA × 1 ms, red). Given the difference in spike initiation sites, C-fiber latency is increased by 2–3 ms for inverted stimuli. The inset shows that a 1 ms stimulus of inverted polarity suppresses the A-fiber-mediated CAP component. **(C)** Dorsal root potential (DRP) recordings from hemisected spinal cord showing Aβ/δ- and C-fiber-driven DRPs. Left: Experimental design. Right: L4 DRPs (averages of 10 traces; recordings from the same preparation) induced by L5 root stimulation activating only Aβ/δ-fibers (+100 μA × 50 μs, black), only C-fibers (−150 μA × 1 ms, red), and Aβ/δ + C-fibers (+150 μA × 1 ms, blue). Inset scale bar: (10 μV, 20 ms). Note that C-fiber-induced DRP peaks at approximately 100 ms.

dorsal root close to its entrance to the spinal cord. The electrodes filled with the bath solution had a resistance of 20–100 kΩ .

Lamina I and X neurons were visualized for the whole cell patch-clamp recordings using the oblique infrared LED illumination technique (Safronov et al., 2007; Szûcs et al., 2009). Patch pipettes pulled from borosilicate glass using a P-87 horizontal puller (Sutter Instruments, USA) had a resistance of 3–5 MΩ after filling with the solution of the following composition: 145 K-gluconate, 2.5 $MgCl_2$, 10 HEPES, 2 Na_2-ATP, 0.5 Na-GTP, and 0.5 EGTA (pH 7.3). Neurons were voltage clamped at −70 or −60 mV. Offset potentials were compensated before seal formation. Liquid junction potentials were not compensated.

MultiClamp 700B amplifier and Digidata 1320A/Digidata 1440 digitizers under the control of the pClamp software (Molecular Devices, CA, USA) were used for data acquisition. Signals were Bessel filtered at 2.6 kHz and sampled at 20 kHz. All chemicals were from Sigma-Aldrich (MO, USA).

2.4. Electrical stimulations

Dorsal roots (L4 and/or L5) were stimulated *via* suction electrodes connected to ISO-Flex (AMPI, Israel) stimulators, as described (Krotov et al., 2019; Fernandes et al., 2020). Positive pulses of current (+150 μA × 1 ms) were applied to activate all primary afferents, including high-threshold-Aδ- and C-afferents. Selective activation of C-fibers was achieved by applying pulses of negative polarity (−150 μA × 1 ms) which induced an anodal block of fast conducting Aβ/δ-fibers (Fernandes et al., 2020). Stimuli were applied at 0.1 Hz to avoid the slowing-down of conduction in C-fibers (Pinto et al., 2008b) and the wind-up phenomenon (Hachisuka et al., 2018).

The monosynaptic input was identified on the basis of the low failure rates (< 30%) and small latency variations (less than 2 ms) as described previously (Pinto et al., 2008b; Krotov et al., 2019). Afferent fibers mediating direct input were classified according to their conduction velocity (CV), which was calculated as the length of the root, from the opening of the suction electrode to the dorsal root entry zone, divided by the latency of the monosynaptic response with a 1 ms allowance for synaptic transmission. Fibers with CV below 0.5 m/s were considered as C-fibers (Pinto et al., 2008a). Afferents with CV ranging from 0.6 to 1.4 m/s were classified as Aδ-afferents. Monosynaptic inputs from faster-conducting Aβ-afferents [CV > 3.5 m/s, (Pinto et al., 2008a)] were observed only in lamina I neurons.

2.5. Data analysis

Recordings were taken for quantitative analysis only if the series resistance of the electrode changed during the experiment by less than 20%. Amplitudes of the monosynaptic excitatory postsynaptic current (EPSC) components and EPSC integrals were analyzed with Clampfit software (Molecular Devices, CA, USA). The responses in control and after conditioning were compared for individual cells using Mann–Whitney non-parametric test. For each cell that showed significant differences, the median conditioned value was normalized to the median control one. Then, the data were pooled and presented as mean ± standard error of the mean (SEM). These data were compared using unpaired Student's *t*-test. Categorical data were compared using Fisher's exact test. Statistical significance was considered at $p < 0.05$.

3. Results

3.1. Studying AD-PI

Our approach relied on two main features. First, we used the *ex vivo* lumbosacral cord preparation which preserved its segmental afferent supply, the circuitries generating AD-PI, and neuronal connections, with an exception of functional descending pathways. Second, selective activation of C-fibers *via* induction of an anodal block of faster-conducting Aβ/δ-fibers. For that, we stimulated the dorsal roots with pulses of inverted (negative) polarity (**Figure 1A**). A normal (positive) pulse depolarized axons at the external end of the suction electrode lip. Spikes initiated by this local depolarization propagated toward the spinal cord. A pulse of inverted polarity produced depolarization (and spike initiation) at the internal end and hyperpolarization (anodal block) at the external end of the suction electrode lip. The pulse duration (1 ms) was adjusted to induce the anodal block of the Aβ/δ-fiber volley and to terminate before the arrival of the slow C-fiber volley. Thus, only the C-fiber volley could reach the spinal cord. Correct adjustment of the stimulation protocol was confirmed by recording CAPs (**Figure 1B**).

It should be noted that the major advantage of this approach is that it allows to use one suction electrode and a rectangular current pulse to activate C-fibers and to simultaneously produce an anodal block of the Aβ/δ-fiber volley. This substantially simplified the experimental design in small preparations with relatively short dorsal roots, where induction of the classical anodal block through an additional pair of polarizing electrodes (Mendell and Wall, 1964; Zimmermann, 1968a,b; Wagman and Price, 1969) becomes more difficult.

AD-PI is considered to be induced by PAD, which could be recorded as passively spreading DRP. Therefore, we recorded DRPs to study Aβ/δ- and C-afferent-induced AD-PI. We found that stimulation of both types of afferent evoked DRPs (**Figure 1C**). Since C-AD DRP peaked at 100–150 ms, the 100 ms interval between paired pulses was used in the experiments with whole-cell recordings to study heterosegmental C-AD-PI.

3.2. Homosegmental Aβ/δ-AD-PI

Homosegmental AD-PI is driven by the primary afferents running in the same segmental dorsal root. For Aβ/δ-fibers, this type of AD-PI was assessed using a 1 ms current pulse of normal and inverted polarity. Anodal block of Aβ/δ-fibers by the inverted stimuli disinhibited mono- and/or polysynaptic EPSCs mediated by the homosegmental C-fibers (**Figure 2**). Disinhibition of the monosynaptic responses occurred in two different ways. In 13–15% of lamina I and 9–17% of lamina X cells, an appearance of a new monosynaptic component (absent in control) reflected a complete Aβ/δ-AD-PI of supplying

C-afferents (Figures 2Aa, b). Such form of Aβ/δ AD-PI was seen for the neurons located in the segment of the primary afferent entrance (the L4 afferent input to the L4 neurons, the L5 afferent input to the L5 neurons) as well as in the adjacent rostral segment (the L5 afferent input to the L4 neurons). In 6 lamina I and 3 lamina X cells, we also observed an increase in the amplitude of already existing EPSCs (Figure 2Ac), suggesting the removal of a partial AD-PI affecting one of the terminal C-fiber branches. Disinhibition patterns were similar for the neighboring spinal segments (Figure 2B): the incidence of the L4 and L5 homosegmental Aβ/δ-AD-PI differed significantly neither for lamina I nor for lamina X ($p > 0.05$, Fisher's exact test). Moreover, the L5 C-fiber input to the L4 neurons was controlled by the L5 Aβ/δ-fibers to a similar extent ($p > 0.05$, Fisher's exact test). Given that both lamina I and X neurons showed Aβ/δ-AD-PI, one may assume that similar mechanisms control primary afferent input to these two major spinal nociceptive-processing areas.

3.3. Heterosegmental C-AD-PI

Given that both normal and inverted stimuli activated C-fibers, it was not possible to study interactions between the homosegmental C-afferents. Therefore, we investigated the inhibition of the afferents running in one root by the afferents from the neighboring segmental dorsal root. Paired-pulse protocol was applied to the L4 and L5 dorsal roots while recording from the L4 spinal neurons. We found that selective L5 C-fiber conditioning by inverted pulse significantly diminished the L4 afferent-mediated EPSCs (Figures 3A, B). The amplitudes of the monosynaptic Aδ-components were decreased by 35–40%, while most monosynaptic C-fiber inputs were inhibited completely. The monosynaptic Aβ-fiber input to lamina I neurons was weakly affected; a 10% amplitude reduction was observed in 1 out of 6 cells tested. Thus, heterosegmental C-AD-PI differently affects various classes of primary afferents.

The inputs from the L5 afferents to the L4 spinal neurons were modulated by the L4 C-fibers in a similar way (Figures 4A–C). Reduction of the monosynaptic Aβ-fiber input (Figure 4A) was observed in 3 out of 8 lamina I neurons and ranged from 11 to 21%. The monosynaptic Aδ responses (Figure 4B) and EPSC integrals were diminished by the C-fiber conditioning to 53–61% and 61%, respectively. Most C-fiber-mediated EPSCs were completely inhibited (Figure 4C). General statistics on the C-fiber-driven control of the afferent input to lamina I and X neurons is presented in Figures 5A, B. Note that for lamina I neurons neither the incidence nor the effect size differed significantly between L4 and L5 heterosegmental C-AD-PI ($p > 0.05$, Fisher's exact test and Student's t-test, respectively). Similarly, these parameters did not show significant differences for lamina X cells.

Heterosegmental C-AD-PI showed its physiological significance in controlling spike discharges in spinal neurons (Figure 6). We tested the effect of the C-fiber conditioning in 15 lamina I and 7 lamina X neurons. In 7 and 2 neurons, respectively, a significant decrease in the overall input and in the number of evoked spikes was observed. On average, the number of spikes was reduced to 41 ± 7% (lamina I) and to 37 ± 20% (lamina X) of control values (Figure 6). Therefore, C-AD-PI is one of the basic mechanisms controlling the excitability of the spinal network.

4. Discussion

In the present work, we used *ex vivo* spinal cord preparation with preserved dorsal roots and the technique of selective C-fiber activation to examine the effect of AD-PI on lamina I and X neurons in the mouse and rat. Our major findings are: (1) C-fiber input to the neurons is controlled by both Aβ/δ-AD-PI and C-AD-PI; (2) Aβ/δ-fiber input is subject to C-AD-PI; (3) the AD-PI is segmentally reciprocal, i.e., afferents from two adjacent dorsal roots reciprocally control input to the spinal neurons; (4) C-AD-PI decreases evoked spike discharges, thus demonstrating its physiological significance; and (5) AD-PI pattern is similar for lamina I and X neurons in the mouse and rat. Thus, AD-PI is likely to represent a general mechanism shaping primary afferent input to the neurons in the nociceptive-processing regions of the spinal cord.

The methodological approach we used for studying AD-PI has two principal advantages. First, our *ex vivo* spinal cord preparation preserved its segmental primary afferent supply and neuronal connectivity, with an exception of functional descending pathways. Unlike the spinal cord slices, the intact preparation allowed us to preserve the rostrocaudal and mediolateral connections between the neurons and to work with two adjacent dorsal roots, that was critically important for studying the heterosegmental AD-PI. Second, the dorsal root stimulation by the inverted pulse protocol allowed to selectively activate C-fibers. Thus, we investigated homosegmental Aβ/δ-AD-PI of C-fibers by comparing responses of neurons to the root stimulation by normal and inverted pulses, and the heterosegmental C-AD-PI by using selective C-fiber conditioning by inverted pulses. The main advantages of our approach are its simplicity, and reliability, and that it does not require any genetic modification of the animal model. At the same time, complementing this approach with optogenetic tools allowing specific activation of neurons or primary afferent/descending fibers may bring further benefits to the elucidation of basic mechanisms of PI.

The supraspinal control was shown to play an important role in shaping the functional connectivity between dorsal horn neurons (Contreras-Hernández et al., 2018; Martín et al., 2019). A transection of descending pathways in our preparation,

10.3389/fncel.2022.1029799

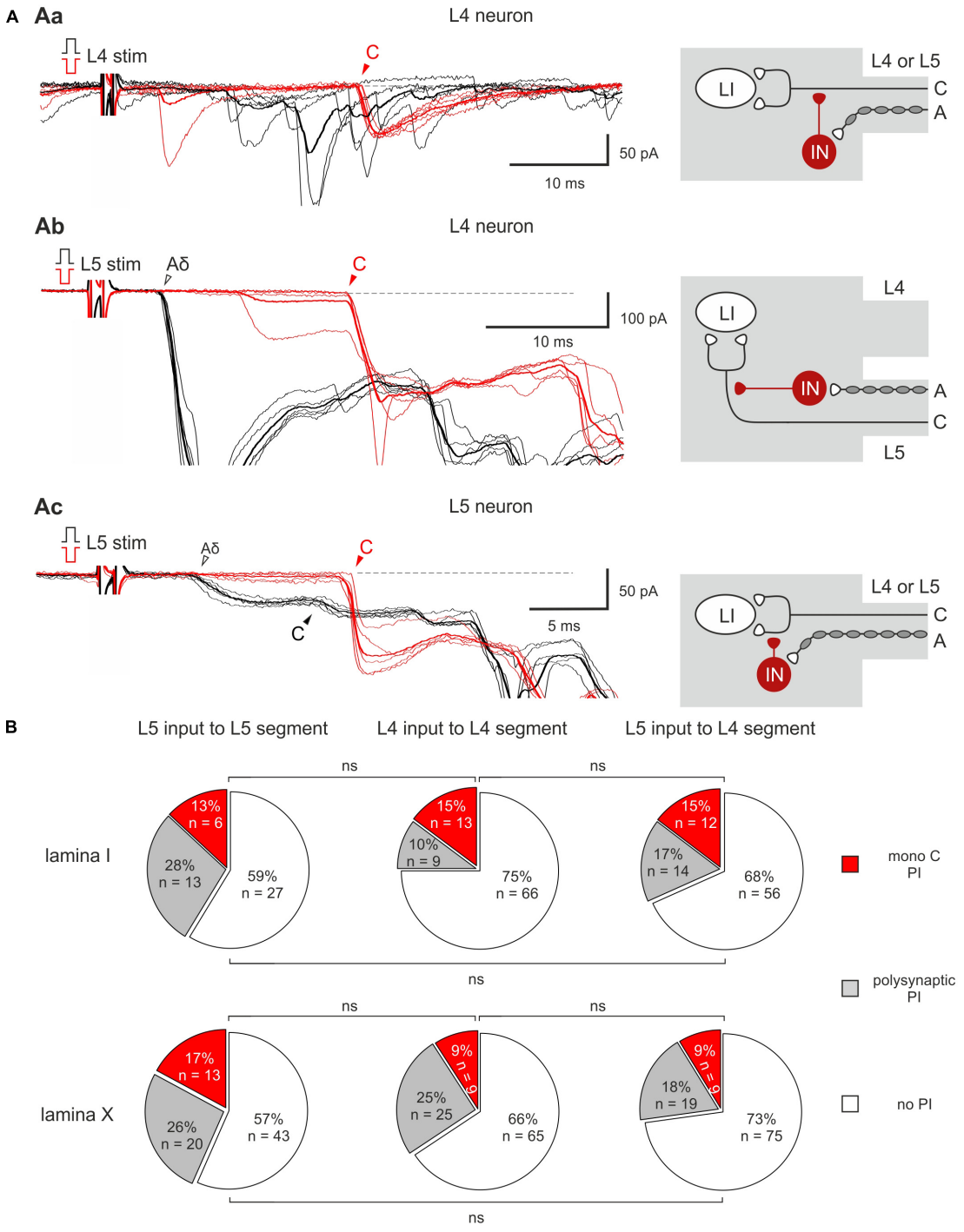

FIGURE 2

Homosegmental Aβ/δ-AD-PI of C-fiber inputs. **(Aa,b)** Left: complete inhibition of monosynaptic C-fiber inputs. The neuron was located in the segment of the primary afferent entrance **(Aa)** and in the adjacent rostral segment **(Ab)**. Right: putative schematics. **(Ac)** Left: partial suppression of a monosynaptic C-fiber input. Right: putative schematics. Individual (five traces) and averaged (bold) excitatory postsynaptic currents (EPSCs) evoked in spinal neurons by dorsal root stimulation by normal (black) and inverted (red) pulses. Normal pulse (+150 μA × 1 ms) was used to activate all primary afferents, while the pulse of inverted polarity (−150 μA × 1 ms) was applied to induce an anodal block of Aβ/δ-fibers and selectively activate C-fibers. The anodal block of Aβ/δ -fibers resulted in the disappearance of the monosynaptic Aδ-fiber-mediated EPSC (open arrowheads) but either in an appearance of a new monosynaptic C-fiber-mediated EPSC **(Aa,b)** or in an increase in the amplitude of already existing EPSC (**Ac**, note a 2-3 ms increase in the latency of the EPSC evoked by inverted pulse stimulation) which were relieved from AD-PI (filled arrowheads). IN, inhibitory interneuron; LI, lamina I neuron. Putative schemes are valid for both lamina I and X neurons. **(B)** Proportion of lamina I (top row) and lamina X (bottom row) neurons showing C-fiber input disinhibition after anodal block of Aβ/δ-fibers. ns, no significant difference (Fisher's exact test).

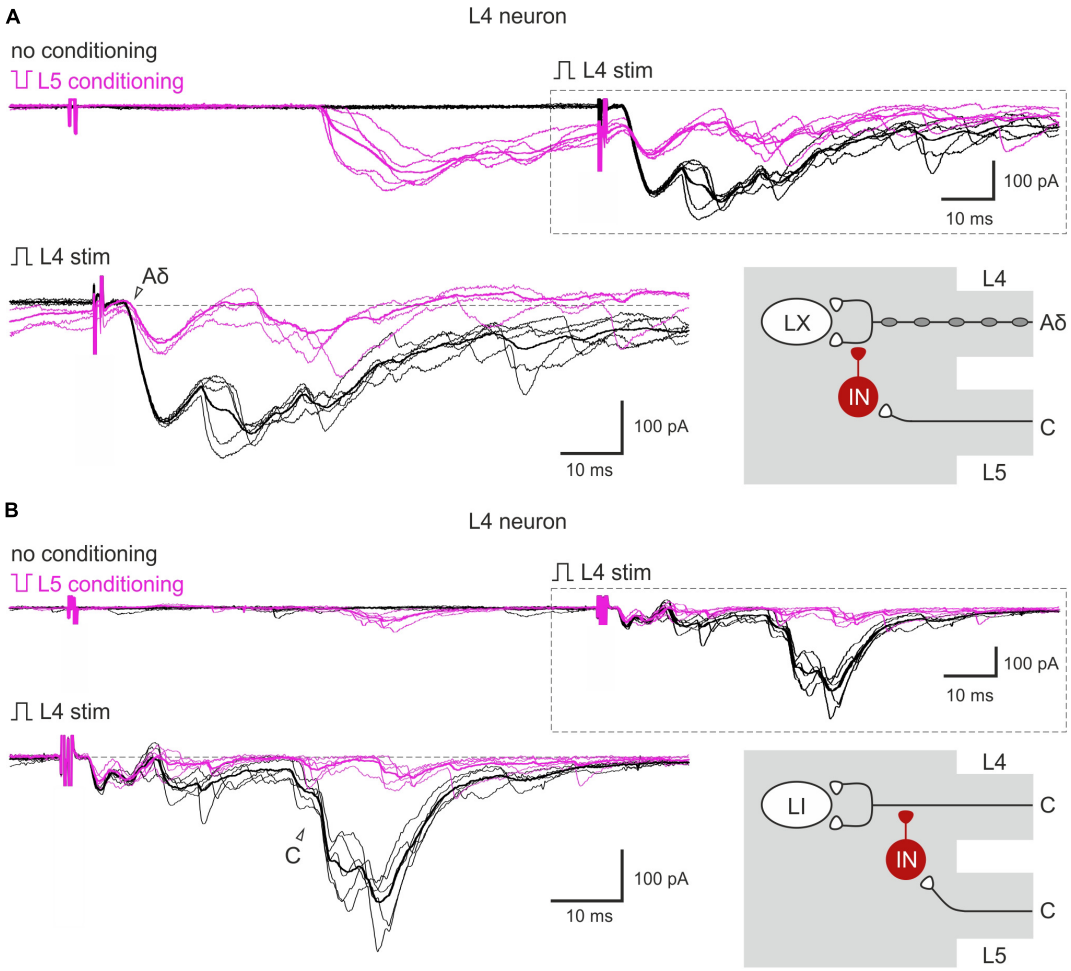

FIGURE 3
Heterosegmental AD-PI: the L5 C-fibers control the L4 afferent input. The L5 C-fibers induced inhibition of the L4 primary afferent inputs to the L4 spinal neurons. Excitatory postsynaptic currents (EPSCs) were evoked by the L4 root stimulation (normal pulse) in control (black) and after conditioning (100 ms interval) L5 root stimulation (inverted pulse) activating only C-fibers (magenta). The heterosegmental C-fiber conditioning induced a partial **(A)** or full **(B)** suppression of the monosynaptic Aδ- and C-fiber-mediated components of EPSCs (open arrowheads). Individual and averaged (bold) traces are shown. Traces in the insets are shown below at higher magnification and with membrane currents before EPSC initiation set to the same level. Putative schematics of AD-PI given on the right are valid for both lamina I and X neurons. IN, inhibitory interneuron; LI, lamina I neuron; LX, lamina X neuron.

allowed us to study spinal segmental mechanisms in the absence of supraspinal control. We have recently shown that descending PI might have a similar extent as segmental PI (Krotov et al., 2022), suggesting an involvement of the same pool of spinal interneurons. Given functional supraspinal input could seriously interfere with the AD-PI, its absence under our experimental conditions allowed unbiased estimates of the percentage of the AD-PI-affected neurons.

Since the classical gate control theory of pain (Melzack and Wall, 1965) suggested that primary afferents activated by innocuous stimuli affect the transmission of nociceptive information, Aβ/δ-AD-PI of nociceptive C-fibers was well expected. Homosegmental Aβ/δ-AD-PI of the C-fiber input was seen for the neurons in the segment of the dorsal root entrance as well as in the adjacent spinal segment.

The low-threshold Aβ/δ-afferent-mediated postsynaptic inhibition of lamina I neurons plays an important role in controlling their firing threshold and excitability (Luz et al., 2014). However, there are several arguments that the contribution of this and other postsynaptic mechanisms to homosegmental Aβ/δ-AD-PI of the C-fibers observed in our study was unlikely. First, the recordings were done in the voltage-clamp mode, in which inward and outward currents are strictly additive. To exclude the possibility that the monosynaptic C-fiber-mediated EPSC could be reduced by the temporarily coinciding Aβ/δ-fiber-mediated inhibitory postsynaptic current (IPSC) of the same kinetics, we confirmed

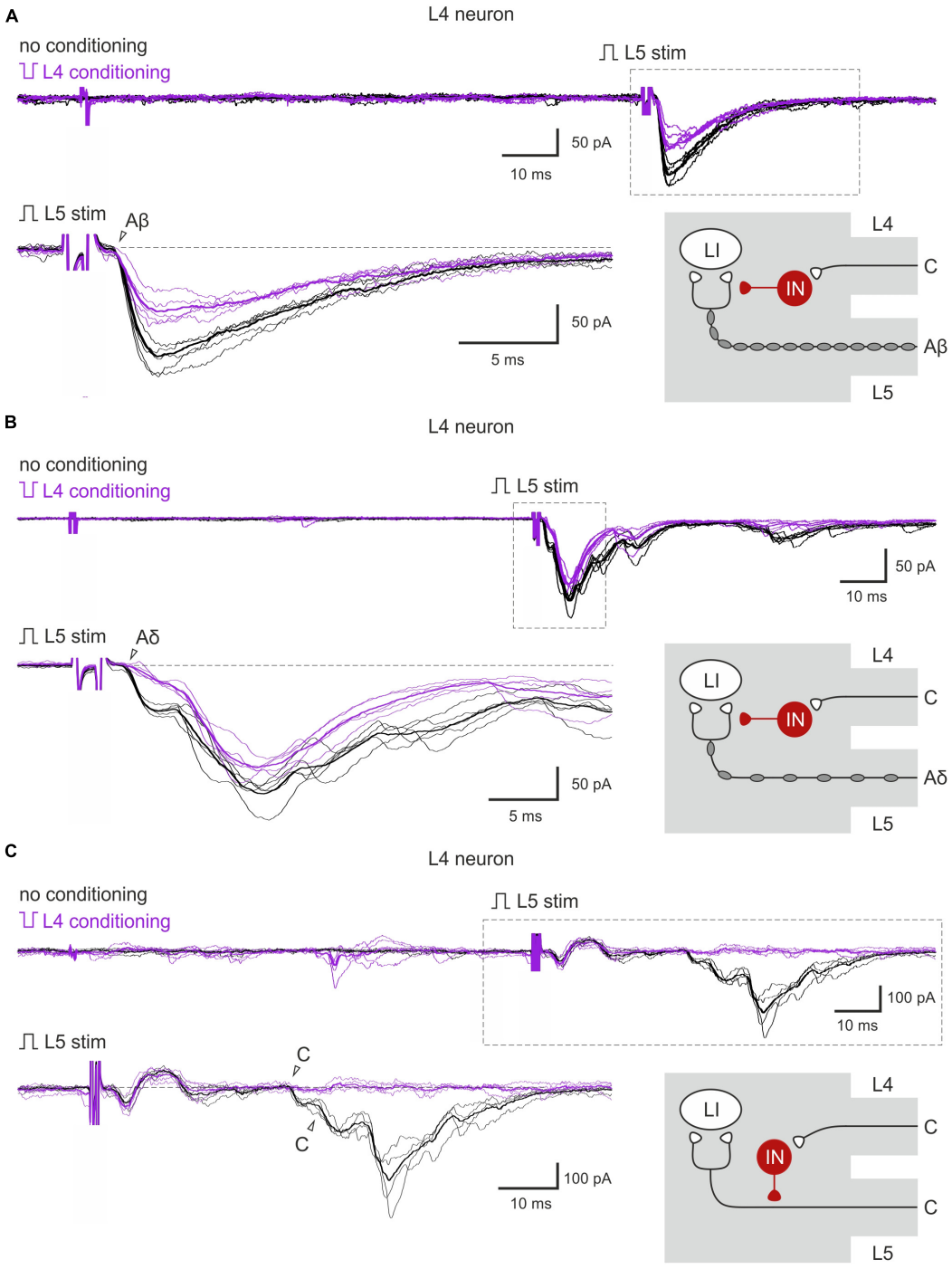

FIGURE 4
Heterosegmental AD-PI: the L4 C-fibers control the L5 afferent input. **(A–C)** Excitatory postsynaptic currents (EPSCs) evoked by L5 root stimulation (normal pulse) in control (black) and after conditioning (inverted pulse) L4 root stimulation (purple). Individual and averaged (bold) EPSCs are shown. Decreased monosynaptic Aβ- **(A)**, Aδ- **(B)**, and C-components **(C)** of the EPSCs are indicated by open arrowheads. Traces in the insets are shown below at higher magnification. Schematics showing PI induction are valid for both lamina I and X neurons. IN, inhibitory interneuron; LI, lamina I neuron.

that the latter was not evoked by selectively activating Aβ/δ-fibers (50 μs stimuli). Thus, the postsynaptic contribution of the GABAergic interneurons that have synaptic contacts with both the central terminals of primary afferents (PI) and spinal neurons (postsynaptic inhibition) (Bardoni et al., 2013; Boyle et al., 2019) could be excluded. Second, we have chosen

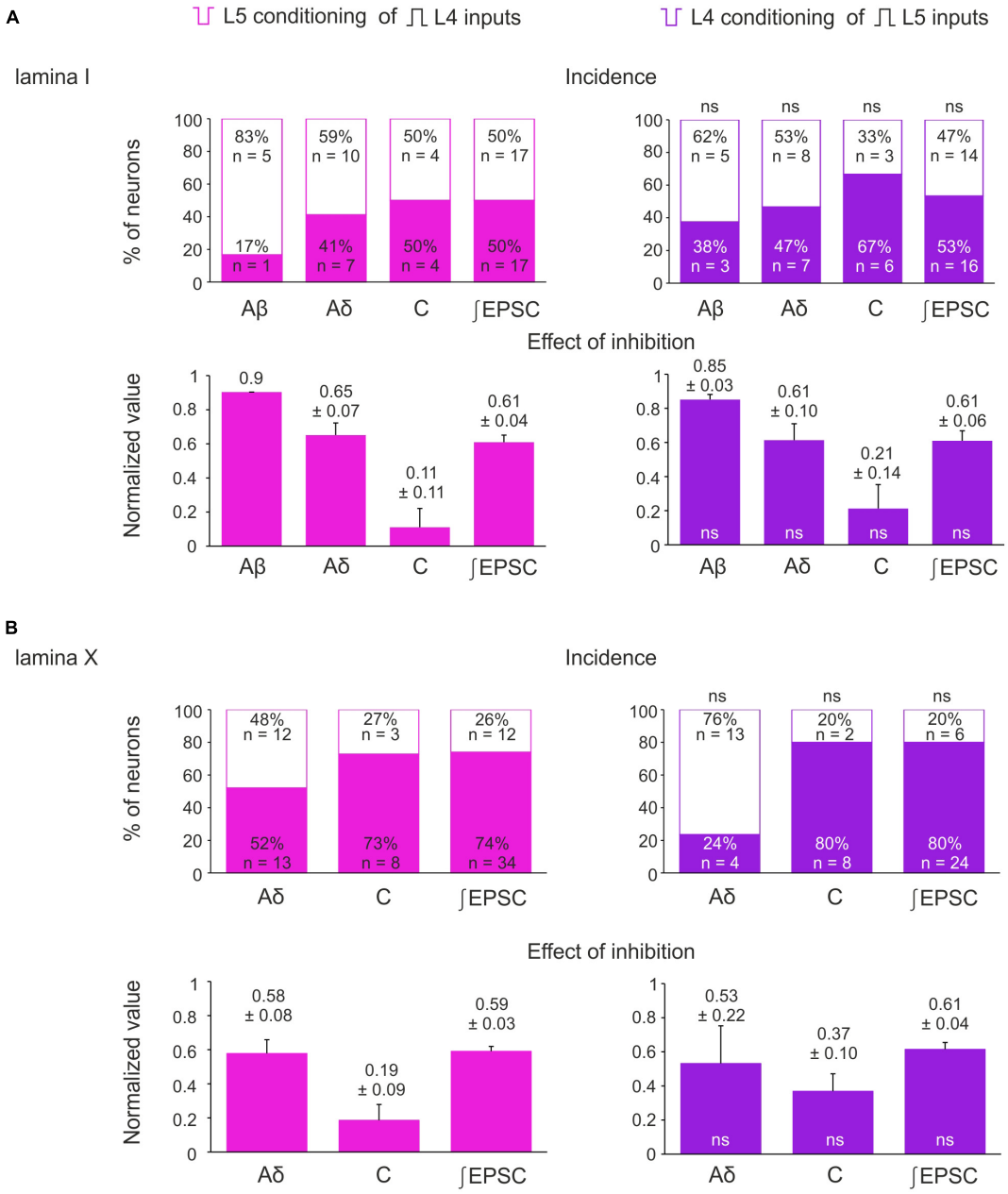

FIGURE 5
Incidence and strength of the heterosegmental C-AD-PI in spinal laminae I and X. **(A,B)** Top rows: percentage of lamina I neurons **(A)** and lamina X neurons **(B)** showing significant changes in the amplitude of their monosynaptic input and the excitatory postsynaptic current (EPSC) area after heterosegmental C-fiber conditioning. Bottom rows: decrease in the monosynaptic input amplitude and the EPSC area caused by the heterosegmental C-fiber conditioning. Data are represented as mean ± standard error of the mean (SEM). ns, no significant difference when compared to respective parameter from the left column (Fisher's exact test and Student's *t*-test for the incidence and the effect of inhibition, respectively).

a 0.1 Hz stimulation frequency to avoid induction of the short-term plasticity or release of kynurenic acid [accumulated in the glial cells (Tuboly et al., 2015)] that could affect the postsynaptic AMPA receptors. Thus, the homosegmental inhibition of C-fibers by Aβ/δ-fibers described here is likely to have a presynaptic nature.

Homotypic C-AD-PI of the C-fiber-induced responses received less attention, despite the fact that C-fibers contribute to the PAD generation (Franz and Iggo, 1968; Zimmermann, 1968a; Zimmerman et al., 2019) and evoke DRPs as strong as those evoked by Aβ/δ-fibers (Zimmerman et al., 2019; Fernandes et al., 2020). The physiological relevance of

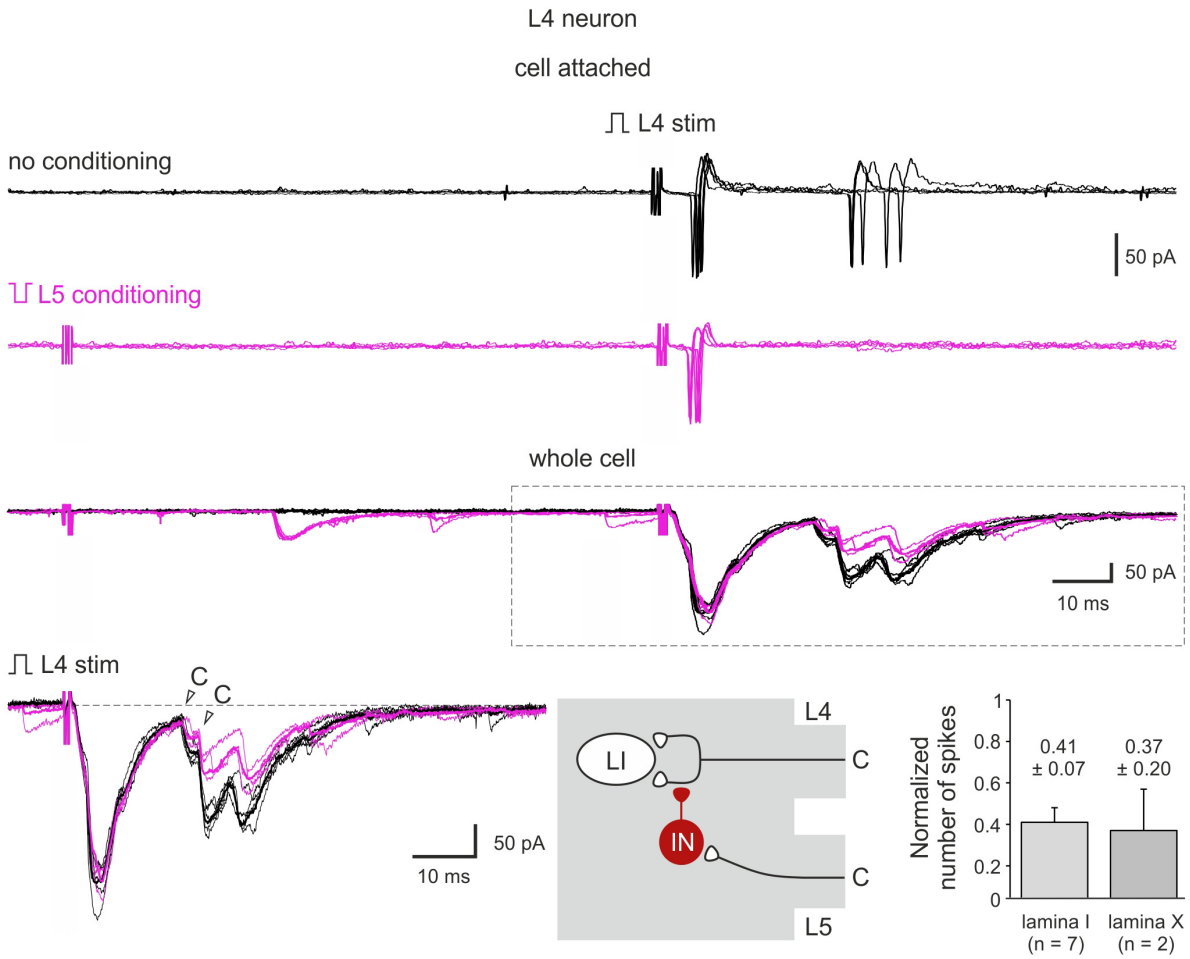

FIGURE 6
C-AD-PI controls spike discharges in spinal neurons. Cell-attached recording of action potential (AP) firing and the whole-cell recordings of the excitatory postsynaptic currents (EPSCs) evoked by the L4 dorsal root stimulation in a lamina I neuron in control (black) and after the L5 C-fiber conditioning (magenta). Individual (five traces) and averaged (bold) traces of the EPSCs are shown. Bottom middle: schematics showing PI induction. IN, inhibitory interneuron; LI, lamina I neuron. Traces in the inset are shown below at higher magnification. Bottom right: decrease in the number of spikes in lamina I and lamina X neurons.

the C-fiber-driven modulation of other C-fibers is yet to be elucidated, but it might indicate an interplay between C-afferents conveying information about different modalities of nociceptive information. The same might be the case for C-AD-PI of Aβ/δ-fiber input. Aδ-afferents (Mackenzie et al., 1975; Simone and Kajander, 1997; Todd, 2010) and, to a lesser extent, Aβ-afferents (Djouhri and Lawson, 2004; Nagi et al., 2019) are also involved in the transmission of noxious stimuli. However, these forms of AD-PI may reflect the presence of complex neuronal networks controlling the processing of noxious and innocuous primary afferent inputs.

AD-PI in lamina I has a plausible mechanistic explanation. Axo-axonic synapses, generally considered as a structural basis for PI (Conradi et al., 1983), target C-fiber terminals forming type I glomeruli in the middle and ventral parts of lamina II (Ribeiro-Da-Silva and Coimbra, 1982; Ribeiro-da-silva et al., 1989; Todd, 1996)—a zone to which ventral dendrites of lamina I neurons protrude (Fernandes et al., 2016, 2020). Some local circuit interneurons have dendrites extending up to lamina III (Fernandes et al., 2016) where type II glomeruli (formed by myelinated A-afferents) are abundant (Ribeiro-Da-Silva and Coimbra, 1982). Glomerular PI can suppress transmission in individual synapses and produce a partial suppression of C- and A-afferent input.

On the other hand, glomeruli are not reported in lamina X. Moreover, lamina I is practically devoid of glomeruli or simple axo-axonic synapses (Ribeiro-Da-Silva and Coimbra, 1982; Ribeiro-da-silva et al., 1989; Alvarez et al., 1993), despite being enriched with Aδ- and C-fiber terminals (Todd, 2010). Although rare axo-axonic synapses might be sufficient for AD-PI induction (Segev, 1990), some other glomeruli-independent mechanisms of AD-PI generation should also be considered.

Non-synaptic AD-PI mechanisms may involve $GABA_A$ receptors, expressed in the central axons and terminals of thin afferents (Knabl et al., 2008; Witschi et al., 2011; Paul et al., 2012; Lorenzo et al., 2014). These receptors might be activated *via* volume transmission by GABA released from interneurons or astrocytes (Christensen et al., 2018; Comitato and Bardoni, 2021). Alternatively, shunting inhibition might be mediated by AMPA and NMDA receptors (Russo et al., 2000; Comitato and Bardoni, 2021), which are also expressed in the central terminals of primary afferents (Liu et al., 1994; Bardoni et al., 2004). All these mechanisms may contribute to the suppression of signals in the non-glomerular terminal boutons or the parent branches of primary afferents. This can explain the complete inhibition of EPSC components observed in our experiments. The non-synaptic mechanism may play a major role in the induction of AD-PI in lamina X neurons and in Aδ- and peptidergic C-fibers that terminate in lamina I (Todd, 2010).

Despite the obvious physiological importance of AD-PI, we still have limited knowledge about its segmental organization. AD-PI induced by stimulating L4 and L5 roots exhibits segmental reciprocity that could be expected from earlier studies of DRPs (Wall and Lidierth, 1997; Lidierth, 2006). In both laminae I and X, inputs from these two adjacent roots are under reciprocal control. This feature might be relevant for the spatial discrimination of stimuli or for avoiding an excessive excitation when the input from one peripheral point arrives *via* adjacent dorsal roots (Pinto et al., 2008b, 2010). Furthermore, C-AD-PI controls spike discharge evoked by the afferent stimulation, indicating that this form of inhibition has a direct impact on the activity of spinal neuronal circuitries. It should be noted that in our experiments the whole dorsal roots were stimulated, and therefore, the reciprocity and functional impact observed reflect afferent interactions at the segmental level. This might not necessarily mean that the reciprocal inhibition occurs and/or has a functional impact at the level of individual afferents. More specific ways of physiological stimulation of different classes of primary afferents would be needed to clarify this issue.

Our study describes how AD-PI affects peripheral inputs to spinal neurons in laminae I and X. For lamina I, the pattern of the AD-PI induction is similar for the mouse (our study) and rat (Fernandes et al., 2020), suggesting a fundamental role of AD-PI in nociceptive processing in mammalians. There is virtually no difference in how the AD-PI affects the neuron populations in laminae I and X; they both exhibit the L4/L5 segmental reciprocity and AD-PI-mediated control of neuronal spike discharges. This may be explained by the fact that both these layers are involved in nociceptive-processing and their neurons show similar intrinsic properties and primary afferent supply (Light and Perl, 1979; Honda, 1985; Honda and Perl, 1985; Fernandes et al., 2016; Krotov et al., 2019). Presynaptic control of the afferent input occurs in a substantial percentage of cells. This observation was done in the experiments in which the whole dorsal root was stimulated and may reflect the fact that AD-PI broadly affects the spinal sensory network. At the same time, AD-PI is not ubiquitous, suggesting that it can control processing of sensory information in specific cell circuitries.

Data availability statement

The raw data supporting the conclusions of this article will be made available by the authors, without undue reservation.

Ethics statement

The animal study was reviewed and approved by the Animal Ethics Committee of the Bogomoletz Institute of Physiology (Kyiv, Ukraine).

Author contributions

VK: concept of the study, research design, electrophysiological recordings, data analysis and interpretation, and manuscript preparation. KA, SR, OH, and YA: electrophysiological recordings and data analysis. BVS: manuscript preparation and critical revision. PB and NV: conceiving the study and manuscript revision. All authors contributed to the article and approved the submitted version.

Funding

This work was supported by the NASU Stipend for Young Scientists (VK), grant of the NAS of Ukraine to research laboratories/groups of young scientists of the NAS of Ukraine for conducting research in priority areas of the development of science and technology in 2022–2023 (OH), PTDC/NEU-NMC/1259/2014 POCI-01-0145-FEDER-016588 and POCI-01-0145-FEDER-016385 (BVS), 1R01NS113189-01 (PB and NV), and NASU grant 0118U007345 (PB).

Acknowledgments

The authors are thankful to Dr. Olga Kopach (University College London) and Mr. Anrdew Dromaretsky (Bogomoletz Institute of Physiology).

Conflict of interest

The authors declare that the research was conducted in the absence of any commercial or financial relationships that could be construed as a potential conflict of interest.

Publisher's note

References

Alvarez, F. J., Kavookjian, A. M., and Light, A. R. (1993). Ultrastructural morphology, synaptic relationships, and CGRP immunoreactivity of physiologically identified C-fiber terminals in the monkey spinal cord. *J. Comp. Neurol.* 329, 472–490. doi: 10.1002/CNE.903290405

Bardoni, R., Takazawa, T., Tong, C. K., Choudhury, P., Scherrer, G., and Macdermott, A. B. (2013). Pre- and postsynaptic inhibitory control in the spinal cord dorsal horn. *Ann. N. Y. Acad. Sci.* 1279, 90–96. doi: 10.1111/NYAS.12056

Bardoni, R., Torsney, C., Tong, C. K., Prandini, M., and MacDermott, A. B. (2004). Presynaptic NMDA receptors modulate glutamate release from primary sensory neurons in rat spinal cord dorsal horn. *J. Neurosci.* 24, 2774–2781. doi: 10.1523/JNEUROSCI.4637-03.2004

Boyle, K. A., Gradwell, M. A., Yasaka, T., Dickie, A. C., Polgár, E., Ganley, R. P., et al. (2019). Defining a spinal microcircuit that gates myelinated afferent input: Implications for tactile allodynia. *Cell Rep.* 28, 526.e6–540.e6. doi: 10.1016/J.CELREP.2019.06.040

Calvillo, O., Madrid, J., and Rudomín, P. (1982). Presynaptic depolarization of unmyelinated primary afferent fibers in the spinal cord of the cat. *Neuroscience* 7, 1389–1400. doi: 10.1016/0306-4522(82)90252-4

Chen, J. T. C., Guo, D., Campanelli, D., Frattini, F., Mayer, F., Zhou, L., et al. (2014). Presynaptic GABAergic inhibition regulated by BDNF contributes to neuropathic pain induction. *Nat. Commun.* 5:5331. doi: 10.1038/NCOMMS6331

Christensen, R. K., Delgado-Lezama, R., Russo, R. E., Lind, B. L., Alcocer, E. L., Rath, M. F., et al. (2018). Spinal dorsal horn astrocytes release GABA in response to synaptic activation. *J. Physiol.* 596, 4983–4994. doi: 10.1113/JP276562

Comitato, A., and Bardoni, R. (2021). Presynaptic inhibition of pain and touch in the spinal cord: From receptors to circuits. *Int. J. Mol. Sci.* 22, 1–13. doi: 10.3390/IJMS22010414

Conradi, S., Cullheim, S., Gollvik, L., and Kellerth, J. O. (1983). Electron microscopic observations on the synaptic contacts of group Ia muscle spindle afferents in the cat lumbosacral spinal cord. *Brain Res.* 265, 31–39. doi: 10.1016/0006-8993(83)91330-6

Contreras-Hernández, E., Chávez, D., Hernández, E., Velázquez, E., Reyes, P., Béjar, J., et al. (2018). Supraspinal modulation of neuronal synchronization by nociceptive stimulation induces an enduring reorganization of dorsal horn neuronal connectivity. *J. Physiol.* 596:1747. doi: 10.1113/JP275228

Djouhri, L., and Lawson, S. N. (2004). Abeta-fiber nociceptive primary afferent neurons: A review of incidence and properties in relation to other afferent A-fiber neurons in mammals. *Brain Res. Brain Res. Rev.* 46, 131–145. doi: 10.1016/J.BRAINRESREV.2004.07.015

Fernandes, E. C., Luz, L. L., Mytakhir, O., Lukoyanov, N. V., Szucs, P., and Safronov, B. V. (2016). Diverse firing properties and Aβ-, Aδ-, and C-afferent inputs of small local circuit neurons in spinal lamina I. *Pain* 157, 475–487. doi: 10.1097/J.PAIN.0000000000000394

Fernandes, E. C., Pechincha, C., Luz, L. L., Kokai, E., Szucs, P., and Safronov, B. V. (2020). Primary afferent-driven presynaptic inhibition of C-fiber inputs to spinal lamina I neurons. *Prog. Neurobiol.* 188:101786. doi: 10.1016/j.pneurobio.2020.101786

Fink, A. J. P., Croce, K. R., Huang, Z. J., Abbott, L. F., Jessell, T. M., and Azim, E. (2014). Presynaptic inhibition of spinal sensory feedback ensures smooth movement. *Nature* 509, 43–48. doi: 10.1038/NATURE13276

Fitzgerald, M., and Woolf, C. J. (1981). Effects of cutaneous nerve and intraspinal conditioning of C-fibre afferent terminal excitability in decerebrate spinal rats. *J. Physiol.* 318, 25–39. doi: 10.1113/JPHYSIOL.1981.SP013848

François, A., Low, S. A., Sypek, E. I., Christensen, A. J., Sotoudeh, C., Beier, K. T., et al. (2017). A brainstem-spinal cord inhibitory circuit for mechanical pain modulation by GABA and enkephalins. *Neuron* 93, 822.e6–839.e6. doi: 10.1016/J.NEURON.2017.01.008

Franz, D. N., and Iggo, A. (1968). Dorsal root potentials and ventral root reflexes evoked by nonmyelinated fibers. *Science* 162, 1140–1142. doi: 10.1126/SCIENCE.162.3858.1140

Guo, D., and Hu, J. (2014). Spinal presynaptic inhibition in pain control. *Neuroscience* 283C, 95–106. doi: 10.1016/j.neuroscience.2014.09.032

Hachisuka, J., Omori, Y., Chiang, M. C., Gold, M. S., Koerber, H. R., and Ross, S. E. (2018). Wind-up in lamina I spinoparabrachial neurons. *Pain* 159, 1484–1493. doi: 10.1097/j.pain.0000000000001229

Hentall, I. D., and Fields, H. L. (1979). Segmental and descending influences on intraspinal thresholds of single C-fibers. *J. Neurophysiol.* 42, 1527–1537. doi: 10.1152/JN.1979.42.6.1527

Honda, C. N. (1985). Visceral and somatic afferent convergence onto neurons near the central canal in the sacral spinal cord of the cat. *J. Neurophysiol.* 53, 1059–1078. doi: 10.1152/jn.1985.53.4.1059

Honda, C. N., and Perl, E. R. (1985). Functional and morphological features of neurons in the midline region of the caudal spinal cord of the cat. *Brain Res.* 340, 285–295. doi: 10.1016/0006-8993(85)90925-4

Knabl, J., Witschi, R., Hösl, K., Reinold, H., Zeilhofer, U. B., Ahmadi, S., et al. (2008). Reversal of pathological pain through specific spinal GABAA receptor subtypes. *Nature* 451, 330–334. doi: 10.1038/NATURE06493

Krotov, V., Agashkov, K., Krasniakova, M., Safronov, B. V., Belan, P., and Voitenko, N. (2022). Segmental and descending control of primary afferent input to the spinal lamina X. *Pain* 163, 2014–2020. doi: 10.1097/j.pain.0000000000002597

Krotov, V., Tokhtamysh, A., Kopach, O., Dromaretsky, A., Sheremet, Y., Belan, P., et al. (2017). Functional characterization of lamina X neurons in ex-vivo spinal cord preparation. *Front. Cell Neurosci.* 11:342. doi: 10.3389/fncel.2017.00342

Krotov, V., Tokhtamysh, A., Safronov, B. V., Belan, P., and Voitenko, N. (2019). High-threshold primary afferent supply of spinal lamina X neurons. *Pain* 160, 1982–1988. doi: 10.1097/j.pain.0000000000001586

Lidierth, M. (2006). Local and diffuse mechanisms of primary afferent depolarization and presynaptic inhibition in the rat spinal cord. *J. Physiol.* 576, 309–327. doi: 10.1113/JPHYSIOL.2006.110577

Light, A. R., and Perl, E. R. (1979). Spinal termination of functionally identified primary afferent neurons with slowly conducting myelinated fibers. *J. Comp. Neurol.* 186, 133–150. doi: 10.1002/cne.901860203

Liu, H., Wang, H., Sheng, M., Jan, L. Y., Jan, Y. N., and Basbaum, A. I. (1994). Evidence for presynaptic N-methyl-D-aspartate autoreceptors in the spinal cord dorsal horn. *Proc. Natl. Acad. Sci. U.S.A.* 91, 8383–8387. doi: 10.1073/PNAS.91.18.8383

Lorenzo, L. E., Godin, A. G., Wang, F., St-Louis, M., Carbonetto, S., Wiseman, P. W., et al. (2014). Gephyrin clusters are absent from small diameter primary afferent terminals despite the presence of GABAA receptors. *J. Neurosci.* 34, 8300–8317. doi: 10.1523/JNEUROSCI.0159-14.2014

Luz, L. L., Fernandes, E. C., Sivado, M., Kokai, E., Szucs, P., and Safronov, B. V. (2015). Monosynaptic convergence of somatic and visceral C-fiber afferents on projection and local circuit neurons in lamina I: A substrate for referred pain. *Pain* 156, 2042–2051. doi: 10.1097/J.PAIN.0000000000000267

Luz, L. L., Szucs, P., and Safronov, B. V. (2014). Peripherally driven low-threshold inhibitory inputs to lamina I local-circuit and projection neurones: A new circuit for gating pain responses. *J. Physiol.* 592, 1519–1534. doi: 10.1113/jphysiol.2013.269472

Mackenzie, R. A., Burke, D., Skuse, N. F., and Lethlean, A. K. (1975). Fibre function and perception during cutaneous nerve block. *J. Neurol. Neurosurg. Psychiatry* 38:865. doi: 10.1136/JNNP.38.9.865

Martín, M., Béjar, J., Chávez, D., Ramírez-Morales, A., Hernández, E., Moreno, L., et al. (2019). Supraspinal shaping of adaptive transitions in the state of functional connectivity between segmentally distributed dorsal horn neuronal

populations in response to nociception and antinociception. *Front. Syst. Neurosci.* 13:47. doi: 10.3389/fnsys.2019.00047

Melzack, R., and Wall, P. D. (1965). Pain mechanisms: A new theory. *Science* 150, 971–979. doi: 10.1126/SCIENCE.150.3699.971

Mendell, L. M., and Wall, P. D. (1964). Presynaptic hyperpolarization: A role for fine afferent fibres. *J. Physiol.* 172, 274–294. doi: 10.1113/JPHYSIOL.1964.SP007417

Nagi, S. S., Marshall, A. G., Makdani, A., Jarocka, E., Liljencrantz, J., Ridderström, M., et al. (2019). An ultrafast system for signaling mechanical pain in human skin. *Sci. Adv.* 5:eaaw1297. doi: 10.1126/sciadv.aaw1297

Paul, J., Zeilhofer, H. U., and Fritschy, J. M. (2012). Selective distribution of GABA(A) receptor subtypes in mouse spinal dorsal horn neurons and primary afferents. *J. Comp. Neurol.* 520, 3895–3911. doi: 10.1002/CNE.23129

Pinto, V., Szûcs, P., Derkach, V. A., and Safronov, B. V. (2008b). Monosynaptic convergence of C- and Adelta-afferent fibres from different segmental dorsal roots on to single substantia gelatinosa neurones in the rat spinal cord. *J. Physiol.* 586, 4165–4177. doi: 10.1113/jphysiol.2008.154898

Pinto, V., Derkach, V. A., and Safronov, B. V. (2008a). Role of TTX-sensitive and TTX-resistant sodium channels in Aδ- and C-fiber conduction and synaptic transmission. *J. Neurophysiol.* 99, 617–628. doi: 10.1152/JN.00944.2007

Pinto, V., Szucs, P., Lima, D., and Safronov, B. V. (2010). Multisegmental A{delta}- and C-fiber input to neurons in lamina I and the lateral spinal nucleus. *J. Neurosci.* 30, 2384–2395. doi: 10.1523/JNEUROSCI.3445-09.2010

Ramírez-Morales, A., Hernández, E., and Rudomin, P. (2021). Nociception induces a differential presynaptic modulation of the synaptic efficacy of nociceptive and proprioceptive joint afferents. *Exp. Brain Res.* 239, 2375–2397. doi: 10.1007/S00221-021-06140-6

Ribeiro-Da-Silva, A., and Coimbra, A. (1982). Two types of synaptic glomeruli and their distribution in laminae I-III of the rat spinal cord. *J. Comp. Neurol.* 209, 176–186. doi: 10.1002/CNE.902090205

Ribeiro-da-silva, A., Tagari, P., and Cuello, A. C. (1989). Morphological characterization of substance P-like immunoreactive glomeruli in the superficial dorsal horn of the rat spinal cord and trigeminal subnucleus caudalis: A quantitative study. *J. Comp. Neurol.* 281, 497–515. doi: 10.1002/CNE.902810402

Rudomin, P., and Schmidt, R. F. (1999). Presynaptic inhibition in the vertebrate spinal cord revisited. *Exp. Brain Res.* 129, 1–37. doi: 10.1007/S002210050933

Russo, R. E., Delgado-Lezama, R., and Hounsgaard, J. (2000). Dorsal root potential produced by a TTX-insensitive micro-circuitry in the turtle spinal cord. *J. Physiol.* 528, 115–122. doi: 10.1111/J.1469-7793.2000.00115.X

Safronov, B. V., Pinto, V., and Derkach, V. A. (2007). High-resolution single-cell imaging for functional studies in the whole brain and spinal cord and thick tissue blocks using light-emitting diode illumination. *J. Neurosci. Methods* 164, 292–298. doi: 10.1016/j.jneumeth.2007.05.010

Segev, I. (1990). Computer study of presynaptic inhibition controlling the spread of action potentials into axonal terminals. *J. Neurophysiol.* 63, 987–998. doi: 10.1152/JN.1990.63.5.987

Simone, D. A., and Kajander, K. C. (1997). Responses of cutaneous A-fiber nociceptors to noxious cold. *J. Neurophysiol.* 77, 2049–2060. doi: 10.1152/JN.1997.77.4.2049

Szûcs, P., Pinto, V., and Safronov, B. V. (2009). Advanced technique of infrared LED imaging of unstained cells and intracellular structures in isolated spinal cord, brainstem, ganglia and cerebellum. *J. Neurosci. Methods* 177, 369–380. doi: 10.1016/j.jneumeth.2008.10.024

Tadokoro, T., Bravo-Hernandez, M., Agashkov, K., Kobayashi, Y., Platoshyn, O., Navarro, M., et al. (2022). Precision spinal gene delivery-induced functional switch in nociceptive neurons reverses neuropathic pain. *Mol. Ther.* 30, 2722–2745. doi: 10.1016/J.YMTHE.2022.04.023

Todd, A. J. (1996). GABA and glycine in synaptic glomeruli of the rat spinal dorsal horn. *Eur. J. Neurosci.* 8, 2492–2498. doi: 10.1111/J.1460-9568.1996.TB01543.X

Todd, A. J. (2010). Neuronal circuitry for pain processing in the dorsal horn. *Nat. Rev. Neurosci.* 11, 823–836. doi: 10.1038/nrn2947

Tuboly, G., Tar, L., Bohar, Z., Safrany-Fark, A., Petrovszki, Z., Kekesi, G., et al. (2015). The inimitable kynurenic acid: The roles of different ionotropic receptors in the action of kynurenic acid at a spinal level. *Brain Res. Bull.* 112, 52–60. doi: 10.1016/J.BRAINRESBULL.2015.02.001

Wagman, I. H., and Price, D. D. (1969). Responses of dorsal horn cells of M. mulatta to cutaneous and sural nerve A and C fiber stimuli. *J. Neurophysiol.* 32, 803–817. doi: 10.1152/JN.1969.32.6.803

Wall, P. D., and Lidierth, M. (1997). Five sources of a dorsal root potential: Their interactions and origins in the superficial dorsal horn. *J. Neurophysiol.* 78, 860–871. doi: 10.1152/JN.1997.78.2.860

Willis, W. D. (1999). Dorsal root potentials and dorsal root reflexes: A double-edged sword. *Exp. Brain Res.* 124, 395–421. doi: 10.1007/S002210050637

Witschi, R., Punnakkal, P., Paul, J., Walczak, J. S., Cervero, F., Fritschy, J. M., et al. (2011). Presynaptic alpha2-GABAA receptors in primary afferent depolarization and spinal pain control. *J. Neurosci.* 31, 8134–8142. doi: 10.1523/JNEUROSCI.6328-10.2011

Zimmerman, A. L., Kovatsis, E. M., Pozsgai, R. Y., Tasnim, A., Zhang, Q., and Ginty, D. D. (2019). Distinct modes of presynaptic inhibition of cutaneous afferents and their functions in behavior. *Neuron* 102, 420.e8–434.e8. doi: 10.1016/J.NEURON.2019.02.002

Zimmermann, M. (1968a). Dorsal root potentials after C-fiber stimulation. *Science* 160, 896–898. doi: 10.1126/SCIENCE.160.3830.896

Zimmermann, M. (1968b). Selective activation of C-fibers. *Pflugers Arch. Gesamte Physiol. Menschen Tiere* 301, 329–333. doi: 10.1007/BF00362643

frontiers | Frontiers in Cellular Neuroscience

TYPE Mini Review
PUBLISHED 24 March 2023
DOI 10.3389/fncel.2023.1153593

OPEN ACCESS

EDITED BY
Jacopo Lamanna,
Vita-Salute San Raffaele University, Italy

REVIEWED BY
Richard J. Weinberg,
University of North Carolina at Chapel Hill, United States
Miquel Bosch,
International University of Catalonia, Spain

*CORRESPONDENCE
Maura Francolini
✉ maura.francolini@unimi.it

†These authors have contributed equally to this work

SPECIALTY SECTION
This article was submitted to Cellular Neurophysiology, a section of the journal Frontiers in Cellular Neuroscience

RECEIVED 29 January 2023
ACCEPTED 13 March 2023
PUBLISHED 24 March 2023

CITATION
Maiellano G, Scandella L and Francolini M (2023) Exploiting volume electron microscopy to investigate structural plasticity and stability of the postsynaptic compartment of central synapses.
Front. Cell. Neurosci. 17:1153593.
doi: 10.3389/fncel.2023.1153593

Exploiting volume electron microscopy to investigate structural plasticity and stability of the postsynaptic compartment of central synapses

Greta Maiellano[1,2†], Lucrezia Scandella[1†] and Maura Francolini[1*]

[1]Department of Medical Biotechnology and Translational Medicine, Università degli Studi di Milano, Milan, Italy, [2]MeLis, CNRS UMR 5284, INSERMU1314, Institut NeuroMyoGène, Université de Lyon, Université Claude Bernard Lyon 1, Lyon, France

Volume reconstruction from electron microscopy datasets is a tool increasingly used to study the ultrastructure of the synapse in the broader context of neuronal network and brain organization. Fine modifications of synapse structure, such as activity-dependent dendritic spine enlargement and changes in the size and shape of the postsynaptic density, occur upon maturation and plasticity. The lack of structural plasticity or the inability to stabilize potentiated synapses are associated with synaptic and neuronal functional impairment. Mapping these rearrangements with the high resolution of electron microscopy proved to be essential in order to establish precise correlations between the geometry of synapses and their functional states. In this review we discuss recent discoveries on the substructure of the postsynaptic compartment of central excitatory synapses and how those are correlated with functional states of the neuronal network. The added value of volume electron microscopy analyses with respect to conventional transmission electron microscopy studies is highlighted considering that some limitations of volume-based methods imposed several adjustments to describe the geometry of this synaptic compartment and new parameters–that are good indicators of synapses strength and activity–have been introduced.

KEYWORDS

volume electron microscopy (vEM), postsynaptic density (PSD), structural plasticity, dendritic spine enlargement, axon-spine interface, synaptic apposition surface, synapse, synaptic stability

Introduction

Our brain discards old and useless information in favor of new and more important ones thanks to one of its amazing properties: synaptic plasticity. Synaptic plasticity underlies the ability to respond to activity-dependent stimuli (Citri and Malenka, 2008; Goto, 2022). The neuronal activity generated by any experience directly modifies the neural circuit by remodeling synaptic transmission itself, which is made possible by the release of

neurotransmitter from the pre- to the postsynaptic terminal. Activity-dependent changes occur structurally at the level of the synapse, either by formation of new synapses or by modification of pre-existing ones, and, therefore influence how we think, feel and behave. Those structural changes affect subsynaptic structures such as the active zone (AZ) in the presynaptic compartment as well as the postsynaptic density (PSD) and dendritic spines in the postsynaptic neuron. These different structures are highly correlated in their size, so their dimensions are often used as a measure of the activity and strength of the synapse.

The notion that alterations in the structure, size and strength of the synapse might be at the basis of important processes like neural development, learning and memory is quite straightforward, as is the idea that an aberrant synaptic plasticity might be connected to pathological conditions (Borczyk et al., 2021). Indeed, alteration and/or disruption of neural circuits can have huge consequences on synapse structure and dynamics as demonstrated by their involvement in diverse pathological conditions such as motor and learning disabilities, altered mental status, cognitive impairment, neurodegenerative diseases (Chidambaram et al., 2019; Borczyk et al., 2021).

These considerations have motivated studies to elucidate how and to what extent synaptic structures change during synaptic plasticity. The use of confocal and two-photon (2P) excitation microscopes, together with the use of fluorescent probes and/or the expression of an ever-growing number of fluorescent proteins and biosensors in living neurons, is an important tool to study synapse structure and dynamics of both *in vitro* and *in vivo* systems, but, due to the limited spatial resolution of optical microscopes, they might fail to detect many of the subtle changes that characterize synaptic structure and plasticity.

Volume electron microscopy techniques in the study of synapses

The ability of the Electron Microscope (EM) to achieve nanometric resolution makes it the best instrument to visualize synapse ultrastructure. However, when visualizing individual Transmission Electron Microscope (TEM) bidimensional projections, the variability related to the plane of the sections and the lack of information on the *z*-axis strongly reduce the amount of data that can be collected from each image (Colombo et al., 2021). These limitations can be overcome to some extent by volume Electron Microscopy (vEM). Volume EM includes all EM methods able to generate a continuous series of bidimensional projections from resin-embedded samples with a depth greater than 1 μm (Peddie et al., 2022). Among vEM techniques TEM based approaches are included, such as serial section TEM (ssTEM) and serial section Electron Tomography (ssET), as well as techniques based on the use of the Scanning Electron Microscope (SEM) to visualize the face of the embedded tissue block by means of the backscattered electrons. The use of the SEM is coupled to the possibility to iteratively section the block as in the serial block face-SEM (SBF-SEM), or to mill out small portions of its surface (focused ion beam-SEM or FIB-SEM) in the SEM chamber. An alternative approach still taking advantage of the SEM backscattered electrons is represented by the array tomography in which long series of ultrathin sections collected on different substrates (coated glass slides, silicon wafers or tapes) are visualized under the SEM electron beam. These methods allow the experimenters, by analyzing three-dimensional vEM datasets, to obtain information on tissues and cells ultrastructure on the *x*, *y*, and *z* axes. These different techniques, although having different spatial resolution (indeed they generate near TEM-quality ultrastructural data but still they do not reach TEM spatial resolution in the *x*, *y* axes) produce datasets from large volumes of tissue allowing for the segmentation and reconstruction of the structure under investigation (Titze and Genoud, 2016; Kubota et al., 2018; Peddie et al., 2022). Even if we recently reported that some relevant aspects of the postsynapse architecture can be faithfully evaluated from TEM bidimensional projections (Colombo et al., 2021), measures from reconstructed SEM-based vEM stacks proved to be the favorite choice when dealing with the analysis of postsynaptic organization and its structural plasticity. The major limitations of these vEM approaches are represented by the large amount of time and computational work needed to analyze volumetric dataset and the paucity of tools able to recognize and segment the object of interest in a fully automated manner.

The ultrastructure of a chemical synapse

Since different physiological and pathological conditions are associated with modifications of synaptic components (Chidambaram et al., 2019), many studies in recent years aimed to define precise parameters to describe its ultrastructure, allowing for detailed and quantitative comparisons. The chemical synapse is a specialized intercellular junction that permits communication through neurotransmitter release between a pre- and a postsynaptic neuron, divided by a thin intercellular space, the synaptic cleft. The efficacy of a presynaptic terminal can be ultrastructurally defined by the size of the presynaptic bouton and by the amount, density and distribution of the synaptic vesicles in the bouton (Cheetham et al., 2007). Vesicles are docked and released at the presynaptic active zone (AZ), a dense meshwork of proteins involved in vesicle docking, priming and fusion (Südhof, 2012). The AZ, in mammalian central synapses, is occasionally visible with TEM as thin electron dense protrusions beneath the plasma membrane (Ackermann et al., 2015). Conversely, the postsynaptic component of the synapse is characterized by the presence of numerous proteins embedded in its membrane and just beneath it, involved in neurotransmitter binding (membrane receptors) and in the intracellular signaling pathway triggered in response to receptor activation. In EM micrographs, these clusters of proteins are detectable as an electron-dense flattened structure, the postsynaptic density (PSD), which can be described in terms of length, thickness and volume (Murru et al., 2017; Longaretti et al., 2020; Vezzoli et al., 2020). The PSD is thicker in excitatory synapses than in inhibitory ones (Tao et al., 2018), and in the case of excitatory synapses the PSD is most often localized on a tiny protrusion of the dendrite, the spine.

Postsynaptic density, synaptic apposition surface (SAS) and axon spine interface (ASI)

In recent years, vEM confirmed an observation about the geometry of the PSD that was already reported from TEM analyses of central synapses (Toni et al., 2001; Morales et al., 2011 and references therein); the PSD is not always a simple discoidal structure whose shape can be simply described with length, thickness and volume, but instead it can undergo morphological changes, which reflect different functional states of the synapse (Hering and Sheng, 2001). To use the geometry of this important component of the postsynapse to quantitatively characterize neuronal connectivity across large portions of the neuropil, huge vEM dataset were generated, and the need to analyze this large amount of data led to the development of automatic software for the segmentation and reconstruction (Morales et al., 2011; Cardona et al., 2012; Berg et al., 2019; Zumbado-Corrales and Esquivel-Rodríguez, 2021), which, in some cases reduced the spatial accuracy of the analysis.

Through FIB-SEM studies several aspects of synapse architecture were defined on reconstructed volumetric datasets. Among those parameters, the synaptic apposition surface (SAS) was defined as the area of close apposition between the membrane of the presynaptic AZ and the membrane of the postsynaptic neuron covering the PSD (Morales et al., 2013). The SAS was introduced as a method to overcome the intrinsic difficulties in identifying, in an automated manner, individual AZs and PSDs that in EM bi-dimensional projections can be sectioned in unfavorable planes (i.e., not perpendicular to the synapse major axis). Since then, the size of the SAS, obtained from vEM datasets, has been considered as a direct indicator of the function and the strength of a synapse since it takes into account features of the pre- and the postsynaptic compartments (i.e., the surface area of the AZ is related to the number of docked vesicles and probability of release, while the size of the PSD as indication of the amount of clustered neurotransmitter receptors). Considering the size, complexity and curvature of the SAS and their relation with the function of the synapse and of the neural network (Santuy et al., 2018), recent studies investigated the alterations in central synapses in Alzheimer's Disease (AD) patients and rodent models: SAS was reduced in human CA1 (Montero-Crespo et al., 2020, 2021) and rat pre-frontal cortex where the PSD volume was equally modified (Jiang et al., 2022). Other reports highlighted an overall loss of excitatory synapses in the hippocampus of patients and mouse model of AD (Neuman et al., 2015) or their mislocalization on dendritic shafts in the transentorhinal cortex of AD patients (Domínguez-Álvaro et al., 2019), in both cases, however, a marked increase in the percentage of perforated or fragmented excitatory synapses was noted.

Through SBF-SEM another parameter was established, the axon spine interface (ASI), defined as the interfacing surface between the presynaptic bouton and the spine head (Bellesi et al., 2015) and it represents the 3D equivalent of the length of the synaptic cleft which can be observed and accurately measured in TEM images (Colombo et al., 2021). The ASI and the PSD size were shown to be strongly correlated as they both become larger upon synaptic potentiation (Cheetham et al., 2014; De Vivo et al., 2017) and both correlated with the amplitude of excitatory postsynaptic currents (Murru et al., 2017; Nagai et al., 2021). Indeed, the tight relationship between the surface area of the ASI and the functional state of the synapse was demonstrated in a number of studies exploring the effects of sleep and sleep deprivation in homeostatic scaling of neural circuits. These studies showed that synaptic potentiation was associated with enlargement of the ASI in a subset of synapses when the animals were exposed to learning tasks during the wake period, while it underwent renormalization during sleep, possibly to consolidate and integrate memories and to avoid circuit saturation (Cirelli and Tononi, 2020). In fact, it has been shown that sleep induced reduction of the ASI both in hippocampal CA1 and primary motor cortex neurons (De Vivo et al., 2017); accordingly, chronic sleep deprivation led to ASI expansion in hippocampal CA1 (Spano et al., 2019; Nagai et al., 2021). Together with a reduction of the ASI, AMPA glutamate receptor (AMPAR) expression at the postsynaptic membrane was reduced after sleep (De Vivo et al., 2017; Miyamoto et al., 2021); and, in line with these findings, the levels of AMPAR and its phosphorylation were shown to diminish during sleep through a mechanism dependent on the increased synaptic concentration of Homer1a (Diering et al., 2017).

Dendritic spines size and shapes

Most excitatory synapses in mammalian neurons are present on dendritic spines, small protrusions which permit the electric and chemical compartmentalization of synaptic input. These dynamic structures vary in shape and size, features which are highly dependent on the maturity and functionality of the synapse itself (Berry and Nedivi, 2017): they originate as dendritic processes, highly dynamic and immature, which rarely form a synapse and, after maturation, they acquire a more complex shape, with a thin neck of various length, and a bulbous head, where the synapse is more frequently established (Yuste and Bonhoeffer, 2004). The morphology and plasticity of dendritic spines has long been studied taking advantage of fluorescence imaging but, given their small size, their shape and volume are optimally studied with vEM (Parajuli et al., 2020; Colombo et al., 2021; Parajuli and Koike, 2021).

Plasticity and its effects on the architecture of the postsynaptic compartment

Several studies have reported a direct correlation between the amount of AMPAR, PSD area and dendritic spine size and shape (Cheetham et al., 2014; Colombo et al., 2021), but several notable exceptions were recently reported (see below). The ability of subsynaptic structures to undergo changes after synaptic stimulation has been explored taking advantage of several models and techniques. Using 2P glutamate uncaging and time-lapse imaging together with TEM, a rapid (within few minutes) enlargement of dendritic spines was observed in rat and mouse hippocampal slices (Bosch et al., 2014; Meyer et al., 2014); interestingly, this enlargement was coupled to a delayed (1 to 3 h) enlargement of the PSD. This enlargement was either persistent (in

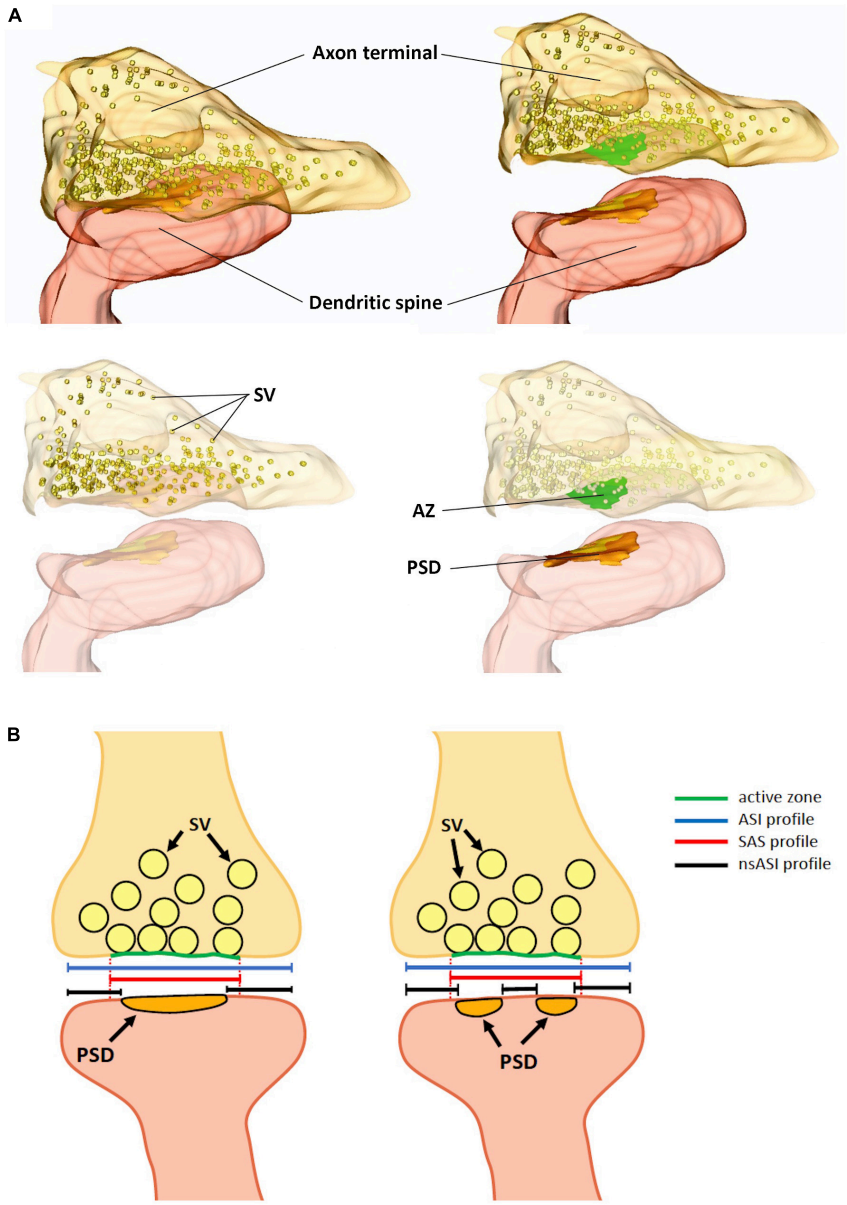

FIGURE 1
(A) Three-dimensional reconstruction of an excitatory synapse, in which the axon terminal, filled with synaptic vesicles (SV) and the active zone (AZ) are visible. In the dendritic spine, the postsynaptic density (PSD) is shown. **(B)** Schematic representation of an excitatory synapse with a macular PSD (left panel) and with a perforated/fragmented PSD (right panel). Dotted red lines are the projection of the active zones on the postsynaptic membrane enclosing the PSD, which define the profile of the synaptic apposition surface (SAS, continuous red line). The axon-spine interface (ASI, blue line), also corresponds to the synaptic cleft length. In the ASI we can distinguish a non-synaptic-ASI (black lines) and a synaptic ASI. The PSD length in mouse hippocampal CA1 pyramidal neurons ranges from 80 to 500 nm; the diameter of the SAS from 80 to 600 nm and the synaptic cleft, (the ASI) could be as long as 700 nm. SV, synaptic vesicles; AZ, active zone; PSD, postsynaptic density.

stabilized spines) or transient and associated with neither increased levels of PSD-95 nor with increased PSD (Meyer et al., 2014). Upon induction of chemical long term potentiation (LTP) in the same mouse model, the increase in spine and PSD size was tightly correlated in small and large dendritic spines, whereas in medium-sized spines the changes in the two structures were independent from each other (Borczyk et al., 2019).

The ability of a synapse to undergo structural changes after synaptic stimulation was also dependent on the presence of membrane-bound intracellular organelles in the spine (Borczyk et al., 2019). Indeed, the presence of the spine apparatus, a specialized compartment of the smooth endoplasmic reticulum found in a subset of dendritic spines, considerably increased the capacity of the synapse to undergo structural changes in neurons in the mouse hippocampus (Perez-Alvarez et al., 2020) and motor cortex (Hedrick et al., 2022). Even if the precise function of the spine apparatus remains elusive, its involvement in LTP-related processes through modulation of calcium dynamics and transport of locally synthesized proteins has been proposed (Jedlicka et al., 2008 and references therein). However, this relation between

the presence of endoplasmic reticulum and the ability of the synapse to undergo plastic changes was not exclusive, as in mice primary motor and somatosensory cortex, the presence of recycling endosomes, involved in receptor trafficking (Cooney et al., 2002), has been shown to positively impact on the ability of a synapse to undergo scaling down during sleep (De Vivo et al., 2017).

Finally, by using 2P glutamate uncaging to promote structural LTP of individual spines in mouse hippocampal organotypic slices, it was shown that a fast dendritic spine enlargement (within 2–3 min from stimulation) was paralleled by PSD perforation and segmentation but not with a concomitant increase in the PSD surface area, suggesting that the increase of the ASI was not faithfully explained by PSD enlargement and introducing the concept of the non-synaptic ASI (*nsASI*) whose surface increases faster than the *canonical* ASI (that is equal to *nsASI* + PSD area) (Sun et al., 2021) (**Figure 1B**).

Thus, while PSD, SAS, and ASI identify different portions of the synapse (**Figures 1A, B**), with ASI and SAS being broader than the PSD, these parameters are strongly correlated and they all correlate, to a variable extent, with the spine head volume (Colombo et al., 2021).

Concluding remarks

The study of synapses in two dimensions, as allowed by single section TEM imaging, implies the loss of spatial information that can be retrieved only in three dimensions with vEM (i.e., PSD complexity and dendritic spine shape) (see Colombo et al., 2021). For this reason, SEM-based vEM techniques are now privileged in studies addressing synaptic structural plasticity and stability on relatively large volumes of the neuropil. None of these techniques, however, offers the same spatial resolution on the x and y axes of TEM, not only due to intrinsic imaging limitations, but also for the necessity to heavily infiltrate samples with metals in order to render them conductive and to achieve adequate backscattered electron contrast. The enhanced contrast is needed to facilitate the automated or semi-automated recognition of the structures of interest. In those datasets it was often challenging to distinguish between the synaptic and non-synaptic portions of the postsynaptic membrane and so it was necessary to introduce new parameters to define synapse geometry. These limitations in lateral resolution can affect to different extent SBF-SEM and FIB-SEM images and indeed it was demonstrated that in FIB-SEM datasets measuring the SAS was easier and more reliable than measuring PSD surfaces (Morales et al., 2013). Importantly, these newly introduced elements describing subsynaptic portions that differ from the PSD itself, were demonstrated to be good predictors of synapse strength and activity (Bellesi et al., 2015; Miyamoto et al., 2021).

Author contributions

GM, LS, and MF contributed to the design of the review, searched and collected all publications relevant to the topic and wrote the first draft of the manuscript. All authors contributed to the manuscript revision, read, and approved the submitted version.

Funding

The fees associated with the publication of this review are charged to the Italian PRIN 2017, grant number 20172C9HLW to MF.

Acknowledgments

The authors are grateful to Dr. Elena Vezzoli (Università degli Studi di Milano), a former Ph.D. student in MF laboratory, and to Pietro Gallese for the graphic representation of the synapse (**Figure 1A**).

Conflict of interest

The authors declare that the research was conducted in the absence of any commercial or financial relationships that could be construed as a potential conflict of interest.

Publisher's note

References

Ackermann, F., Waites, C. L., and Garner, C. C. (2015). Presynaptic active zones in invertebrates and vertebrates. *EMBO Rep.* 16, 923–938. doi: 10.15252/embr.201540434

Bellesi, M., de Vivo, L., Tononi, G., and Cirelli, C. (2015). Effects of sleep and wake on astrocytes: Clues from molecular and ultrastructural studies. *BMC Biol.* 13:66. doi: 10.1186/s12915-015-0176-7

Berg, S., Kutra, D., Kroeger, T., Straehle, C. N., Kausler, B. X., Haubold, C., et al. (2019). Ilastik: Interactive machine learning for (Bio)Image analysis. *Nat. Methods* 16, 1226–1232. doi: 10.1038/s41592-019-0582-9

Berry, K. P., and Nedivi, E. (2017). Spine dynamics: Are they all the same? *Neuron* 96, 43–55. doi: 10.1016/j.neuron.2017.08.008

Borczyk, M., Radwanska, K., and Giese, K. P. (2021). The importance of ultrastructural analysis of memory. *Brain Res. Bull.* 173, 28–36. doi: 10.1016/j.brainresbull.2021.04.019

Borczyk, M., Śliwińska, M. A., Caly, A., Bernas, T., and Radwanska, K. (2019). Neuronal plasticity affects correlation between the size of dendritic spine and its postsynaptic density. *Sci. Rep.* 9:1693. doi: 10.1038/s41598-018-38412-7

Bosch, M., Castro, J., Saneyoshi, T., Matsuno, H., Sur, M., and Hayashi, Y. (2014). Structural and molecular remodeling of dendritic spine substructures during long-term potentiation. *Neuron* 82, 444–459. doi: 10.1016/j.neuron.2014.03.021

Cardona, A., Saalfeld, S., Schindelin, J., Arganda-Carreras, I., Preibisch, S., Longair, M., et al. (2012). TrakEM2 software for neural circuit reconstruction. *PLoS One* 7:e38011. doi: 10.1371/journal.pone.0038011

Cheetham, C. E. J., Barnes, S. J., Albieri, G., Knott, G. W., and Finnerty, G. T. (2014). Pansynaptic enlargement at adult cortical connections strengthened by experience. *Cereb. Cortex* 24, 521–531. doi: 10.1093/cercor/bhs334

Cheetham, C. E. J., Hammond, M. S. L., Edwards, C. E. J., and Finnerty, G. T. (2007). Sensory experience alters cortical connectivity and synaptic function site specifically. *J. Neurosci.* 27, 3456–3465. doi: 10.1523/JNEUROSCI.5143-06.2007

Chidambaram, S. B., Rathipriya, A. G., Bolla, S. R., Bhat, A., Ray, B., Mahalakshmi, A. M., et al. (2019). Dendritic spines: Revisiting the physiological role. *Progr. Neuro Psychopharmacol. Biol. Psychiatry* 92, 161–193. doi: 10.1016/j.pnpbp.2019.01.005

Cirelli, C., and Tononi, G. (2020). Effects of sleep and waking on the synaptic ultrastructure. *Philos. Trans. R. Soc. B Biol. Sci.* 375:235. doi: 10.1098/rstb.2019.0235

Citri, A., and Malenka, R. C. (2008). Synaptic plasticity: Multiple forms, functions, and mechanisms. *Neuropsychopharmacology* 33, 18–41. doi: 10.1038/sj.npp.1301559

Colombo, M. N., Maiellano, G., Putignano, S., Scandella, L., and Francolini, M. (2021). Comparative 2D and 3D ultrastructural analyses of dendritic spines from CA1 pyramidal neurons in the mouse hippocampus. *Int. J. Mol. Sci.* 22, 1–16. doi: 10.3390/ijms22031188

Cooney, J. R., Hurlburt, J. L., Selig, D. K., Harris, K. M., and Fiala, J. C. (2002). Endosomal compartments serve multiple hippocampal dendritic spines from a widespread rather than a local store of recycling membrane. *J. Neurosci.* 22, 2215–2224. doi: 10.1523/jneurosci.22-06-02215.2002

De Vivo, L., Bellesi, M., Marshall, W., Bushong, E. A., Ellisman, M. H., Tononi, G., et al. (2017). Ultrastructural evidence for synaptic scaling across the wake/sleep cycle. *Science* 355, 507–510. doi: 10.1126/science.aah5982

Diering, G. H., Nirujogi, R. S., Roth, R. H., Worley, P. F., Pandey, A., and Huganir, R. L. (2017). Homer1a drives homeostatic scaling-down of excitatory synapses during sleep. *Science* 355, 511–515. doi: 10.1126/science.aai8355

Domínguez-Álvaro, M., Montero-Crespo, M., Blazquez-Llorca, L., DeFelipe, J., and Alonso-Nanclares, L. (2019). 3D electron microscopy study of synaptic organization of the normal human transentorhinal cortex and its possible alterations in Alzheimer's disease. *eNeuro* 6, 1–17. doi: 10.1523/ENEURO.0140-19.2019

Goto, A. (2022). Synaptic plasticity during systems memory consolidation. *Neurosci. Res.* 183, 1–6. doi: 10.1016/j.neures.2022.05.008

Hedrick, N. G., Lu, Z., Bushong, E., Singhi, S., Nguyen, P., Magańa, Y., et al. (2022). Learning binds new inputs into functional synaptic clusters via spinogenesis. *Nat. Neurosci.* 25, 726–737. doi: 10.1038/s41593-022-01086-6

Hering, H., and Sheng, M. (2001). Dendritic spines: Structure, function and regulation. *Nat. Rev. Neurosci.* 2, 880–888. doi: 10.1038/35104061

Jedlicka, P., Vlachos, A., Schwarzacher, S. W., and Deller, T. (2008). A role for the spine apparatus in LTP and spatial learning. *Behav. Brain Res.* 192, 12–19. doi: 10.1016/j.bbr.2008.02.033

Jiang, Y., Li, L., Pang, K., Liu, J., Chen, B., Yuan, J., et al. (2022). Synaptic degeneration in the prefrontal cortex of a rat AD model revealed by volume electron microscopy. *J. Mol. Cell. Biol.* 14:mjac012. doi: 10.1093/jmcb/mjac012

Kubota, Y., Sohn, J., and Kawaguchi, Y. (2018). Large volume electron microscopy and neural microcircuit analysis. *Front. Neural Circ.* 12:98. doi: 10.3389/fncir.2018.00098

Longaretti, A., Forastieri, C., Toffolo, E., Caffino, L., Locarno, A., Miseviėiûtë, I., et al. (2020). LSD1 is an environmental stress-sensitive negative modulator of the glutamatergic synapse. *Neurobiol. Stress* 13:100280. doi: 10.1016/j.ynstr.2020.100280

Meyer, D., Bonhoeffer, T., and Scheuss, V. (2014). Balance and stability of synaptic structures during synaptic plasticity. *Neuron* 82, 430–443. doi: 10.1016/j.neuron.2014.02.031

Miyamoto, D., Marshall, W., Tononi, G., and Cirelli, C. (2021). Net decrease in spine-surface GluA1-containing AMPA receptors after post-learning sleep in the adult mouse cortex. *Nat. Commun.* 12:2881. doi: 10.1038/s41467-021-23156-2

Montero-Crespo, M., Domínguez-Álvaro, M., Alonso-Nanclares, L., DeFelipe, J., and Blazquez-Llorca, L. (2021). Three-dimensional analysis of synaptic organization in the hippocampal CA1 field in Alzheimer's disease. *Brain* 144, 553–573. doi: 10.1093/brain/awaa406

Montero-Crespo, M., Dominguez-Alvaro, M., Rondon-Carrillo, P., Alonso-Nanclares, L., DeFelipe, J., and Blazquez-Llorca, L. (2020). Three-dimensional synaptic organization of the human hippocampal CA1 field. *eLife* 9:e57013. doi: 10.7554/eLife.57013

Morales, J., Alonso-Nanclares, L., Rodríguez, J. R., DeFelipe, J., Rodríguez, Á, and Merchán-Pérez, Á (2011). ESPINA: A tool for the automated segmentation and counting of synapses in large stacks of electron microscopy images. *Front. Neuroanat.* 5:2. doi: 10.3389/fnana.2011.00018

Morales, J., Rodríguez, A., Rodríguez, J. R., DeFelipe, J., and Merchán-Pérez, A. (2013). Characterization and extraction of the synaptic apposition surface for synaptic geometry analysis. *Front. Neuroanat.* 7:20. doi: 10.3389/fnana.2013.00020

Murru, L., Vezzoli, E., Longatti, A., Ponzoni, L., Falqui, A., Folci, A., et al. (2017). Pharmacological modulation of AMPAR rescues intellectual disability-like phenotype in Tm4sf2-/y mice. *Cereb. Cortex* 27, 5369–5384. doi: 10.1093/cercor/bhx221

Nagai, H., de Vivo, L., Marshall, W., Tononi, G., and Cirelli, C. (2021). Effects of severe sleep disruption on the synaptic ultrastructure of young mice. *eNeuro* 8, 1–12. doi: 10.1523/ENEURO.0077-21.2021

Neuman, K. M., Molina-Campos, E., Musial, T. F., Price, A. L., Oh, K. J., Wolke, M. L., et al. (2015). Evidence for Alzheimer's disease-linked synapse loss and compensation in mouse and human hippocampal CA1 pyramidal neurons. *Brain Struct. Funct.* 220, 3143–3165. doi: 10.1007/s00429-014-0848-z

Parajuli, L. K., and Koike, M. (2021). Three-dimensional structure of dendritic spines revealed by volume electron microscopy techniques. *Front. Neuroanat.* 15:627368. doi: 10.3389/fnana.2021.627368

Parajuli, L. K., Wako, K., Maruo, S., Kakuta, S., Taguchi, T., Ikuno, M., et al. (2020). Developmental changes in dendritic spine morphology in the striatum and their alteration in an a53t α-synuclein transgenic mouse model of parkinson's disease. *eNeuro* 7, 1–14. doi: 10.1523/ENEURO.0072-20.2020

Peddie, C. J., Genoud, C., Kreshuk, A., Meechan, K., Micheva, K. D., Narayan, K., et al. (2022). Volume electron microscopy. *Nat. Rev. Methods Primers* 2, 1–23. doi: 10.1038/s43586-022-00131-9

Perez-Alvarez, A., Yin, S., Schulze, C., Hammer, J. A., Wagner, W., and Oertner, T. G. (2020). Endoplasmic reticulum visits highly active spines and prevents runaway potentiation of synapses. *Nat. Commun.* 11:5083. doi: 10.1038/s41467-020-18889-5

Santuy, A., Rodríguez, J.-R., DeFelipe, J., and Merchán-Pérez, A. (2018). Study of the size and shape of synapses in the juvenile rat somatosensory cortex with 3D electron microscopy. *eNeuro* 5, 1–14. doi: 10.1523/ENEURO.0377-17.2017

Spano, G. M., Banningh, S. W., Marshall, W., de Vivo, L., Bellesi, M., Loschky, S. S., et al. (2019). Sleep deprivation by exposure to novel objects increases synapse density and axon-spine interface in the hippocampal CA1 region of adolescent mice. *J. Neurosci.* 39, 6613–6625. doi: 10.1523/JNEUROSCI.0380-19.2019

Südhof, T. C. (2012). The presynaptic active zone. *Neuron* 75, 11–25. doi: 10.1016/j.neuron.2012.06.012

Sun, Y., Smirnov, M., Kamasawa, N., and Yasuda, R. (2021). Rapid ultrastructural changes in the PSD and surrounding membrane after induction of structural LTP in single dendritic sine. *J. Neurosci.* 41, 7003–7014. doi: 10.1523/JNEUROSCI.1964-20.2021

Tao, C. L., Liu, Y. T., Sun, R., Zhang, B., Qi, L., Shivakoti, S., et al. (2018). Differentiation and characterization of excitatory and inhibitory synapses by cryo-electron tomography and correlative microscopy. *J. Neurosci.* 38, 1493–1510. doi: 10.1523/JNEUROSCI.1548-17.2017

Titze, B., and Genoud, C. (2016). Volume scanning electron microscopy for imaging biological ultrastructure. *Biol. Cell* 108, 307–323. doi: 10.1111/boc.201600024

Toni, N., Buchs, P. A., Nikonenko, I., Povilaitite, P., Parisi, L., and Muller, D. (2001). Remodeling of synaptic membranes after induction of long-term potentiation. *J. Neurosci.* 21, 6245–6251. doi: 10.1523/JNEUROSCI.21-16-06245.2001

Vezzoli, E., Calì, C., De Roo, M., Ponzoni, L., Sogne, E., Gagnon, N., et al. (2020). Ultrastructural evidence for a role of astrocytes and glycogen-derived lactate in learning-dependent synaptic stabilization. *Cereb. Cortex* 30, 2114–2127. doi: 10.1093/cercor/bhz226

Yuste, R., and Bonhoeffer, T. (2004). Genesis of dendritic spines: Insights from ultrastructural and imaging studies. *Nat. Rev. Neurosci.* 5, 24–34. doi: 10.1038/nrn1300

Zumbado-Corrales, M., and Esquivel-Rodríguez, J. (2021). Evoseg: Automated electron microscopy segmentation through random forests and evolutionary optimization. *Biomimetics* 6:37. doi: 10.3390/biomimetics6020037

frontiers | Frontiers in Cellular Neuroscience

TYPE Original Research
PUBLISHED 31 March 2023
DOI 10.3389/fncel.2023.1120651

OPEN ACCESS

EDITED BY
Jacopo Lamanna,
Vita-Salute San Raffaele University, Italy

REVIEWED BY
David Perrais,
Centre National de la Recherche Scientifique (CNRS), France
Rex Kerr,
Calico Life Sciences LLC, United States

*CORRESPONDENCE
Alexander Gottschalk
✉ a.gottschalk@em.uni-frankfurt.de

SPECIALTY SECTION
This article was submitted to Cellular Neurophysiology, a section of the journal Frontiers in Cellular Neuroscience

RECEIVED 10 December 2022
ACCEPTED 15 March 2023
PUBLISHED 31 March 2023

CITATION
Seidenthal M, Jánosi B, Rosenkranz N, Schuh N, Elvers N, Willoughby M, Zhao X and Gottschalk A (2023) pOpsicle: An all-optical reporter system for synaptic vesicle recycling combining pH-sensitive fluorescent proteins with optogenetic manipulation of neuronal activity.
Front. Cell. Neurosci. 17:1120651.
doi: 10.3389/fncel.2023.1120651

pOpsicle: An all-optical reporter system for synaptic vesicle recycling combining pH-sensitive fluorescent proteins with optogenetic manipulation of neuronal activity

Marius Seidenthal[1,2], Barbara Jánosi[1,2], Nils Rosenkranz[1,2], Noah Schuh[1,2], Nora Elvers[1,2], Miles Willoughby[1,2], Xinda Zhao[1,2] and Alexander Gottschalk[1,2]*

[1]Buchmann Institute for Molecular Life Sciences, Goethe University Frankfurt, Frankfurt, Germany, [2]Institute of Biophysical Chemistry, Department of Biochemistry, Chemistry and Pharmacy, Goethe University, Frankfurt, Germany

pH-sensitive fluorescent proteins are widely used to study synaptic vesicle (SV) fusion and recycling. When targeted to the lumen of SVs, fluorescence of these proteins is quenched by the acidic pH. Following SV fusion, they are exposed to extracellular neutral pH, resulting in a fluorescence increase. SV fusion, recycling and acidification can thus be tracked by tagging integral SV proteins with pH-sensitive proteins. Neurotransmission is generally activated by electrical stimulation, which is not feasible in small, intact animals. Previous *in vivo* approaches depended on distinct (sensory) stimuli, thus limiting the addressable neuron types. To overcome these limitations, we established an all-optical approach to stimulate and visualize SV fusion and recycling. We combined distinct pH-sensitive fluorescent proteins (inserted into the SV protein synaptogyrin) and light-gated channelrhodopsins (ChRs) for optical stimulation, overcoming optical crosstalk and thus enabling an all-optical approach. We generated two different variants of the pH-sensitive optogenetic reporter of vesicle recycling (pOpsicle) and tested them in cholinergic neurons of intact *Caenorhabditis elegans* nematodes. First, we combined the red fluorescent protein pHuji with the blue-light gated ChR2(H134R), and second, the green fluorescent pHluorin combined with the novel red-shifted ChR ChrimsonSA. In both cases, fluorescence increases were observed after optical stimulation. Increase and subsequent decline of fluorescence was affected by mutations of proteins involved in SV fusion and endocytosis. These results establish pOpsicle as a non-invasive, all-optical approach to investigate different steps of the SV cycle.

KEYWORDS

neurotransmission, exo- and endocytosis, optogenetics, *Caenorhabditis elegans*, synaptic plasticity

1. Introduction

Chemical synaptic transmission, the release of neurotransmitters into the synaptic cleft, depends on synaptic vesicle (SV) exocytosis (Sudhof, 2013). To efficiently sustain neurotransmitter release during phases of (high) neuronal activity, SV-associated proteins and lipids must be recycled from the plasma membrane, thus allowing regeneration of ready-to-release SVs (Gan and Watanabe, 2018; Chanaday et al., 2019). Several modes of SV recycling have been uncovered, including classical clathrin-mediated endocytosis, activity-dependent bulk endocytosis, kiss-and-run release and the recently described ultrafast endocytosis (Heuser and Reese, 1973; Kittelmann et al., 2013; Watanabe et al., 2013a,b; Morton et al., 2015; Watanabe and Boucrot, 2017; Shin et al., 2021). It is still under debate which of these processes happen under which conditions, and whether some of these represent short-cuts in the SV cycle, e.g., bypassing the endosome. Also, the exact involvement of known, and the discovery of novel, recycling factors mediating these events is the subject of ongoing research (Gan and Watanabe, 2018; Yu et al., 2018). To study SV fusion and recycling, methods such as electron microscopy (EM), measurement of membrane capacitance, and super-resolution microscopy are used. However, these methods are either limited in their temporal resolution (EM) or applicability to different neuronal cell types (membrane capacitance measurements and super-resolution microscopy) (von Gersdorff and Matthews, 1999; Yu et al., 2018; Shin et al., 2021).

Another method to indirectly visualize and quantify exocytosis and recycling of proteins is through tagging with pH-sensitive fluorescent proteins (Miesenbock et al., 1998). SVs acidification precedes and is required for refilling with neurotransmitters during the recycling process (Egashira et al., 2015; Gowrisankaran and Milosevic, 2020). For this reason, the fluorescence of pH-sensitive proteins, such as the green fluorescent pHluorin, when targeted to the acidic intraluminal side of the SV membrane, is quenched by the low-pH environment (Sankaranarayanan et al., 2000). Typically, the utilized reporters are either fused to the vesicular glutamate transporter or inserted into loops of the tetraspan membrane protein synaptophysin (Voglmaier et al., 2006; Luo et al., 2021). Upon SV fusion with the plasma membrane, the fluorescence increases due to exposure to the neutral extracellular medium and dequenching of the fluorophore (**Figure 1**). Following stimulation, the fluorescence decreases depending on the rate of endocytosis, sorting and reacidification of SVs. This way, positive or negative influences on the speed of SV retrieval can be quantified (Morton et al., 2015; Watanabe et al., 2018). Several variants of pH-sensitive fluorescent proteins have been created, covering almost the entire spectrum of visible light (Miesenbock et al., 1998; Shen et al., 2014; Liu et al., 2021). This opens the door for multiplexing with other fluorophores or optical actuators (Li and Tsien, 2012; Jackson and Burrone, 2016).

Most studies utilizing pH-sensitive fluorescent proteins in mammalian organisms are performed using cultured neurons or semi-intact preparations such as hippocampal slices (Rose et al., 2013; Watanabe et al., 2018). *In vivo* studies are rare and usually performed in translucent non-mammalian model systems such as *Danio rerio* and *Drosophila melanogaster* larvae or *Caenorhabditis elegans* (Poskanzer et al., 2003; Koudelka et al., 2016; Ventimiglia and Bargmann, 2017; Seitz and Rizzoli, 2019). Electrical stimulation can be used to trigger neurotransmission, but this is comparatively invasive and labor-intensive, particularly if it involves dissection. Alternatively, exposure to stimuli such as odors can be used. However, this is difficult to control, and limited to applications in sensory neurons (Choi et al., 2021). Thus, an all-optical solution that is not limited to certain cell types would be ideal, e.g., a combination of genetically encoded non-invasive tools for *in vivo* stimulation of neurons, and pH-sensitive fluorescent proteins. One possibility to manipulate neurotransmission is through transgenic expression of channelrhodopsins (ChRs), which are light-gated cation channels that can be used to depolarize neurons (Nagel et al., 2003, 2005; Boyden et al., 2005; Liewald et al., 2008). Light absorption leads to isomerization of the chromophore all-*trans* retinal (ATR) and opening of the channel pore. A variety of ChRs that are activated by different wavelengths have been discovered or engineered (Guru et al., 2015; Schild and Glauser, 2015; Chang, 2019). This enables multiplexing with both short- or long-wavelength absorbing fluorophores (Wabnig et al., 2015; Hawk et al., 2021; Vierock et al., 2021). In this work, we characterize two different combinations of ChRs with pH-sensitive fluorescent proteins in living *C. elegans* nematodes. We first tested pHuji, a recently described red fluorescent protein, together with the well described blue light-gated ChR2 (Nagel et al., 2005; Shen et al., 2014). To determine whether the increase in fluorescence during stimulation is dependent on SV fusion, we analyzed reduction-of-function mutants of synaptobrevin (SNB-1), which is an essential vesicular soluble N-ethylmaleimide-sensitive-factor attachment receptor (v-SNARE) and thus involved in SV fusion (Nonet et al., 1998; Liu et al., 2018). Similarly, to examine whether the rate of the fluorescence decay after stimulation depended on the rate of SV recycling, we analyzed mutants lacking the established SV recycling factors synaptojanin/UNC-26, endophilin/UNC-57 and synaptotagmin/SNT-1, which are involved in different steps of SV recycling, such as membrane bending and clathrin-uncoating (Jorgensen et al., 1995; Harris et al., 2000; Schuske et al., 2003; Kittelmann et al., 2013; Watanabe et al., 2018; Yu et al., 2018; Mochida, 2022). SNT-1 is the primary sensor of calcium for exocytosis, but also regulates endocytosis, by recruiting adapter complex 2 (AP2) to the plasma membrane (Poskanzer et al., 2003; Yu et al., 2013; Mochida, 2022). The pHuji approach could be used to estimate the extent of SV release but was unable to efficiently report recycling kinetics. We thus swapped both the actuator and the sensor to different excitation wavelengths. We used the recently described red-light activated ChR ChrimsonSA and the well-established green fluorescent pHluorin (Miesenbock et al., 1998; Oda et al., 2018; Seidenthal et al., 2022). Using this combination, we could stimulate and visualize SV exo- and endocytosis in an all-optical, non-invasive manner *in vivo*. We termed this approach the pH-sensitive optogenetic reporter of vesicle recycling (pOpsicle). We tested the pOpsicle method in cholinergic motor neurons and in the glutamatergic/tyraminergic interneuron RIM. pOpsicle should be applicable to most neuronal cell types and is, to our knowledge, the only all-optical approach to study SV recycling using ChRs and pH-sensitive fluorescent proteins in living animals to date. Our approach expands the possibilities to study SV recycling at the *C. elegans* neuromuscular junction (NMJ) which previously could only be done by indirect

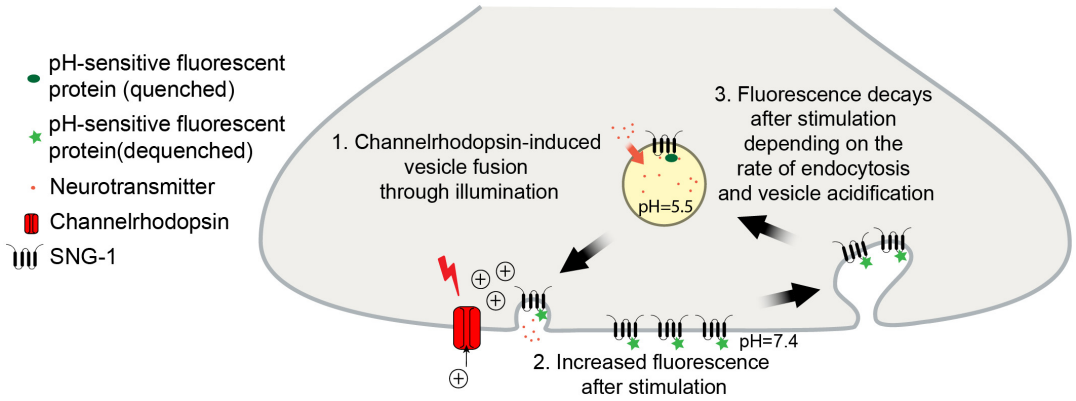

FIGURE 1
Schematic of the pOpsicle assay. pH-sensitive fluorescent proteins fused to SNG-1 are exposed to the neutral extracellular medium in response to optogenetic stimulation which leads to an increase in fluorescence.

measurement of postsynaptic effects using electrophysiology, Ca^{2+} imaging, or by (non-)time-resolved EM (Liewald et al., 2008; Kittelmann et al., 2013; Wabnig et al., 2015; Steuer Costa et al., 2017; Yu et al., 2018).

2. Materials and methods

2.1. Molecular biology

For the expression of SNG-1 fusion constructs and channelrhodopsins in *C. elegans*, the *punc-17* promotor (cholinergic motor neurons) and a short version of the *ptdc-1* promotor (RIM interneurons) were used. **pcDNA3-SypHluorin 4x (S4x)** was a gift from Stephen Heinemann & Yongling Zhu (Addgene plasmid #37005[1]; RRID:Addgene_37005). **pJB14** (*TOPO vector::2xpHluorin*) was generated using the TOPO cloning kit (Thermo Fisher Scientific Inc., USA) by amplifying two copies of pHluorin cDNA from the pcDNA3-SypHluorin 4x (S4x) plasmid with primers oBJ51 (5′-ATATCGAACCGTCTTCAGATATGGATCTAGCCACC-3′) and oBJ62 (5′-TATATTCGCCGTCTTCTCCACCGCATGTGATTCGAGCTCC-3′). **pJB10** (*punc-17::sng-1::unc-54-3′UTR*) was generated through Gibson assembly by digesting pRM348 with *BmtI* and *BsiWI* (*punc-17* and backbone), by amplifying pAG52 (*sng-1*) with primers oBJ58 (5′-TCAGGAGGACCCTTGGCTAGATGGAGAACGTGCGTGCTTATG-3′) and oBJ59 (5′-ATGACTCGAGCTAATAACCATATCCTTCCGACTGAG-3′) and by amplifying pAH03 (*unc-54-3′UTR*) with oBJ60 (5′-ATATGGTTATTAGCTCGAGTCATGGTCGACAAG-3′), and oBJ61 (5′-AAACGCGCGAGACGAAAGGGCCCAAACAGTTATGTTTGGTATATTGGG-3′). **pJB11** (*punc-17:: sng-1::2xpHluorin::unc-54-3′UTR*) was generated by digestion of pJB10 and pJB14 with *BbsI* and subsequent ligation to introduce two copies of pHluorin cDNA into the sequence encoding the first intraluminal loop of SNG-1. **pDisplay-pHuji** was a gift from Robert Campbell (Addgene plasmid #61556[2]; RRID:Addgene_61556). pDisplay-pHuji was amplified using primers oBJ104 (5′-GCAGAAGAAAACCATGGGCTG-3′) and oBJ105 (5′-CAGCCCATGGTTTTCTTCTGC-3′) to remove the *BbsI* restriction site to generate **pJB24**. **pJB25** (*punc-17::sng-1::pHuji::unc-54-3′UTR*) was generated *via* Gibson assembly by digesting pJB10 with *BbsI* and amplifying pJB24 with primers oBJ107 (5′-ATATCGAAAAGTCTTCAGGTGGAGGTGGAAGTATGGTGAGCAAGGGCGAG-3′) and oBJ108 (5′-TATATTCGCCGTCTTCGGTGGAGGTGGAAGTCTTGTACAGCTCGTCCATG-3′) which contain the sequence for a GGGGS linker to add in front of the coding region of pHuji. **pJB26** (*punc-17::ChR2(H134R)::myc*) was generated by amplifying *ChR2(H134R)::myc* using primers oBJ113 (5′-GAACGCTAGCACCACTAGATCCATCTAGAG-3′) and oBJ114 (5′-GCATGCTAGCCACCAGACAAGTTGGTAA-3′) which was introduced into pRM348 by restriction digest with *NheI* and subsequent ligation. **pMSE01** (*punc-17::ChrimsonSA::unc-54-3′UTR*) was generated by amplifying pDV07 (*punc-17::ChrimsonWT::unc-54-3′UTR*) with oMSE16 (5′-CGAGTGGCTGCTGGCTTGCCCCGTGAT-3′) and oMSE017 (5′-ATCACGGGGCAAGCCAGCAGCCACTCG-3′) to introduce the point mutation (S169A). **pMSE23** (*ptdc-1s::ChrimsonSA::unc-54-3′UTR*) was generated by amplifying *ptdc-1s* from pXY07 (*ptdc-1s::GFP*) with primers oMSE105 (5′-TCCCGGCCGCCATGGCCGCGATTTCTGTATGAGCCGCCCG-3′) and oMSE106 (5′-AAAGACTTTCGATGAATTACTTGGGCGGTCCTGAAAAATG-3′), amplifying the ChrimsonSA backbone from pMSE01 with oMSE107 (5′-CATTTTTCAGGACCGCCCAAGTAATTCATCGAAAGTCTTTCTATTTTCCGCATCTCTTGTTCAAGGGATTGG-3′) and oMSE108 (5′-CGGGCGGCTCATACAGAAATCGCGGCCATGGCGGCCG-3′) and combined the fragments using Gibson assembly. **pMSE24** (*ptdc-1s::sng-1::pHluorin::unc-54-3′UTR*) was generated by amplifying the *sng-1::pHluorin* backbone from pBJ11 with oMSE114 (5′-AGGGTCGACCATGACTCGAGCTAATAACCATATCCTTC-3′) and oMSE115 (5′-GTAATTCATCGAAAGTCTTTCTATTTTCCG

1 http://n2t.net/addgene:37005

2 http://n2t.net/addgene:61556

CATCTCTTGTTCAAGGGATTGG-3′) and with oMSE108 and oMSE113 (5′-GAAGGATATGGTTATTAGCTCGAGTCATGGT CGACCCT-3′) and fusing these fragments with the *ptdc-1s* using Gibson assembly.

2.2. Cultivation of *C. elegans*

Caenorhabditis elegans strains were kept under standard conditions on nematode growth medium (NGM) plates seeded with the *Escherichia coli* strain OP50, obtained from the *Caenorhabditis* Genetics Center (CGC, University of Minnesota, USA), at 20°C (Brenner, 1974). The N2 Bristol strain was provided by the CGC and used as wild type. Transgenic animals were generated as described previously (Fire, 1986). An overview of transgenic and mutant strains used or generated in this work can be found in **Table 1**. For experiments, well-fed L4 larvae were picked ∼18 h before the assays. For RIM experiments, only animals showing marker fluorescence were used. Animals were supplemented with ATR (Sigma-Aldrich, USA) by adding 100 µl OP50 containing 200 µM ATR to 10 ml NGM agar dishes. Experiments were performed on at least two separate days with animals picked from different plates.

2.3. Measurement of *C. elegans* body length

Body length assays were performed as described previously (Liewald et al., 2008; Seidenthal et al., 2022). Briefly, light from a 50 W HBO lamp was filtered with a 450–490 nm bandpass excitation filter for ChR2(H134R) and with a 568.5–591.5 nm filter for ChrimsonSA stimulation. ChR2(H134R) was stimulated at 340 µW/mm^2. ChrimsonSA was stimulated and tested for crosstalk at a light intensity of 40 µW/mm^2. Brightfield light was filtered with a 665–715 nm filter to avoid unwanted activation of channelrhodopsins. Videos of single animals were acquired and then analyzed using the WormRuler software (Seidenthal et al., 2022). Body length of each worm was normalized to the 5 s period before stimulation and values >120 or <80% of the initial body length were discarded as these are biomechanically impossible and result from artifacts in the background correction.

2.4. Measurement of crawling speed and reversals using the multi-worm-tracker

Videos of crawling animals were acquired as described previously (Vettkötter et al., 2022) and crawling speed measured using the multi-worm-tracker (MWT) setup (Swierczek et al., 2011). Animals were washed three times with M9 buffer to remove OP50 bacteria. They were then transferred to unseeded NGM plates and kept in darkness for 15 min. A light stimulus was applied using a custom-build LED ring (Alustar 3W 30°, ledxon, 623 nm) which was controlled by an Arduino Uno (Arduino, Italy) device running a custom-written Arduino script. Videos were acquired using a high-resolution camera (Falcon 4M30, DALSA) and crawling speed of single animals as well as reversal count (in bins of 10 s) were extracted using "Choreography" software (Swierczek et al., 2011) and summarized using a custom Python script.

2.5. Microscopy and imaging

For fluorescence imaging, animals were placed upon 7% agarose pads in M9 buffer. Animals were immobilized using a 20 mM Levamisole-hydrochloride (Sigma-Aldrich, USA) solution in M9 and visualized on an Axio Observer Z1 microscope (Zeiss, Germany) equipped with a 100× oil objective. Fluorescent proteins and channelrhodopsins were excited using a 460 and a 590 nm LED system (Lumen 100, Prior Scientific, UK) coupled *via* a beamsplitter. pHuji and ChR2(H134R) were excited using a double band pass filter (460–500 and 570–600 nm) combined with a 605 nm beam splitter (AHF Analysentechnik, Germany). 460 nm LED light to stimulate ChR2(H134R) was set to 340 µW/mm^2 intensity. pHuji fluorescence was excited at 280 µW/mm^2 and filtered using a 615–680 nm emission filter and visualized using an EMCCD camera (Evolve 512 Delta, Teledyne Photometrics, USA). pHluorin and ChrimsonSA were excited using a 450–490/555–590 nm double band pass filter combined with a GFP/mCherry beamsplitter (AHF Analysentechnik, Germany). 590 nm LED light intensity to stimulate ChrimsonSA and excite pHluorin was set to 40 µW/mm^2. pHluorin fluorescence was filtered using a 502.5–537.5 nm band pass emission filter and visualized using a sCMOS camera (Kinetix 22, Teledyne Photometrics, USA). For increased ChrimsonSA stimulation at 280 µW/mm^2, we used the same excitation filter as for pHuji experiments but combined with a FITC/TxRed double band pass beamsplitter and a 515–555 nm emission filter (AHF Analysentechnik, Germany). pHluorin fluorescence was again excited with 40 µW/mm^2. The dorsal nerve cord (DNC) was visualized using the basal pHuji or pHluorin fluorescence. For cholinergic neurons, a region in the posterior third of the animal was imaged, where an abundance of synaptic puncta can be found. For RIM experiments, fluorescent neuronal extensions in the head region were visualized. Videos were captured using the µManager v.1.4.22 software (Edelstein et al., 2014). pHuji – pOpsicle experiments were performed with 50 ms exposure time (20 fps), pHluorin – pOpsicle experiments with 200 ms exposure (5 fps). Stimulation of channelrhodopsins was triggered using a custom written *Autohotkey* script to activate and deactivate LEDs. Representative images displaying entire worms were acquired using a 40× oil objective and stitched together using the ImageJ *Stitching* Plugin (Preibisch et al., 2009). The representative image of RIM neurons (**Figure 5A**) was made using the *Z Project* function to generate a projection of slices acquired throughout the head region.

2.6. Quantification of fluorescence

Example images were processed, and fluorescence was quantified using ImageJ v1.53 (Schindelin et al., 2012). A region of interest (ROI) was placed on the DNC or RIM neuron using the *Segmented Line* tool. Pixel width of the line was adjusted according to the width of the fluorescent signal. A background ROI was

TABLE 1 *Caenorhabditis elegans* strains.

Strain	Genotype	Source
ZX214	*snt-1(md290)*	CGC (Jorgensen et al., 1995)
ZX307	*snb-1(md247)*	CGC (Miller et al., 1996)
ZX451	*unc-57(e406)*	CGC (Brenner, 1974)
ZX1629	*unc-26(s1710)*	CGC (Harris et al., 2000)
ZX2835	*sng-1(ok234); zxIs138[punc-17::SNG-1::pHuji; punc-17::ChR2(H134R)::myc; pmyo-2::CFP]*	This study
ZX2836	*unc-26(s1710); sng-1(ok234); zxIs138[punc-17::SNG-1::pHuji; punc-17::ChR2(H134R)::myc; pmyo-2::CFP]*	This study
ZX2837	*snt-1(md290); sng-1(ok234); zxIs138[punc-17::SNG-1::pHuji; punc-17::ChR2(H134R)::myc; pmyo-2::CFP]*	This study
ZX2838	*unc-57(e406); sng-1(ok234); zxIs138[punc-17::SNG-1::pHuji; punc-17::ChR2(H134R)::myc; pmyo-2::CFP]*	This study
ZX2850	*snb-1(md247); sng-1(ok234); zxIs138[punc-17::SNG-1::pHuji; punc-17::ChR2(H134R)::myc; pmyo-2::CFP]*	This study
ZX2853	*lite-1(ce314); sng-1(ok234); zxIs138[punc-17::SNG-1::pHuji; punc-17::ChR2(H134R)::myc; pmyo-2::CFP]*	This study
ZX3197	*zxIs152[punc-17::Chrimson(S169A); punc-17::SNG-1::pHluorin; pmyo-2::mCherry]*	This study
ZX3217	*unc-26(s1710); zxIs152[punc-17::Chrimson(S169A); punc-17::SNG-1::pHluorin; pmyo-2::mCherry]*	This study
ZX3218	*snb-1(md247); zxIs152[punc-17::Chrimson(S169A); punc-17::SNG-1::pHluorin; pmyo-2::mCherry]*	This study
ZX3254	*unc-57(e406); zxIs152[punc-17::Chrimson(S169A); punc-17::SNG-1::pHluorin; pmyo-2::mCherry]*	This study
ZX3402	*snt-1(md290); zxIs152[punc-17::Chrimson(S169A); punc-17::SNG-1::pHluorin; pmyo-2::mCherry]*	This study
ZX3422	*zxEx1418[pmyo-2::mCherry; ptdc-1s::ChrimsonSA; ptdc-1s::SNG-1::pHluorin]*	This study

set in close proximity to the imaging ROI, inside the worm (but avoiding gut autofluorescence) and fluorescence was quantified using the *Multi Measure* function. XY-drift was corrected using the *Template Matching* ImageJ plugin, if necessary. Animals that moved excessively or drifted in the focal plane were discarded. Fluorescence was normalized to the average fluorescence before stimulation (F_0) to compare different animals:

$$\frac{\triangle F}{F_0} = \frac{F - F_0}{F_0}$$

A custom written python script was used for background subtraction, normalization and (if needed) filtering of animals according to whether they show a strong response during stimulation (available on GitHub[3]). For this, the maximum background corrected fluorescence during stimulation was calculated (as a moving average of 1 s). If this was higher than the average background corrected fluorescence before the stimulation +3 × standard deviations (of background corrected fluorescence before stimulation; minimum of two arbitrary units of fluorescence increase), the animal was counted as a strong responder (adapted from Choi et al., 2021); see **Supplementary Figure 6A** for example traces that fit or do not fit these parameters; animals not fitting the cut-off showed no discernable light-evoked effect on DNC fluorescence. Also, animals that showed an increase of the fluorescence after the end of the stimulus, or animals showing spontaneous events, were excluded. These measures were necessary for the calculation of fluorescence rise and decay kinetics because data from "non-responders" could not be properly fitted. Fluorescence was not corrected for bleaching since bleaching rates were difficult to estimate robustly in the presence of alternating light protocols. Attempts to correct for bleaching led to a progressive deviation toward the end of the acquisition. However, the measured background fluorescence bleached with a similar rate as the fluorescence in the DNC. Thus, subtraction of background fluorescence was sufficient to correct for bleaching in most cases. Fluorescence signal increases in the pOpsicle assay were calculated using the mean of the normalized fluorescence at the first second after stimulation (±SEM) for pHuji experiments or the mean of seconds 15–20 (±SEM) for pHluorin experiments. Regression analysis, to calculate the rate of fluorescence rise and decay, was performed using Graphpad Prism 9.4.1. The equations "Plateau followed by one-phase exponential association" (1) and "Plateau followed by one-phase exponential decay" (2) were fitted to the fluorescence increase during stimulation and decay after stimulation and the time constants τ calculated for each animal. The curve fits were constrained between minimum and maximum fluorescence values to receive reasonable τ values:

$$\text{If t} < \text{t}_0 : f(t) = f_0; \text{If t} \geq t_0 : f(t)\ f_0 + \left(Max - f_0\right) * \left(1 - e^{-\frac{t}{\tau}}\right) \quad (1)$$

$$\text{If t} < \text{t}_0 : f(t)\ f_0; \text{If t} \geq t_0 : f(t)\ \left(f_0 - Min\right) * e^{-\frac{t}{\tau}} + Min \quad (2)$$

where. t, time (in seconds); t_0, timepoint of experimental intervention; set to the first timepoint after the start or stop of stimulation; f_0, value of $f(t)$ at t_0; set to 0 (for Equation 1) or maximum fluorescence values (for Equation 2, as a moving average of five frame intervals); Max, maximum fluorescence during or immediately after stimulation as a moving average of five frame intervals (for Equation 1); Min, minimum fluorescence after stimulation as a moving average of 5 s intervals (for Equation 2); τ, time constant (in seconds; higher τ values indicate a slower rise or decay).

As above, each fit was inspected. Individual fits that showed no increase during stimulation were discarded from analysis as

3 https://github.com/MariusSeidenthal/pHluorin_Imaging_Analysis

they could not be fitted properly (**Supplementary Figure 6A**). Similarly, data sets that displayed an increase rather than a decay after stimulation were also discarded.

2.7. *Caenorhabditis elegans* primary neuronal cell culture

For the preparation of *C. elegans* primary cell culture, established protocols were adapted and modified (Christensen et al., 2002; Strange et al., 2007). Gravid adult worms were grown on enriched peptone plates with nystatin (NEP agar) seeded with Na22 *E. coli* (CGC; Zhang et al., 2011). Worms were washed off the plate using double-distilled water (ddH_2O) and transferred to 15 ml centrifuge tubes. A total of 2 ml of household bleach as well as 1 ml of 5 M NaOH solution were added to 7 ml of worm suspension. The solution was vortexed for at least 5 min at maximum speed to get rid of adult worm bodies. All the following steps were performed under a sterile workbench. The solution, now containing only eggs, was centrifuged at 500 g for 1 min. Excess liquid was removed, and the pellet was resuspended in ddH_2O. Washing was repeated three times. The egg pellet was resuspended in 500 µl freshly thawed chitinase (1 U/ml, Sigma-Aldrich, USA) and transferred to a 1.5 ml tube. The tube was placed into a shaker for 90 min at room temperature to digest the chitin shell of the eggs. The chitinase reaction was stopped with 800 µl L-15 full medium (Gibco, USA) containing 10% fetal calf serum (FCS) as well as Pen/Strep (50 U/ml penicillin + 50 µg/ml streptomycin; Sigma-Aldrich, USA). After centrifugation at 900 *g*, excess liquid was discarded, and the pellet was resuspended in 500 µl L-15 full medium. Using a 2 ml syringe with an 18-gauge needle, the solution was aspirated and released back into the tube 15–20 times to dissociate the cells. After dissociation, 1 ml L-15 full medium was added to the tube and taken up into the syringe. With the cell solution inside the syringe, the needle was replaced by a 5 µm filter (Millipore, Germany). The solution was released through the filter into a fresh tube. The original tube was refilled with 1 ml L-15 full medium, the filter was replaced by the needle and the procedure was repeated to release the solution into another tube. This was repeated four to six times, depending on the initial number of eggs (more eggs = less repetitions). Filtered cell solutions were centrifuged at 900 *g* and most of the supernatant was discarded. Cell pellets were resuspended in the remaining medium and pooled. A total of 500–1,000 µl L-15 full medium were added to the suspension and the solution was seeded on 1–2 peanut lectin (Sigma-Aldrich, USA) coated glass bottom petri dishes (ibidi, Germany). Petri dishes were filled with 1 ml L-15 full medium and cells were allowed to adhere for 24 h in a 20°C sterile incubator (Memmert, Germany) before exchanging the medium. Treatment with ATR was performed after two days. Medium was replaced with a 10 µM ATR solution in L15 full medium and the cells incubated for at least 12 h at 20°C. Prior to measurement, cells were washed two times with L-15 full medium without ATR. Neurons were imaged three to four days after seeding. The filter setup was identical to the one used to visualize pHluorin in intact animals, yet neurons were visualized using a 40× objective and 200 ms exposure time. To reduce bleaching during NH_4Cl treatment frame rate was reduced to one frame every 5 s. The camera shutter and 460 nm LED were controlled using a custom-written Arduino script (kindly provided by Ichiro Aoki). Buffers used to either de-quench or quench pHluorin fluorescence were adapted from Dittman and Kaplan (2006) and added manually by pipetting 1 ml of the respective solution onto the petri dish and then removing the same amount of liquid. Before starting a new acquisition, cells were washed three times using the control saline buffer (pH 7.4). Fluorescence was quantified as in living animals. A ROI was set on top of neurite extensions using the ImageJ "Segmented line" tool with a background ROI set in proximity. The releasable fraction of SVs (RF) was calculated for individual cells as the ratio of the mean normalized fluorescence during optogenetic stimulation to the normalized fluorescence during treatment with NH_4Cl containing buffer (mean of 85–90 s; Egashira et al., 2016):

$$RF = \frac{F_{MaxStim}}{F_{NH_4Cl}}$$

2.8. Statistical analysis

Statistical analysis and plotting of graphs were done using Graphpad Prism 9.4.1. Unpaired *t*-tests were performed if two normally distributed datasets were compared and one-way ANOVA (with Dunnett's or Tukey's correction) or two-way ANOVA (with Šídák's correction) for three or more datasets. Fluorescence rise and decay constants were compared using the Mann–Whitney test (for two datasets) and the Kruskal–Wallis tests (with Dunn's correction) or by applying multiple Mann–Whitney tests (with Holm–Šídák's correction) for three or more datasets.

3. Results

3.1. Synaptogyrin-pHuji may be used to quantify SV exocytosis but is unable to efficiently report recycling

To enable an all-optical method for analysis of SV exo- and endocytosis, we used proteins with presumably low optical crosstalk. First, we tested the recently described red fluorescent pHuji protein which shows a 22-fold increase of fluorescence when transferred from intravesicular to extracellular pH (Shen et al., 2014), combined with the blue light-gated ChR2(H134R; hereafter called ChR2) for stimulation of neurotransmission (Nagel et al., 2005). Overlap of the pHuji and ChR2 excitation spectra is minimal (Azimi Hashemi et al., 2014; Shen et al., 2014; Lambert, 2019; **Supplementary Figure 1A**). *C. elegans* proteins can be targeted to, e.g., cholinergic or GABAergic motor neurons using specific promoters, and for subcellular localization of pHuji we chose the ubiquitous (in neurons) integral SV membrane protein synaptogyrin-1 (SNG-1; Zhao and Nonet, 2001; Abraham et al., 2006). SNG-1 was previously used to target proteins to SVs (Liu et al., 2019; Vettkötter et al., 2022). We inserted pHuji into the second intraluminal loop of SNG-1 (**Figure 1**) and co-expressed it with ChR2 in cholinergic motor neurons using the promotor of *unc-17*, encoding the vesicular acetylcholine transporter (Alfonso et al., 1993; Miller et al., 1996; Liewald et al., 2008). SNG-1::pHuji

could be observed throughout the cholinergic nervous system, i.e., nerve ring, ventral and dorsal nerve cords (VNC/DNC; **Supplementary Figure 1B**) and dorsal neuronal extensions (**Supplementary Figure 1C**). Fluorescent puncta in the DNC indicate accumulation of SNG-1::pHuji at NMJs (Sieburth et al., 2005). Next, we analyzed whether neurotransmission can be activated in these animals using ChR2, which typically leads to muscle contraction and reduction of body length through acetylcholine release (Liewald et al., 2008). As expected, blue light caused a decrease of body length of animals when grown in the presence of ATR (**Supplementary Figure 1D**), but not in no-ATR controls. Next, we quantified fluorescence of SNG-1::pHuji in the posterior DNC where NMJs are abundant (Sieburth et al., 2005) before, during and after ChR2 photostimulation (**Supplementary Figures 1C, E**). Since pHuji fluorescence was relatively dim, we could not quantify fluorescence during the stimulation period, as blue light increased autofluorescence and/or further excited pHuji, thus erroneously increasing the measured signal. Alternating light protocols also failed, likely due to the photoswitching nature of pHuji (Liu et al., 2021). However, we could compare the fluorescence before and after stimulation. Animals treated with ATR showed a significantly increased fluorescence after stimulation (19 ± 3% $\Delta F/F_0$), compared to animals without ATR (2 ± 2%, $^{***}p < 0.001$; **Supplementary Figure 1E**). This increase gradually declined toward the fluorescence level in animals grown without ATR, most likely indicating recycling of externalized SNG-1::pHuji (and thus of SVs). We termed the pHuji-ChR2 combination "red pOpsicle." To determine whether the red-pOpsicle assay reports on altered SV exo- and endocytosis, we crossed the line carrying the ChR2 and SNG-1::pHuji transgene into mutants known to affect the SV cycle (see section "1. Introduction"; **Supplementary Figure 2**). Compared to wild type, *snb-1(md247)* mutants showed a significantly lower fluorescence increase after stimulation with blue light [wild type: 15 ± 2%, *snb-1(md247)*: 2 ± 2%; **Supplementary Figures 2A, B**], indicating lower amounts of SVs containing SNG-1::pHuji being exocytosed. Deletion mutants of SV recycling factors, *unc-26(s1710)* and *unc-57(e406)*, displayed a higher increase in pHuji fluorescence than wild type animals [**Supplementary Figure 2C**: wild type 17 ± 3%, *unc-26(s1710)* 31 ± 5%, $^{*}p < 0.05$; **Supplementary Figure 2D**: wild type 16 ± 3%, *unc-57(e406)* 30 ± 4%, $^{*}p < 0.05$]. This was surprising since both mutants were previously shown to be depleted of ready-to-release SVs and should therefore not be able to externalize as many SVs as wild type animals (Harris et al., 2000; Schuske et al., 2003). Nevertheless, they showed prolonged increased fluorescence during acquisition compared to wild type. *snt-1(md290)* knockout mutants displayed a similar signal increase and decay trend as wild type [**Supplementary Figure 2E**: wild type 14 ± 3%, *snt-1(md290)* 18 ± 3%, ns $p > 0.05$]. We calculated the kinetics of fluorescence decay after stimulation using a one-phase exponential decay model (**Supplementary Figures 2F–H**). However, no significant difference in the rate of the fluorescence decay was observed. We thus wondered if the pHuji/ChR2 combination works properly. One concern was that photophobic reactions to blue light, mediated by the photoreceptor LITE-1, may affect the measured fluorescence increase and recycling rate (Edwards et al., 2008). However, we did not observe any significant difference between *lite-1(ce314)* knockout mutants and wild type animals in the pOpsicle assay, independent of ATR treatment (**Supplementary Figures 2I, J**). We suggest that the previously reported photo-switching behavior of pHuji in blue light (Liu et al., 2021) likely explains the slight increase in fluorescence in animals without ATR after stimulation and could also influence the decay kinetics in animals with ATR (**Supplementary Figures 1E, 2I**). Since pHuji appeared unable to properly track SV recycling, we investigated another protein combination for the pOpsicle assay.

3.2. Improving pOpsicle through combination of pHluorin with ChrimsonSA

We tested the more commonly used green fluorescent pHluorin as a pH-sensitive fluorophore which moreover features brighter fluorescence (Miesenbock et al., 1998; Li et al., 2022). Since pHluorin has overlapping excitation spectra with ChR2, we needed to exchange ChR2 with a red light activated channelrhodopsin. The recently described ChrimsonSA (for super red-shifted and accelerated), which is a mutated variant (S169A) of Chrimson, seemed to be a suitable candidate (Oda et al., 2018). Previously, we could show that ChrimsonSA can be used to depolarize *C. elegans* motor neurons upon stimulation with red light (Seidenthal et al., 2022; **Figure 2A**). Two copies of pHluorin were inserted into the second intraluminal loop of SNG-1 as multiple pHluorin insertions have been shown to increase the signal-to-noise ratio (Zhu et al., 2009). We co-expressed this fusion construct with ChrimsonSA in cholinergic motor neurons and observed basal pHluorin fluorescence throughout the cholinergic nervous system (**Figure 2B**). SNG-1::pHluorin also localizes to neuronal extensions of DA and DB neurons innervating dorsal muscle cells (**Figure 2C**). Fluorescent puncta in the DNC indicate an accumulation of pHluorin at NMJs. We then tested for crosstalk of pHluorin imaging light with ChrimsonSA activation using contraction assays (**Figures 2D, E**). The intensity of blue light used to visualize pHluorin (470 nm, 40 $\mu W/mm^2$) did not lead to a significant decrease in body length of animals treated with ATR. In contrast to this, 40 $\mu W/mm^2$ of 580 nm light was sufficient to trigger contraction of body wall muscles. This indicates that ChrimsonSA is functioning properly to depolarize cholinergic motor neurons yet is not pre-activated by blue light. Next, we performed pOpsicle assays with pHluorin animals ("green pOpsicle"). We observed spontaneous pHluorin increases in some animals, independent of treatment with ATR or light stimulation (**Supplementary Figure 3A**), verifying that pHluorin imaging can report on exocytosis. During photostimulation, DNC fluorescence gradually increased by 21 ± 2% upon continuous 590 nm stimulation in ATR-treated animals (**Figures 2F–I**, see **Supplementary Figure 3B** for a representation of all experiments, and **Supplementary Movie 1**). The signal approached a plateau after ∼10 s, indicating that most SNG-1::pHluorin was externalized at this point. Animals without ATR showed no increase upon stimulation (0 ± 1%, $^{***}p < 0.001$; **Figures 2H, I**). The increase in fluorescence was especially high in synaptic puncta along the DNC, indicating locations of highly active SV release sites (**Figures 2F, G**). Following the end of the stimulation, like in red pOpsicle experiments, the signal gradually decreased toward levels before stimulation. We also tested a higher light intensity to stimulate ChrimsonSA (280 $\mu W/mm^2$)

10.3389/fncel.2023.1120651

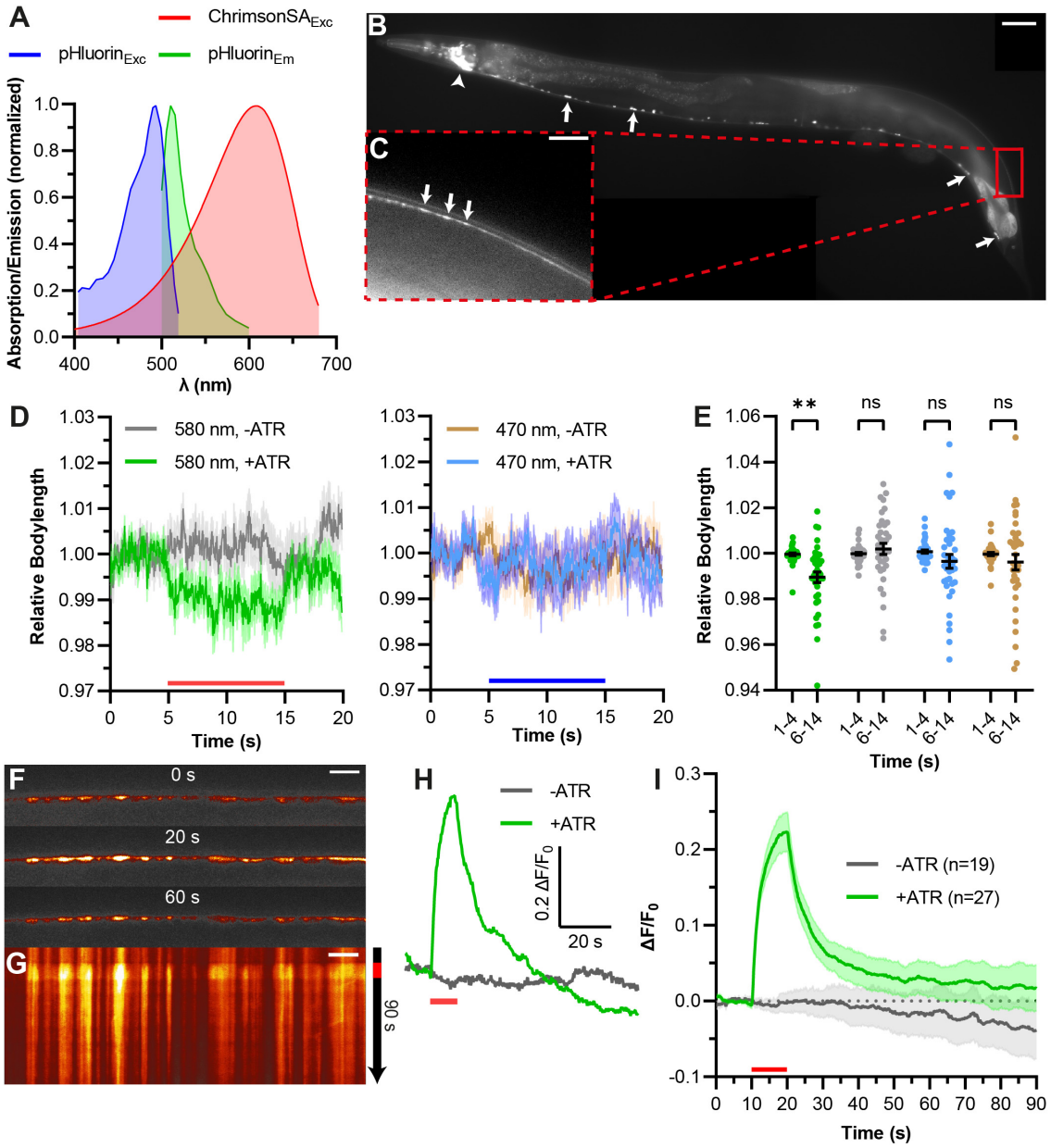

FIGURE 2
Combining ChrimsonSA with pHluorin ("green pOpsicle") for stimulation and visualization of exo- and endocytosis. **(A)** Relative excitation and emission spectra of ChrimsonSA and super-ecliptic pHluorin, normalized to the maximum absorption/emission amplitude. **(B)** Representative image of *C. elegans* expressing SNG-1::pHluorin in cholinergic neurons. Arrows represent cell bodies of A- and B-type motor neurons (ventral nerve cord). Arrowhead represents cholinergic neurons in the head ganglia. 40× magnification. Scale bar, 50 μm. **(C)** Enlarged view of the DNC in panel **(B)**. Arrows represent fluorescent puncta, representing *en passant* synaptic terminals. Scale bar, 10 μm. **(D)** Mean relative body length (±SEM) of animals expressing ChrimsonSA and pHluorin optionally treated with ATR, as indicated, normalized to the average body length before stimulation. A 10 s continuous light pulse (580 or 470 nm as indicated, 40 μW/mm^2; indicated by red and blue bars) was applied after 5 s. Number of animals (*n*), accumulated from *N* = 3 biological replicates. **(E)** Statistical analysis of animals shown in panel **(D)**. Each dot represents the mean normalized body length of a single animal during the indicated period. Two-way ANOVA with Šídák's correction ($^{ns}p > 0.05$, $^{**}p < 0.01$). **(F)** Representative images of pHluorin fluorescence in the DNC of an animal treated with ATR at different time points during the pOpsicle assay, as indicated. A 10 s continuous light pulse (590 nm, 40 μW/mm^2) was applied after 10 s. The ImageJ *Smart* Look-Up-Table was used. 100× magnification. Scale bar, 5 μm. **(G)** Kymograph representing the change in fluorescence of the DNC represented in panel **(F)** over a time course of 90 s. The red bar indicates the period of light stimulus. Scale bar, 5 μm. **(H)** Representative traces of normalized DNC fluorescence of individual animals with or without ATR. A 10 s continuous light pulse (590 nm, 40 μW/mm^2) was applied after 10 s (red bar). **(I)** Mean (±SEM) change in DNC fluorescence of animals supplemented with and without ATR. A 10 s continuous light pulse (590 nm, 40 μW/mm^2) was applied after 10 s (red bar). Number of animals (*n*), accumulated from *N* = 4 (+ATR), and *N* = 3 (−ATR) biological replicates.

and observed a slightly higher increase in fluorescence yet overall similar trend (Supplementary Figure 3C; 30 ± 3%, $^{*}p < 0.05$ compared to 40 μW/mm^2). Similarly, stronger light stimulation led to a linearly increasing contraction in behavioral experiments (Supplementary Figure 3D). For subsequent analyses we used 40 μW/mm^2 since it seemed sufficient to release

most SVs and stronger stimulation may trigger unphysiological effects.

To further characterize parameters of the "green pOpsicle" assay, e.g., releasable fraction of total pHluorin, we replicated it in neurons of primary cell cultures from dissociated *C. elegans* embryos (**Supplementary Figures 4A, B**). pHluorin fluorescence could be observed in neurite extensions and in cell bodies, surrounding nuclei (**Supplementary Figure 4A**). This fluorescence increased in some neurons when illuminated (and when treated with ATR) even though the signal size was lower than in intact animals, where this was the case for each individual recording (**Figure 2I** and **Supplementary Figure 4B**). A total of 18 of 52 neurons showed a strong response (for a definition of "strong response," see section "Materials and methods"). Next, we calculated the fraction of releasable SVs by ChrimsonSA stimulation. To this end, we first stimulated cultured neurons with light and then applied a pH 7.4 NH_4Cl buffer (**Supplementary Figure 4C**), which can be used to increase the pH within SVs and calculate the SV-associated portion of pHluorins (Sankaranarayanan et al., 2000; Dittman and Kaplan, 2006; Rose et al., 2013; Egashira et al., 2016). To minimize bleaching, we reduced the exposure to blue light by decreasing the frame rate of pHluorin acquisition. When exposed to NH_4Cl (pH 7.4), pHluorin fluorescence in neurites rapidly increased (**Supplementary Figures 4C–E**). The same culture was then treated with a low pH buffer (pH 5.6) to quench the surface fraction of pHluorin (**Supplementary Figures 4C, F**). The fluorescence immediately decreased to levels below the basal fluorescence, demonstrating the pH-dependency of pHluorin fluorescence. The fraction of releasable SVs was determined by calculation of the ratio of maximum fluorescence during light stimulation and during NH_4Cl treatment (**Supplementary Figure 4G**): 10 s continuous light stimulation released 20.20% (±3.72%) of SNG-1::pHluorin molecules attached to SVs, which is comparable to previous measurements in hippocampal slices that used synaptophysin::pHluorin as a reporter (Rose et al., 2013). To test a different, less vigorous stimulation regime, which may be more reminiscent to endogenous activity, we applied 2 Hz pulsed light (**Supplementary Figure 4C**). This led to a reduced release of SVs compared to continuous light (**Supplementary Figure 4G**, 10.61 ± 1.87%). Even though the fraction of releasable SVs by optogenetic stimulation is within a typical range compared to other reports, we conclude that in intact animals the signal size is higher and the assay more reliable in living animals indicating that a higher portion of SVs is exocytosed (**Figure 2I** and **Supplementary Figure 4B**).

3.3. Quantification of SV exo- and endocytosis kinetics by the pHluorin pOpsicle assay

Next, we used green pOpsicle to analyze mutants affecting SV fusion (*snb-1(md247), snt-1(md290)*) and/or recycling (*unc-26(s1710), unc-57(e406), snt-1(md290)*) (**Figure 3**). In *snb-1(md247)* mutants, the signal increase during stimulation was almost completely abolished (**Figures 3A, B** and **Supplementary Figure 5A**). Only 2 of 19 animals showed a relevant response (compared to 23/23 in wild type), demonstrating that the increase of fluorescence during stimulation reports on SV exocytosis. Synaptojanin (*unc-26(s1710)*) mutant animals also exhibited a reduced signal compared to wild type (**Figures 3C, D** and **Supplementary Figure 5B**). Thus, green pOpsicle faithfully revealed the expected depletion of SVs in *unc-26(s1710)* mutants (Harris et al., 2000), unlike pHuji that displayed a higher fluorescence after stimulation (**Supplementary Figure 2C**). To allow calculating the kinetics of fluorescence rise and decay, animals which showed no significant increase in fluorescence or no decay after stimulation were removed from our analyses (**Supplementary Figure 6A**). We observed a significantly slower rise of fluorescence in *unc-26(s1710)* mutant compared to wild type animals, as could be seen by the increased time constants of the signal curves obtained from single animals, when fitted to a one-phase exponential association kinetic ($\tau_{Rise,wildtype}$ = 2.3 s, $\tau_{Rise,\ unc-26}$ = 3.6 s; **Figure 3E**). This could indicate an exocytosis defect, or it could be due to the reduced number of SVs that are available for fusion in the *unc-26(s1710)* mutant (Dong et al., 2015). The kinetics of the fluorescence decay after stimulation showed a strong reduction, as expected for the SV recycling mutant (**Figure 3F**). Consequently, the calculated time constants of one-phase exponential decay were significantly increased in *unc-26(s1710)* mutants ($\tau_{Decay,wildtype}$ = 15.2 s, $\tau_{Decay,\ unc-26}$ = 24.2 s), closely matching previous results measured in mammalian cortical neurons lacking synaptojanin after strong stimulation (Cao et al., 2017). Wild type animals on the other hand showed decay time constants which are in the range of previous measurements in *C. elegans* sensory neurons or mammalian hippocampal neurons (Kwon and Chapman, 2011; Ventimiglia and Bargmann, 2017; Watanabe et al., 2018; Li et al., 2022). Endophilin (*unc-57(e406)*) mutants exhibited similar trends as *unc-26(s1710)* with a significantly reduced signal and significantly slower association and decay kinetics compared to wild type ($\tau_{Rise,wildtype}$ = 2.7 s, $\tau_{Rise,\ unc-57}$ = 3.3 s, $\tau_{Decay,wildtype}$ = 15.2 s, $\tau_{Decay,\ unc-57}$ = 24.7 s; **Figures 3G–J** and **Supplementary Figure 5C**). The time constants obtained for *unc-57(e406)* mutants closely matched those of *unc-26(s1710)* mutants, in line with the function of synaptojanin and endophilin in similar cellular processes (Harris et al., 2000; Dong et al., 2015; Watanabe et al., 2018). Synaptotagmin [*snt-1(md290)*] mutants also displayed a smaller increase in fluorescence (**Figures 3K, L** and **Supplementary Figure 5D**). The time constants of fluorescence rise were significantly increased in mutant animals ($\tau_{Rise,wildtype}$ = 3.1 s, $\tau_{Rise,snt-1}$ = 5.6 s; **Figure 3M**), demonstrating the role of SNT-1 in SV fusion (Liewald et al., 2008; Yu et al., 2013). We further observed a significantly delayed decrease of fluorescence after stimulation, indicating that SNT-1 is involved in SV recycling at *C. elegans* NMJs (Poskanzer et al., 2003; Mochida, 2022; $\tau_{Decay,wildtype}$ = 11.1 s, $\tau_{Decay,\ snt-1}$ = 31.1 s; **Figure 3N**). Since the increase in fluorescence was generally lower in mutant animals, we wondered whether higher time constants of decay were caused by a lower activation of synaptic transmission rather than decreased SV recycling rates. We thus compared decay time constants of individual animals with the respective signal size. However, there was no significant correlation within any of the analyzed genotypes (**Supplementary Figures 6B–D**). Therefore,

10.3389/fncel.2023.1120651

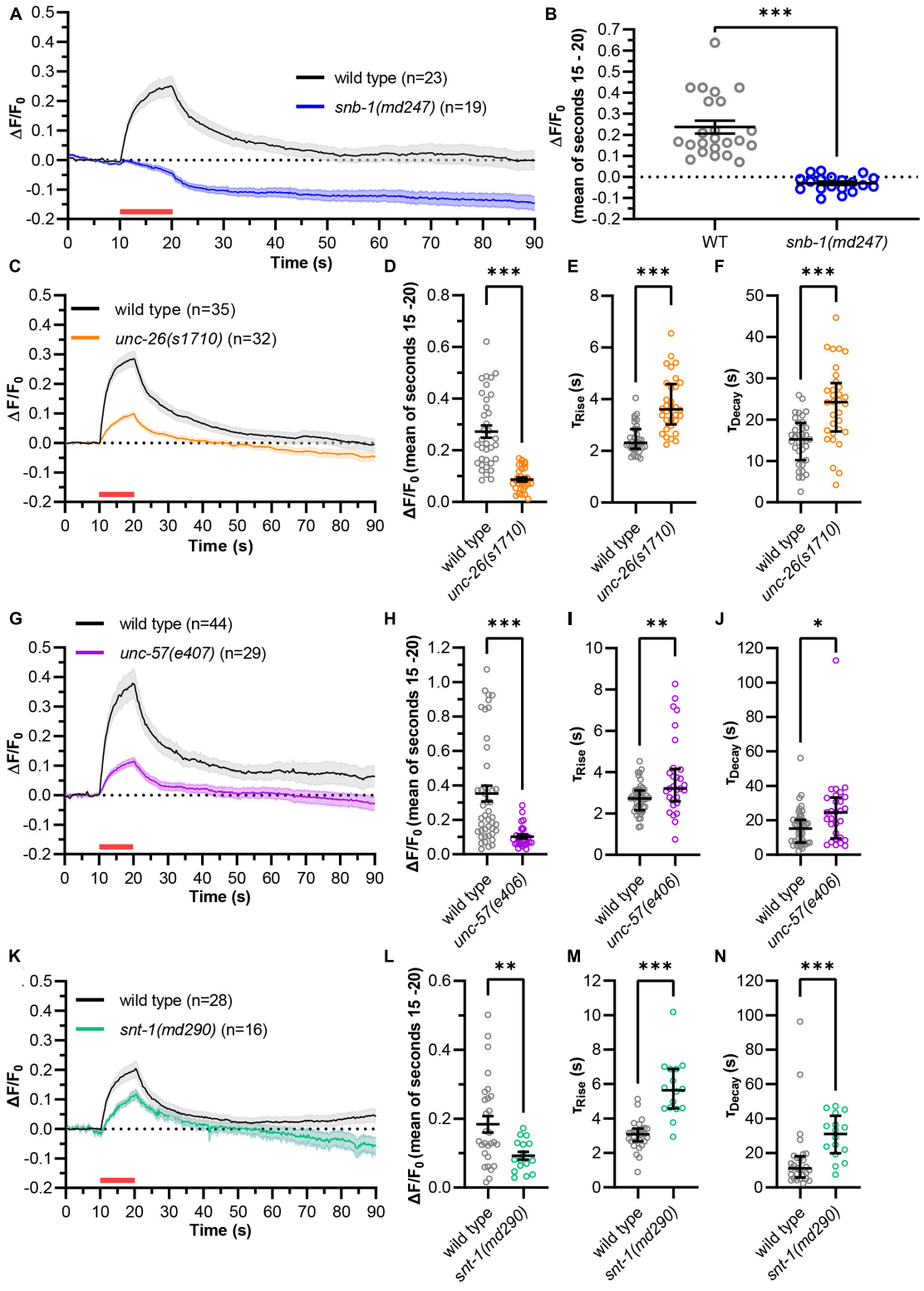

FIGURE 3
"Green" pOpsicle reports on mutations affecting SV fusion and endocytosis. **(A,C,G,K)** Mean (±SEM) change of fluorescence of SNG-1::pHluorin co-expressed with ChrimsonSA in cholinergic motor neurons. DNC of wild type and mutant animals, as indicated. A 10 s continuous light pulse (590 nm, 40 μW/mm^2; indicated by a red bar) was applied after 10 s. Number of animals (*n*), accumulated from *N* = 4–6 biological replicates. **(B,D,H,L)** Fluorescent signal of individual wild type and mutant animals at the end of stimulation (15–20 s). Mean (±SEM). Unpaired *t*-test (**$p < 0.01$, ***$p < 0.001$). **(E,I,M)** Calculated fluorescence rise constants of single animals using a one-phase exponential fit during stimulation (10–20 s). Median with interquartile range. Mann–Whitney test (**$p < 0.01$, ***$p < 0.001$). **(F,J,N)** Calculated fluorescence decay constants of single animals using a one-phase exponential fit after stimulation (20–90 s). Median with interquartile range. Mann–Whitney test (*$p < 0.05$, ***$p < 0.001$). In panels **(C–N)**, animals showing an increase <3 standard deviations during stimulation, or no decay of fluorescence following stimulation, were excluded [wild type: 4 of 111 animals, *unc-26(s1710)*: 7 of 39, *unc-57(e406)*: 18 of 47, *snt-1(md290)*: 23 of 39].

recycling rates likely do not depend on the amount of SV fusion in this assay.

3.4. Pulsed stimulation to potentially access different recycling mechanisms

Continuous photostimulation induces maximal depolarization and transmitter release, likely causing bulk endocytosis as the extreme form of ultrafast endocytosis (Kittelmann et al., 2013). To assess whether less vigorous, possibly more physiological activation also affects slower recycling, we applied 2 Hz pulsed stimulation (100 ms light pulses; **Figure 4**). The mutant strains again showed significantly reduced signal amplitudes compared to wild type (**Figures 4A, B** and **Supplementary Figure 7**) but no significantly increased time constants of fluorescence rise ($\tau_{Rise,wildtype}$ = 4.2 s, $\tau_{Rise,\ unc-26}$ = 6.0 s, $\tau_{Rise,\ unc-57}$ = 4.7 s, $\tau_{Rise,\ snt-1}$ = 4.7 s; **Figure 4C**). When comparing pulsed and continuous stimulation we observed a tendency toward decreased fluorescence amplitudes and significantly increased rise time constants, indicating that pulsed stimulation leads to a reduced activation of neurotransmission (**Supplementary Figures 8A, B**). For the recycling phase, pulsed stimulation again resulted in significantly larger decay time constants in *unc-57(e406)* and *unc-26(s1710)* mutants compared to wild type ($\tau_{Decay,wildtype}$ = 20.9 s, $\tau_{Decay,\ unc-26}$ = 41.1 s, $\tau_{Decay,\ unc-57}$ = 45.1 s; **Figure 4D**), however, *snt-1(md290)* mutant animals showed no significant difference ($\tau_{Decay,\ snt-1}$ = 28.6 s). Possibly, SNT-1 is dispensable for recycling at lower levels of stimulation. Decay time constants for pulsed stimulation were significantly increased in *unc-57(e406)* and *unc-26(s1710)* mutants indicating that a compensatory mechanism, which is independent of endophilin and synaptojanin, may be activated after strong stimulation (**Supplementary Figure 8C**).

3.5. pOpsicle reports on SV turnover in the single pair of RIM interneurons

While the green pOpsicle assay worked well in cholinergic motor neurons, it remained to be shown that this system works in other neuronal cell types. The RIM interneuron pair integrates signals from sensory neurons to regulate forward and reversal locomotion, using gap junctions as well as glutamate and tyramine signaling (Piggott et al., 2011; Li et al., 2020; Sordillo and Bargmann, 2021). We expressed SNG-1::pHluorin and ChrimsonSA in RIM using the *tdc-1* promotor. Green fluorescence could be observed in neuronal extensions surrounding the pharynx, suggesting correct localization of SNG-1::pHluorin (**Figure 5A**). To explore ChrimsonSA functionality in this neuron pair, we measured animal crawling speed (**Figure 5B**). Optogenetic depolarization of RIM neurons previously induced reversals and reduced crawling speed (Guo et al., 2009; Li et al., 2020; Sordillo and Bargmann, 2021). Consistent with this, illumination with red light slowed down crawling speed of RIM pOpsicle animals treated with ATR and the number of reversals was increased (**Figures 5B, C**). This indicated that ChrimsonSA depolarized RIM neurons when activated. Consequently, SNG-1::pHluorin fluorescence in synaptic puncta was significantly increased by ChrimsonSA activation (**Figures 5D, E**, **Supplementary Figure 9**, and **Supplementary Movie 2**), while control animals without ATR showed no change (+ATR 6 ± 2%, −ATR −1 ± 1%, $^{***}p < 0.001$; **Figure 5F**). The signal increase was significantly slower than in cholinergic neurons ($\tau_{Rise,RIM}$ = 5.7 s, $\tau_{Rise,cholinergic}$ = 2.4 s; **Figure 5G**), as was the decay of fluorescence following the end of stimulation ($\tau_{Decay,RIM}$ = 42.3 s, $\tau_{Decay,cholinergic}$ = 16.0 s; **Figure 5H**). These results indicate that different classes of neurons may have diverging kinetics of SV exo- and endocytosis in *C. elegans*. Thus, the pOpsicle assay can be adapted to different neuronal cell types.

4. Discussion

Here, we present the first all-optical method to investigate SV recycling *in vivo* by combining pH-sensitive fluorescent proteins with ChRs. With pOpsicle, factors that influence the extent and rate of exo- and endocytosis can be investigated with minor experimental effort and equipment. We described two approaches using different pH-sensitive fluorescent proteins. pHuji could only be used to quantify the extent of exocytosis after stimulation. The low quantum yield and photoswitching behavior of this protein influenced the emitted fluorescence in a way that precluded quantification of exo- and endocytosis kinetics (Shen et al., 2014; Liu et al., 2021). Using pHluorin and ChrimsonSA, however, solved these problems, enabling calculation of fluorescence rise and decay time constants, which characterize different rates of exo- and endocytosis (Li et al., 2022). Neuronal primary culture of pHluorin expressing neurons could further open the way for investigation of exocytosis independent of SV recycling, e.g., by applying pharmacological agents such as bafilomycin A to inhibit SV acidification (Subramanian and Morozov, 2011; Li et al., 2022).

The pOpsicle system should be applicable to various neuronal cell types with minor modifications as exemplified by expression in cholinergic neurons and RIM interneurons. Establishing pOpsicle in various cell types could unveil disparities in SV exo- and endocytosis between different neuron classes, as has been shown for sensory neurons in *C. elegans* (Ventimiglia and Bargmann, 2017). Hitherto, electrophysiological recordings or Ca^{2+} imaging in body wall muscles were the method of choice to quantify neurotransmitter release in *C. elegans* in a time-resolved manner (Liewald et al., 2008; Wabnig et al., 2015). However, these only report postsynaptic effects which might be altered by unrelated phenomena such as neurotransmitter-receptor upregulation (Hammond-Weinberger et al., 2020). By using pOpsicle, a direct observation of the presynaptic SV cycle was achieved. This way, we could observe slowed SV fusion and endocytosis in RIM interneurons compared to cholinergic motor neurons. The faster release and recycling in cholinergic neurons may be in line with their function in mediating locomotion, and the likely high SV turnover needed, while the slower release rate could be important to the dual role of RIM in regulating reversal behavior (Li et al., 2020; Sordillo and Bargmann, 2021; Bach et al., 2023). While RIM promotes reversals through activation AVA and AVE neurons *via* gap junctions, and by mutual interaction with RIS, glutamate signaling inhibits reversal probability by reducing the amplitude of Ca^{2+} spikes within AVA and AVE and tyramine inhibits RIS (Li et al., 2020; Bach et al., 2023). A delayed release

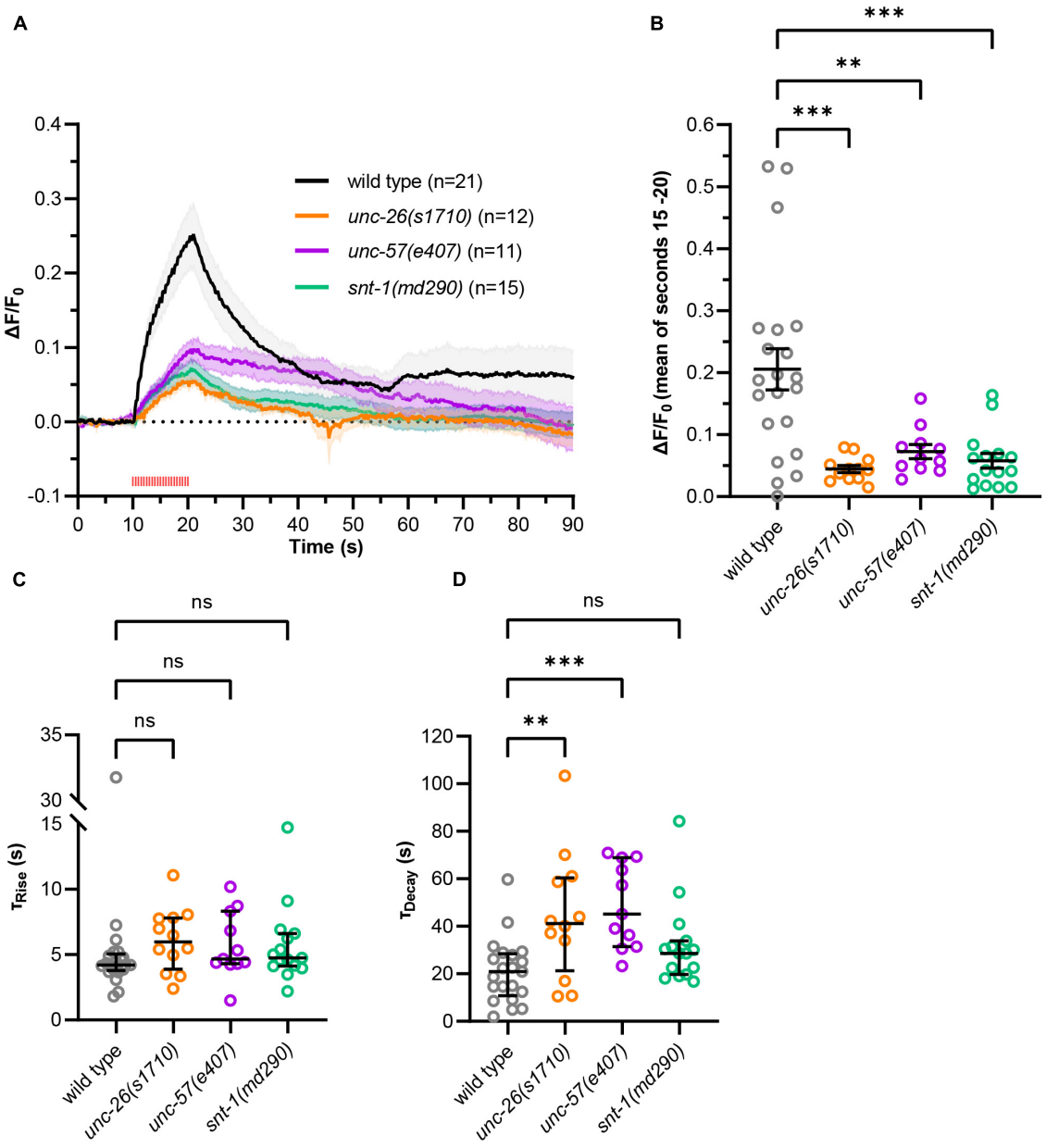

FIGURE 4
Using pulsed, more physiological optogenetic stimulation. **(A)** As in **Figure 3**, but using 2 Hz pulsed light stimulation (100 ms pulses, 590 nm, 40 μW/mm^2, red tick marks) applied after 10 s for 10 s. Using this stimulation regime, more animals were excluded from analysis [wild type: 17 of 38 animals, *unc-26(s1710)*: 18 of 30, *unc-57(e406)*: 22 of 33, *snt-1(md290)*: 39 of 54] accumulated from $N = 5–6$ biological replicates. **(B)** Fluorescent signal of individual wild type and mutant animals at the end of stimulation (15–20 s). Mean (±SEM). One-way ANOVAs with Dunnett's correction ($^{**}p < 0.01$, $^{***}p < 0.001$). **(C)** Calculated fluorescence rise constants of single animals using a one-phase exponential fit during stimulation (10–20 s). Median with interquartile range. Kruskal–Wallis test with Dunn's correction ($^{ns}p > 0.05$). **(D)** Calculated fluorescence decay constants of single animals using a one-phase exponential fit after stimulation (20–90 s). Median with interquartile range. Kruskal–Wallis test with Dunn's correction ($^{ns}p > 0.05$, $^{**}p < 0.01$, $^{***}p < 0.001$).

of glutamate and tyramine from RIM may thus promote a fast reaction to noxious stimuli by initiation of reversals. Observation of pHluorin dynamics in freely moving worms may solve this issue. However, we note that it was imperative for the assay to work that the animals were kept as immobile as possible.

With green pOpsicle, we could reveal differences in recycling kinetics of synaptojanin and endophilin knockout mutants between continuous and pulsed stimulation. Discrepancies in the rate of recycling may be caused by different degrees of stimulation which trigger distinct routes of SV retrieval (Watanabe and Boucrot, 2017). Activity-dependent bulk endocytosis (ADBE) after strong optogenetic stimulation was shown to occur in *unc-57(e406)* and *unc-26(s1710)* knockout mutants and may be the main pathway of retrieval after continuous stimulation (Kittelmann et al., 2013; Nicholson-Fish et al., 2016; Yu et al., 2018). Moderate, pulsed stimulation however may trigger other endocytic mechanisms such as ultrafast and clathrin-mediated endocytosis, which are dependent on endophilin and synaptojanin (Milosevic et al., 2011;

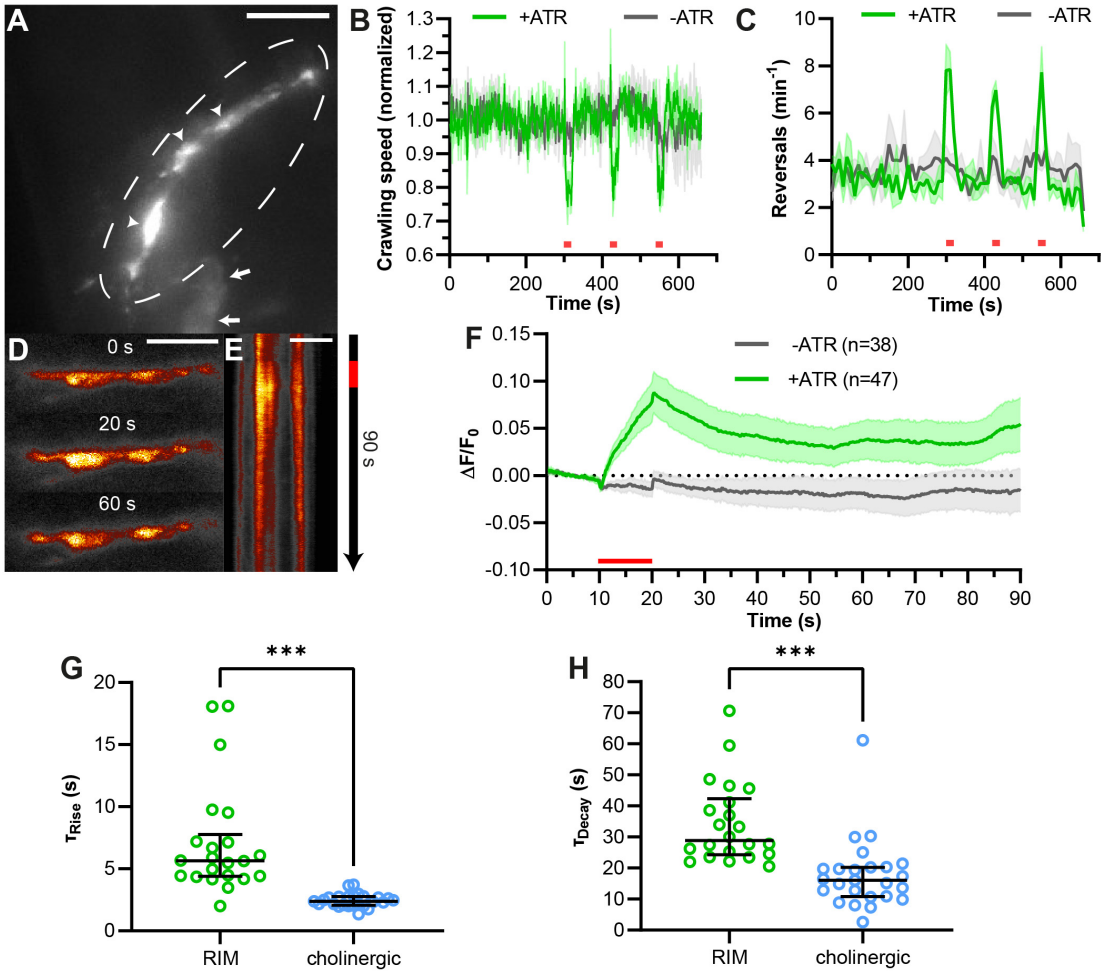

FIGURE 5
pOpsicle assay in the RIM interneuron pair. **(A)** Representative *Z*-projected image of *C. elegans* expressing SNG-1::pHluorin in RIM neurons using the promotor of *tdc-1*. 40× magnification. Arrows represent cell bodies of RIM neurons. Circle represents RIM axon in the nerve ring. Arrowheads represent fluorescent puncta, representing *en passant* synaptic terminals. 40× magnification. Scale bar, 5 μm. **(B)** Mean crawling speed (±SEM) of animals expressing ChrimsonSA and pHluorin in RIM neurons normalized to the average before the first light pulse. Three 20 s light pulses (623 nm, 400 μW/mm^2) were applied at 300, 420, and 540 s as indicated by red bars. **(C)** Mean (±SEM) number of reversals per minute per animal. Light stimulation as in panel **(B)**. In panels **(B,C)**, *N* = 3 populations of animals were tested. **(D)** Representative images acquired at different time points during the pOpsicle assay, pHluorin fluorescence in RIM neurons, animal treated with ATR. A 10 s continuous light pulse (590 nm, 40 μW/mm^2) was applied after 10 s. The ImageJ *Smart* Look-Up-Table was used. 100× magnification. Scale bar, 5 μm. **(E)** Kymograph representing the change in fluorescence in RIM neurons as shown in panel **(D)** over a time course of 90 s. The red bar indicates the period of light stimulus. Scale bar, 5 μm. **(F)** Mean (±SEM) pHluorin fluorescence in RIM neurons of animals with and without ATR. A 10 s continuous light pulse (590 nm, 40 μW/mm^2) was applied after 10 s. Number of animals (*n*), accumulated from *N* = 5 (+ATR) or *N* = 4 (−ATR) biological replicates. **(G)** Comparison of fluorescence rise constants of single animals expressing pHluorin and ChrimsonSA in RIM neurons or in cholinergic neurons, using a one-phase exponential fit during stimulation (10–20 s). Median with interquartile range. Mann–Whitney test (***$p < 0.001$). **(H)** Comparison of fluorescence decay constants of single animals as in panel **(G)**, using a one-phase exponential fit after stimulation (20–90 s). Median with interquartile range. Mann–Whitney test (***$p < 0.001$). **(G,H)** Only animals showing a strong response during stimulation and a decay of fluorescence after stimulation were taken into consideration (RIM: 22 of 47 animals, cholinergic neurons: 25 of 27 animals as depicted in **Figure 2**).

Watanabe et al., 2018). *snt-1(md290)* mutants displayed more severe recycling defects after strong stimulation, indicating that it is dispensable for recycling at lower activity. This is in stark contrast to previous results in mammalian hippocampal neurons in which synaptotagmin promotes slow small-scale endocytosis, while inhibiting bulk retrieval during sustained neurotransmission (Chen et al., 2022). Although a role of SNT-1 in the slow clathrin-mediated endocytosis is likely also in *C. elegans* and simply not efficiently reported by pOpsicle, a role in inhibition of bulk endocytosis might not be conserved between nematodes and mammals. Previously, *snt-1(md290)* mutants have shown earlier fatigue of postsynaptic currents during strong optogenetic depolarization of cholinergic motor neurons indicating a compensatory SV recycling defect during strong sustained neurotransmission (Liewald et al., 2008; Wabnig et al., 2015).

Finally, SNG-1::pHluorin can further be used as a sensor for spontaneous neuronal activity and SV endocytosis in *C. elegans*, independent of optogenetic stimulation (**Supplementary Figure 3A**). This opens the way for multiplexing with other fluorescent reporters of neuronal activity such as genetically encoded Ca^{2+} or voltage indicators (Dreosti and Lagnado, 2011; Jackson and Burrone, 2016; Azimi Hashemi et al., 2019). The

combination of simultaneous imaging of SV dynamics and membrane potential changes could help to unravel the complicated interplay of interneurons in the control of locomotion by differentiating between electrical and chemical transmission.

Data availability statement

The original contributions presented in this study are included in the article/**Supplementary material**, further inquiries can be directed to the corresponding author.

Author contributions

MS, BJ, and XZ created the plasmids and generated the strains. MS performed the pOpsicle, cell culture, and contraction assays. MW tested the ChrimsonSA in cholinergic neurons. NS and NE generated and tested the ChrimsonSA/pHluorin strains. NR generated the primary neuronal cell cultures. MS, BJ, and AG designed and coordinated the study. MS and AG wrote the manuscript. AG supervised the work. All authors read and approved the final manuscript.

Funding

This project was funded by Deutsche Forschungsgemeinschaft, Collaborative Research Centre 1080 project B02 (grant DFG CRC1080/B2 to AG).

Acknowledgments

We are indebted to Franziska Baumbach, Hans-Werner Müller, and Eva Dunkel for their expert technical assistance, and members of the Gottschalk Group for critical comments regarding the manuscript. We thank Dennis Vettkötter for providing MWT software and Ichiro Aoki for Arduino scripts and μManager settings to control LEDs and camera shutter for pulsed stimulation. We thank Johannes Vierock for providing ChrimsonSA absorption spectra. We also thank Maximilian Bach for advice on RIM experiments, and the *Caenorhabditis* Genetics Center (CGC), which is funded by the NIH Office of Research Infrastructure Programs (P40 OD010440), for providing strains.

Conflict of interest

The authors declare that the research was conducted in the absence of any commercial or financial relationships that could be construed as a potential conflict of interest.

Publisher's note

Supplementary material

The Supplementary Material for this article can be found online at: https://www.frontiersin.org/articles/10.3389/fncel.2023.1120651/full#supplementary-material

References

Abraham, C., Hutter, H., Palfreyman, M. T., Spatkowski, G., Weimer, R. M., Windoffer, R., et al. (2006). Synaptic tetraspan vesicle membrane proteins are conserved but not needed for synaptogenesis and neuronal function in *Caenorhabditis elegans*. *Proc. Natl. Acad. Sci. U S A.* 103, 8227–8232. doi: 10.1073/pnas.0509400103

Alfonso, A., Grundahl, K., Duerr, J. S., Han, H. P., and Rand, J. B. (1993). The *Caenorhabditis elegans* unc-17 gene: a putative vesicular acetylcholine transporter. *Science* 261, 617–619. doi: 10.1126/science.8342028

Azimi Hashemi, N., Bergs, A. C. F., Schuler, C., Scheiwe, A. R., Steuer Costa, W., Bach, M., et al. (2019). Rhodopsin-based voltage imaging tools for use in muscles and neurons of *Caenorhabditis elegans*. *Proc. Natl. Acad. Sci. U S A.* 116, 17051–17060. doi: 10.1073/pnas.1902443116

Azimi Hashemi, N., Erbguth, K., Vogt, A., Riemensperger, T., Rauch, E., Woodmansee, D., et al. (2014). Synthetic retinal analogues modify the spectral and kinetic characteristics of microbial rhodopsin optogenetic tools. *Nat. Commun.* 5:5810. doi: 10.1038/ncomms6810

Bach, M., Bergs, A., Mulcahy, B., Zhen, M., and Gottschalk, A. (2023). Coordinated electrical and chemical signaling between two neurons orchestrates switching of motor states. *bioRxiv [preprint]* doi: 10.1101/2023.01.04.522780

Boyden, E. S., Zhang, F., Bamberg, E., Nagel, G., and Deisseroth, K. (2005). Millisecond-timescale, genetically targeted optical control of neural activity. *Nat. Neurosci.* 8, 1263–1268. doi: 10.1038/nn1525

Brenner, S. (1974). The genetics of *Caenorhabditis elegans*. *Genetics* 77, 71–94. doi: 10.1093/genetics/77.1.71

Cao, M., Wu, Y., Ashrafi, G., McCartney, A. J., Wheeler, H., Bushong, E. A., et al. (2017). Parkinson sac domain mutation in synaptojanin 1 impairs clathrin uncoating at synapses and triggers dystrophic changes in dopaminergic axons. *Neuron* 93, 882–896 e5. doi: 10.1016/j.neuron.2017.01.019.

Chanaday, N. L., Cousin, M. A., Milosevic, I., Watanabe, S., and Morgan, J. R. (2019). The synaptic vesicle cycle revisited: new insights into the modes and mechanisms. *J. Neurosci.* 39, 8209–8216. doi: 10.1523/JNEUROSCI.1158-19.2019

Chang, R. B. (2019). Optogenetic control of the peripheral nervous system. *Cold Spring Harb. Perspect. Med.* 9:a034397. doi: 10.1101/cshperspect.a034397

Chen, Y., Hu, S., Wu, X., Xie, Z., Wang, Y., Wang, B., et al. (2022). Synaptotagmin-1 is a bidirectional Ca(2+) sensor for neuronal endocytosis. *Proc. Natl. Acad. Sci. U S A.* 119:e2111051119. doi: 10.1073/pnas.2111051119

Choi, J. H., Horowitz, L. B., and Ringstad, N. (2021). Opponent vesicular transporters regulate the strength of glutamatergic neurotransmission in a *C. elegans* sensory circuit. *Nat. Commun.* 12:6334. doi: 10.1038/s41467-021-26575-3

Christensen, M., Estevez, A., Yin, X., Fox, R., Morrison, R., McDonnell, M., et al. (2002). A primary culture system for functional analysis of *C. elegans* neurons and muscle cells. *Neuron* 33, 503–514. doi: 10.1016/s0896-6273(02)00591-3

Dittman, J. S., and Kaplan, J. M. (2006). Factors regulating the abundance and localization of synaptobrevin in the plasma membrane. *Proc. Natl. Acad. Sci. U S A.* 103, 11399–11404.

Dong, Y., Gou, Y., Li, Y., Liu, Y., and Bai, J. (2015). Synaptojanin cooperates in vivo with endophilin through an unexpected mechanism. *eLife* 4:e05660. doi: 10.7554/eLife.05660

Dreosti, E., and Lagnado, L. (2011). Optical reporters of synaptic activity in neural circuits. *Exp. Physiol.* 96, 4–12. doi: 10.1113/expphysiol.2009.051953

Edelstein, A. D., Tsuchida, M. A., Amodaj, N., Pinkard, H., Vale, R. D., and Stuurman, N. (2014). Advanced methods of microscope control using muManager software. *J. Biol. Methods* 1:e10. doi: 10.14440/jbm.2014.36

Edwards, S. L., Charlie, N. K., Milfort, M. C., Brown, B. S., Gravlin, C. N., Knecht, J. E., et al. (2008). A novel molecular solution for ultraviolet light detection in *Caenorhabditis elegans*. *PLoS Biol.* 6:e198. doi: 10.1371/journal.pbio.0060198

Egashira, Y., Takase, M., and Takamori, S. (2015). Monitoring of vacuolar-type H+ ATPase-mediated proton influx into synaptic vesicles. *J. Neurosci.* 35, 3701–3710. doi: 10.1523/JNEUROSCI.4160-14.2015

Egashira, Y., Takase, M., Watanabe, S., Ishida, J., Fukamizu, A., Kaneko, R., et al. (2016). Unique pH dynamics in GABAergic synaptic vesicles illuminates the mechanism and kinetics of GABA loading. *Proc. Natl. Acad. Sci. U S A.* 113, 10702–10707. doi: 10.1073/pnas.1604527113

Fire, A. (1986). Integrative transformation of Caenorhabditis elegans. *EMBO J.* 5, 2673–2680. doi: 10.1002/j.1460-2075.1986.tb04550.x

Gan, Q., and Watanabe, S. (2018). Synaptic vesicle endocytosis in different model systems. *Front. Cell Neurosci.* 12:171. doi: 10.3389/fncel.2018.00171

Gowrisankaran, S., and Milosevic, I. (2020). Regulation of synaptic vesicle acidification at the neuronal synapse. *IUBMB Life* 72, 568–576. doi: 10.1002/iub.2235

Guo, Z. V., Hart, A. C., and Ramanathan, S. (2009). Optical interrogation of neural circuits in *Caenorhabditis elegans*. *Nat. Methods* 6, 891–896. doi: 10.1038/nmeth.1397

Guru, A., Post, R. J., Ho, Y. Y., and Warden, M. R. (2015). Making sense of optogenetics. *Int. J. Neuropsychopharmacol.* 18:yv079. doi: 10.1093/ijnp/pyv079

Hammond-Weinberger, D. R., Wang, Y., Glavis-Bloom, A., and Spitzer, N. C. (2020). Mechanism for neurotransmitter-receptor matching. *Proc. Natl. Acad. Sci. U S A.* 117, 4368–4374. doi: 10.1073/pnas.1916600117

Harris, T. W., Hartwieg, E., Horvitz, H. R., and Jorgensen, E. M. (2000). Mutations in synaptojanin disrupt synaptic vesicle recycling. *J. Cell Biol.* 150, 589–600.

Hawk, J. D., Wisdom, E. M., Sengupta, T., Kashlan, Z. D., and Colon-Ramos, D. A. (2021). A genetically encoded tool for reconstituting synthetic modulatory neurotransmission and reconnect neural circuits in vivo. *Nat. Commun.* 12:4795. doi: 10.1038/s41467-021-24690-9

Heuser, J. E., and Reese, T. S. (1973). Evidence for recycling of synaptic vesicle membrane during transmitter release at the frog neuromuscular junction. *J. Cell Biol.* 57, 315–344. doi: 10.1083/jcb.57.2.315

Jackson, R. E., and Burrone, J. (2016). Visualizing presynaptic calcium dynamics and vesicle fusion with a single genetically encoded reporter at individual synapses. *Front. Synaptic Neurosci.* 8:21. doi: 10.3389/fnsyn.2016.00021

Jorgensen, E. M., Hartwieg, E., Schuske, K., Nonet, M. L., Jin, Y., and Horvitz, H. R. (1995). Defective recycling of synaptic vesicles in synaptotagmin mutants of *Caenorhabditis elegans*. *Nature* 378, 196–199. doi: 10.1038/378196a0

Kittelmann, M., Liewald, J. F., Hegermann, J., Schultheis, C., Brauner, M., Steuer Costa, W., et al. (2013). In vivo synaptic recovery following optogenetic hyperstimulation. *Proc. Natl. Acad. Sci. U S A.* 110, E3007–E3016. doi: 10.1073/pnas.1305679110

Koudelka, S., Voas, M. G., Almeida, R. G., Baraban, M., Soetaert, J., Meyer, M. P., et al. (2016). Individual neuronal subtypes exhibit diversity in CNS myelination mediated by synaptic vesicle release. *Curr. Biol.* 26, 1447–1455. doi: 10.1016/j.cub.2016.03.070

Kwon, S. E., and Chapman, E. R. (2011). Synaptophysin regulates the kinetics of synaptic vesicle endocytosis in central neurons. *Neuron* 70, 847–854. doi: 10.1016/j.neuron.2011.04.001

Lambert, T. J. (2019). FPbase: a community-editable fluorescent protein database. *Nat. Methods* 16, 277–278. doi: 10.1038/s41592-019-0352-8

Li, H., Datunashvili, M., Reyes, R. C., and Voglmaier, S. M. (2022). Inositol hexakisphosphate kinases differentially regulate trafficking of vesicular glutamate transporters 1 and 2. *Front. Cell Neurosci.* 16:926794. doi: 10.3389/fncel.2022.926794

Li, Y., and Tsien, R. W. (2012). pHTomato, a red, genetically encoded indicator that enables multiplex interrogation of synaptic activity. *Nat. Neurosci.* 15, 1047–1053. doi: 10.1038/nn.3126

Li, Z., Zhou, J., Wani, K., Yu, T., Ronan, E. A., Piggott, B. J., et al. (2020). A C. elegans neuron both promotes and suppresses motor behavior to fine tune motor output. *bioRxiv [preprint]* doi: 10.1101/2020.11.02.354472

Liewald, J. F., Brauner, M., Stephens, G. J., Bouhours, M., Schultheis, C., Zhen, M., et al. (2008). Optogenetic analysis of synaptic function. *Nat. Methods* 5, 895–902. doi: 10.1038/nmeth.1252

Liu, A., Huang, X., He, W., Xue, F., Yang, Y., Liu, J., et al. (2021). pHmScarlet is a pH-sensitive red fluorescent protein to monitor exocytosis docking and fusion steps. *Nat. Commun.* 12:1413. doi: 10.1038/s41467-021-21666-7

Liu, H., Li, L., Wang, W., Gong, J., Yang, X., and Hu, Z. (2018). Spontaneous vesicle fusion is differentially regulated at cholinergic and GABAergic synapses. *Cell Rep.* 22, 2334–2345. doi: 10.1016/j.celrep.2018.02.023

Liu, Q., Sinnen, B. L., Boxer, E. E., Schneider, M. W., Grybko, M. J., Buchta, W. C., et al. (2019). A photoactivatable botulinum neurotoxin for inducible control of neurotransmission. *Neuron* 101, 863–875.e6. doi: 10.1016/j.neuron.2019.01.002.

Luo, J. K., Melland, H., Nithianantharajah, J., and Gordon, S. L. (2021). Postsynaptic neuroligin-1 mediates presynaptic endocytosis during neuronal activity. *Front. Mol. Neurosci.* 14:744845. doi: 10.3389/fnmol.2021.744845

Miesenbock, G., De Angelis, D. A., and Rothman, J. E. (1998). Visualizing secretion and synaptic transmission with pH-sensitive green fluorescent proteins. *Nature* 394, 192–195. doi: 10.1038/28190

Miller, K. G., Alfonso, A., Nguyen, M., Crowell, J. A., Johnson, C. D., and Rand, J. B. (1996). A genetic selection for *Caenorhabditis elegans* synaptic transmission mutants. *Proc. Natl. Acad. Sci. U S A.* 93, 12593–12598. doi: 10.1073/pnas.93.22.12593

Milosevic, I., Giovedi, S., Lou, X., Raimondi, A., Collesi, C., Shen, H., et al. (2011). Recruitment of endophilin to clathrin-coated pit necks is required for efficient vesicle uncoating after fission. *Neuron* 72, 587–601. doi: 10.1016/j.neuron.2011.08.029

Mochida, S. (2022). Mechanisms of synaptic vesicle exo- and endocytosis. *Biomedicines* 10:1593. doi: 10.3390/biomedicines10071593

Morton, A., Marland, J. R., and Cousin, M. A. (2015). Synaptic vesicle exocytosis and increased cytosolic calcium are both necessary but not sufficient for activity-dependent bulk endocytosis. *J. Neurochem.* 134, 405–415. doi: 10.1111/jnc.13132

Nagel, G., Brauner, M., Liewald, J. F., Adeishvili, N., Bamberg, E., and Gottschalk, A. (2005). Light activation of channelrhodopsin-2 in excitable cells of *Caenorhabditis elegans* triggers rapid behavioral responses. *Curr. Biol.* 15, 2279–2284. doi: 10.1016/j.cub.2005.11.032

Nagel, G., Szellas, T., Huhn, W., Kateriya, S., Adeishvili, N., Berthold, P., et al. (2003). Channelrhodopsin-2, a directly light-gated cation-selective membrane channel. *Proc. Natl. Acad. Sci. U S A.* 100, 13940–13945.

Nicholson-Fish, J. C., Smillie, K. J., and Cousin, M. A. (2016). Monitoring activity-dependent bulk endocytosis with the genetically-encoded reporter VAMP4-pHluorin. *J. Neurosci. Methods* 266, 1–10. doi: 10.1016/j.jneumeth.2016.03.011

Nonet, M. L., Saifee, O., Zhao, H., Rand, J. B., and Wei, L. (1998). Synaptic transmission deficits in *Caenorhabditis elegans* synaptobrevin mutants. *J. Neurosci.* 18, 70–80. doi: 10.1523/JNEUROSCI.18-01-00070.1998

Oda, K., Vierock, J., Oishi, S., Rodriguez-Rozada, S., Taniguchi, R., Yamashita, K., et al. (2018). Crystal structure of the red light-activated channelrhodopsin Chrimson. *Nat. Commun.* 9:3949. doi: 10.1038/s41467-018-06421-9

Piggott, B. J., Liu, J., Feng, Z., Wescott, S. A., and Xu, X. Z. (2011). The neural circuits and synaptic mechanisms underlying motor initiation in *C. elegans*. *Cell* 147, 922–933. doi: 10.1016/j.cell.2011.08.053

Poskanzer, K. E., Marek, K. W., Sweeney, S. T., and Davis, G. W. (2003). Synaptotagmin I is necessary for compensatory synaptic vesicle endocytosis in vivo. *Nature* 426, 559–563. doi: 10.1038/nature02184

Preibisch, S., Saalfeld, S., and Tomancak, P. (2009). Globally optimal stitching of tiled 3D microscopic image acquisitions. *Bioinformatics* 25, 1463–1465. doi: 10.1093/bioinformatics/btp184

Rose, T., Schoenenberger, P., Jezek, K., and Oertner, T. G. (2013). Developmental refinement of vesicle cycling at Schaffer collateral synapses. *Neuron* 77, 1109–1121. doi: 10.1016/j.neuron.2013.01.021

Sankaranarayanan, S., De Angelis, D., Rothman, J. E., and Ryan, T. A. (2000). The use of pHluorins for optical measurements of presynaptic activity. *Biophys. J.* 79, 2199–2208. doi: 10.1016/S0006-3495(00)76468-X

Schild, L. C., and Glauser, D. A. (2015). Dual color neural activation and behavior control with chrimson and CoChR in *Caenorhabditis elegans*. *Genetics* 200, 1029–1034. doi: 10.1534/genetics.115.177956

Schindelin, J., Arganda-Carreras, I., Frise, E., Kaynig, V., Longair, M., Pietzsch, T., et al. (2012). Fiji: an open-source platform for biological-image analysis. *Nat. Methods* 9, 676–682. doi: 10.1038/nmeth.2019

Schuske, K. R., Richmond, J. E., Matthies, D. S., Davis, W. S., Runz, S., Rube, D. A., et al. (2003). Endophilin is required for synaptic vesicle endocytosis by localizing synaptojanin. *Neuron* 40, 749–762. doi: 10.1016/s0896-6273(03)00667-6

Seidenthal, M., Vettkötter, D., and Gottschalk, A. (2022). WormRuler: a software to track body length used to characterize a super red-shifted channelrhodopsin in *Caenorhabditis elegans*. *MicroPubl. Biol.* 2022:10.17912/micropub.biology.000607. doi: 10.17912/micropub.biology.000607

Seitz, K. J., and Rizzoli, S. O. (2019). GFP nanobodies reveal recently-exocytosed pHluorin molecules. *Sci. Rep.* 9:7773. doi: 10.1038/s41598-019-44262-8

Shen, Y., Rosendale, M., Campbell, R. E., and Perrais, D. (2014). pHuji, a pH-sensitive red fluorescent protein for imaging of exo- and endocytosis. *J. Cell Biol.* 207, 419–432. doi: 10.1083/jcb.201404107

Shin, W., Wei, L., Arpino, G., Ge, L., Guo, X., Chan, C. Y., et al. (2021). Preformed Omega-profile closure and kiss-and-run mediate endocytosis and diverse endocytic

modes in neuroendocrine chromaffin cells. *Neuron* 109, 3119–3134.e5. doi: 10.1016/j.neuron.2021.07.019

Sieburth, D., Ch'ng, Q., Dybbs, M., Tavazoie, M., Kennedy, S., Wang, D., et al. (2005). Systematic analysis of genes required for synapse structure and function. *Nature* 436, 510–517. doi: 10.1038/nature03809

Sordillo, A., and Bargmann, C. I. (2021). Behavioral control by depolarized and hyperpolarized states of an integrating neuron. *eLife* 10, e67723. doi: 10.7554/eLife.67723

Steuer Costa, W., Yu, S. C., Liewald, J. F., and Gottschalk, A. (2017). Fast cAMP modulation of neurotransmission via neuropeptide signals and vesicle loading. *Curr. Biol.* 27, 495–507. doi: 10.1016/j.cub.2016.12.055

Strange, K., Christensen, M., and Morrison, R. (2007). Primary culture of *Caenorhabditis elegans* developing embryo cells for electrophysiological, cell biological and molecular studies. *Nat. Protoc.* 2, 1003–1012. doi: 10.1038/nprot.2007.143

Subramanian, J., and Morozov, A. (2011). Erk1/2 inhibit synaptic vesicle exocytosis through L-type calcium channels. *J. Neurosci.* 31, 4755–4764. doi: 10.1523/JNEUROSCI.6594-10.2011

Sudhof, T. C. (2013). Neurotransmitter release: the last millisecond in the life of a synaptic vesicle. *Neuron* 80, 675–690. doi: 10.1016/j.neuron.2013.10.022

Swierczek, N. A., Giles, A. C., Rankin, C. H., and Kerr, R. A. (2011). High-throughput behavioral analysis in *C. elegans*. *Nat. Methods* 8, 592–598. doi: 10.1038/nmeth.1625

Ventimiglia, D., and Bargmann, C. I. (2017). Diverse modes of synaptic signaling, regulation, and plasticity distinguish two classes of *C. elegans* glutamatergic neurons. *eLife* 6:e31234. doi: 10.7554/eLife.31234

Vettkötter, D., Schneider, M., Goulden, B. D., Dill, H., Liewald, J., Zeiler, S., et al. (2022). Rapid and reversible optogenetic silencing of synaptic transmission by clustering of synaptic vesicles. *Nat. Commun.* 13:7827. doi: 10.1038/s41467-022-35324-z

Vierock, J., Rodriguez-Rozada, S., Dieter, A., Pieper, F., Sims, R., Tenedini, F., et al. (2021). BiPOLES is an optogenetic tool developed for bidirectional dual-color control of neurons. *Nat. Commun.* 12:4527. doi: 10.1038/s41467-021-24759-5

Voglmaier, S. M., Kam, K., Yang, H., Fortin, D. L., Hua, Z., Nicoll, R. A., et al. (2006). Distinct endocytic pathways control the rate and extent of synaptic vesicle protein recycling. *Neuron* 51, 71–84. doi: 10.1016/j.neuron.2006.05.027

von Gersdorff, H., and Matthews, G. (1999). Electrophysiology of synaptic vesicle cycling. *Annu. Rev. Physiol.* 61, 725–752. doi: 10.1146/annurev.physiol.61.1.725

Wabnig, S., Liewald, J. F., Yu, S. C., and Gottschalk, A. (2015). High-Throughput all-optical analysis of synaptic transmission and synaptic vesicle recycling in *Caenorhabditis elegans*. *PLoS One* 10:e0135584. doi: 10.1371/journal.pone.0135584

Watanabe, S., and Boucrot, E. (2017). Fast and ultrafast endocytosis. *Curr. Opin. Cell Biol.* 47, 64–71. doi: 10.1016/j.ceb.2017.02.013

Watanabe, S., Liu, Q., Davis, M. W., Hollopeter, G., Thomas, N., Jorgensen, N. B., et al. (2013a). Ultrafast endocytosis at *Caenorhabditis elegans* neuromuscular junctions. *eLife* 2:e00723. doi: 10.7554/eLife.00723

Watanabe, S., Rost, B. R., Camacho-Perez, M., Davis, M. W., Sohl-Kielczynski, B., Rosenmund, C., et al. (2013b). Ultrafast endocytosis at mouse hippocampal synapses. *Nature* 504, 242–247. doi: 10.1038/nature12809

Watanabe, S., Mamer, L. E., Raychaudhuri, S., Luvsanjav, D., Eisen, J., Trimbuch, T., et al. (2018). Synaptojanin and endophilin mediate neck formation during ultrafast endocytosis. *Neuron* 98, 1184–1197.e6. doi: 10.1016/j.neuron.2018.06.005.

Yu, S. C., Janosi, B., Liewald, J. F., Wabnig, S., and Gottschalk, A. (2018). Endophilin A and B join forces with clathrin to mediate synaptic vesicle recycling in *Caenorhabditis elegans*. *Front. Mol. Neurosci.* 11:196. doi: 10.3389/fnmol.2018.00196

Yu, S. C., Klosterman, S. M., Martin, A. A., Gracheva, E. O., and Richmond, J. E. (2013). Differential roles for snapin and synaptotagmin in the synaptic vesicle cycle. *PLoS One* 8:e57842. doi: 10.1371/journal.pone.0057842

Zhang, S., Banerjee, D., and Kuhn, J. R. (2011). Isolation and culture of larval cells from *C. elegans*. *PLoS One* 6:e19505. doi: 10.1371/journal.pone.0019505

Zhao, H., and Nonet, M. L. (2001). A conserved mechanism of synaptogyrin localization. *Mol. Biol. Cell* 12, 2275–2289. doi: 10.1091/mbc.12.8.2275

Zhu, Y., Xu, J., and Heinemann, S. F. (2009). Two pathways of synaptic vesicle retrieval revealed by single-vesicle imaging. *Neuron* 61, 397–411. doi: 10.1016/j.neuron.2008.12.024

frontiers | Frontiers in Cellular Neuroscience

TYPE Brief Research Report
PUBLISHED 24 May 2023
DOI 10.3389/fncel.2023.1160245

OPEN ACCESS

EDITED BY
Jacopo Lamanna,
Vita-Salute San Raffaele University, Italy

REVIEWED BY
Eric Schreiter,
Janelia Research Campus, United States
Elena G. Govorunova,
University of Texas Health Science Center at Houston, United States

*CORRESPONDENCE
Gyorgy Lur
✉ glur@uci.edu

RECEIVED 06 February 2023
ACCEPTED 05 May 2023
PUBLISHED 24 May 2023

CITATION
Rindner DJ and Lur G (2023) Practical considerations in an era of multicolor optogenetics.
Front. Cell. Neurosci. 17:1160245.
doi: 10.3389/fncel.2023.1160245

Practical considerations in an era of multicolor optogenetics

Daniel J. Rindner and Gyorgy Lur*

Department of Neurobiology and Behavior, University of California, Irvine, Irvine, CA, United States

The ability to control synaptic communication is indispensable to modern neuroscience. Until recently, only single-pathway manipulations were possible due to limited availability of opsins activated by distinct wavelengths. However, extensive protein engineering and screening efforts have drastically expanded the optogenetic toolkit, ushering in an era of multicolor approaches for studying neural circuits. Nonetheless, opsins with truly discrete spectra are scarce. Experimenters must therefore take care to avoid unintended cross-activation of optogenetic tools (crosstalk). Here, we demonstrate the multidimensional nature of crosstalk in a single model synaptic pathway, testing stimulus wavelength, irradiance, duration, and opsin choice. We then propose a "lookup table" method for maximizing the dynamic range of opsin responses on an experiment-by-experiment basis.

KEYWORDS

optogenetics, crosstalk, dual-color, red-shifted, channelrhodopsin, stimulation

Introduction

Multicolor optogenetic approaches are enormously valuable for studying the function of complex neural circuits. Optogenetic constructs with distinct wavelength sensitivity can be combined in actuator pairs, sensor pairs, or an actuator and sensor together in independent pathways, relying on spectral separation to bypass limitations imposed by spatial overlap of the tools. However, most current red-shifted optogenetic constructs exhibit sensitivity to blue light, leading to cross-activation concerns regardless of the precise tool combination used. For our exploration of crosstalk, we focus exclusively on excitatory actuators. Optogenetic actuators include light-activated ion channels, ion pumps, and G protein-coupled receptors (Rost et al., 2017; Emiliani et al., 2022), of which channelrhodopsins are perhaps the most widely used for circuit manipulation. The earliest described channelrhodopsins were channelrhodopsin-1 (ChR1) (Nagel et al., 2002) and channelrhodopsin-2 (ChR2) (Nagel et al., 2003), discovered in the algal species *C. reinhardtii* (**Figure 1A**). ChR2 quickly became the protein backbone of many engineering efforts to increase speed (Lin et al., 2009; Gunaydin et al., 2010) and photocurrent amplitude (Nagel et al., 2005; Berndt et al., 2011), leading to the optimization of the protein for mammalian expression (Boyden et al., 2005). The excitation peak of wild-type ChR2 is at 470 nm (Nagel et al., 2003). Similarly, activation spectra for many popular mutant variants–ChR2(H134R) (Nagel et al., 2005), ChEF/ChIEF (Lin et al., 2009), ChETA (Gunaydin et al., 2010), ChR2(E123T/T159C) (Berndt et al., 2011)–as well as newly identified channelrhodopsins such as sdChR (Hochbaum et al., 2014) and Chronos (Klapoetke et al., 2014), peak in the 460–500 nm range (**Figure 1A**). Notably, these blue-light-activated opsins [referred to as "blue opsin(s)" going forward] also exhibit

minimal sensitivity to wavelengths above 550 nm. Thus, an ideal red-shifted actuator for dual-color applications will be strongly activated by wavelengths longer than 550 nm, and insensitive to those under 500 nm.

VChR1, discovered in the algae *V. carteri*, was the first-reported opsin red-shifted over 50 nm from ChR2, with an excitation peak at 530 nm (Zhang et al., 2008; **Figure 1A**). However, VChR1 has considerable blue-light sensitivity, which prevented its immediate use in dual-color applications. Perhaps the first widely adopted red opsin was the fusion protein C1V1 (Yizhar et al., 2011), a portmanteau of its component opsins ChR1 and VChR1. While the C1V1 peak absorption was hardly red-shifted compared to VChR1, it had appreciably less sensitivity to wavelengths under 500 nm (Yizhar et al., 2011). Still, C1V1 retains ∼40% absorbance of 470 nm light commonly used for activating blue optogenetic tools (Yizhar et al., 2011). The search for other red-shifted channelrhodopsins has yielded many protein alternatives, including ReaChR (Lin et al., 2013), Chrimson and ChrimsonR (Klapoetke et al., 2014), ChrimsonSA (Oda et al., 2018), ChRmine (Marshel et al., 2019), and frChRmine (Kishi et al., 2022). Nonetheless, all currently known red-shifted actuators [referred to as "red opsin(s)" going forward] exhibit non-negligible blue-light sensitivity, which can lead to possible cross-activation during blue stimulation periods if not properly controlled for.

Two strategies exist to minimize crosstalk, which have been applied to opsin combinations including Chronos/ChrimsonR (Klapoetke et al., 2014; Bauer et al., 2021; Christoffel et al., 2021), CheRiff/ChrimsonR (Anisimova et al., 2023), ChR2/ReaChR (Hooks et al., 2015), and ChR2(H134R)/ChrimsonR (Chiu et al., 2018; Birdsong et al., 2019; Prasad et al., 2020; Xia et al., 2020; Joffe et al., 2022; Rindner et al., 2022). Indeed, the precise strategy used will depend on experimental context. The first, introduced by Hooks et al. (2015), is often used to test pathway convergence (Prasad et al., 2020; Bauer et al., 2021; Shelton et al., 2022). This approach involves utilizing a long, 50–250 ms, red light stimulus to forcibly inactivate the red opsin expressing neuron population before immediately stimulating the blue opsin. As the blue stimulus is applied while axons expressing the red opsin remain unresponsive, any postsynaptic response can be solely attributed to activation of blue opsin expressing cells. However, this method is not feasible in contexts where precise timing between blue and red channels is desired, for example in studies of spike-timing-dependent plasticity (Anisimova et al., 2023) or synaptic integration (Xia et al., 2020; Rindner et al., 2022). A second strategy is to limit stimulation parameters to ranges which do not cross-activate opsins (Klapoetke et al., 2014; Birdsong et al., 2019; Xia et al., 2020; Joffe et al., 2022; Rindner et al., 2022; Anisimova et al., 2023). With this approach, blue stimulus irradiance, and less commonly duration, are first titrated in a separate experimental population where only the red opsin is expressed. The upper blue light exposure limit averting red opsin cross-activation is then used across all later experiments. This approach requires thorough testing (described in detail in Section "Results"), however, it allows maximum temporal control of independent neuron populations. A caveat of this approach is that population-derived blue light exposure limits may provide inadequate excitation in instances where blue opsin expression levels are low, resulting in cases where experiments must be discarded (Xia et al., 2020). This is particularly true when near-violet stimulation wavelengths, over 50 nm blue-shifted from the excitation peak of most blue opsins, are chosen [for example, 405 nm in Anisimova et al. (2023)] in an effort to minimize cross-activation of red opsins. Thus, alternative strategies that maximize the dynamic range of crosstalk-free blue stimulus could improve the throughput of dual-color optogenetic experiments.

Here, we focus on a single synaptic pathway to test how the scope of experimental variables chosen by the investigator (**Figure 1B**) influences crosstalk risk, showcasing an example control experiment expanding on those done by others. We demonstrate an exhaustive test of crosstalk parameters, systematically varying the irradiance and duration of three different stimulus wavelengths–405, 440, and 630 nm. In consideration of the range of opsins available, we furthermore test crosstalk between three commonly used actuators–ChR2(H134R), Chronos, and ChrimsonR. We lastly propose a "lookup table" approach leveraging red opsin responses on a cell-by-cell basis to maximize crosstalk-free blue excitation in multicolor optogenetic experiments.

Results

Multidimensional considerations in crosstalk testing

To demonstrate how stimulus wavelength, irradiance, duration, and opsin choice affect crosstalk in a system, we first chose a model synaptic pathway from the auditory cortex (AUD) to the posterior parietal cortex (PPC). AUD neurons synapse on pyramidal cells in PPC layer 5 and provide strong excitation when optogenetically stimulated (Rindner et al., 2022). We expressed ChR2(H134R), Chronos, or ChrimsonR in AUD using adeno-associated viral vectors (see Section "Methods") and recorded light-evoked responses in layer 5 pyramidal cells of the PPC using whole-cell patch-clamp (**Figure 1C**). By varying stimulus irradiance or duration, we determined the dose-response relationship to excitation by 405 nm (blue/violet) (**Figures 2A, B**), 440 nm (blue) (**Figures 2C, D**), and 630 nm (red) (**Figures 2E, F**) LEDs. When expressed in AUD afferents, ChR2(H134R) and Chronos drove robust postsynaptic responses to 405 and 440 nm stimuli (**Figures 2A–D**). Stimulation of either opsin with 630 nm resulted in no detectable response (see Section "Methods") across the range of irradiances or durations tested (**Figures 2E, F**; **Table 1**). In contrast, when afferents expressed ChrimsonR, light-evoked responses could be observed to stimulation with 405 nm (**Figure 2B**), 440 nm (**Figures 2C, D**) and 630 nm (**Figures 2E, F**; **Table 1**) wavelengths, as expected given the blue shoulder of the ChrimsonR activation spectra (Klapoetke et al., 2014). Notably, brief, low-irradiance stimulation at 405 nm and 440 nm averted ChrimsonR responses while eliciting EPSPs driven by ChR2(H134R)- and Chronos-expressing afferents (**Figures 2A–D**). This parameter range represents the ideal excitation window (indicated by horizontal bars in **Figures 2A–D**) where ChrimsonR can be used in tandem with ChR2(H134R) (light blue) or Chronos (gray) without substantial risk of cross-activation on a population level. To determine the ideal blue opsin and

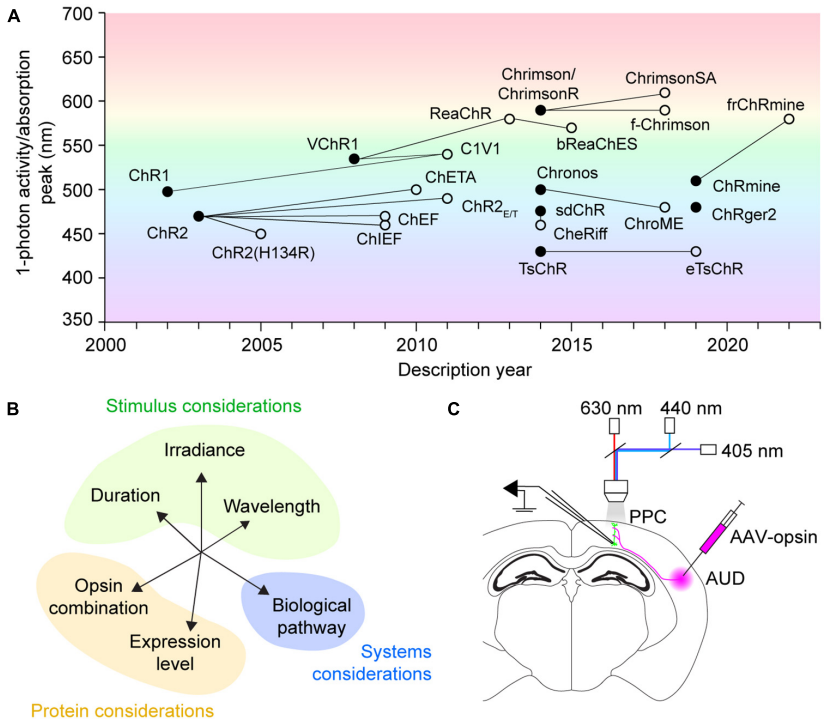

FIGURE 1
History, concerns, and testing of multicolor optogenetics. **(A)** Discovery history of commonly used channelrhodopsins for neural excitation. Filled circles designate novel opsins discovered by screening or created with rational design. Empty circles indicate mutant opsin variants, with connecting lines to their protein backbones. The mutant variant ChrimsonR overlaps with the native opsin Chrimson. Figure background color illustrates the wavelength of 1-photon activity/absorption peaks. **(B)** A representation of the multidimensional factors affecting opsin crosstalk. Each should be considered when designing any multicolor optogenetic experiment. **(C)** Schematic of experimental testing for crosstalk between excitatory optogenetic actuators for use in acute slice synapse activation applications. PPC, posterior parietal cortex; AUD, auditory cortex; AAV-opsin, adeno-associated virus carrying opsin construct, either ChR2(H134R), Chronos, or ChrimsonR.

wavelength combination for high dynamic range, crosstalk-free use with ChrimsonR, we next collapsed across irradiance and duration and compared peak ChR2(H134R) and Chronos responses at the maximum 405 and 440 nm radiant exposure level averting ChrimsonR responses (405 nm: 42.12 mJ/m^2; 440 nm: 26.17 mJ/m^2). Largest crosstalk-free blue opsin evoked EPSPs were obtained when ChR2(H134R)-expressing afferents were stimulated at 440 nm (ChR2(H134R): 11.14 mV at 405 nm, 17.31 mV at 440 nm; Chronos: 12.09 mV at 405 nm, 13.05 mV at 440 nm). These results suggest that, within the tested blue opsin and wavelength combinations, ChR2(H134R) excited at 440 nm allowed for the highest dynamic range activation of the AUD to PPC synaptic pathway.

Experiment-to-experiment maximization of crosstalk-free blue excitation

By definition, a population-derived maximum usable blue light exposure underestimates the true crosstalk-free exposure limit in a majority of experiments. To maximize crosstalk-free blue light stimulus, we next asked whether the upper limit of blue radiant exposure could be determined on an experiment-to-experiment basis, accounting for variable red opsin expression levels. We hypothesized that in dual-color experiments, red light responses could be used to estimate red opsin expression levels and predict sensitivity to blue light induced cross-activation. Indeed, within-cell comparison of EPSPs evoked by ChrimsonR-expressing afferents suggested that the maximum usable 440 nm radiant exposure level that averts cross-activation, increases linearly with the minimum 630 nm exposure necessary to evoke a response (Pearson r = 0.715, p = 0.046, n = 8; Figure 3A). We therefore propose that this red opsin "lookup table" (Figure 3A) can be pre-established in red opsin-only expressing preparations and later referenced in dual-color experiments to determine an experiment-specific maximum blue radiant exposure for crosstalk-free excitation. To quantify the improvement in blue opsin dynamic range using the lookup table approach, we compared ChR2(H134R)-evoked responses at the population-derived maximum usable 440 nm radiant exposure level (4.40 ± 1.07 mV, mean ± SEM) to peak responses with blue light exposure calibrated for individual experiments (8.88 ± 1.97 mV) (Figure 3B). We found that use of this lookup table allows an up to two-fold increase in the blue opsin response dynamic range (p = 0.001, n = 12, paired t-test).

Discussion

The expansion of the optogenetic toolkit brings exciting new opportunities in neuroscience. With high-performance, spectrally shifted actuators becoming widely available, many groups have

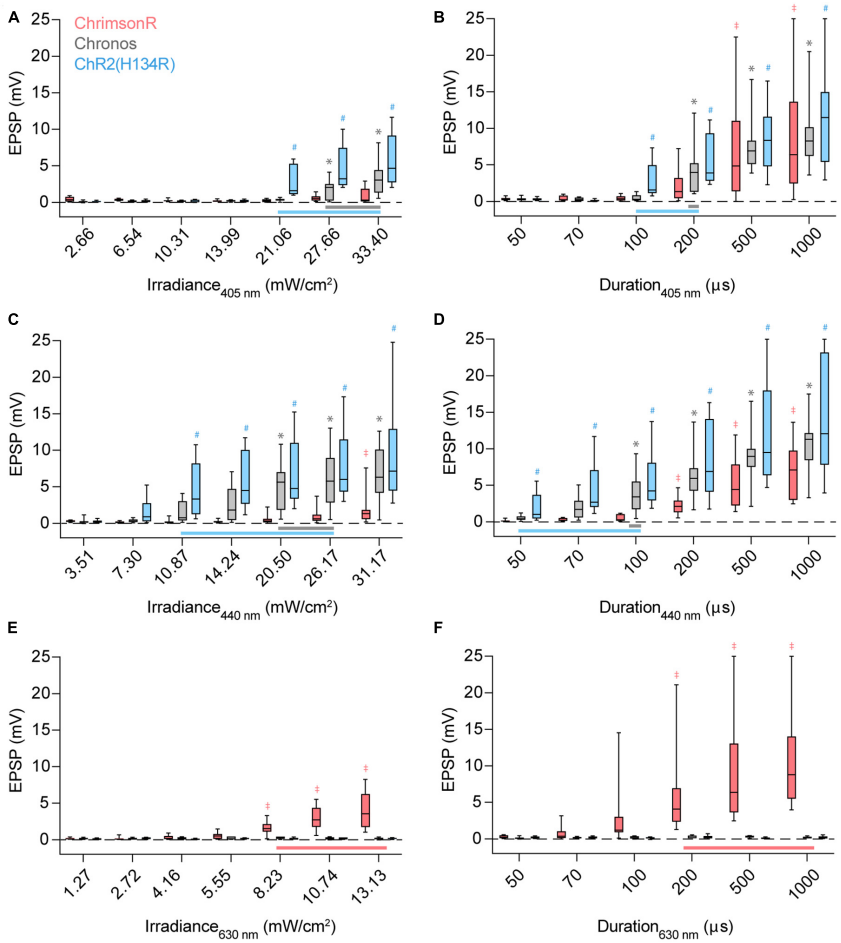

FIGURE 2
Stimulus irradiance, duration, wavelength, and opsin choice contribute to crosstalk risk. **(A)** Excitatory postsynaptic potential (EPSP) amplitudes when ChrimsonR (red), Chronos (gray), or ChR2(H134R) (blue)-expressing afferents are stimulated by a 100 µs pulse of 405 nm light with increasing irradiance. Vertical bars extend from the 25th to 75th percentiles, with the median represented by a horizontal line. Whiskers indicate minimum and maximum recorded values. Horizontal bars at bottom **(A–D)** represent the stimulus parameter range which can be used to activate Chronos (gray) or ChR2(H134R) (blue) without cross-activating ChrimsonR. Symbols above the boxes indicate opsin [*: Chronos, #: ChR2(H134R), ‡: ChrimsonR] and stimulus parameter combinations resulting in population-level non-zero responses [$p < 0.05$, *t*-test, experimental replicates (*n*) listed in **Table 1**]. **(B)** Response amplitudes when afferents are stimulated with a 21.06 mW/cm^2 pulse of 405 nm light with increasing pulse durations. **(C)** Response amplitudes when afferents are stimulated with a 100 µs pulse of 440 nm light with increasing irradiance. **(D)** Response amplitudes when afferents are stimulated with a 20.50 mW/cm^2 pulse of 440 nm light with increasing pulse durations. **(E)** Response amplitudes when afferents are stimulated with a 100 µs pulse of 630 nm light with increasing irradiance. **(F)** Response amplitudes when afferents are stimulated with a 8.23 mW/cm^2 pulse of 630 nm light with increasing pulse durations. Red horizontal bar at bottom **(E,F)** represents the stimulus parameter range which can be used to activate ChrimsonR without cross-activating Chronos and ChR2(H134R). $^{‡,*,\#}p < 0.05$, *t*-test.

begun to newly implement multicolor optogenetic strategies, for example to stimulate converging synaptic pathways (Hooks et al., 2015; Birdsong et al., 2019; Bauer et al., 2021; Joffe et al., 2022; Rindner et al., 2022; Anisimova et al., 2023), activate intermingled cell types (Yizhar et al., 2011), or bidirectionally control neuronal populations (Han and Boyden, 2007; Zhang et al., 2007; Atallah et al., 2012; Kampasi et al., 2016; Christoffel et al., 2021; Vierock et al., 2021; Li et al., 2022). Here, we focus on synapse activation to consider how multiple experimenter-controlled variables (**Figure 1B**) combine to affect crosstalk. We furthermore introduce a red opsin "lookup table" approach for calibrating maximum blue light exposures on an experiment-to-experiment basis.

Indeed, stimulus irradiance and duration are often considered for their impact on crosstalk. However, our data indicates that cross-activation is a highly multidimensional issue, determined by interactions between stimulus irradiance, duration, wavelength, and additionally opsin choice. Ideally, each dimension should be properly tested when designing a dual-color optogenetic experiment. This is important as theoretical advantages for dual-color optogenetics, particularly those measured directly in opsin-expressing cells, may not translate to similar advantages in a given biological system. For example, Chronos has large photocurrents and faster kinetics than ChR2(H134R) (Klapoetke et al., 2014). However, postsynaptic responses to ChR2(H134R) activation were detected at lower irradiances (**Figures 2A, C**; **Table 1**) and durations (**Figures 2B, D**; **Table 1**) than Chronos in the AUD to PPC synaptic pathway (although, note the 440 nm stimulus used here is ~50 nm blue-shifted from the excitation peak of Chronos). Furthermore, 440 nm stimulation consistently required lower

TABLE 1 Experimental replicates and statistical test results.

	405 nm irradiance (mW/cm^2)							405 nm duration (μs)					
	2.66	6.54	10.31	13.99	21.06	27.66	30.4	50	70	100	200	500	1,000
ChrimsonR	(7)	(7)	(8)	(8)	(8)	(8)	(8)	(8)	(8)	(8)	(8)	(8)	(8)
	0.996	0.999	>0.999	>0.999	0.999	0.997	0.747	>0.999	>0.999	0.999	0.158	**0.03**	**0.023**
Chronos	(9)	(9)	(9)	(9)	(11)	(11)	(11)	(10)	(10)	(10)	(11)	(11)	(11)
	>0.999	>0.999	>0.999	>0.999	>0.999	**0.031**	**0.002**	>0.999	>0.999	0.976	**0.003**	**<0.001**	**<0.001**
ChR2(H134R)	(8)	(8)	(8)	(8)	(8)	(8)	(8)	(10)	(10)	(10)	(10)	(10)	(10)
	>0.999	>0.999	>0.999	0.999	**0.018**	**0.005**	**0.003**	>0.999	>0.999	**0.022**	**0.001**	**<0.001**	**<0.001**
	440 nm irradiance (mW/cm^2)							440 nm duration (μs)					
	3.51	7.3	10.87	14.24	20.5	26.17	31.17	50	70	100	200	500	1,000
ChrimsonR	(11)	(11)	(11)	(11)	(11)	(11)	(11)	(11)	(11)	(11)	(11)	(11)	(11)
	>0.999	>0.999	>0.999	>0.999	0.887	0.209	**0.043**	>0.999	0.997	0.762	**<0.001**	**<0.001**	**<0.001**
Chronos	(10)	(10)	(10)	(10)	(11)	(11)	(11)	(12)	(12)	(12)	(12)	(12)	(12)
	>0.999	>0.999	0.058	0.054	**<0.001**	**<0.001**	**<0.001**	0.994	0.059	**0.002**	**<0.001**	**<0.001**	**<0.001**
ChR2(H134R)	(13)	(14)	(14)	(14)	(14)	(14)	(14)	(14)	(14)	(14)	(14)	(14)	(14)
	>0.999	0.361	**<0.001**	**<0.001**	**<0.001**	**<0.001**	**<0.001**	**0.017**	**<0.001**	**<0.001**	**<0.001**	**<0.001**	**<0.001**
	630 nm irradiance (mW/cm^2)							630 nm duration (μs)					
	1.27	2.72	4.16	5.55	8.23	10.74	13.13	50	70	100	200	500	1,000
ChrimsonR	(11)	(11)	(11)	(11)	(12)	(12)	(12)	(11)	(11)	(11)	(11)	(11)	(11)
	>0.999	>0.999	>0.999	0.98	**0.001**	**<0.001**	**<0.001**	>0.999	0.62	0.069	**0.005**	**<0.001**	**<0.001**
Chronos	(7)	(7)	(7)	(7)	(7)	(7)	(7)	(7)	(7)	(7)	(7)	(8)	(8)
	>0.999	>0.999	>0.999	>0.999	0.996	0.998	>0.999	0.999	>0.999	>0.999	0.999	>0.999	>0.999
ChR2(H134R)	(8)	(8)	(8)	(8)	(8)	(8)	(8)	(9)	(9)	(9)	(9)	(9)	(9)
	>0.999	>0.999	>0.999	>0.999	0.992	>0.999	>0.999	>0.999	>0.999	0.991	0.998	>0.999	>0.999

Experimental replicates (n) (top) and paired *t*-test *p*-values (bottom) of the recorded postsynaptic response to opsin excitation by indicated stimulus parameters. Bolded *p*-values indicate $p < 0.05$.

irradiances and durations (at comparable irradiances: 405 nm, 21.06 mJ/m^2; 440 nm, 20.50 mJ/m^2) than 405 nm to elicit detectable responses, from both ChR2(H134R)- and Chronos-expressing fibers (**Figures 2A–D**; **Table 1**). This resulted in a narrowing of the 405 nm ideal excitation window. Thus, using near-violet stimulation to avoid red opsin activation may paradoxically promote crosstalk, as the lower sensitivity of currently available blue opsins to these wavelengths necessitates use of higher radiant exposure level stimuli. These data suggest that while favorable opsin or stimulus properties may offer theoretical advantages in dual-color applications, in-house testing is necessary to select the ideal opsin combination for any particular use case.

The ability to elicit large, crosstalk-free opsin responses is critical for experimenters. Predictably, raising stimulus irradiance or duration will increase photon exposure and thus also response magnitude (given that certain biological factors, like number of synapses, do not saturate). One limiting factor can therefore be the experimental hardware, as irradiance will be limited by the power output of the stimulus light source. In our setup, this was most noticeable in our exploration of 630 nm responses, where a comparatively weak LED was used. In contrast, stimulus duration can be increased without constraint, its impact on membrane responses limited only by the charge integration kinetics of the cell and the relatively slow process of opsin desensitization. In practice, stimulus duration may therefore offer the greatest opportunity to increase response amplitudes, given that cross-activation radiant exposure thresholds are not exceeded. Blue opsins are largely insensitive to red light (**Figures 2E, F**). Thus, red opsin responses can be enhanced by simply increasing stimulus radiant exposure levels, with upper light limits capped by hardware rather than crosstalk risks (however, note that cross-activation by blue stimuli may be possible by radiant exposure levels higher than tested here). In contrast, red opsins are sensitive to blue wavelengths (**Figures 2A–C**; Yizhar et al., 2011; Lin et al., 2013; Klapoetke et al., 2014; Oda et al., 2018; Marshel et al., 2019; Kishi et al., 2022). The need to restrict blue radiant exposure levels below the red opsin's activation threshold can therefore limit an experimenter's potential to elicit large blue opsin responses. Here, we propose a lookup table approach for determining the maximum crosstalk-free blue radiant exposure using a functional assessment of red opsin expression levels, thereby maximizing the dynamic range available in each individual experiment (**Figure 3A**). In our hands, this approach increased blue light responses up to two-fold (**Figure 3B**). To ensure applicability to future experiments, the lookup table should encompass a large range of expression levels in each pathway or cell population. While light-evoked responses often scale with the observed brightness of the fluorescent tag carried by the opsin, this relationship can be construct specific and, in some cases,

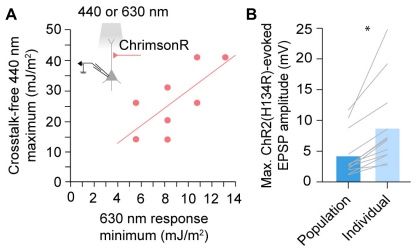

FIGURE 3
A red opsin "lookup table" for maximizing blue stimulus dynamic range. **(A)** Comparison of the minimum 630 nm radiant exposure necessary to elicit a detectable ChrimsonR postsynaptic response and maximum 440 nm radiant exposure averting a cross-activated excitatory postsynaptic potential (EPSP). Dots represent individual cells. Solid line represents the linear regression. Pearson $r = 0.715$, $n = 8$, $p = 0.046$. **(B)** Maximum evoked EPSP amplitudes when afferents expressing ChR2(H134R) are stimulated at population-derived or individually-derived blue radiant exposure limits. Gray lines represent individual cells. *$p < 0.05$, $n = 12$, paired t-test.

fluorescence signal from the tag may not ensure the presence of an evoked response (Klapoetke et al., 2014). We therefore propose that directly measured opsin responses are a more reliable predictors of crosstalk thresholds when constructing this lookup table.

In synapse activation experiments, crosstalk can be measured in opsin-expressing cells or downstream in postsynaptic neurons. We agree with previous studies (Birdsong et al., 2019; Xia et al., 2020; Joffe et al., 2022) that downstream measurements better capture the functional implication of cross-activation. Nonetheless, it is likely that ChrimsonR photocurrents were activated at lower blue light intensities and durations than discernible from postsynaptic responses alone. However, this stimulus may either not activate enough ChrimsonR to trigger action potential firing in the afferents or engage enough synapses to produce a detectable response in the recorded postsynaptic neuron. Additionally, while the lookup table approach can improve blue opsin response ranges, it may overestimate crosstalk-free light levels for adjacent cells more strongly innervated by opsin expressing afferents. It is important to remember that crosstalk is subject to filtering by the biological system studied. In extreme cases, indirect measures including behavioral (Schild and Glauser, 2015) or paired-pulse response characteristics (Christoffel et al., 2021) can also been used as evidence against appreciable crosstalk, although opsin cross-activation almost certainly occurred. It is the experimenter's responsibility to consider subthreshold effects of such cross-activation and determine their potentially confounding influence on the process studied. As in any experiment, there is no substitute for high-quality controls for ensuring the validity of results. Whenever possible, swapping opsins between cell populations is one such necessary control.

Cross-activation concerns are not specific to excitatory actuator pairs. Other optogenetic tool combinations are equally subject to crosstalk, including excitatory with inhibitory actuators (Han and Boyden, 2007; Zhang et al., 2007; Atallah et al., 2012; Kampasi et al., 2016; Christoffel et al., 2021; Vierock et al., 2021; Li et al., 2022), actuators with sensors (Lim et al., 2012; Rickgauer et al., 2014; Packer et al., 2015; Carrillo-Reid et al., 2016; Yang et al., 2018; Seidenthal et al., 2023), and sensors with sensors (Zhao et al., 2011; Akerboom et al., 2013; Li et al., 2013; Han et al., 2019). Multicolor sensitivity is also a core feature of bistable step-function opsins (Berndt et al., 2009; Yizhar et al., 2011; Wietek et al., 2017; Gong et al., 2020), where an additional wavelength-to-response relationship must be carefully considered. Efforts to produce optogenetic tools with decreased blue light sensitivity and further red-shifted peak activation are ongoing (Mermet-Joret et al., 2021; Kishi et al., 2022). Parallel modifications to blue-activated tools may also decrease crosstalk risk. High-photocurrent, high-sensitivity blue opsins, such as ChRger2, could further reduce the necessary blue radiant exposure to stimulate neurons (Bedbrook et al., 2019), thus reducing crosstalk risk. Opsins with fast activation kinetics, such as Chronos and ChroME (Mardinly et al., 2018), have also been successfully applied in multicolor experiments. A third avenue that saw limited success was to further blue-shift action spectra. TsChR, a channelrhodopsin discovered in *T. striata*, has an excitation peak at 430 nm and is the most blue-shifted channelrhodopsin known to date (Klapoetke et al., 2014). Membrane trafficking of TsChR was further optimized to generate eTsChR (Farhi et al., 2019). While promising, the efficacy of eTsChR in multicolor applications has yet to be verified. The continued spectral and kinetic expansion of the optogenetic toolkit, combined with experimental strategies for minimizing crosstalk, will ultimately broaden the adoption of dual-color approaches for studying brain function.

Methods

Animals

Wild-type C57BL/6 mice of both sexes were used for all experiments. Mice were bred and maintained with *ad libitum* access to food and water on 12-h light/dark cycles in University of California, Irvine vivarium facilities. All mice were housed and used in accordance with the NIH guidelines on the care and use of laboratory animals.

Optogenetic construct expression

To express various optogenetic constructs, we transcranially injected either AAV2.9-hSyn-hChR2(H134R)-EYFP (titer: 3.6×10^{12}, Addgene: 26973-AAV9) (Zhang et al., 2010), AAV2.9-hSyn-ChrimsonR-tdTomato (titer: 2.9×10^{12}, Addgene: 59171-AAV9) (Klapoetke et al., 2014), or AAV2.9-Syn-Chronos-GFP.WPRE.bGH (titer: 1.6×10^{12}, originally obtained from the Penn Vector Core, now available from Addgene: 59170) (Klapoetke et al., 2014). Injections were targeted to auditory cortex (AUD, coordinates from bregma: anterior-posterior −2.8 mm, medial-lateral 4.1 mm, dorsal-ventral 0.8 mm) under isoflurane anesthesia between postnatal day (p) 28–40. Opsin constructs (150 nL) were injected at a rate of 25 nl/minute and allowed to express for (in days): ChR2(H134R), 32.2 ± 5; ChrimsonR, 29.9 ± 2.4; Chronos, 28.0 ± 7.2; mean ± standard deviation. Opsin expression was visually inspected at the beginning of all physiology experiments via band-pass illumination with a X-Cite mercury lamp (Excelitas

Technologies, Waltham, MA, United States). Slices were discarded if opsin-expressing fibers were not visually apparent.

Electrophysiology

Electrophysiology recordings were performed in 400 μm thick coronal brain slices prepared on a vibrating microtome (smz7000-2, Campden Instruments, Lafayette, IN, United States) cut to contain the PPC (approximate coordinates from bregma: anterior-posterior: 2.0 mm, medial-lateral: 1.3–1.8 mm). After cutting, slices were maintained at 32°C for 15 min in solution comprised of (in mM): 110 choline, 25 $NaHCO_3$, 1.25 NaH_2PO_4, 3 KCl, 7 $MgCl_2$, 0.5 $CaCl_2$, 10 glucose, 11.6 sodium ascorbate, and 3.1 sodium pyruvate, bubbled with carbogen gas (95% O_2, 5% CO_2). Slices were then transferred to room-temperature ACSF comprised of (in mM): 126 NaCl, 25 $NaHCO_3$, 1.25 NaH_2PO_4, 3 KCl, 1 $MgCl_2$, 2 $CaCl_2$, and 10 glucose, and allowed to recover for a minimum of 20 min before recording.

Whole-cell recordings were performed in a submersion-type recording chamber mounted on an Olympus, Tokyo, Japan BX61-WI microscope. The extracellular bath solution consisted of oxygenated ACSF maintained at close to physiological temperature (32–34°C). Recording glass micropipettes were pulled on a P-1000 puller (Sutter Instrument, Novato, CA, United States) to have pipette resistances of 2–4 MΩ. Intracellular solution contained (in mM): 135 $KMeSO_3$, 10 HEPES, 4 $MgCl_2$, Na_2ATP, 0.4 NaGTP, and 10 sodium creatine phosphate, adjusted to pH 7.3 with KOH. Signals were amplified on a MultiClamp 700B amplifier (Molecular Devices, San Jose, CA, United States) and digitized on National Instruments DAQ boards. Data were sampled at 10 kHz, filtered at 4 kHz, and acquired using WaveSurfer (HHMI Janelia Research Campus). Recordings were targeted to pyramidal cells in layer 5 (depth from pia: 0.5–0.65 mm), identified by their characteristic wide somatic morphology and non-fast-spiking firing patterns. Cells were held at ∼−75 mV, and series resistance constantly monitored for changes greater than 20% at which point cells were discarded. All analysis routines were custom written in Python 3.7.

Multi-color optogenetic stimulation

Multi-color excitation light was delivered through a 40x water immersion objective lens (Olympus, Tokyo, Japan). 405 nm, 440 nm, and 630 nm high speed LEDs (Sutter Instrument, Novato, CA, United States) were integrated into the light path using an optical beam combiner (Lambda OBC, Sutter Instrument, Novato, CA, United States) mounted directly to the microscope. We used a reverse mounting order such that higher power LEDs were mounted further from the OBC output. Stimulus properties (irradiance, duration) were controlled using WaveSurfer with a sampling rate of 100 kHz. All LED irradiances were tested using a stimulus duration of 100 μs and measured at the microscope objective with a PM100D power meter and S121C sensor (Thorlabs, Newton, NJ, United States). All durations were tested with a stimulus irradiance of (in mW/cm^2): 21.06 (405 nm), 20.50 (440 nm), or 8.23 (630 nm).

Experimental design and statistical analysis

On occasion, stimulus parameters were sufficient to evoke action potentials in recorded neurons. In these instances, EPSP amplitudes were fixed at 25 mV. The PPC and AUD are reciprocally connected (Zingg et al., 2014), raising the risk of retrograde opsin expression in PPC contributing to evoked responses. However, opsin-expressing PPC cells were never observed, excluding this possibility. Non-zero postsynaptic responses were determined by comparing the maximum post-stimulus membrane potential to the peak-to-peak noise estimate taken pre-stimulus using paired *t*-tests performed in Python 3.7. Stimulus parameters were tested through 10 repeated measurements in each cell. Each repeat was considered a single experimental replicate (n) when determining single cell response minimums. Responses from a given neuron were averaged to form a single experimental replicate when determining population response minimums. No more than two cells were recorded from the same animal for a given condition.

Data availability statement

The raw data supporting the conclusions of this article will be made available by the authors, without undue reservation.

Ethics statement

This animal study was reviewed and approved by University of California, Irvine IACUC, AUP-20-076.

Author contributions

DR performed all recordings, analyzed the data, and wrote the manuscript. GL provided experimental resources and editorial comments. Both authors contributed to the experimental design and approved the submitted version.

Funding

This study was supported by the NIMH: R01MH123686 (GL), the NINDS: R01NS127785 (GL), and the NIDCD: T32DC010775 (DR).

Conflict of interest

The authors declare that the research was conducted in the absence of any commercial or financial relationships that could be construed as a potential conflict of interest.

Publisher's note

References

Akerboom, J., Carreras Calderón, N., Tian, L., Wabnig, S., Prigge, M., Tolö, J., et al. (2013). Genetically encoded calcium indicators for multi-color neural activity imaging and combination with optogenetics. *Front. Mol. Neurosci.* 6:2. doi: 10.3389/fnmol.2013.00002

Anisimova, M., van Bommel, B., Wang, R., Mikhaylova, M., Wiegert, J. S., Oertner, T. G., et al. (2023). Spike-timing-dependent plasticity rewards synchrony rather than causality. *Cereb. Cortex* 33, 23–34. doi: 10.1093/cercor/bhac050

Atallah, B. V., Bruns, W., Carandini, M., and Scanziani, M. (2012). Parvalbumin-expressing interneurons linearly transform cortical responses to visual stimuli. *Neuron* 73, 159–170. doi: 10.1016/j.neuron.2011.12.013

Bauer, J., Weiler, S., Fernholz, M. H. P., Laubender, D., Scheuss, V., Hübener, M., et al. (2021). Limited functional convergence of eye-specific inputs in the retinogeniculate pathway of the mouse. *Neuron* 109, 2457–2468.e12. doi: 10.1016/j.neuron.2021.05.036

Bedbrook, C. N., Yang, K. K., Robinson, J. E., Mackey, E. D., Gradinaru, V., and Arnold, F. H. (2019). Machine learning-guided channelrhodopsin engineering enables minimally invasive optogenetics. *Nat. Methods* 16, 1176–1184. doi: 10.1038/s41592-019-0583-8

Berndt, A., Schoenenberger, P., Mattis, J., Tye, K. M., Deisseroth, K., Hegemann, P., et al. (2011). High-efficiency channelrhodopsins for fast neuronal stimulation at low light levels. *Proc. Natl. Acad. Sci. U.S.A.* 108, 7595–7600. doi: 10.1073/pnas.1017210108

Berndt, A., Yizhar, O., Gunaydin, L. A., Hegemann, P., and Deisseroth, K. (2009). Bi-stable neural state switches. *Nat. Neurosci.* 12, 229–234. doi: 10.1038/nn.2247

Birdsong, W. T., Jongbloets, B. C., Engeln, K. A., Wang, D., Scherrer, G., and Mao, T. (2019). Synapse-specific opioid modulation of thalamo-cortico-striatal circuits. *eLife* 8:e45146. doi: 10.7554/eLife.45146

Boyden, E. S., Zhang, F., Bamberg, E., Nagel, G., and Deisseroth, K. (2005). Millisecond-timescale, genetically targeted optical control of neural activity. *Nat. Neurosci.* 8, 1263–1268. doi: 10.1038/nn1525

Carrillo-Reid, L., Yang, W., Bando, Y., Peterka, D. S., and Yuste, R. (2016). Imprinting and recalling cortical ensembles. *Science* 353, 691–694. doi: 10.1126/science.aaf7560

Chiu, C. Q., Martenson, J. S., Yamazaki, M., Natsume, R., Sakimura, K., Tomita, S., et al. (2018). Input-specific NMDAR-dependent potentiation of dendritic GABAergic inhibition. *Neuron* 97, 368–377.e3. doi: 10.1016/j.neuron.2017.12.032

Christoffel, D. J., Walsh, J. J., Heifets, B. D., Hoerbelt, P., Neuner, S., Sun, G., et al. (2021). Input-specific modulation of murine nucleus accumbens differentially regulates hedonic feeding. *Nat. Commun.* 12:2135. doi: 10.1038/s41467-021-22430-7

Emiliani, V., Entcheva, E., Hedrich, R., Hegemann, P., Konrad, K. R., Lüscher, C., et al. (2022). Optogenetics for light control of biological systems. *Nat. Rev. Methods Primer* 2, 1–25. doi: 10.1038/s43586-022-00136-4

Farhi, S. L., Parot, V. J., Grama, A., Yamagata, M., Abdelfattah, A. S., Adam, Y., et al. (2019). Wide-area all-optical neurophysiology in acute brain slices. *J. Neurosci.* 39, 4889–4908. doi: 10.1523/JNEUROSCI.0168-19.2019

Gong, X., Mendoza-Halliday, D., Ting, J. T., Kaiser, T., Sun, X., Bastos, A. M., et al. (2020). An ultra-sensitive step-function opsin for minimally invasive optogenetic stimulation in mice and macaques. *Neuron* 107, 38–51.e8. doi: 10.1016/j.neuron.2020.03.032

Gunaydin, L. A., Yizhar, O., Berndt, A., Sohal, V. S., Deisseroth, K., and Hegemann, P. (2010). Ultrafast optogenetic control. *Nat. Neurosci.* 13, 387–392. doi: 10.1038/nn.2495

Han, S., Yang, W., and Yuste, R. (2019). Two-color volumetric imaging of neuronal activity of cortical columns. *Cell Rep.* 27, 2229–2240.e4. doi: 10.1016/j.celrep.2019.04.075

Han, X., and Boyden, E. S. (2007). Multiple-color optical activation, silencing, and desynchronization of neural activity, with single-spike temporal resolution. *PLoS One* 2:e299. doi: 10.1371/journal.pone.0000299

Hochbaum, D. R., Zhao, Y., Farhi, S. L., Klapoetke, N., Werley, C. A., Kapoor, V., et al. (2014). All-optical electrophysiology in mammalian neurons using engineered microbial rhodopsins. *Nat. Methods* 11, 825–833. doi: 10.1038/nmeth.3000

Hooks, B. M., Lin, J. Y., Guo, C., and Svoboda, K. (2015). Dual-channel circuit mapping reveals sensorimotor convergence in the primary motor cortex. *J. Neurosci.* 35, 4418–4426. doi: 10.1523/JNEUROSCI.3741-14.2015

Joffe, M. E., Maksymetz, J., Luschinger, J. R., Dogra, S., Ferranti, A. S., Luessen, D. J., et al. (2022). Acute restraint stress redirects prefrontal cortex circuit function through mGlu5 receptor plasticity on somatostatin-expressing interneurons. *Neuron* 110, 1068–1083.e5. doi: 10.1016/j.neuron.2021.12.027

Kampasi, K., Stark, E., Seymour, J., Na, K., Winful, H. G., Buzsáki, G., et al. (2016). Fiberless multicolor neural optoelectrode for *in vivo* circuit analysis. *Sci. Rep.* 6:30961. doi: 10.1038/srep30961

Kishi, K. E., Kim, Y. S., Fukuda, M., Inoue, M., Kusakizako, T., Wang, P. Y., et al. (2022). Structural basis for channel conduction in the pump-like channelrhodopsin ChRmine. *Cell* 185, 672–689.e23. doi: 10.1016/j.cell.2022.01.007

Klapoetke, N. C., Murata, Y., Kim, S. S., Pulver, S. R., Birdsey-Benson, A., Cho, Y. K., et al. (2014). Independent optical excitation of distinct neural populations. *Nat. Methods* 11, 338–346. doi: 10.1038/nmeth.2836

Li, H., Li, Y., Lei, Z., Wang, K., and Guo, A. (2013). Transformation of odor selectivity from projection neurons to single mushroom body neurons mapped with dual-color calcium imaging. *Proc. Natl. Acad. Sci. U.S.A.* 110, 12084–12089. doi: 10.1073/pnas.1305857110

Li, L., Lu, L., Ren, Y., Tang, G., Zhao, Y., Cai, X., et al. (2022). Colocalized, bidirectional optogenetic modulations in freely behaving mice with a wireless dual-color optoelectronic probe. *Nat. Commun.* 13:839. doi: 10.1038/s41467-022-28539-7

Lim, D., Mohajerani, M., LeDue, J., Boyd, J., Chen, S., and Murphy, T. (2012). *In vivo* large-scale cortical mapping using channelrhodopsin-2 stimulation in transgenic mice reveals asymmetric and reciprocal relationships between cortical areas. *Front. Neural Circuits* 6:11. doi: 10.3389/fncir.2012.00011

Lin, J. Y., Knutsen, P. M., Muller, A., Kleinfeld, D., and Tsien, R. Y. (2013). ReaChR: a red-shifted variant of channelrhodopsin enables deep transcranial optogenetic excitation. *Nat. Neurosci.* 16, 1499–1508. doi: 10.1038/nn.3502

Lin, J. Y., Lin, M. Z., Steinbach, P., and Tsien, R. Y. (2009). Characterization of engineered channelrhodopsin variants with improved properties and kinetics. *Biophys. J.* 96, 1803–1814. doi: 10.1016/j.bpj.2008.11.034

Mardinly, A. R., Oldenburg, I. A., Pégard, N. C., Sridharan, S., Lyall, E. H., Chesnov, K., et al. (2018). Precise multimodal optical control of neural ensemble activity. *Nat. Neurosci.* 21, 881–893. doi: 10.1038/s41593-018-0139-8

Marshel, J. H., Kim, Y. S., Machado, T. A., Quirin, S., Benson, B., Kadmon, J., et al. (2019). Cortical layer–specific critical dynamics triggering perception. *Science* 365:eaaw5202. doi: 10.1126/science.aaw5202

Mermet-Joret, N., Moreno, A., Zbela, A., Ellendersen, B. E., Krauth, N., von Philipsborn, A., et al. (2021). Dual-color optical activation and suppression of neurons with high temporal precision. *bioRxiv* [preprint] doi: 10.1101/2021.05.05.442824

Nagel, G., Brauner, M., Liewald, J. F., Adeishvili, N., Bamberg, E., and Gottschalk, A. (2005). Light activation of channelrhodopsin-2 in excitable cells of *Caenorhabditis elegans* triggers rapid behavioral responses. *Curr. Biol. CB* 15, 2279–2284. doi: 10.1016/j.cub.2005.11.032

Nagel, G., Ollig, D., Fuhrmann, M., Kateriya, S., Musti, A. M., Bamberg, E., et al. (2002). Channelrhodopsin-1: a light-gated proton channel in green algae. *Science* 296, 2395–2398. doi: 10.1126/science.1072068

Nagel, G., Szellas, T., Huhn, W., Kateriya, S., Adeishvili, N., Berthold, P., et al. (2003). Channelrhodopsin-2, a directly light-gated cation-selective membrane channel. *Proc. Natl. Acad. Sci. U.S.A.* 100, 13940–13945. doi: 10.1073/pnas.1936192100

Oda, K., Vierock, J., Oishi, S., Rodriguez-Rozada, S., Taniguchi, R., Yamashita, K., et al. (2018). Crystal structure of the red light-activated channelrhodopsin Chrimson. *Nat. Commun.* 9:3949. doi: 10.1038/s41467-018-06421-9

Packer, A. M., Russell, L. E., Dalgleish, H. W. P., and Häusser, M. (2015). Simultaneous all-optical manipulation and recording of neural circuit activity with cellular resolution *in vivo*. *Nat. Methods* 12, 140–146. doi: 10.1038/nmeth.3217

Prasad, A. A., Xie, C., Chaichim, C., Nguyen, J. H., McClusky, H. E., Killcross, S., et al. (2020). Complementary roles for ventral pallidum cell types and their projections in relapse. *J. Neurosci.* 40, 880–893. doi: 10.1523/JNEUROSCI.0262-19.2019

Rickgauer, J. P., Deisseroth, K., and Tank, D. W. (2014). Simultaneous cellular-resolution optical perturbation and imaging of place cell firing fields. *Nat. Neurosci.* 17, 1816–1824. doi: 10.1038/nn.3866

Rindner, D. J., Proddutur, A., and Lur, G. (2022). Cell-type-specific integration of feedforward and feedback synaptic inputs in the posterior parietal cortex. *Neuron* 110, 3760–3773.e5. doi: 10.1016/j.neuron.2022.08.019

Rost, B. R., Schneider-Warme, F., Schmitz, D., and Hegemann, P. (2017). Optogenetic tools for subcellular applications in neuroscience. *Neuron* 96, 572–603. doi: 10.1016/j.neuron.2017.09.047

Schild, L. C., and Glauser, D. A. (2015). Dual color neural activation and behavior control with Chrimson and CoChR in *Caenorhabditis elegans*. *Genetics* 200, 1029–1034. doi: 10.1534/genetics.115.177956

Seidenthal, M., Jánosi, B., Rosenkranz, N., Schuh, N., Elvers, N., Willoughby, M., et al. (2023). pOpsicle: an all-optical reporter system for synaptic vesicle recycling combining pH-sensitive fluorescent proteins with optogenetic manipulation of neuronal activity. *Front. Cell. Neurosci* 17:1120651. doi: 10.3389/fncel.2023.1120651

Shelton, A. M., Oliver, D. K., Grimstvedt, J. S., Lazarte, I. P., Kapoor, I., Swann, J. A., et al. (2022). Single neurons and networks in the claustrum integrate input from widespread cortical sources. *bioRxiv* [preprint] doi: 10.1101/2022.05.06.490864

Vierock, J., Rodriguez-Rozada, S., Dieter, A., Pieper, F., Sims, R., Tenedini, F., et al. (2021). BiPOLES is an optogenetic tool developed for bidirectional dual-color control of neurons. *Nat. Commun.* 12:4527. doi: 10.1038/s41467-021-24759-5

Wietek, J., Rodriguez-Rozada, S., Tutas, J., Tenedini, F., Grimm, C., Oertner, T. G., et al. (2017). Anion-conducting channelrhodopsins with tuned spectra and modified kinetics engineered for optogenetic manipulation of behavior. *Sci. Rep.* 7:14957. doi: 10.1038/s41598-017-14330-y

Xia, S., Yu, J., Huang, X., Sesack, S. R., Huang, Y. H., Schlüter, O. M., et al. (2020). Cortical and thalamic interaction with amygdala-to-accumbens synapses. *J. Neurosci.* 40, 7119–7132. doi: 10.1523/JNEUROSCI.1121-20.2020

Yang, W., Carrillo-Reid, L., Bando, Y., Peterka, D. S., and Yuste, R. (2018). Simultaneous two-photon imaging and two-photon optogenetics of cortical circuits in three dimensions. *eLife* 7:e32671. doi: 10.7554/eLife.32671

Yizhar, O., Fenno, L. E., Prigge, M., Schneider, F., Davidson, T. J., O'Shea, D. J., et al. (2011). Neocortical excitation/inhibition balance in information processing and social dysfunction. *Nature* 477, 171–178. doi: 10.1038/nature10360

Zhang, F., Gradinaru, V., Adamantidis, A. R., Durand, R., Airan, R. D., de Lecea, L., et al. (2010). Optogenetic interrogation of neural circuits: technology for probing mammalian brain structures. *Nat. Protoc.* 5, 439–456. doi: 10.1038/nprot.2009.226

Zhang, F., Prigge, M., Beyrière, F., Tsunoda, S. P., Mattis, J., Yizhar, O., et al. (2008). Red-shifted optogenetic excitation: a tool for fast neural control derived from *Volvox carteri*. *Nat. Neurosci.* 11, 631–633. doi: 10.1038/nn.2120

Zhang, F., Wang, L.-P., Brauner, M., Liewald, J. F., Kay, K., Watzke, N., et al. (2007). Multimodal fast optical interrogation of neural circuitry. *Nature* 446, 633–639. doi: 10.1038/nature05744

Zhao, Y., Araki, S., Wu, J., Teramoto, T., Chang, Y.-F., Nakano, M., et al. (2011). An expanded palette of genetically encoded Ca2+ indicators. *Science* 333, 1888–1891. doi: 10.1126/science.1208592

Zingg, B., Hintiryan, H., Gou, L., Song, M. Y., Bay, M., Bienkowski, M. S., et al. (2014). Neural networks of the mouse neocortex. *Cell* 156, 1096–1111. doi: 10.1016/j.cell.2014.02.023

frontiers | Frontiers in Cellular Neuroscience

TYPE Original Research
PUBLISHED 16 June 2023
DOI 10.3389/fncel.2023.1132241

OPEN ACCESS

EDITED BY
Jacopo Lamanna,
Vita-Salute San Raffaele University, Italy

REVIEWED BY
Alev Erisir,
University of Virginia, United States
Sara Spadini,
San Raffaele Hospital (IRCCS), Italy

*CORRESPONDENCE
Ying-Ying Liu
yingyliu@fmmu.edu.cn

†These authors have contributed equally to this work

RECEIVED 27 December 2022
ACCEPTED 05 June 2023
PUBLISHED 16 June 2023

CITATION
Kang J, Lu N, Yang S, Guo B, Zhu Y, Wu S, Huang X, Wong-Riley MTT and Liu Y-Y (2023) Alterations in synapses and mitochondria induced by acute or chronic intermittent hypoxia in the pre-Bötzinger complex of rats: an ultrastructural triple-labeling study with immunocytochemistry and histochemistry. *Front. Cell. Neurosci.* 17:1132241. doi: 10.3389/fncel.2023.1132241

Alterations in synapses and mitochondria induced by acute or chronic intermittent hypoxia in the pre-Bötzinger complex of rats: an ultrastructural triple-labeling study with immunocytochemistry and histochemistry

Junjun Kang[1†], Naining Lu[1†], Shoujing Yang[2†], Baolin Guo[1], Yuanyuan Zhu[1], Shengxi Wu[1], Xiaofeng Huang[3], Margaret T. T. Wong-Riley[4] and Ying-Ying Liu[1*]

[1]Department of Neurobiology, The Fourth Military Medical University, Xi'an, China, [2]Department of Pathology, The Fourth Military Medical University, Xi'an, China, [3]Department of Pathology, Xi'an Gaoxin Hospital, Xi'an, China, [4]Department of Cell Biology, Neurobiology and Anatomy, Medical College of Wisconsin, Milwaukee, WI, United States

Introduction: The pre-Bötzinger complex (pre-BötC), a kernel of inspiratory rhythmogenesis, is a heterogeneous network with excitatory glutamatergic and inhibitory GABAergic and glycinergic neurons. Inspiratory rhythm generation relies on synchronous activation of glutamatergic neuron, whilst inhibitory neurons play a critical role in shaping the breathing pattern, endowing the rhythm with flexibility in adapting to environmental, metabolic, and behavioral needs. Here we report ultrastructural alterations in excitatory, asymmetric synapses (AS) and inhibitory, symmetric synapses (SS), especially perforated synapses with discontinuous postsynaptic densities (PSDs) in the pre-BötC in rats exposed to daily acute intermittent hypoxia (dAIH) or chronic (C) IH.

Methods: We utilized for the first time a combination of somatostatin (SST) and neurokinin 1 receptor (NK1R) double immunocytochemistry with cytochrome oxidase histochemistry, to reveal synaptic characteristics and mitochondrial dynamic in the pre-BötC.

Results: We found perforated synapses with synaptic vesicles accumulated in distinct pools in apposition to each discrete PSD segments. dAIH induced significant increases in the PSD size of macular AS, and the proportion of perforated synapses. AS were predominant in the dAIH group, whereas SS were in a high proportion in the CIH group. dAIH significantly increased SST and NK1R expressions, whereas CIH led to a decrease. Desmosome-like contacts (DLC) were characterized for the first time in the pre-BötC. They were distributed alongside of synapses, especially SS. Mitochondria appeared in more proximity to DLC than synapses, suggestive of a higher energy demand of the DLC. Findings of single spines with dual AS and SS innervation provide morphological

evidence of excitation-inhibition interplay within a single spine in the pre-BötC. In particular, we characterized spine-shaft microdomains of concentrated synapses coupled with mitochondrial positioning that could serve as a structural basis for synchrony of spine-shaft communication. Mitochondria were found within spines and ultrastructural features of mitochondrial fusion and fission were depicted for the first time in the pre-BötC.

Conclusion: We provide ultrastructural evidence of excitation-inhibition synapses in shafts and spines, and DLC in association with synapses that coincide with mitochondrial dynamic in their contribution to respiratory plasticity in the pre-BötC.

KEYWORDS

neuroplasticity, synapse, ultrastructure, mitochondria, desmosome-like contact, intermittent hypoxia, pre-Bötzinger complex

Introduction

Neural networks are executed through structural and functional plasticity of synapses to adapt to continuous environmental changes (Citri and Malenka, 2008). Alterations in the synaptic strength with either increased or decreased synaptic plasticity are thought to represent the cellular mechanisms of learning and memory, characterized as long-term potentiation (LTP, Abbott and Nelson, 2000; Sutton et al., 2006). Synaptic plasticity is tightly correlated with structural changes such as the larger postsynaptic density (PSD) area and spine volume, and increases in perforated PSDs in hippocampal and cortical synapses (Toni et al., 2001; Stewart et al., 2005; Holler et al., 2021). While synaptic plasticity has largely focused on excitatory glutamatergic activity, inhibitory GABAergic synaptic plasticity is also receiving attention, thereby excitatory and inhibitory synapses are assumed to co-orchestrate in contribution to neuroplasticity (Chiu et al., 2013, 2019; Ravasenga et al., 2022). Long-term facilitation (LTF), characterized as a progressive and sustained increase in respiratory motor output lasting for hours, is induced by a moderate, acute intermittent hypoxia (AIH), which represents a form of the respiratory system plasticity (Mitchell et al., 2001; Baker-Herman and Mitchell, 2002). Preconditioning animals with a daily AIH (dAIH) can promote respiratory and motor functional recovery after spinal cord injuries (Gonzalez-Rothi et al., 2015; Vose et al., 2022). Conversely, a severe chronic intermittent hypoxia (CIH), which mimics the recurrent episodes of obstructive sleep apnea (OSA) in patients, causes detrimental consequences (Del Rio et al., 2016). However, ultrastructural evaluation of synaptic characteristics, and excitatory and inhibitory synaptic relationship relevant to respiratory plasticity remains little investigated.

The pre-Bötzinger complex (pre-BötC), a presumed kernel essential for inspiratory rhythmogenesis in the ventrolateral medulla, is involved in respiratory plasticity (Barnett et al., 2017; Garcia et al., 2019). CIH imparts inspiratory rhythmogenesis in a state-dependent manner in the isolated pre-BötC, leading to a loss of transmission fidelity in the local respiratory circuit (Garcia et al., 2016, 2017). Regardless of the electrophysiological information, knowledge of synaptic ultrastructural alterations, including the PSD area and complexity, excitatory and inhibitory balance, and dendritic spine features is essential for the understanding of synaptic strength, efficacy, and plasticity. However, synapse-specific ultrastructural modifications in response to respiratory plasticity have not been precisely characterized in the pre-BötC.

Pre-BötC neurons are heterogeneous and composed of excitatory glutamatergic and inhibitory GABAergic and glycinergic neurons (Kuwana et al., 2006; Wallén-Mackenzie et al., 2006; Winter et al., 2009). Neurokinin 1 receptors (NK1R) and somatostatin (SST) are highly expressed in some of glutamatergic neurons, thereby being used as markers of the pre-BötC in animals (Guyenet and Wang, 2001; Stornetta et al., 2003; Gray et al., 2010) and humans (Schwarzacher et al., 2011). We have demonstrated that SST is colocalized with NK1R in small fusiform and some medium-sized NK1R-positive ($NK1R^+$) neurons, and SST^+ terminals form asymmetric synapses (AS) and symmetric synapses (SS) with $NK1R^+$ neurons in the pre-BötC in normoxic (NOR) rats (Wei et al., 2012). Here, with a combination of SST and NK1R double immunocytochemistry and cytochrome oxidase (CO) histochemistry, we sought to determine ultrastructural changes in synapses and mitochondrial dynamics in the pre-BötC in rats preconditioned with dAIH or CIH. We analyzed excitatory and inhibitory synaptic parameters in dendrites, especially perforated synapses that have been assumed to be associated with synaptic efficiency and plasticity (Toni et al., 2001; Stewart et al., 2005). In particular, we characterized a synapse-specific compartment, the spine-shaft microdomain and its association with mitochondria. Desmosome-like contacts (DLC) were featured for the first time in the pre-BötC. Moreover, we documented ultrastructural characteristics of mitochondrial fusion and fission. We provided ultrastructural basis for possible synchronization between synapses and mitochondria in a compartment-specific manner within dendritic shafts and

Abbreviations: AS, asymmetric synapses; BSA, bovine serum albumin; CIH, chronic intermittent hypoxia; CO, cytochrome oxidase; dAIH, daily acute intermittent hypoxia; DLC, desmosome-like contacts; NK1R, neurokinin 1 receptor; PB, phosphate buffer; PBS, phosphate buffered saline; pre-BötC, pre-Bötzinger complex; ROS, reactive oxygen species; SS, symmetric synapses; SST, somatostatin.

spines in their contribution to respiratory plasticity in the pre-BötC.

Materials and methods

Animals and intermittent hypoxic treatments

Adult Sprague-Dawley rats (230–250 g) were housed in a room with a constant temperature and a 12 h light/dark cycle. Water and food were available *ad libitum*. All experimental procedures were approved by the Northwest China Committee of Experimental Animal Care and conformed to the Guide for the Care and Use of Laboratory Animals published by the National Institutes of Health (NIH). All efforts were made to minimize animal suffering and to reduce the number of animals used.

Animals were randomly divided into NOR, dAIH and CIH groups ($n = 18$ for each group). The hypoxic animals were kept in an acrylic chamber for normobaric hypoxia. Hypoxic conditions were established with a mixture of room air and pure N_2, and monitored by an oxygen analyzer (Attendor 120, Innovation Instrument CO., LTD, Ningbo, China). The dAIH protocol consisted of 5-min episodes of hypoxia (10% O_2) interspersed with 5-min room air intervals. Changes in O_2 levels in the chamber were reached within 20 s during hypoxic episodes. Animals experienced dAIH protocol for 2 h at 9:00–11:00 am each day for 2 weeks. For the CIH treatment, levels of oxygen in the chamber were cycling between 21 to 5 ± 0.5% per minute (i.e., 60 hypoxic episodes per hour) for 8 h per day for 10 consecutive days. The chamber was kept at a constant temperature (22 ± 1°C per day for 10 consecutive days. The chaeuthanized 1 h after the last episode of intermittent hypoxia.

Immunofluorescent histochemistry

Eight animals for each group were deeply anaesthetized with 1% sodium pentobarbital intraperitoneally (50 mg/kg body weight) and were euthanized by transcardial perfusion with 150 ml saline, followed by 500 ml ice cold 4% paraformaldehyde in 0.1 M phosphate buffer (PB, pH 7.4). Brains were removed and post-fixed in the same fixative for 2 h at 4°C. They were then cryoprotected in 30% sucrose in 0.1 M PB overnight at 4°C. Alternate serial coronal sections of brainstems containing the pre-BötC region were cut at 12 μm thickness on a cryostat (CM1900, Leica, Heidelberger, Germany) and mounted on gelatin-coated slides for SST and NK1R immunohistochemistry. All subsequent immunohistochemical procedures were done at room temperature. Slides were blocked and then incubated overnight with a cocktail of primary antibodies of goat anti-SST (1:400, sc-7819, Santa Cruz) and rabbit anti-NK1R (1:5,000, S8305, Sigma, St. Louis, MO) diluted in phosphate buffered saline (PBS) containing 2% bovine serum albumin (BSA) and 0.5% Triton X-100. Secondary antibodies were a mixture of Alexa 488-conjugated anti-goat IgG and Texas Red conjugated anti-rabbit IgG (1:800, Molecular Probes, Eugene, Oregon) in PBS containing 0.3% Triton X-100 for 4 h. After rinsing in PBS, slides were then coverslipped with anti-fading medium and examined with a confocal laser-scanning microscope (Fluoview 1000, Olympus) using laser beams of 543 nm and 488 nm with appropriate emission filters for Texas Red (590–610 nm) and Alexa 488 (510–525 nm), respectively. SST and NK1R immunoreactivities were detected with identical conditions under a microscope equipped with a 40 × objective. Representative photomicrographs were captured with a 12-bit color CCD camera (DP-70, Olympus), acquired at a resolution of 1,360 × 1,024 pixels, and stored in JPEG format.

CO histochemistry

Four rats from each group were deeply anesthetized and perfused transcardially with 150 ml saline, followed by 50 ml ice-cold mixture of 4% paraformaldehyde and 0.05% glutaraldehyde in 0.1 M PB for 1 h. Brainstems were removed and postfixed by immersion in the same fixative for 4 h at 4mersion in the same fixative for μm thicknesses were prepared with a vibratome (VS1000s, Leica). Sections (n = 18–20) including the pre-BötC region were collected from each brainstem. The basic protocol for CO histochemistry was as described previously (Liu et al., 2001). Briefly, sections were incubated in 0.1 M PB containing 25 mg 3, 3'-diaminobenzidine (DAB, Sigma), 15 mg cytochrome c, type III (Sigma), and 2 g sucrose per 50 ml solution. They were incubated at 37 for 3 h in the dark. All sections from three groups were reacted together to avoid differences due to slight variations, such as temperature, medium composition, or incubation time. After CO histochemistry, sections were washed three times, 5 min for each in cold 0.1 M PB. As CO-negative control experiment, two NOR rats were perfused and sectioned as above, and performed SST and NK1R immunocytochemistry procedures, avoiding CO histochemistry.

Pre-embedding immunogold-silver cytochemistry

CO-reacted sections were then processed for SST and NK1R immunocytochemistry. Sections were blocked for 2 h in PBS containing 5% BSA and 0.05% Triton X-100 and were then incubated overnight in the mixed antibodies of goat anti-SST and rabbit anti-NK1R diluted as described above. After rinsing in PBS, they were then incubated in horseradish peroxidase conjugated anti-goat IgG (1:400, Molecular Probes, Eugene, Oregon) and anti-rabbit IgG conjugated to 1.4 nm gold particles (1:100, Nanoprobes, Stony Brook, NY). Sections were rinsed and postfixed in 2% glutaraldehyde in PBS for 45 min. Signals of NK1R immunoreactivity were detected by silver enhancement kit (HQ Silver Kit, Nanoprobes) in the dark. Prior to, and after silver enhancing, sections were rinsed several times with deionized water. After rinsing in PBS, they were visualized by the glucose oxidase-DAB method for SST immunoreactivity. Sections were postfixed in 0.5% osmium tetroxide in 0.1 M PB for 2 h. They were then dehydrated with graded ethanol, replaced with propylene oxide, and finally embedded in Epon 812 between plastic sheets. After polymerization, flat-embedded sections were examined under the light microscope. Three-four sections containing SST and NK1R immunoreactivities in the pre-BötC were selected, trimmed

under a stereomicroscope, and then glued onto blank resin stubs. Serial ultrathin sections were cut with a diamond knife (Diatome, Hatfield, PA) and an Ultramicrotome (Leica EM UC6, Wetzlar, Germany), and mounted on formvar-coated mesh grids (6–8 sections/grid). They were then counterstained and examined under the electron microscope (JEM-1230, JEOL LTD, Tokyo, Japan) equipped with CCD camera and its application software (832 SC1000, Gatan, Warrendale, PA). Electron micrographs (n = 80) of postsynaptic dendrites that were labeled by NK1R-immunogold particles and had synapses with distinct synaptic clefts in the pre-BötC from one brainstem, a total of 320 of dendritic profiles from each group were collected for quantitative analysis with Image-Pro Plus software (Media Cybernetics, Inc.). The quantitative analysis was carried out by a person unaware of the protocols. Regions of PSDs were circled and the area was determined with "area measurement" function. The length and area of PSDs, and the distance between the nearest edges of DLC and PSDs (**Figure 3F**, curve) were calculated and presented as mean ± SEM. Statistical significance was determined by one-way ANOVA, followed by Kruskal–Wallis test (a *post hoc* test) to identify individual comparisons. The closest distances of mitochondria to the center of DLC and PSDs (**Figure 3F**, straight lines) were analyzed by Mann Whitney U test. $p < 0.05$ was considered significant.

Western blot analysis

Western blot analysis was performed according to the standard protocol. Tissues from the ventrolateral medulla oblongata in 18 rats (n = 6 for each group) were dissected and homogenized. SDS-PAGE was conducted and protein transferred to PVDF membrane. After the membrane was blocked with 5% non-fat milk, goat-anti SST (1:1,500), rabbit anti-NK1R (1:15,000), or mouse anti-β-actin antibody (1:5,000, Sigma) were incubated with protein-loaded membrane at 4°C overnight. Horseradish peroxidase-conjugated anti-goat, anti-rabbit or anti-mouse secondary antibodies were incubated for 1 h at room temperature. Bands were visualized with a Pierce ECL kit (Thermo Fisher, Rockford) and images were analyzed by Image J. All values were expressed as mean ± SEM. $p < 0.05$ was considered significant.

Results

This was the first time that a triple labeling with a combination of SST and NK1R double immunocytochemistry and CO histochemistry at the ultrastructural level was reported in the pre-BötC. We identified AS and SS established by presynaptic SST^+ or SST^- terminals with postsynaptic $NK1R^+$ dendrites in the pre-BötC. NK1R immunogold particles were localized mainly along the inner surface of the plasma membrane in somata and dendrites, as represented in **Figure 1**. The particles were also found in association with the rough endoplasmic reticulum (**Figure 1C**) and some multivesicular bodies (thin open arrowheads in **Figures 1D, E**), indicative of NK1R recycling of synthesis, membrane translocation, endocytosis and degradation, a process that is reminiscent of muscarinic acetylcholine receptor 2 in striatal interneurons (Bernard et al., 1998). SST immunoperoxidase reaction product was distributed in somata (**Figures 1A, B**), axonal terminals (**Figure 1D**), and primary dendrites (**Figure 1B**). In somata, SST^+ product was specifically expressed in the Golgi apparatus (**Figure 1C**), consistent with previous descriptions (Johansson, 1978). CO reaction product was expressed on the inner mitochondrial membrane, filling the intracristate space, as showed in **Figure 2**, consistent with our previous studies (Kang et al., 2019, 2020). Three categories of CO-reactive mitochondria were defined to reflect CO activity, according to previous reports (Wong-Riley, 1989; Wong-Riley et al., 1989): darkly reactive mitochondria with more than 50% of the inner mitochondrial membrane and intracristate space bearing CO reaction product, as showed in **Figures 2A–C** (thin solid arrows), moderate ones with less than 50% of inner mitochondrial membrane and intracristate space covered with reaction product (open arrows with solid arrowheads in **Figures 2A–C**), and light ones with little or no detectable reaction product (open arrows in **Figures 2A, C**). **Figure 2D** shows mitochondria as CO negative control, with omission of CO histochemistry procedure.

Synaptic ultrastructural features in dendritic shafts in the pre-BötC

Synapses in the pre-BötC were mainly constructed on dendritic shafts (**Figures 2A–C**, **3**, **4**, **8**), and axo-spinous synapses were rarely detectable (**Figure 9**). $NK1R^+$ dendrites received both AS and SS innervation, as represented in **Figure 2**. AS are featured with prominent PSDs (thick arrows in **Figures 2B, C**), corresponding to excitatory synapses, and SS have less pronounced PSDs (arrowheads in **Figures 2A–C**), referring to inhibitory synapses (Peters et al., 1991). The majority of PSDs had a single plate, termed macular synapses as represented in **Figures 2B, C**. Perforated synapses, featured by discontinuous PSDs with two or more separate segments were identified in the pre-BötC (thick arrows in **Figures 1D, F**, solid arrows in 3A with T1, B, D, E, 4). The other characteristic of perforated synapses is their large size, as PSDs with a single perforation are larger than a simple macular one, and the largest have two or more perforations (Peters and Kaiserman-Abramof, 1969; Jones and Harris, 1995). Indeed, multiple perforated synapses with two or more perforations were encountered in the pre-BötC, representing larger and more complex PSDs (solid arrows with T1 in **Figure 3A**, thin solid arrows with T2 in **Figure 4B**). **Figures 4B, C** display perforated AS (thick solid arrows) and SS (thin solid arrows) with curved PSDs that were localized in large dendritic shafts, and also extended into restricted spaces, facing other synapses (solid arrowheads). Synaptic vesicles could be found accumulated in distinct pools opposed each discrete segments of PSDs (open arrowheads).

Synaptic characteristics were analyzed separately in terminals with or without SST immunoreactivity in the pre-BötC. Synapses with blurred clefts and PSDs due to the plane of sections were not included in analyses. A total of 1,543 synapses formed by SST^- terminals, including 514 in the NOR, 519 in the dAIH and 510 in the CIH groups were analyzed from over 60 grids derived from four brainstems (3–4 pre-BötC areas/brainstem, about 6–8 ultrathin sections/grid) in each group. Macular synapses accounted for a dominant proportion in the NOR (82.5%), dAIH (79.2%), and CIH

10.3389/fncel.2023.1132241

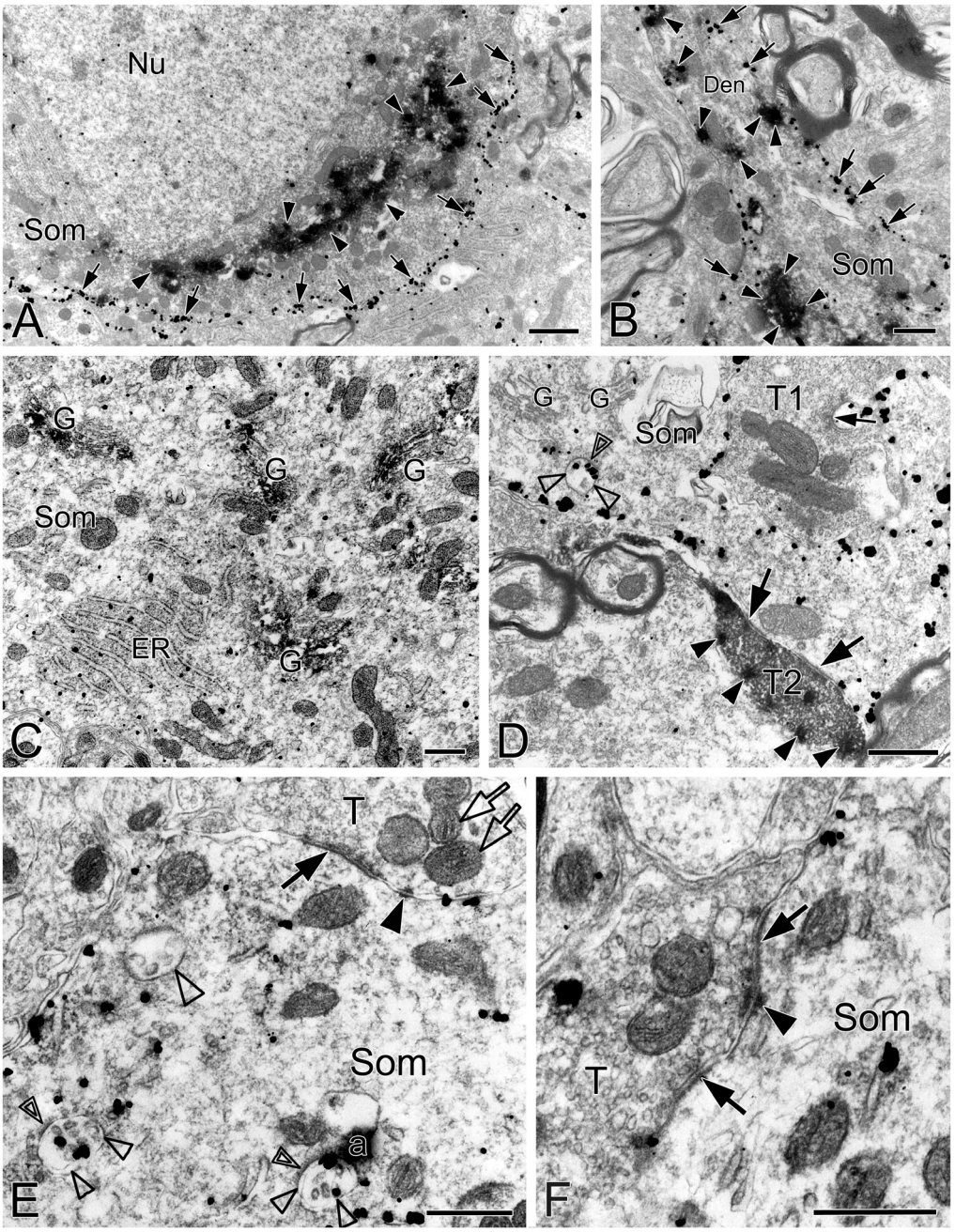

FIGURE 1
Electron micrographs showing SST and NK1R immunoreactivities in the pre-BötC. NK1R immunogold particles were localized mainly along the inner surface of the plasma membrane [arrows in panels **(A,B)**]. The particles were also distributed in the rough endoplasmic reticulum **(C)** and multivesicular body [open arrowheads in panel **(D)**, open thin arrowheads in panel **(E)**]. Some multivesicular bodies had clathrin coat [double open arrowheads in panels **(D,E)**]. Multivesicular bodies with no NK1R immunoreactivity were also visible [open thick arrowhead in panel **(E)**]. SST immunoperoxidase reaction product was observed in somata [arrowheads in panels **(A,B)**], primary dendrites [arrowheads in panel **(B)**], and large dense-core vesicles in terminals [solid arrowheads in panel **(D)**]. SST was specifically expressed in the Golgi apparatus **(C)**. Perforated symmetric synapses (SS, solid thick arrows in panel **(D,F)**] and horseshoe-shaped SS [solid thin arrow in panel **(D)** were visualized. Desmosome-like contacts (DLC) were seen alongside of SS (solid arrowhead in panel **(E)**] or between two SS [solid arrowhead in panel **(F)**]. Mitochondria seemed in more proximity to DLC [open arrows in panel **(E)**]. Nu: nucleus, Som: soma, ER: endoplasmic reticulum, G: Golgi apparatus, T: terminal, Den: dendrite. a: artificial. Scale bars in panels **(A,B)**: 1 μm, in panels **(C–F)**: 0.5 μm.

(82.6%) groups, and the rest were perforated synapses (Figure 5A). The proportion of AS reached 65.2% in the dAIH, as compared to 57% in the NOR and 54.9% in the CIH groups. Conversely, macular SS were declined to 25.8% in the dAIH, as compared to 34.6% in the NOR and 36.3% in the CIH groups. Perforated synapses accounted for a higher proportion in the dAIH (20.8%) than in the NOR (17.5%) and CIH (17.4%) groups (Figure 5A). The mean length of macular synapses was significantly increased in the dAIH group, when compared to the CIH group ($p < 0.01$ in AS, $p < 0.001$ in SS), but had no significant difference when compared to the NOR

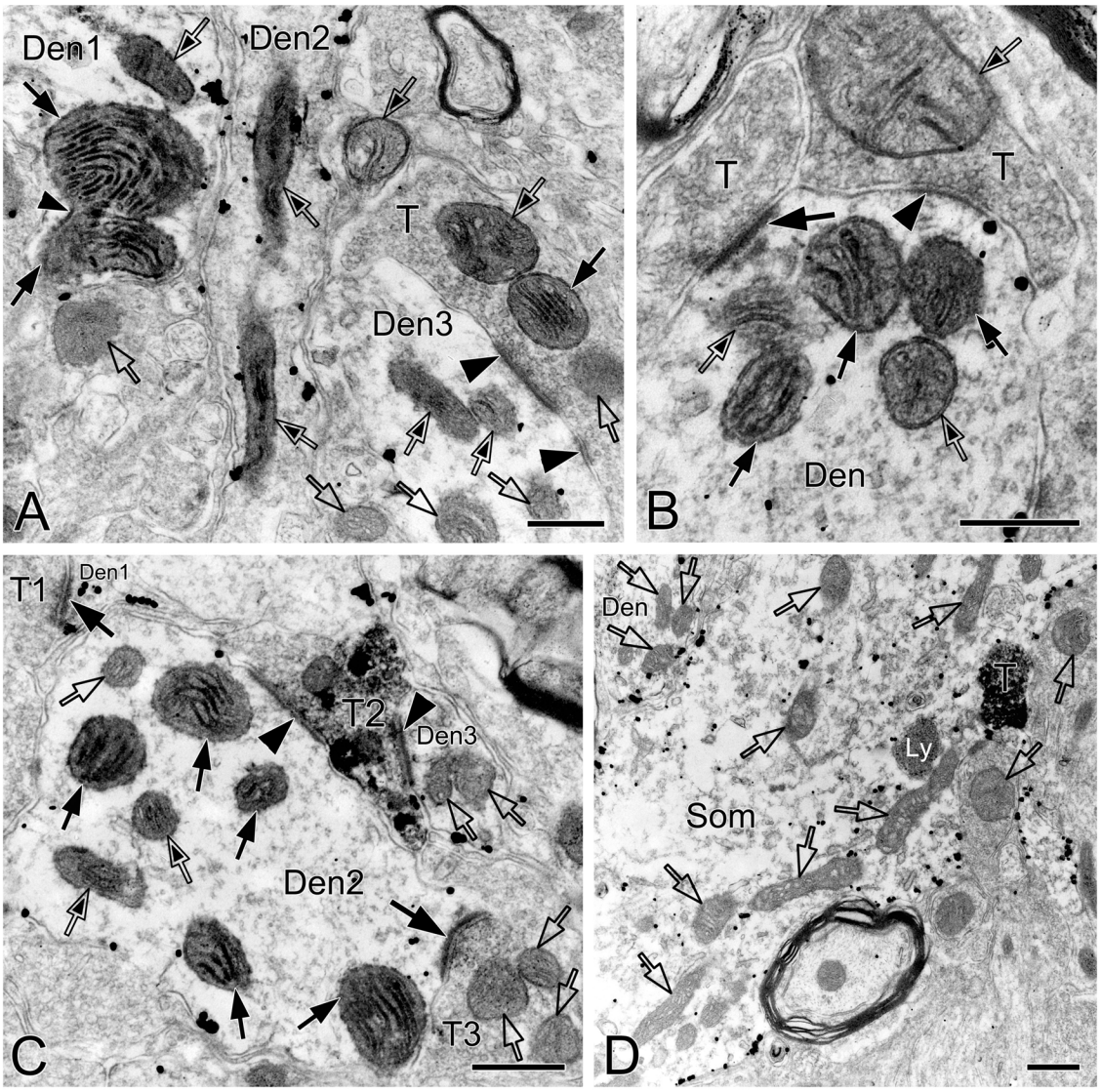

FIGURE 2
Electron micrographs showing CO-reactive mitochondria in the pre-BötC. Mitochondria with dark (solid thin arrows), moderate (open arrows with solid arrowheads), and light (open arrows) CO reactivity were identified in NK1R^{+} dendrites **(A–C)**. Open arrows in panel **(D)** indicated mitochondria with no CO histochemistry. Thin arrowhead in panel **(A)** pointed to the presumable fused membrane of two mitochondria. Som: soma, Den: dendrite, T: terminal. Ly: lysosome. Scale bars: 0.5 μm.

group (Figure 5C). Significant increases in the mean area were found in the dAIH group, as compared to the NOR ($p < 0.05$ in SS) and the CIH ($p < 0.0001$ in AS, $p < 0.01$ in SS) groups, and also in the NOR, as compared to the CIH groups ($p < 0.05$ in AS, Figure 5C). Perforated synapses had much larger PSDs than macular ones, roughly by 70% (AS)–80% (SS) in length, and 60% (AS)–90% (SS) in area (Figure not showed).

DLC ultrastructural features in the pre-BötC

DLC were identified for the first time in the pre-BötC (arrowheads in Figures 1E, F, 3, 4D, 8C, E). The DLC were originally described in Mauthner neurons in goldfish (Nakajima, 1974). They are localized adjacent to chemical synapses and gap junctions, and respond to LTP tetanic stimulations, thereby named mixed synapses together with chemical synapses and gap junctions that are assumed to represent chemical and electrical neurotransmission, respectively, occurring within the same terminal (Nakajima, 1974; Moshkov et al., 1998, Dzeban et al., 2004). DLC in the pre-BötC were featured by both prominent, dense membranes in apposition forming narrow clefts, which usually contained fibrous bridges, similar to synaptic clefts (solid thick arrowheads in Figures 3, 4D, 8C, E). Synaptic vesicles were frequently encountered in the DLC, and some were obviously accumulated, reminiscent of those in synapses (open arrowheads in Figures 3B–E, 4D, 8E). They were found alongside of AS (Figures 3F, 8C, E) or SS (Figures 1E, F, 3A–E, 4D), and some were resided between two segments of perforated synapses (solid

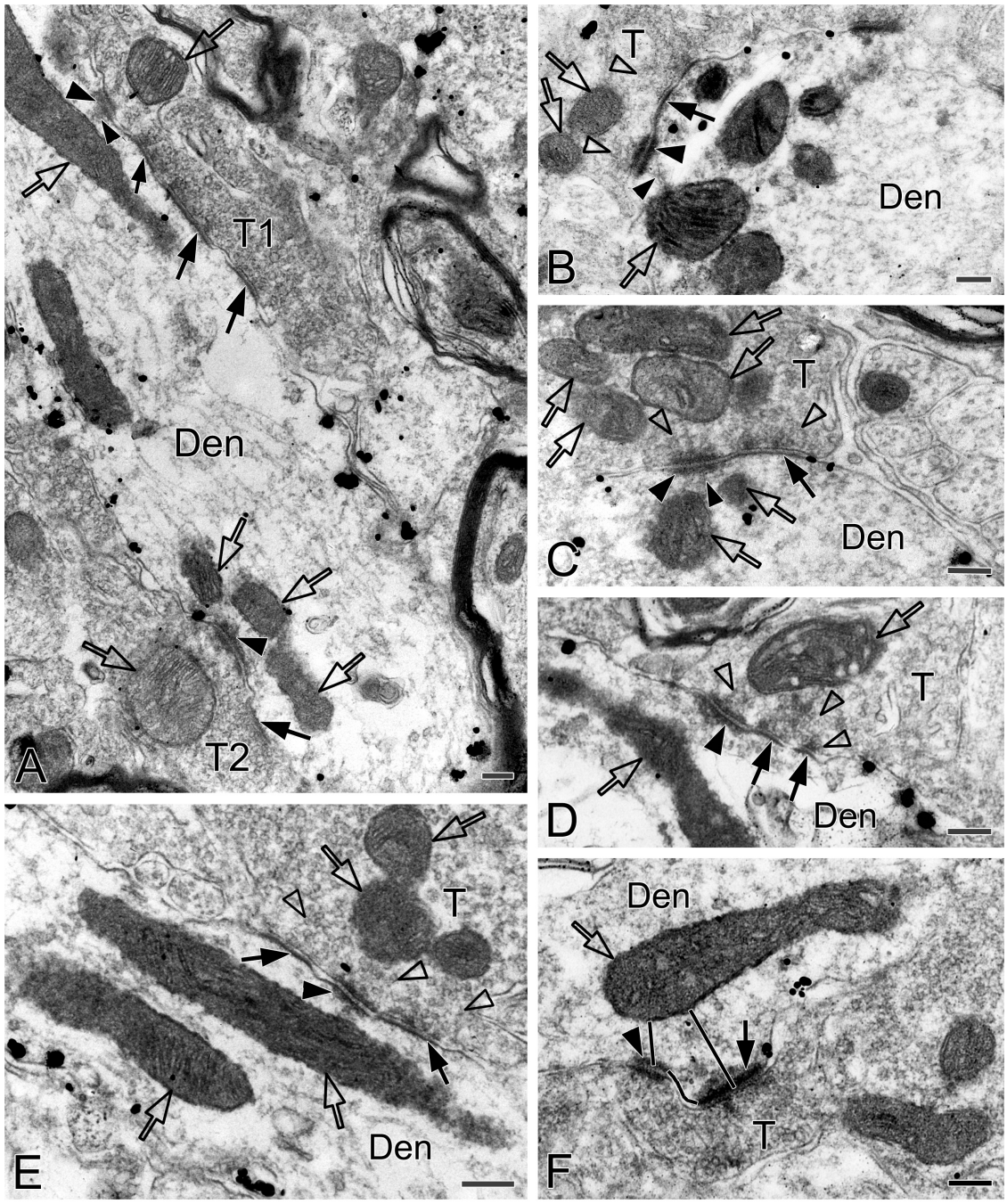

FIGURE 3
Electron micrographs showing perforated synapses, DLC and mitochondria in the pre-BötC. Perforated synapses had discontinuous postsynaptic densities [PSDs, solid arrows in panels **(A,B,D,E)**]. DLC were found alongside of synapses [solid thick arrowheads in panels **(A–D,F)**] or between two segments of perforated synapses [solid arrowhead in panel **(E)**]. PSDs were seen in continuity to the dense membranes of DLC **(B–D)**. Open arrowheads pointed to synaptic vesicles accumulated in distinct pools opposed each discrete PSD segments and DLC. Open arrows showed mitochondria in proximity to DLC. Filamentous or flocculent elements could be found between the mitochondria and the DLC [solid thin arrowheads in panels **(A–C)**]. Curve in panel **(F)** represented the distance between the DLC and the synapse, and straight lines in panel **(F)** showed the closest distances of mitochondria to the center of DLC and PSDs. Den: dendrite, T: terminal. Scale bars: 0.2 μm.

arrowheads in Figures 1F, 3E). DLC seemed in more association with SS than AS. Dense membranes of DLC could be found in connection with PSDs, and fibrous bridges were continuous between them (Figures 1F, 3B–D). A total of 142 DLC (59 in NOR, 52 in dAIH, 31 in CIH) were examined in the pre-BötC. They were resided mainly alongside of synapses and with higher proportions in the NOR (74.6%) and the dAIH (75%) groups than in the CIH group (64.5%). The rest were in isolation with no synapse discernible in the same terminals (Figure 6A). They presented in more association with SS (45.8% in NOR, 48.1% in dAIH, 38.7% in CIH) than AS (28.8% in NOR, 26.9% in dAIH, 25.8% in CIH, Figure 6A). DLC were found more alongside of perforated synapses

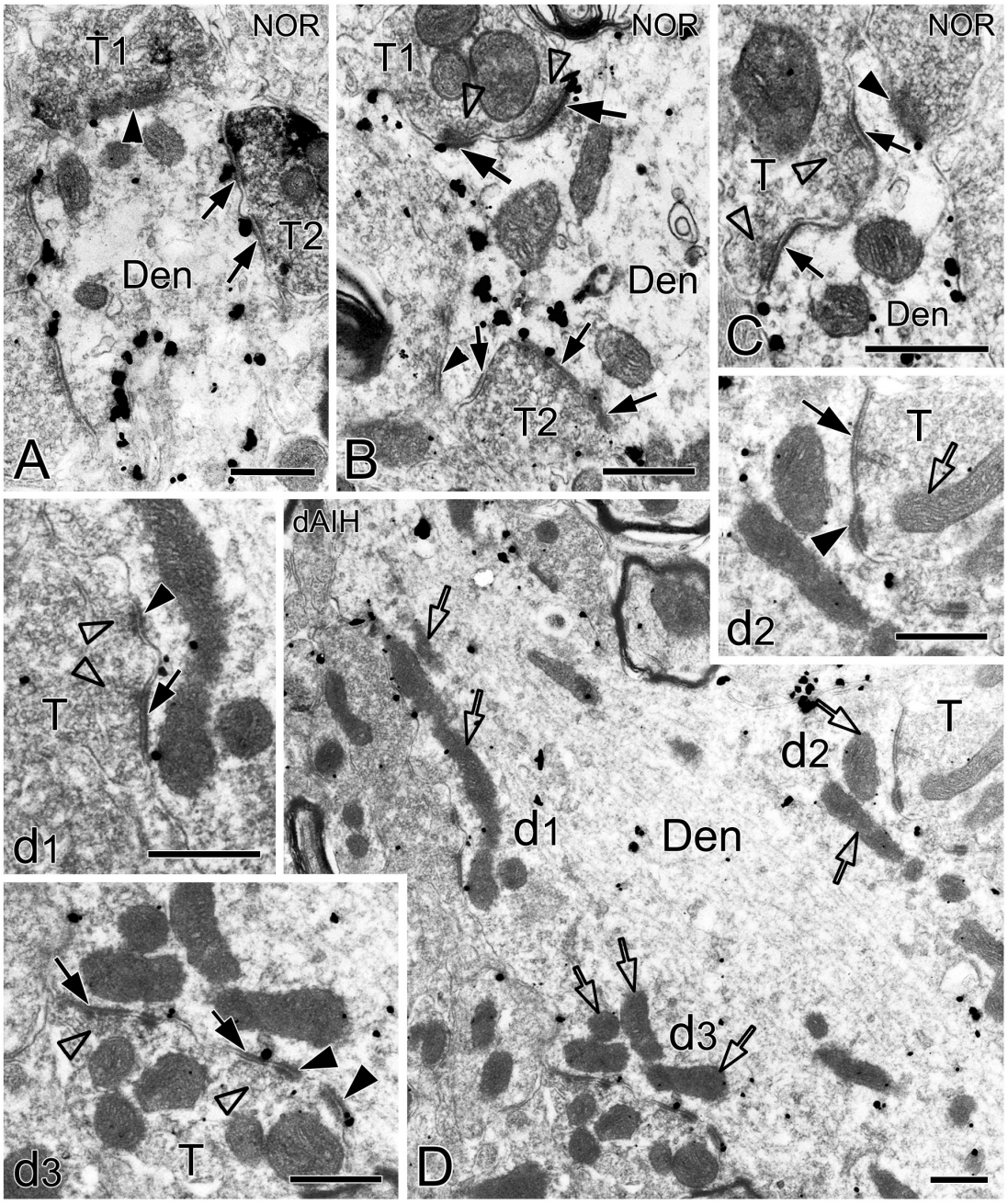

FIGURE 4
Electron micrographs showing perforated synapses in the pre-BötC. An SST$^+$ terminal made perforated SS with a NK1R$^+$ dendrite [arrows in panel **(A)**]. Perforated synapses were found to be localized in large dendritic shafts, and also extended into restricted spaces [thin arrows in panels **(B,C)**]. Synaptic vesicles could be seen accumulated in distinct pools opposed each discrete segment of PSDs [open arrowheads in panels (**B,C**,d1,d3)]. Solid arrowheads in panels (d1–d3) pointed to DLC. A mitochondrion was found in more proximity to a DLC than SS [open arrow in panel (d2)]. Areas labeled by panels (d1–d3 in **D**) were magnified in insets. T: terminal, Den: dendrite. Scale bars: 0.5 μm.

(12.9%), especially perforated AS (9.7%) in the CIH group than in the NOR (5.1%) and dAIH (7.7%) groups (Figure 6A). They were in more proximity to synapses in the dAIH than in the CIH group ($p < 0.05$), but had no significant difference, when compared to the NOR group (Figure 6B). There was also no significant difference in the distance of DLC to AS and SS, respectively, in three group (Figure not showed).

Of note, mitochondria appeared in greater proximity to DLC than synapses (open arrows in Figures 1E, 3, 4D with Figures 4 d2, 8C, E). Mitochondrial cristae were found in parallel toward DLC (open arrows in Figures 3A–E, 8C). Filamentous or flocculent elements could be seen between the mitochondria and the DLC (solid thin arrowheads in Figures 3A–C). A total of 240 mitochondria in terminals (95 in NOR, 77 in dAIH, 68 in CIH) and 194 ones in dendrites (75 in NOR, 72 in dAIH, 47 in CIH) were analyzed for the distance to DLC and synapses, respectively, and CO activity in the pre-BötC. Indeed, mitochondria were found in more proximity to DLC than synapses, especially in

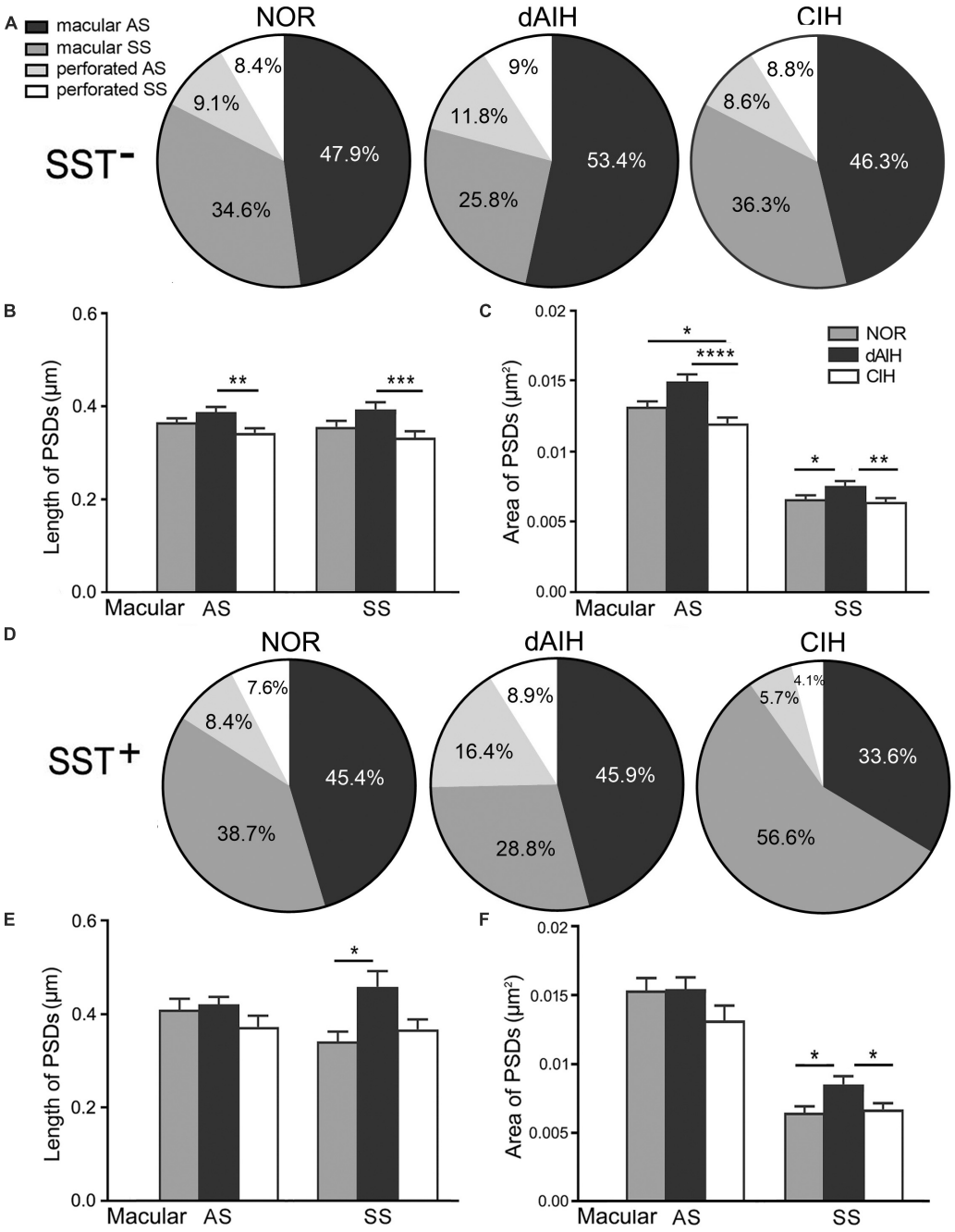

FIGURE 5
Percentages and the size of synapses formed by SST$^-$ **(A–C)** or SST$^+$ **(D–F)** terminals onto NK1R$^+$ dendrites in the pre-BötC in the normoxic (NOR), daily acute intermittent hypoxia (dAIH) and chronic intermittent hypoxia (CIH) groups. Pie charts illustrated proportions of macular and perforated AS and SS **(A,D)**. The mean length of PSDs in SST$^-$ AS and SS showed significant increases in the dAIH group, as compared to the CIH group (Kruskal–Wallis test, $p = 0.0047$ in AS, $p = 0.0009$ in SS), but had no significant differences while compared to the NOR group **(B)**. The mean area was also significantly increased in the dAIH group, as compared to the CIH group [**(C)** Kruskal–Wallis test, $p < 0.0001$ in AS, $p = 0.0055$ in SS]. Significant increases in the mean area were also identified in AS in the NOR group, as compared to the CIH group (Kruskal–Wallis test, $p = 0.0159$) and in SS in comparison with the dAIH group [**(C)** Kruskal–Wallis test, $p = 0.0312$]. Significant increase in the PSD size was identified only in SST$^+$ SS in the dAIH group, as compared to the NOR [**(E,F)** Kruskal–Wallis test, $p = 0.0249$ in length; $p = 0.0327$ in area]. The mean area was also significantly increased in the dAIH group, as compared to the CIH group [**(F)** Kruskal–Wallis test, $p = 0.021$]. *$p < 0.05$, **$p < 0.01$, ***$p < 0.001$, ****$p < 0.0001$.

terminals (Figure 6C, $p < 0.001$ in NOR and CIH; $p < 0.01$ in dAIH). A similar trend was also identified in dendrites, although showing no significant difference in the CIH group (Figure 6C). The distance of mitochondrial positioning to DLC appeared to be more consistent with less variance in terminals and dendrites that had both DLC and synapses (Figure 6C) than those with isolated DLC only, although the later showed no significant difference (Figure 6D). High proportions of darkly CO-reactive mitochondria were identified in dendrites in the dAIH (52.8%) and NOR (41.3%) groups, where darkly to moderately reactive ones reached 88.9 and

10.3389/fncel.2023.1132241

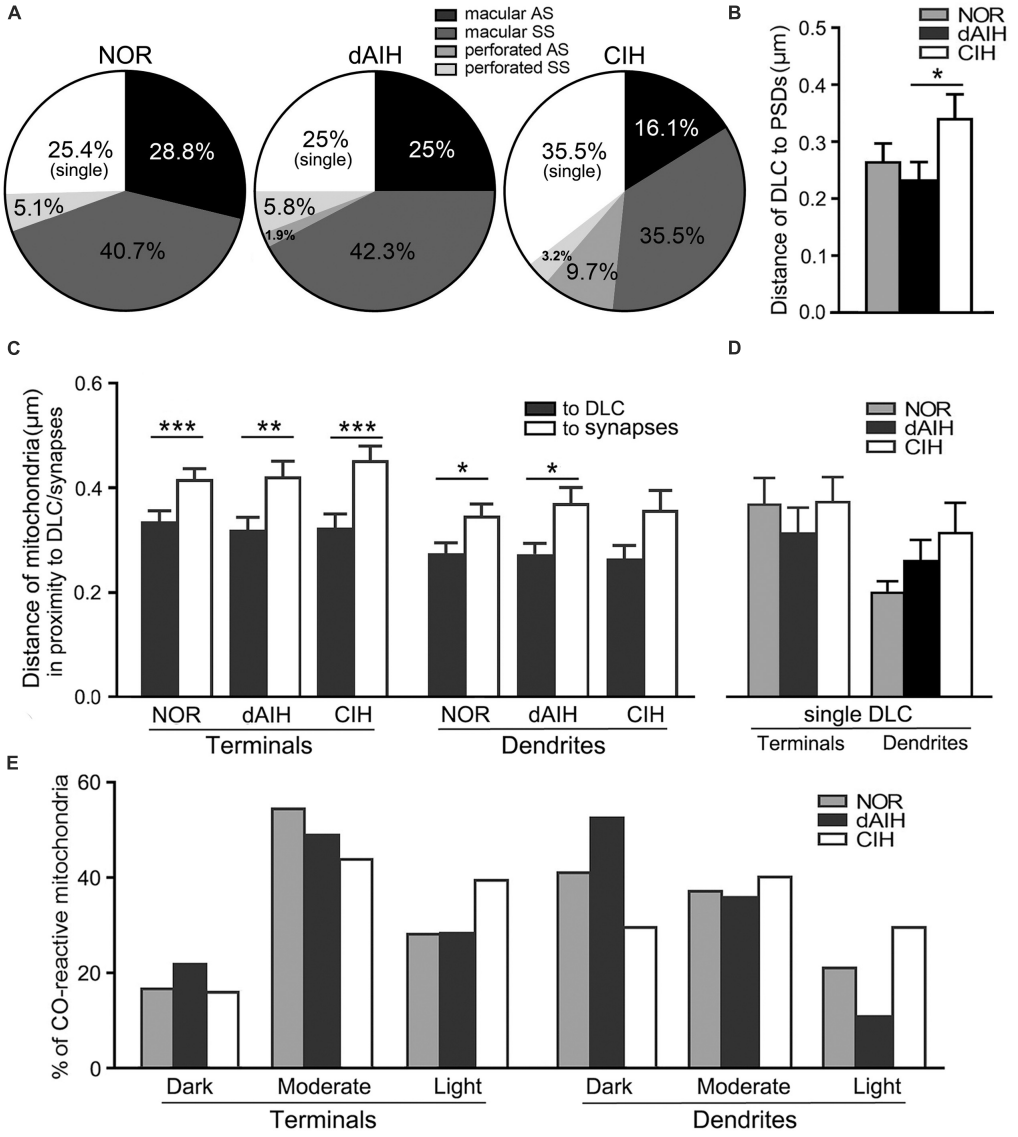

FIGURE 6
DLC relationships with synapses and mitochondria in the pre-BötC in the NOR, dAIH and CIH groups. Pie charts presented proportions of DLC in association with macular and perforated AS and SS **(A)**. DLC were in more proximity to synapses in the dAIH than the CIH group [**(B)** Kruskal–Wallis test, $p = 0.035$]. Mitochondria were found in more proximity to DLC than synapses in terminals [**(C)** Mann Whitney U test, $p = 0.001$ in NOR, $p = 0.0059$ in dAIH, $p = 0.0004$ in CIH] and in dendrites [**(C)** Mann Whitney U test, $p = 0.023$ in NOR, $p = 0.019$ in dAIH, $p = 0.089$ in CIH]. The distance of mitochondria to isolated DLC showed no significant differences of three groups **(D)**. Percentages of darkly, moderately and lightly CO-reactive mitochondria in proximity to DLC in terminals and dendrites were displayed in three groups **(E)**. $*p < 0.05$, $**p < 0.01$, $***p < 0.001$.

78.6%, respectively. Moderately CO-reactive ones were prevalent in terminals (54.7% in NOR, 49.4% in dAIH, 44.1% in CIH). The highest proportions of lightly CO-reactive ones were evident in the CIH group, accounting for 39.7% in terminals and 29.8% in dendrites (Figure 6E).

SST expression in the pre-BötC NK1R$^+$ neurons

SST was expressed in a group of small fusiform neurons that often overlapped with NK1R in the pre-BötC (Figures 7A, B). SST immunoreactivity appeared in somata and punctuate-like boutons, some of which were in close apposition to processes and somata that were NK1R$^+$ (Figures 7A, B). Large NK1R$^+$ neurons lacked SST immunoreactivity (Figures 7B, C). dAIH significantly increased expressions of SST and NK1R, whereas CIH led to a significant decline of both in the pre-BötC region (Figure 7D).

SST immunoreactive product displayed an uneven flocculent or spot-like appearance when colocalized with NK1R in somata (arrowheads in Figure 1A, B) and primary dendrites (arrowheads with Den in Figure 1B) under the electron microscope. In terminals, SST typically resided within large dense-core vesicles (Figure 1D with T2, Figure 8A with T1); however, it could be diffuse throughout the terminals, depending on the extent to which sections were exposed to the DAB reaction, as exemplified in

10.3389/fncel.2023.1132241

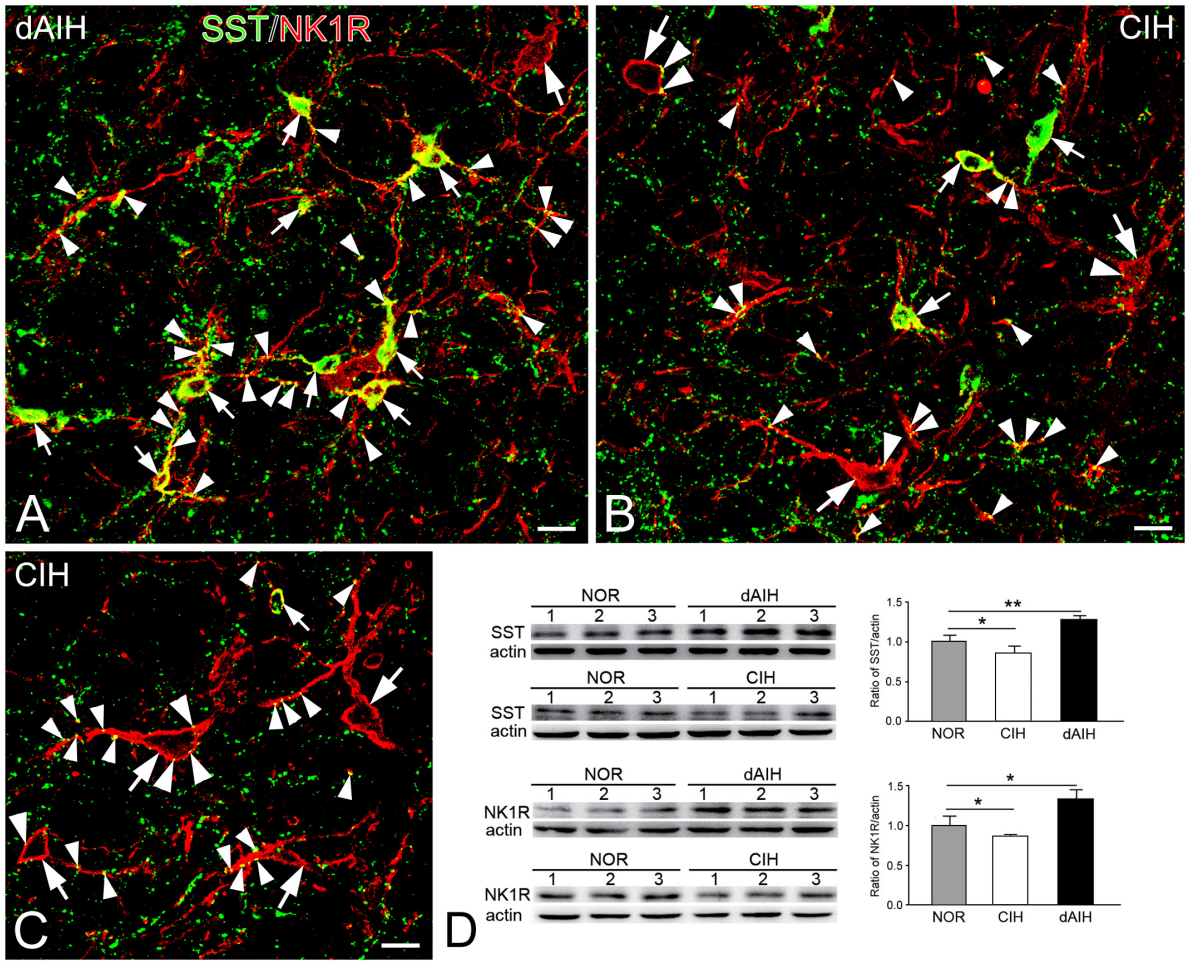

FIGURE 7
Expressions of SST and NK1R in the pre-BötC in the NOR, dAIH and CIH groups. SST immunoreactivity is visualized with Alexa 488 (green) and NK1R immunoreactivity with Texas Red (red). Thin arrows presented colocalization of two fluorophores in small fusiform neurons **(A–C)**. SST^+ boutons were found in close association with $NK1R^+$ somata (thick arrowheads) and processes (thin arrowheads). Thick arrows illustrated $NK1R^+$ large neurons **(B,C)**. Western blots showing bands detected with antibodies against SST, NK1R and actin in tissues of the ventrolateral medulla oblongata, including the pre-BötC region **(D)**. Darker bands were found in lanes with protein extracts from the dAIH group, while lighter ones were from the CIH group. Scale bars: 20 μm, $*p < 0.05$, $**p < 0.01$.

Figure 2C with T2, D. SST^+ terminals made AS or SS on $NK1R^+$ dendritic shafts (Figure 2C with T2, Figures 4A, 8A, B with T1, Figures 4C, D, 9A with T2, T3), spines (Figure 9A with T1, E), and somata (Figure 1D). An SST^+ terminal could be found to form SS (arrowheads in Figure 2C) or AS (arrows in Figure 8D) with two $NK1R^+$ dendrites.

A total of 387 synapses (119 in NOR, 146 in dAIH, 122 in CIH) established by SST^+ terminals were analyzed in the pre-BötC. AS accounted for the highest proportion (62.3%) in the dAIH and the lowest (39.3%) in the CIH, as compared to the NOR group (53.8%). Perforated synapses were in the highest proportion of 25.3% (16.4% AS, 8.9% SS) in the dAIH group, as compared to 16% in the NOR and 9.8% in the CIH groups (Figure 5D). In contrast, macular SS were prevalent in the CIH (56.6%, Figure 5D). Significant increases in the mean length and area of PSDs were found only in macular SS in the dAIH group, as compared to the NOR group (Figures 5E, F, $p < 0.05$), and also in the mean area in the dAIH group, as compared to the CIH group (Figure 5F, $p < 0.05$).

Ultrastructural characteristics of the spine-shaft microdomain in the pre-BötC

Identification of spines requires that the spine must be visually traced to the parent dendrite, which is uncommon and also a challenge under the electron microscope that the section passes through both the head and the neck connecting it to the parent dendrite. However, three categories of dendritic spines described in previous reports (Peters and Kaiserman-Abramof, 1970; Harris and Kater, 1994) were defined in the pre-BötC, including mushroom spines with a narrow neck and a large head (Figures 9D, E), thin spines with a slender neck and a smaller head (Figure 9A), and stubby spines with the width of the neck similar to the length (Figure 9C). We found multiple-synapse spines composed of one AS (thick open arrowheads in Figures 9B, F) and one SS (thin open arrowheads in Figures 9B, F) in the pre-BötC. SST^+ peptidergic modulatory synapses were also identified in spines (Figure 9A with T1, E). Figure 9D illustrates a presumed

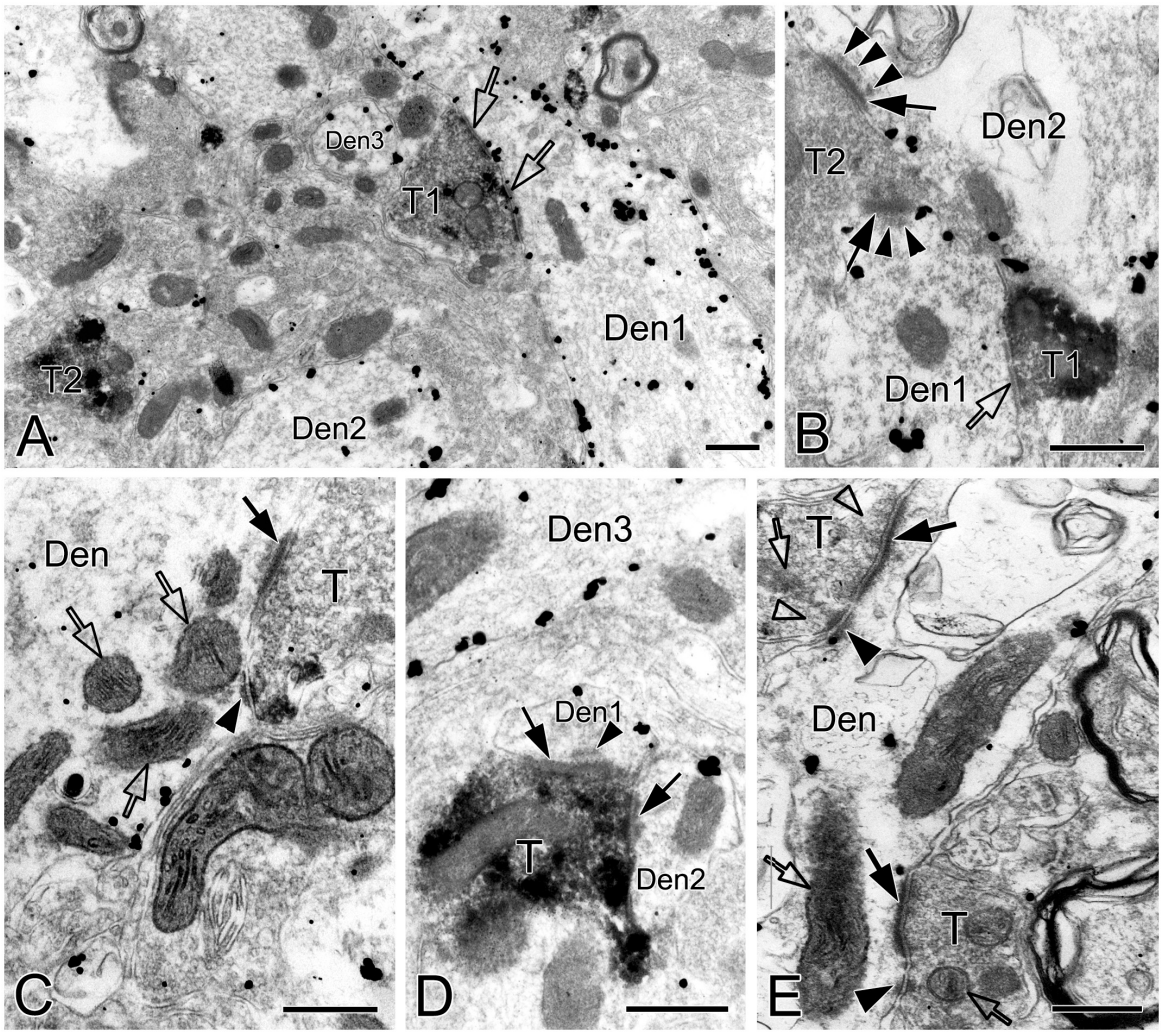

FIGURE 8
Electron micrographs showing AS, SS and DLC formed by SST$^+$ terminals in the pre-BötC. SST$^+$ terminals made SS [open arrows in panel **(A,B)**] and AS [solid arrows in panels **(C,D)**] onto NK1R$^+$ dendrites. Arrowheads in panels **(B,D)** pointed to postsynaptic dense bodies. DLC were found alongside of AS [arrowheads in panels **(C,E)**]. Mitochondria could be seen in proximity to DLC [open arrows in panels **(C,E)**]. Synaptic vesicles appeared in accumulation in distinct pools opposed to PSDs and DLC [open arrowheads in panel **(E)**].

SS formed by a peptidergic terminal containing large dense-core vesicles, positioning partly in the spine and partly in the parent shaft (open arrow), and a AS on the head (open arrowhead) for seeming excitatory-inhibitory modification in a single spine. Synapses in parent shafts adjacent to the base of the neck could be seen in oblique distribution toward spines (open arrows in Figures 9A, B), some of which even extended into spines through the neck (open arrow in Figure 9D), establishing a structural base, characterized as the spine-shaft microdomain for the spine and shaft communication. Figure 9A presents three SST$^+$ terminals in distinct synaptic formations: one AS on the spine (T1), one shaft SS in the spine-shaft microdomain (T2), and another SS on the shaft (T3), indicating SST-mediated diverse synaptic modifications.

Mitochondria presented tight correlation with synapses in spine-shaft microdomains in the pre-BötC. We found for the first time that mitochondria were within spines in the pre-BötC (solid arrowheads in Figures 9A–C, F). Some were distributed partly in spines and partly in parent shafts (solid arrows in Figures 9A, C, F), and some were in parent shafts near the base of the spine neck (solid arrows in Figures 9B, D, E). Figure 9F displays three mitochondria, two in parallel in a multiple-synapse spine (solid arrowhead), and another at the neck of the spine (arrow). Of 145 mitochondria (45 in NOR, 53 in dAIH, 47 in CIH) examined in 90 spine-shaft microdomains (28 in NOR, 31 in dAIH, 31 in CIH), a majority of mitochondria (58.5%) were found positioning completely or partly in spines in the dAIH group, whereas they were predominantly in parent shafts in the NOR (55.5%) and CIH (63.8%) groups (Figure 9G). There were no significant differences in the mean length and area of mitochondria of three groups (Figure 9H). Most mitochondria were darkly to moderately CO-reactive in the NOR (66.7%) and dAIH (73.6%) groups, whereas moderate to light ones (81.4%) were predominant in the CIH group (78.7%, Figure 9I), indicating increased mitochondrial activity induced by dAIH.

10.3389/fncel.2023.1132241

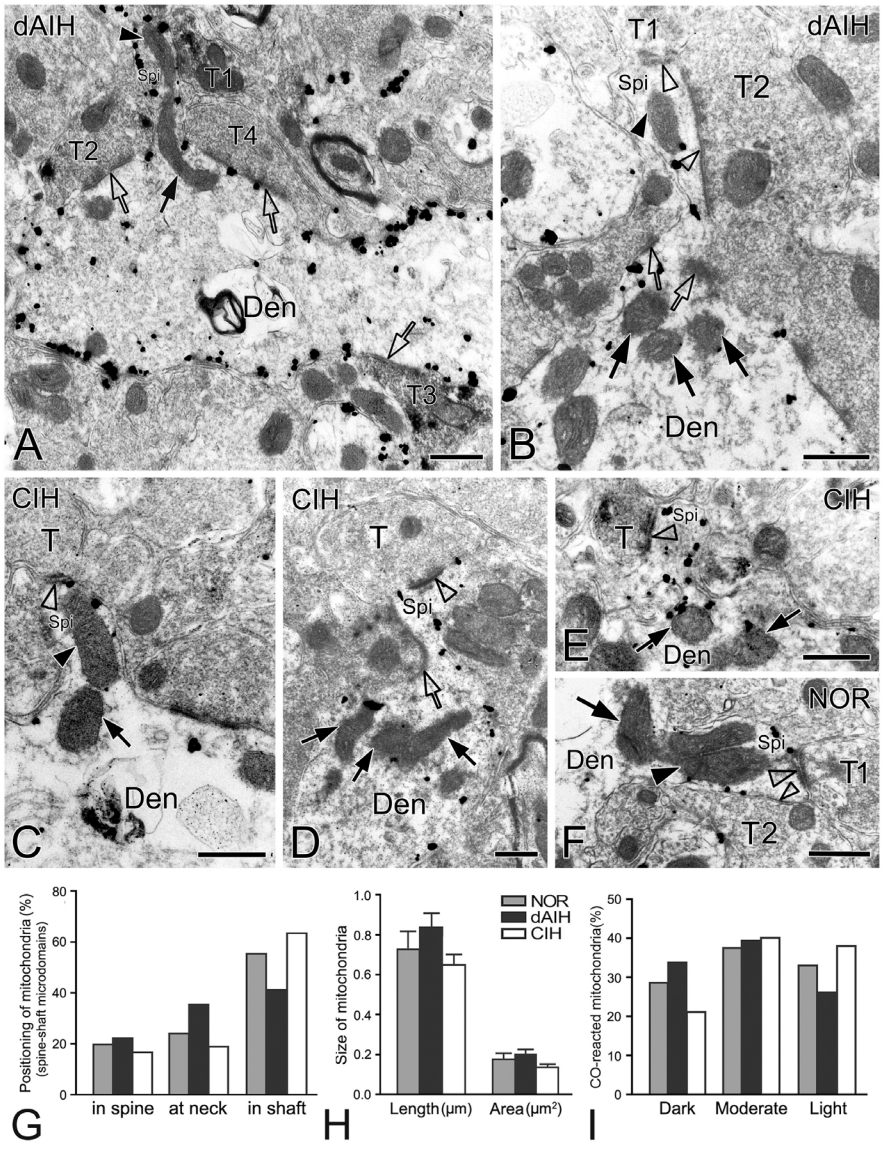

FIGURE 9
Electron micrographs and histograms showing spines and associated mitochondria in the pre-BötC in three groups. Spine-shaft microdomains presented synapses in spines [synapse with T1 in panel **(A)**, open arrowheads in panel **(B)**] and in parent shafts adjacent to the base of the spine neck [open arrows in panels **(A,B)**], which were coupled with mitochondria positioning in spines [solid arrowhead in panels **(A,B)**], at the spine neck [solid arrow in panel **(A)**] and in parent shafts near the base of the spine neck [solid arrows in panel **(B)**]. Multiple-synapse spines with both AS and SS were detectable [open arrowheads in panels **(B,F)**]. A presumed SS at the spine neck [open arrow in panel **(D)**] extended into a spine that also received an AS on the head [open arrowhead in panel **(D)**]. Mitochondria seemed successively in spines [solid arrowheads in panels **(C,F)**] with a follower at the spine neck [arrows in panels **(C,F)**]. SST^{+} terminals made synapses onto spines [synapse with T1 in panel **(A)**, open arrowhead in panel **(E)**], in the spine-shaft microdomain [open arrow with T2 in panel **(A)**], and on the shaft [open arrow with T3 in panel **(A)**]. T: terminal, Den: dendrite, Spi: spine. Scale bars: 0.5 μm. Histograms showed mitochondrial positioning **(G)**, size **(H)** and co reaction **(I)** in spine-shaft microdomains.

Ultrastructural characteristics of mitochondrial fusion and fission in the pre-BötC

We defined distinct ultrastructural morphologies of mitochondrial fusion and fission, which were much less known in *in vivo* animal studies, and lacking in those on the pre-BötC. Morphological features of mitochondrial fusion were characterized as three steps, based on our observations: first, the outer membrane of two apposed mitochondria interconnected and fused with a slight curvature toward the inner membrane, forming a narrow intermembrane space (arrowheads in Figures 10A–C). Second, the two inner membranes were in close apposition to enlarge the membrane contact area, where dot-like contacts could be visualized (Figures 10A, B). The inner membranes fused partly (Figures 10B, C) to completely (Figure 10D), leading to an elongated and enlarged mitochondrion (Figures 10A–D). Third, the cristae appeared in rearrangement, seemingly perpendicular toward (Figures 10A, B) or across the fused inner membranes (Figures 10C, D). Ultrastructural characteristics of mitochondrial fission were identified between two smaller mitochondria (solid

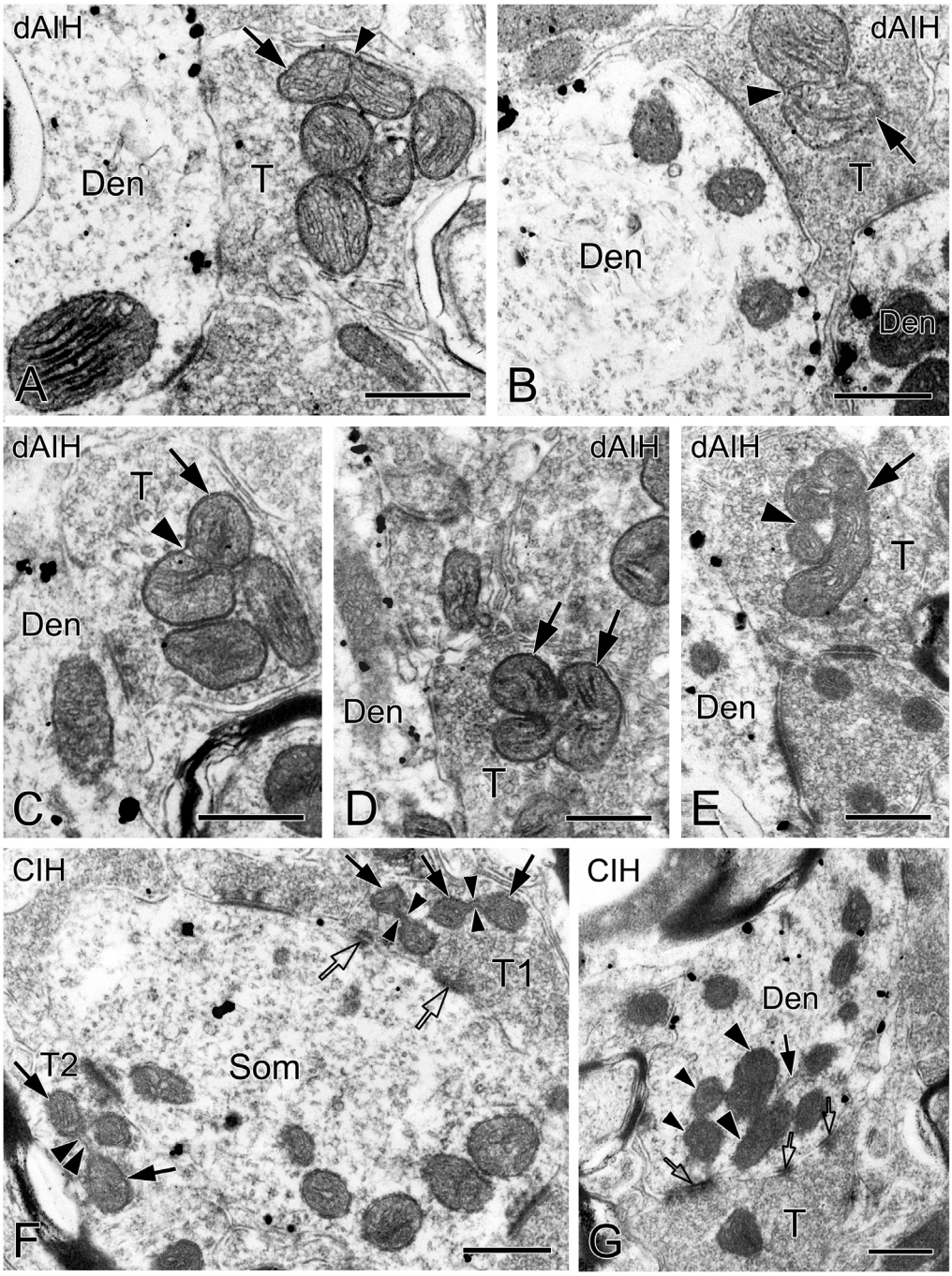

FIGURE 10
Electron micrographs showing mitochondrial fusion and fission in the pre-BötC. Fusion was identified between two larger mitochondria [arrows in panels **(A–D)**]. The fused outer membrane was clearly visible with a slight curvature toward the inner membrane [arrowheads in panels **(A–C)**]. Fission was found between two smaller mitochondria [arrows in panel **(F)**] interconnected by a mitochondrial tubule [arrowheads in panel **(F)**]. A cluster of mitochondria overlapped in close proximity to a perforated synapse [open arrows in panel **(G)**], of which the larger two (thick arrowheads) seemed in fusion, and the smaller two (thin arrowheads) in fission. The endoplasmic reticulum was commonly visible among mitochondria [solid arrow in panel **(G)**]. Filamentous or flocculent elements could be found between mitochondria [arrowhead in panel **(E)**]. Den: dendrite, T: terminal. Scale bars: 0.5 μm.

arrows in Figure 10F) that were linked by a mitochondrial tubule (arrowheads in Figure 10F), as described in an *in vitro* study (Basu et al., 2017). However, morphologies of mitochondrial fusion or fission were not always clearly visible because of the obscured membrane due to ultrathin sectioning (thin arrowhead in Figure 2A, arrowhead in 10E). Figure 10G displays a cluster of dendritic mitochondria in close proximity to a perforated synapse (open arrows), of which the larger two (thick arrowheads) seem to be in fusion with dark cristae interconnected between them, whereas the smaller two (thin arrowheads) could be in fission.

Discussion

The pre-BötC is a heterogeneous network, containing nearly half excitatory glutamatergic neurons expressing the developing brain homeobox 1 (Dbx1$^+$) and half inhibitory GABAergic and glycinergic neurons (Kuwana et al., 2006; Wallén-Mackenzie et al., 2006; Winter et al., 2009). SST and NK1R partially co-localize with glutamatergic Dbx1$^+$ neurons (Cui et al., 2016; de Sousa Abreu et al., 2022). Inspiratory rhythm generation relies on a synchronous convergence of glutamatergic excitatory drive (Smith et al., 1991; Gray et al., 2001; Feldman et al., 2013), whilst inhibitory neurons play a critical role in shaping breathing movements by mediating apneas, stabilizing the rhythm, and broadening the dynamic range of inspiration, endowing the rhythm with flexibility to adapt to environmental, metabolic, and behavioral needs (Cui et al., 2016; Baertsch et al., 2018; Ashhad and Feldman, 2020). In the present study, we found that first, dAIH induced significant increases in the PSD size of macular AS and the proportion of perforated synapses in the pre-BötC. dAIH shifted excitation-inhibition balance toward a higher excitation with dominant AS in shafts, whereas CIH led to a higher inhibition with increased SS, especially SS formed by SST$^+$ terminals. Second, DLC were featured for the first time in the pre-BötC. They were localized mainly alongside of synapses, especially SS, and in more proximity to them in the dAIH than CIH group. Mitochondria appeared in more proximity to DLC than synapses of three groups. Third, multiple synapses with dual AS and SS innervation, including peptidergic SST$^+$ synapses, were identified on the same spines. Spine-shaft microdomains established by synapses in spines and parent shafts coupled with mitochondrial positioning was characterized for the first time in the pre-BötC, which may form the basis for synchronizing spine-shaft communications. Finally, we depicted ultrastructural features of mitochondrial fusion and fission in the pre-BötC for the first time. We provided ultrastructural evidence that synapses and DLC coupled with mitochondrial activity are closely associated in synapse-specific compartments in the pre-BötC, most likely participating in respiratory plasticity.

Ultrastructural alterations of SST$^-$ synapses in dendritic shafts

Synaptic ultrastructural alterations correlate with functional activity of synapses. In cortical and hippocampal synapses, the shape and surface area of PSDs directly correlate with neurotransmitter release probability, synaptic strength, efficiency, and plasticity (Holderith et al., 2012; Eltokhi et al., 2020; Holler et al., 2021). The PSD surface area is proportional to the number of postsynaptic receptors, the larger the surface of the PSD, the higher the absolute number of AMPARs and NMDARs (Kharazia and Weinberg, 1999; Tarusawa et al., 2009). Perforated synapses were first described in rat cerebral cortex by Peters and Kaiserman-Abramof (1969), characterized by their large size and discontinuity of the PSDs when sectioned passing at right angles to synapses. Their presence increases the extent of the edge of PSDs and hence the size of the total synaptic active zone (Peters and Kaiserman-Abramof, 1969; Jones and Harris, 1995). The considerably large PSDs of perforated synapses have more receptors to be facilitated for synaptic transmission in correlation with synaptic plasticity and long-lasting memory (Toni et al., 2001; Ganeshina et al., 2004; Stewart et al., 2005; Spruston, 2008). During chemically induced LTP, macular PSDs are able to transform into perforated PSDs, to facilitate PSD expansion by adding new molecules from peri-synaptic areas (Stewart et al., 2005). Perforated synapses can be identified in single section, stereological analyses, or 3D reconstruction that were then classified as fenestrated, horseshoe-shaped, and segmented shapes (Geinisman et al., 1987; Harris et al., 1992). However, the present study was performed on 50 μm thick sections with preembedding immunoreactivities that labeled surface neurons within a few microns in-depth, thereby limiting 3D analyses. Indeed, SST and NK1R double immunoreactivity precisely delineated AS and SS, of whose perforated synapses were characterized for the first time in the pre-BötC. Perforated synapses presented remarkably larger PSDs than macular synapses. dAIH increased the proportion of perforated synapses, especially in AS, implying increased synaptic transmission probability and synaptic strength. The finding of synaptic vesicles accumulated in distinct pools in apposition to each discrete PSD segments suggests that they may function as independent units of each segment, equivalent to increasing the number of release sites, to enhance synaptic transmission efficacy (Toni et al., 2001; Ganeshina et al., 2004). Consistently, the structure and composition of PSDs are dynamic, which can be rapidly modified in alignment with presynaptic release sites, so called as nanocolumns (Tang et al., 2016). Cryo-electron tomography reveals trans-synaptic assemblies that link presynaptic vesicles with putative postsynaptic receptors, bridging the cleft for trans-synaptic coordination of synaptic transmission and plasticity (Martinez-Sanchez et al., 2021). Fibrous bridges examined in synaptic clefts in the pre-BötC may play a role, at least, as a structural basis for the trans-synaptic coordination and plasticity. Moreover, fibrous bridges were also identified in DLC resided alongside of synapses and some were continuously connected with synaptic clefts, as represented in **Figures 3C, D**, which may be morphological evidence of DLC in synchrony with synaptic activity that respond to respiratory plasticity.

The balance of synaptic excitation-inhibition is a crucial determinant of network output, including pre-BötC neurons (Baertsch et al., 2018; Ashhad and Feldman, 2020). While dAIH induced a significant increase in the PSD size of macular AS, it was increased as well in the macular SS, implying a synchronized excitation-inhibition balance with appropriate inhibition in modulation of the network augmented plasticity. Alterations in AS and SS compositions with dominant AS in the dAIH group and high SS proportion in the CIH group suggest excitation-inhibition balance shifting toward a higher excitation associated with LTF expression and a higher inhibition associated with OSA. A moderate dAIH preconditioning may stimulate glutamatergic microcircuits in the pre-BötC that increase Ca^{2+} entry through NMDA receptors, and in turn, recruit AMPA receptor insertion into synapses, thereby enlarging the PSD size and the number of AS for augmented respiratory plasticity. Conversely, severe CIH challenges induce excessive Ca^{2+} influx and increased ROS generation (Semenza and Prabhakar, 2015), leading to calcium overload and oxidative stress that may render the network unstable and less plastic with a robust inhibition and apnea in association with detrimental consequence of OSA.

DLC relationships with synapses

DLC are assumed as a composition of mixed synapses with chemical synapses and gap junctions, responding to tetanization-induced LTP in Mauthner neurons in goldfish (Moshkov et al., 1998, Dzeban et al., 2004). DLC consist predominantly of filamentous actin, which possesses electroconductivity, and is well-known to be involved in mechanisms of LTP and synaptic plasticity (Pinho et al., 2020). Fibrous bridges in the clefts of DLC are associated with polymerizd actin, which may be the structural substrate of electrotonic transmission (Dzeban et al., 2004), functioning directly via shunting chemical synapses, or indirectly through interaction with gap junctions in response to synaptic plasticity (Moshkov et al., 1998). Indeed, DLC examined in the pre-BötC manifested a close association with synapses, especially SS, even that dense membranes of DLC and PSDs, as well as fibrous bridges within clefts were connected continuously, implying possible chemical synapses and DLC electroconductive interactions. The interactions could be more intimate under dAIH challenge, given that DLC appeared more alongside of synapses and were in more proximity to them in the dAIH group than in the CIH group. If considering DLC in involvement in modulating the balance of synaptic excitation-inhibition in the pre-BötC, as described above, they could be more in coordination with inhibitory synapses under dAIH challenge, to maintain an appropriate augmentation, as near half of DLC stayed adjacent to SS that were almost double the amount of DLC associated with AS in the dAIH group. On the contrary, DLC may turn to a close association with perforated AS in synergism with synaptic excitation in the CIH group, while the balance of excitation-inhibition tends to shift toward inhibition exerted by CIH challenge. Our ultrastructural findings implicate the network communications between DLC and synapses, macular and perforated synapses, and excitation and inhibition balance in the pre-BötC in their contribution to respiratory plasticity, which however, remain to be explored.

Mitochondria positioning in more proximity to DLC than synapses reflect robust activity of DLC that needs high energy supply as synaptic property rather than a simple contact. Higher proportion of darkly CO-reactive mitochondria in dendrites than terminals suggests a higher energy demand at postsynaptic compartments than presynaptic compartments, where moderately CO-reactive ones were predominant. The energy requirement could be stable and continuous for DLC in synchrony with synaptic activity, thereby corresponding to a more consistent mitochondrial positioning to DLC in terminals and dendrites that had both DLC and synapses than those with isolated DLC only. If they should be named mixed synapses as described in the Mauthner neurons, they are composed of chemical synapses and DLC only, as we have not found gap junctions between neurons, except ones between glial cells in the pre-BötC (Kang et al., 2017). Their colocalizations may indicate chemical and electrotonic neurotransmission and interaction occurring within the same terminal, which, however, remains to be investigated. DLC in cone pedicles in the retina of macaque monkeys do not express desmosome proteins, such as desmocollin, desmoplakin, plakoglobin, pan-cadherin and catenin (Paffenholz et al., 1999), but are associated with glutamate receptors (Haverkamp et al., 2000). Whether DLC identified in the pre-BötC express distinct receptors and neurotransmitters remains to be explored.

Ultrastructural alterations of SST$^+$ synapses in dendritic shafts

The pre-BötC neurons receive both SST$^+$ AS and SS innervation (Wei et al., 2012; Cui et al., 2016). SST$^+$ AS inputs are most likely from glutamatergic pre-BötC neurons (Cui et al., 2016; de Sousa Abreu et al., 2022). SST$^+$ SS inputs may arise mainly from sources outside the pre-BötC, such as the nucleus of the solitary tract, Kölliker-Fuse nucleus, or the parabrachial nuclei that contain SST$^+$ inhibitory neurons projecting onto the pre-BötC (Epelbaum et al., 1994; Bou Farah et al., 2016). The colocalization of SST with glutamate and their probable corelease imply that SST may prevent the network from overexcitation to maintain a proper rhythm stability in a phase- and state-dependent manner (Ramírez-Jarquín et al., 2012). In the present study, the proportion of SST$^+$ AS was remarkably increased in the pre-BötC in the dAIH group. It is possible that terminals previously with less or undetectable SST immunoreactivity acquired recognizable amount of SST to maintain the augmented glutamatergic stability. Conversely, SST$^+$ SS were predominant in the CIH group. An increase in the PSD size in macular SS, not AS, induced by dAIH implicates an inhibitory compensatory mechanism in maintaining excitation within certain limits and stability (Cui et al., 2016; Baertsch et al., 2018). SST, as an inhibitory neuromodulator, directly depresses pre-BötC-generated rhythms (Ramírez-Jarquín et al., 2012). SST modulation is required for proper gasping, as the blockade of SST receptor 2 compromises auto-resuscitation (Ramírez-Jarquín et al., 2012). SST is also found decline in the pre-BötC in victims with sudden infant death syndrome (Lavezzi and Matturri, 2008). Reduction of SST expression exerted by CIH in the pre-BötC may be relevant to gasping dysfunction, which, however, remains to be determined.

Spine-shaft microdomains in the pre-BötC

Both excitatory and inhibitory inputs are involved in fine-tuning synaptic integration and plasticity in dendritic shafts and spines (Chen et al., 2012; Chiu et al., 2018). It is reported that excitatory synapses on dually innervated spines are more stable than those on singly innervated spines. Inhibitory synapses are more dynamic than excitatory synapses on the same dually innervated spines, thereby excitatory synapses are almost exclusively one-time events of removal and addition, whereas inhibitory synapses are frequently transient or recurrent in the same location, manifesting substantial and dynamic rearrangements of GABAergic synapses in mediating synaptic plasticity (Chen et al., 2012; Villa et al., 2016). GABAergic PSDs, similar to glutamatergic synapses, enable rapid diffusion in the plasma membrane to disperse synaptic GABA receptors, or conversely, transiently interact with scaffold proteins for synaptic accumulation (Bannai et al., 2015; Bertholet et al., 2016). GABAergic synapses in the cortex can directly impinge onto

glutamatergic spines, exerting highly compartmentalized control of excitation (Chen et al., 2012; Chiu et al., 2013; Villa et al., 2016). Multiple-synapse spines with dual AS and SS innervation in the pre-BötC were found in the pre-BötC. The positioning of SS partly in the shaft and partly in the spine, as exemplified in **Figure 9D** may represent a highly dynamic state that SS at the neck are processing insertion or dispersal of inhibitory receptors in the postsynaptic membrane in synchrony with excitatory synaptic activity within a single spine. The spine-shaft microdomain characterized by accumulated synapses in spines, at the neck, and in parent shafts, coupled with mitochondrial positioning provides a structural evidence for the spine-shaft communication. Our finding is consistent with understanding of functional short-range crosstalk between the spine and the parent shaft that excitatory plasticity at an individual spine can affect neighboring GABAergic synapses in the parent shaft, and further likely to influence dendritic information processing and integration (Ravasenga et al., 2022).

Mitochondrial dynamics in the spine-shaft microdomains and their fusion and fission in the pre-BötC

Mitochondria are highly dynamic in structure and function in correspondence with respiratory plasticity elicited by dAIH and CIH in dendrites in the pre-BötC (Kang et al., 2019, 2020). In the present study, we found that mitochondria in spine-shaft microdomains were positioned diversely within spines, partly in spines and partly in shafts, or in shafts adjacent to the base of the spine neck. dAIH elicited more mitochondria extending into the spine, implying high energy expenditure of synapses for augmented LTF expression. Mitochondrial recruitment to synapses is associated with local Ca^{2+} elevation during sustained synaptic activities (Seager et al., 2020). dAIH-induced mitochondrial positioning in spines could be attributed to local elevated Ca^{2+} influx that facilitates mitochondrion-spine communication. Conversely, the majority of mitochondria with light CO reaction stayed in parent shafts in the CIH group, which may be interpreted as CIH-elicited Ca^{2+} overload and ROS increase that negatively impact CO activity and mitochondrial entrance into spines.

Mitochondria are in a perpetual state of fusion and fission to maintain their structure, quality, and function (Seager et al., 2020). An imbalance of these two opposite processes, particularly an excess of fission can be detrimental to mitochondrial function (Fischer et al., 2016). We found that mitochondrial fusion appeared between larger mitochondria with dark CO reactivity, being consistent with a robust mitochondrial activity, whereas fission was observed between two smaller mitochondria. The structural evidence will guide a functional understanding of mitochondrial fusion and fission associated with respiratory plasticity.

In summary, the present study demonstrates synaptic ultrastructural alterations in the pre-BötC induced by dAIH and CIH. Alterations in AS and SS composition, the PSD size, and the number of perforated synapses implicate a shift of excitation-inhibition balance toward a higher excitation under dAIH challenge, and conversely, a higher inhibition induced by CIH. The excitation-inhibition network is precisely displayed in spine-shaft microdomains, such that multiple-synapse spines have dual AS and SS innervation, and SS at the spine neck extend into spines for crosstalk with AS in spines, establishing structural evidence for understanding spine-shaft communication. The close association of DLC with synapses may imply chemical and electrotonic neurotransmission and interactions occurring within the same terminal, which are in synchrony with mitochondrial dynamics in structure, positioning and CO activity. Our ultrastructural evidence highlights the excitation-inhibition network in shafts and spines, and DLC in association with synapses that coincide with mitochondrial dynamic in their contribution to respiratory plasticity in the pre-BötC.

Data availability statement

The original contributions presented in this study are included in the article/supplementary material, further inquiries can be directed to the corresponding author.

Ethics statement

The animal study was reviewed and approved by the Northwest China Committee of Experimental Animal Care.

Author contributions

Y-YL designed and performed the experiments, and wrote the manuscript. JK, NL, and SY performed the research. BG and YZ contributed hypoxic animal preparations. SW and XH analyzed the data. MW-R reviewed the manuscript. All authors contributed to the work and approved the submitted version.

Funding

This study was supported by Natural Science Foundation of China (grants: 31971055 and 82101203).

Conflict of interest

The authors declare that the research was conducted in the absence of any commercial or financial relationships that could be construed as a potential conflict of interest.

Publisher's note

References

Abbott, L. F., and Nelson, S. B. (2000). Synaptic plasticity: taming the beast. *Nat. Neurosci.* 3(Suppl.), 1178–1183. doi: 10.1038/81453

Ashhad, S., and Feldman, J. L. (2020). Emergent elements of inspiratory rhythmogenesis: network synchronization and synchrony propagation. *Neuron* 106, 482.e4–497.e4. doi: 10.1016/j.neuron.2020.02.005

Baertsch, N. A., Baertsch, H. C., and Ramirez, J. M. (2018). The interdependence of excitation and inhibition for the control of dynamic breathing rhythms. *Nat. Commun.* 9:843. doi: 10.1038/s41467-018-03223-x

Baker-Herman, T. L., and Mitchell, G. S. (2002). Phrenic long-term facilitation requires spinal serotonin receptor activation and protein synthesis. *J. Neurosci.* 22, 6239–6246.

Bannai, H., Niwa, F., Sherwood, M. W., Shrivastava, A. N., Arizono, M., Miyamoto, A., et al. (2015). Bidirectional control of synaptic $GABA_AR$ clustering by glutamate and calcium. *Cell Rep.* 13, 2768–2780. doi: 10.1016/j.celrep.2015.12.002

Barnett, W. H., Abdala, A. P., Paton, J. F., Rybak, I. A., Zoccal, D. B., and Molkov, Y. I. (2017). Chemoreception and neuroplasticity in respiratory circuits. *Exp. Neurol.* 287, 153–164.

Basu, K., Lajoie, D., Aumentado-Armstrong, T., Chen, J., Koning, R. I., Bossy, B., et al. (2017). Molecular mechanism of DRP1 assembly studied in vitro by cryo-electron microscopy. *PLoS One* 12:e0179397. doi: 10.1371/journal.pone.0179397

Bernard, V., Laribi, O., Levey, A. I., and Bloch, B. (1998). Subcellular redistribution of m2 muscarinic acetylcholine receptors in striatal interneurons *in vivo* after acute cholinergic stimulation. *J. Neurosci.* 18, 10207–10218. doi: 10.1523/JNEUROSCI.18-23-10207.1998

Bertholet, A. M., Delerue, T., Millet, A. M., Moulis, M. F., David, C., Daloyau, M., et al. (2016). Mitochondrial fusion/fission dynamics in neurodegeneration and neuronal plasticity. *Neurobiol. Dis.* 90, 3–19.

Bou Farah, L., Bowman, B. R., Bokiniec, P., Karim, S., Le, S., Goodchild, A. K., et al. (2016). Somatostatin in the rat rostral ventrolateral medulla: origins and mechanism of action. *J. Comp. Neurol.* 524, 323–342.

Chen, J. L., Villa, K. L., Cha, J. W., So, P. T., Kubota, Y., and Nedivi, E. (2012). Clustered dynamics of inhibitory synapses and dendritic spines in the adult neocortex. *Neuron* 74, 361–373. doi: 10.1016/j.neuron.2012.02.030

Chiu, C. Q., Barberis, A., and Higley, M. J. (2019). Preserving the balance: diverse forms of long-term GABAergic synaptic plasticity. *Nat. Rev. Neurosci.* 20, 272–281. doi: 10.1038/s41583-019-0141-5

Chiu, C. Q., Lur, G., Morse, T. M., Carnevale, N. T., Ellis-Davies, G. C., and Higley, M. J. (2013). Compartmentalization of GABAergic inhibition by dendritic spines. *Science* 340, 759–762.

Chiu, C. Q., Martenson, J. S., Yamazaki, M., Natsume, R., Sakimura, K., Tomita, S., et al. (2018). Input-specific NMDAR-dependent potentiation of dendritic GABAergic inhibition. *Neuron* 97, 368.e3–377.e3. doi: 10.1016/j.neuron.2017.12.032

Citri, A., and Malenka, R. C. (2008). Synaptic plasticity: multiple forms, functions, and mechanisms. *Neuropsychopharmacology* 33, 18–41.

Cui, Y., Kam, K., Sherman, D., Janczewski, W. A., Zheng, Y., and Feldman, J. L. (2016). Defining preBötzinger complex rhythm- and pattern-generating neural microcircuits invivo. *Neuron* 91, 602–614. doi: 10.1016/j.neuron.2016.07.003

de Sousa Abreu, R. P., Bondarenko, E., and Feldman, J. L. (2022). Phase- and state-dependent modulation of breathing pattern by preBötzinger complex somatostatin expressing neurons. *J. Physiol.* 600, 143–165. doi: 10.1113/JP282002

Del Rio, R., Andrade, D. C., Lucero, C., Arias, P., and Iturriaga, R. (2016). Carotid body ablation abrogates hypertension and autonomic alterations induced by intermittent hypoxia in rats. *Hypertension* 68, 436–445. doi: 10.1161/HYPERTENSIONAHA.116.07255

Dzeban, D. A., Mukhtasimova, N. F., Pavlik, L. L., and Moshkov, D. A. (2004). Ultrastructure of dosmosome-like contacts of mixed synapses of Mauthner neurons in long-term potentiation. *Neurosci. Behav. Physiol.* 34:627–632.

Eltokhi, A., Santuy, A., Merchan-Perez, A., and Sprengel, R. (2020). Glutamatergic dysfunction and synaptic ultrastructural alterations in schizophrenia and autism spectrum disorder: evidence from human and rodent studies. *Int. J. Mol. Sci.* 22:59. doi: 10.3390/ijms22010059

Epelbaum, J., Dournaud, P., Fodor, M., and Viollet, C. (1994). The neurobiology of somatostatin. *Crit. Rev. Neurobiol.* 8, 25–44.

Feldman, J. L., Del Negro, C. A., and Gray, P. A. (2013). Understanding the rhythm of breathing: so near, yet so far. *Annu. Rev. Physiol.* 75, 423–452. doi: 10.1146/annurev-physiol-040510-130049

Fischer, T. D., Hylin, M. J., Zhao, J., Moore, A. N., Waxham, M. N., and Dash, P. K. (2016). Altered mitochondrial dynamics and TBI pathophysiology. *Front. Syst. Neurosci.* 10:29. doi: 10.3389/fnsys.2016.00029

Ganeshina, O., Berry, R. W., Petralia, R. S., Nicholson, D. A., and Geinisman, Y. (2004). Differences in the expression of AMPA and NMDA receptors between axospinous perforated and nonperforated synapses are related to the configuration and size of postsynaptic densities. *J. Comp. Neurol.* 468, 86–95. doi: 10.1002/cne.10950

Garcia, A. J. III, Dashevskiy, T., Khuu, M. A., and Ramirez, J. M. (2017). Chronic intermittent hypoxia differentially impacts different states of inspiratory activity at the level of the preBötzinger complex. *Front. Physiol.* 8:571. doi: 10.3389/fphys.2017.00571

Garcia, A. J. III, Viemari, J. C., and Khuu, M. A. (2019). Respiratory rhythm generation, hypoxia, and oxidative stress-implications for development. *Respir. Physiol. Neurobiol.* 270:103259. doi: 10.1016/j.resp.2019.103259

Garcia, A. J. III, Zanella, S., Dashevskiy, T., Khan, S. A., Khuu, M. A., Prabhakar, N. R., et al. (2016). Chronic intermittent hypoxia alters local respiratory circuit function at the level of the preBötzinger complex. *Front. Neurosci.* 10:4. doi: 10.3389/fnins.2016.00004

Geinisman, Y., Morrell, F., and de Toledo-Morrell, L. (1987). Axospinous synapses with segmented postsynaptic densities: a morphologically distinct synaptic subtype contributing to the number of profiles of 'perforated' synapses visualized in random sections. *Brain Res.* 423, 179–188. doi: 10.1016/0006-8993(87)90838-9

Gonzalez-Rothi, E. J., Lee, K. Z., Dale, E. A., Reier, P. J., Mitchell, G. S., and Fuller, D. D. (2015). Intermittent hypoxia and neurorehabilitation. *J. Appl. Physiol.* 119, 1455–1465.

Gray, P. A., Hayes, J. A., Ling, G. Y., Llona, I., Tupal, S., Picardo, M. C., et al. (2010). Developmental origin of preBotzinger complex respiratory neurons. *J. Neurosci.* 30, 14883–14895.

Gray, P. A., Janczewski, W. A., Mellen, N., McCrimmon, D. R., and Feldman, J. L. (2001). Normal breathing requires preBötzinger complex neurokinin-1 receptor-expressing neurons. *Nat. Neurosci.* 4, 927–930. doi: 10.1038/nn0901-927

Guyenet, P. G., and Wang, H. (2001). Pre-Botzinger neurons with preinspiratory discharges "*in vivo*" express NK1 receptors in the rat. *J. Neurophysiol.* 86, 438–446. doi: 10.1152/jn.2001.86.1.438

Harris, K. M., Jensen, F. E., and Tsao, B. (1992). Three-dimensional structure of dendritic spines and synapses in rat hippocampus (CA1) at postnatal day 15 and adult ages: implications for the maturation of synaptic physiology and long-term potentiation. *J. Neurosci.* 12, 2685–2705. doi: 10.1523/JNEUROSCI.12-07-02685.1992

Harris, K. M., and Kater, S. B. (1994). Dendritic spines: cellular specializations imparting both stability and flexibility to synaptic function. *Annu. Rev. Neurosci.* 17, 341–371. doi: 10.1146/annurev.ne.17.030194.002013

Haverkamp, S., Grünert, U., and Wässle, H. (2000). The cone pedicle, a complex synapse in the retina. *Neuron* 27, 85–95.

Holderith, N., Lorincz, A., Katona, G., Rózsa, B., Kulik, A., Watanabe, M., et al. (2012). Release probability of hippocampal glutamatergic terminals scales with the size of the active zone. *Nat. Neurosci.* 15, 988–997.

Holler, S., Kostinger, G., Martin, K. A. C., Schuhknecht, G. F. P., and Stratford, K. J. (2021). Structure and function of a neocortical synapse. *Nature* 591, 111–116.

Johansson, O. (1978). Localization of somatostatin-like immunoreactivity in the Golgi apparatus. *Hisochemistry* 58, 167–176.

Jones, D. G., and Harris, R. J. (1995). An analysis of contemporary morphological concepts of synaptic remodelling in the CNS: perforated synapses revisited. *Rev. Neurosci.* 6, 177–219. doi: 10.1515/revneuro.1995.6.3.177

Kang, J. J., Fung, M. L., Zhang, K., Lam, C. S., Wu, S. X., Huang, X. F., et al. (2020). Chronic intermittent hypoxia alters the dendritic mitochondrial structure and activity in the pre-Botzinger complex of rats. *FASEB J.* 34, 14588–14601. doi: 10.1096/fj.201902141R

Kang, J. J., Guo, B., Liang, W. H., Lam, C. S., Wu, S. X., Huang, X. F., et al. (2019). Daily acute intermittent hypoxia induced dynamic changes in dendritic mitochondrial ultrastructure and cytochrome oxidase activity in the pre-Botzinger complex of rats. *Exp. Neurol.* 313, 124–134.

Kang, J. J., Liang, W. H., Lam, C. S., Huang, X. F., Yang, S. J., and Wong-Riley, M. T. (2017). Catecholaminergic neurons in synapticconnectionswith pre-Bötzingercomplex neuronsin therostralventrolateralmedulla innormoxic anddailyacuteintermittent hypoxicrats. *Exp. Neurol.* 287, 165–175.

Kharazia, V. N., and Weinberg, R. J. (1999). Immunogold localization of AMPA and NMDA receptors in somatic sensory cortex of albino rat. *J. Comp. Neurol.* 412, 292–302. doi: 10.1002/(sici)1096-9861(19990920)412:2<292::aid-cne8>3.0.co;2-g

Kuwana, S., Tsunekawa, N., Yanagawa, Y., Okada, Y., Kuribayashi, J., and Obata, K. (2006). Electrophysiological and morphological characteristics of GABAergic respiratory neurons in the mouse pre-Bötzinger complex. *Eur. J. Neurosci.* 23, 667–674. doi: 10.1111/j.1460-9568.2006.04591.x

Lavezzi, A. M., and Matturri, L. (2008). Functional neuroanatomy of the human pre-Bötzinger complex with particular reference to sudden unexplained perinatal and infant death. *Neuropathology* 28, 10–16. doi: 10.1111/j.1440-1789.2007.00824.x

Liu, Y. Y., Ju, G., and Wong-Riley, M. T. (2001). Distribution and colocalization of neurotransmitters and receptors in the pre-Botzinger complex of rats. *J. Appl. Physiol.* 91, 1387–1395. doi: 10.1152/jappl.2001.91.3.1387

Martinez-Sanchez, A., Laugks, U., Kochovski, Z., Papantoniou, C., Zinzula, L., Baumeister, W., et al. (2021). Trans-synaptic assemblies link synaptic vesicles and neuroreceptors. *Sci. Adv.* 7:eabe6204. doi: 10.1126/sciadv.abe6204

Mitchell, G. S., Baker, T. L., Nanda, S. A., Fuller, D. D., Zabka, A. G., Hodgeman, B. A., et al. (2001). Invited review: intermittent hypoxia and respiratory plasticity. *J. Appl. Physiol.* 90, 2466–2475.

Moshkov, D. A., Mukhtasimova, N. F., Pavlik, L. L., Tiras, N. R., and Pakhotina, I. D. (1998). *In vitro* long-term potentiation of electrotonic responses of goldfish Mauthner cells is accompanied by ultrastructural changes at afferent mixed synapses. *Neurosicence* 87, 591–605. doi: 10.1016/s0306-4522(98)00121-3

Nakajima, Y. (1974). Fine structure of the synaptic endings on the Mauthner cell of the goldfish. *J. Comp. Neurol.* 156, 375–402.

Paffenholz, R., Kuhn, C., Grund, C., Stehr, S., and Franke, W. W. (1999). The arm-repeat protein NPRAP (Neurojungin) is a constituent of the plaques of the outer limiting zone in the retina, defining a novel type of adhering junction. *Exp. Cell Res.* 250, 452–464. doi: 10.1006/excr.1999.4534

Peters, A., and Kaiserman-Abramof, I. R. (1969). The small pyramidal neuron of the rat cerebral cortex. The synapses upon dendritic spines. *Z. Zellforsch.* 100, 487–506.

Peters, A., and Kaiserman-Abramof, I. R. (1970). The small pyramidal neuron of the rat cerebral cortex. The perikaryon, dendrites and spines. *Am. J. Anat.* 127, 321–355.

Peters, A., Palay, S. L., and Webster, D. E. F. H. (1991). *The fine structure of the nervous system: Neurons and their supporting cells*, 3rd Edn. Oxford: Oxford University Press, 138–199.

Pinho, J., Marcut, C., and Fonseca, R. (2020). Actin remodeling, the synaptic tag and the maintenance of synaptic plasticity. *IUBMB Life* 72, 577–589. doi: 10.1002/iub.2261

Ramírez-Jarquín, J. O., Lara-Hernández, S., López-Guerrero, J. J., Aguileta, M. A., Rivera-Angulo, A. J., Sampieri, A., et al. (2012). Somatostatin modulates generation of inspiratory rhythms and determines asphyxia survival. *Peptides* 34, 360–372. doi: 10.1016/j.peptides.2012.02.011

Ravasenga, T., Ruben, M., Regio, V., Polenghi, A., Petrini, E. M., and Barberis, A. (2022). Spatial regulation of coordinated excitatory and inhibitory synaptic plasticity at dendritic synapses. *Cell Rep.* 38:110347.

Schwarzacher, S. W., Rüb, U., and Deller, T. (2011). Neuroanatomical characteristics of the human pre-Bötzinger complex and its involvement in neurodegenerative brainstem diseases. *Brain* 134, 24–35. doi: 10.1093/brain/awq327

Seager, R., Lee, L., Henley, J. M., and Wilkinson, K. A. (2020). Mechanisms and roles of mitochondrial localisation and dynamics in neuronal function. *Neuronal Signal* 4:Ns20200008.

Semenza, G. L., and Prabhakar, N. R. (2015). Neural regulation of hypoxia-inducible factors and redox state drives the pathogenesis of hypertension in a rodent model of sleep apnea. *J. Appl. Physiol.* 119, 1152–1156. doi: 10.1152/japplphysiol.00162.2015

Smith, J. C., Ellenberger, H. H., Ballanyi, K., Richter, D. W., and Feldman, J. L. (1991). Pre-Bötzinger complex: a brainstem region that may generate respiratory rhythm in mammals. *Science* 254, 726–729. doi: 10.1126/science.1683005

Spruston, N. (2008). Neuroscience: strength in numbers. *Nature* 452, 420–421.

Stewart, M. G., Medvedev, N. I., Popov, V. I., Schoepfer, R., Davies, H. A., Murphy, K., et al. (2005). Chemically induced long-term potentiation increases the number of perforated and complex postsynaptic densities but does not alter dendritic spine volume in CA1 of adult mouse hippocampal slices. *Eur. J. Neurosci.* 21, 3368–3378. doi: 10.1111/j.1460-9568.2005.04174.x

Stornetta, R. L., Rosin, D. L., Wang, H., Sevigny, C. P., Weston, M. C., and Guyenet, P. G. (2003). A group of glutamatergic interneurons expressing high levels of both neurokinin-1 receptors and somatostatin identifies the region of the pre-Bötzinger complex. *J. Comp. Neurol.* 455, 499–512. doi: 10.1002/cne.10504

Sutton, M. A., Ito, H. T., Cressy, P., Kempf, C., Woo, J. C., and Schuman, E. M. (2006). Miniature neurotransmission stabilizes synaptic function via tonic suppression of local dendritic protein synthesis. *Cell* 125, 785–799. doi: 10.1016/j.cell.2006.03.040

Tang, A. H., Chen, H., Li, T. P., Metzbower, S. R., MacGillavry, H. D., and Blanpied, T. A. (2016). A trans-synaptic nanocolumn aligns neurotransmitter release to receptors. *Nature* 536, 210–214.

Tarusawa, E., Matsui, K., Budisantoso, T., Molnár, E., Watanabe, M., Matsui, M., et al. (2009). Input-specific intrasynaptic arrangements of ionotropic glutamate receptors and their impact on postsynaptic responses. *J. Neurosci.* 29, 12896–12908. doi: 10.1523/JNEUROSCI.6160-08.2009

Toni, N., Buchs, P. A., Nikonenko, I., Povilaitite, P., Parisi, L., and Muller, D. (2001). Remodeling of synaptic membranes after induction of long-term potentiation. *J. Neurosci.* 21, 6245–6251. doi: 10.1523/JNEUROSCI.21-16-06245.2001

Villa, K. L., Berry, K. P., Subramanian, J., Cha, J. W., Oh, W. C., Kwon, H. B., et al. (2016). Inhibitory synapses are repeatedly assembled and removed at persistent sites *in vivo*. *Neuron* 89, 756–769.

Vose, A. K., Welch, J. F., Nair, J., Dale, E. A., Fox, E. J., Muir, G. D., et al. (2022). Therapeutic acute intermittent hypoxia: a translational roadmap for spinal cord injury and neuromuscular disease. *Exp. Neurol.* 347:113891. doi: 10.1016/j.expneurol.2021.113891

Wallén-Mackenzie, A., Gezelius, H., Thoby-Brisson, M., Nygård, A., Enjin, A., Fujiyama, F., et al. (2006). Vesicular glutamate transporter 2 is required for central respiratory rhythm generation but not for locomotor central pattern generation. *J. Neurosci.* 26, 12294–12307. doi: 10.1523/JNEUROSCI.3855-06.2006

Wei, X. Y., Zhao, Y., Wong-Riley, M. T., Ju, G., and Liu, Y. Y. (2012). Synaptic relationship between somatostatin- and neurokinin-1 receptor-immunoreactive neurons in the pre-Bötzinger complex of rats. *J. Neurochem.* 122, 923–933. doi: 10.1111/j.1471-4159.2012.07862.x

Winter, S. M., Fresemann, J., Schnell, C., Oku, Y., Hirrlinger, J., and Hülsmann, S. (2009). Glycinergic interneurons are functionally integrated into the inspiratory network of mouse medullary slices. *Pflugers Arch.* 458, 459–469. doi: 10.1007/s00424-009-0647-1

Wong-Riley, M. T., Tripathi, S. C., Trusk, T. C., and Hoppe, D. A. (1989). Effect of retinal impulse blockage on cytochrome oxidase-rich zones in the macaque striate cortex: i. Quantitative electron-microscopic (EM) analysis of neurons. *Vis. Neurosci.* 2, 483–497.

Wong-Riley, M. T. T. (1989). Cytochrome oxidase: an endogenous metabolic marker for neuronal activity. *Trends Neurosci.* 12, 94–101.

frontiers | Frontiers in Cellular Neuroscience

TYPE Original Research
PUBLISHED 13 July 2023
DOI 10.3389/fncel.2023.1153970

OPEN ACCESS

EDITED BY
Jacopo Lamanna,
Vita-Salute San Raffaele University, Italy

REVIEWED BY
Guanxiao Qi,
Helmholtz Association of German Research Centers (HZ), Germany
Nobuyoshi Matsumoto,
The University of Tokyo, Japan

*CORRESPONDENCE
Joon Ho Choi
✉ joonchoi@kbri.re.kr

RECEIVED 30 January 2023
ACCEPTED 27 June 2023
PUBLISHED 13 July 2023

CITATION
Yoo M, Yang Y-S, Rah J-C and Choi JH (2023) Different resting membrane potentials in posterior parietal cortex and prefrontal cortex in the view of recurrent synaptic strengths and neural network dynamics. *Front. Cell. Neurosci.* 17:1153970. doi: 10.3389/fncel.2023.1153970

Different resting membrane potentials in posterior parietal cortex and prefrontal cortex in the view of recurrent synaptic strengths and neural network dynamics

Minsu Yoo[1], Yoon-Sil Yang[1], Jong-Cheol Rah[1,2] and Joon Ho Choi[1]*

[1]Korea Brain Research Institute, Daegu, Republic of Korea, [2]Daegu Gyeongbuk Institute of Science and Technology, Daegu, Republic of Korea

In this study, we introduce the importance of elevated membrane potentials (MPs) in the prefrontal cortex (PFC) compared to that in the posterior parietal cortex (PPC), based on new observations of different MP levels in these areas. Through experimental data and spiking neural network modeling, we investigated a possible mechanism of the elevated membrane potential in the PFC and how these physiological differences affect neural network dynamics and cognitive functions in the PPC and PFC. Our findings indicate that NMDA receptors may be a main contributor to the elevated MP in the PFC region and highlight the potential of using a modeling toolkit to investigate the means by which changes in synaptic properties can affect neural dynamics and potentiate desirable cognitive functions through population activities in the corresponding brain regions.

KEYWORDS

membrane potential, PFC, PPC, working-memory, network dynamics

1. Introduction

Both the prefrontal cortex (PFC) and posterior parietal cortex (PPC) are critically involved in working memory and decision-making, but their network dynamics differ significantly. For example, in a decision-making task, the PPC encodes evidence with gradually increasing population firing rates, while neurons in the PFC represent them in a categorical manner, showing relatively more abrupt increases in firing rates than the PPC (Hanks et al., 2015). These distinctions in neural network dynamics may give rise to advantageous cognitive functions that compensate for each other in a multiregional manner by forming feedback and feedforward connections between the PFC and PPC (Murray et al., 2017). According to that theoretical study, the relatively gradual increase in the population firing rate in PPC enables the neural network to have less error rate in making decisions, but it is easier to be distracted by another type of choice during the working memory duration. However, the neural activities in the PFC tend to be more rigorous against distractors. These tendencies have been observed in several animal studies (di Pellegrino and Wise, 1993; Constantinidis and Steinmetz, 1996; Qi et al., 2010). Moreover, the main cause of this difference is purportedly the more strongly connected recurrent synapses in the PFC than in the PPC (Murray et al., 2017).

In our experiment, resting membrane potentials (RMPs) in the PFC were significantly higher (∼10 mV) than those in the PPC. Although the study by Murray et al. (2017) showed that recurrent synaptic structures are the main cause of the distinctive neuronal dynamics, the rate-model used in the study is not capable of applying the different levels of RMPs that we observed in our experiment. Therefore, in this study, we used a spiking neural network introduced in a previous study to investigate how different membrane potential levels affect the neural network dynamics of the PPC and PFC, eliciting cognitive functions in these areas (Wang, 2002). One of the most important features of the spiking neural network (SNN) model is that it considers three major synaptic inputs with different time scales to neurons in the network. This helps us understand the type of synaptic inputs that contribute the most to lifted RMPs.

In addition, we compared the effectiveness of the two parameters, recurrent synaptic strength and RMPs. Our results indicate that RMPs are necessary to be elevated for neural networks to behave more uniquely for the necessary cognitive functions: slow ramping up in the PPC and faster in the PFC. Finally, we suggest another possible factor for the lifted RMPs based on the fact that the PFC has stronger recurrent synapses. Neurons in the neural network continue firing, and the recorded neurons may have continuous random inputs from other neurons in the network. By simulating this situation, we show that NMDA synaptic inputs varied by different recurrent synaptic strengths, which may be the main cause for the different membrane potential levels in the PPC and PFC areas.

2. Materials and methods

2.1. Animals

All animal experiments were conducted with approval from the Animal Experiment Ethics Committee (approval no. IACUC-20-00007) of the Korea Brain Research Institute (KBRI). All experiments were performed using male C57BL/6N mice.

2.2. Brain slice preparation

Brain slices were obtained from 7 to 9-week-old male C57BL/6N mice. Animal care and treatment protocols were approved by the Animal Care and Use Committee of the KBRI. After decapitating the mice, their brains were quickly removed and placed in an ice-cold cutting solution of the following composition (in mM): choline chloride, 110; KCl, 2.5; $NaHCO_3$, 25; NaH_2PO_4, 1.25; glucose, 25; $CaCl_2$, 0.5; $MgCl_2 \cdot 6H_2O$, 7; sodium ascorbic acid, 11.6; and pyruvic acid, 3. Coronal slices (300 μm) were prepared using a vibratome (VT1200S, Leica, Wetzlar, Germany) and were incubated at 32°C for at least 30 min. During the preparation of acute slices, the solution was oxygenated with 95% O_2 and 5% CO_2.

2.3. Electrophysiological recordings

Acute slices of the PPC (−2.0 mm AP, ± 1.5 mm ML from bregma, −0.5 mm DV from the brain surface) and PFC (+1.0 mm AP, ± 0.5 mm ML from bregma, −0.5 mm DV from the brain surface) of mice were placed in a recording chamber filled with a continuous flow of carbogen-saturated (95% O_2, 5% CO_2) aCSF containing the following (in mM): 119 NaCl, 2.5 KCl, 26 $NaHCO_3$, 1.25 NaH2PO4, 20 glucose, 2 $CaCl_2$, 1 $MgSO_4$, 0.4 ascorbic acid, and 2 pyruvic acid for whole-cell patch-clamp recordings. L5 pyramidal neurons of the slices were visualized using infrared differential interference contrast (IR-DIC) microscopy with a BX51WI upright microscope (Olympus, Japan) and a water-immersed 40 objective lens (numerical aperture 0.8). Patch electrodes with 3–5 $M\Omega$ tip resistances were prepared using a pipette puller (Shutter Instrument, USA) and filled with an internal solution containing (in mM) 20 KCl, 125 K-gluconate, 10 HEPES, 4 NaCl, 0.5 EGTA, 4 ATP, 0.3 TrisGTP, and 10 phosphocreatine (pH 7.2, ∼290–300 mOsm). None of the patched neurons showed spontaneous action potentials, and RMPs were determined by averaging a 100 *ms* recording period at 0 pA in current clamp mode. The initial 100 *ms* of recording data were acquired prior to the application of current clamping in the experiment, allowing us to measure the resting membrane potential before introducing any artificial current through whole cell recording techniques. In order to differentiate between pyramidal cells and interneuron cells, we employed two key criteria: their responses to current injection and the shapes of their action potentials. Notably, when current was injected, the fast-spiking neurons (interneurons) exhibited a greater frequency of firing action potentials compared to the regular-spiking neurons (pyramidal neurons). Additionally, the two types of neurons displayed discernible differences in the shapes of their action potentials. Each type possessed a characteristic waveform pattern that set them apart. The fast-spiking interneurons displayed action potentials with shorter durations and sharper peaks, while the regular-spiking pyramidal neurons exhibited action potentials with longer durations and more gradual peaks, indicative of their role in sustained neuronal activity and the coordination of complex neural processes.

2.4. Data analysis and statistics

Data collection and analysis were performed using Clampfit 10.4 (Axon Instruments, Foster City, CA) and AxoGraph X (AxoGraph, Canberra, Australia). Additional data analysis was performed using MATLAB (Mathworks, Natick, MA, USA) or MS Excel (Microsoft, Redmond, WA) to determine statistical significance. The differences in RMP levels were tested using a *t*-test, and the results were considered significant for *p*-values less than 0.05. *P*-values less than 0.01 or 0.001 were indicated on data plots. Error bars in all figures indicate standard errors unless otherwise noted.

2.5. Cortical network model

In this study, we employed a recurrent network model, as previously described. For further information, please refer to the original manuscript (Wang, 2002). The neural network simulation code is also publicly accessible, as reported by Gerstner et al. (2014). Here is a brief overview of the model we used.

The model was introduced by Wang (2002) was devised by Amit and Brunel (1997) and Wang (1999), which represents a local

circuit in the posterior parietal and prefrontal cortices (Amit and Brunel, 1997; Wang, 1999). It has N neurons, 80% of which are pyramidal cells and 20% are interneurons (Braitenberg and Schüz, 1998). To mimic physiological measurements, in which a group of cells responds to a preferred stimulus while the rest are indifferent, each stimulus activates a small and distinct subpopulation of $f\ N_E$ excitatory cells ($f\ =\ 0.15$). The remaining $(1\ -\ 2f)\ N_E$ neurons did not respond to either of the stimuli. The network encodes only two directions of stimuli (left or right) and uses a small subpopulation of neurons to respond to each stimulus. Simulations were performed with $N_E\ =\ 384$ and $N_I\ =\ 96$.

2.5.1. Neurons

Specific properties of neurons can be defined in the model so that distinctive properties of neurons, such as RMPs and membrane capacitance, found in experiments, can be applied to study how they can affect neural activities differently under identical given conditions.

Both pyramidal cells and interneurons in the model are represented as leaky integrate-and-fire neurons (Tuckwell, 1988). They are characterized by a resting potential of $V_L\ =\ -70\ mV$, a firing threshold of $V_{th}\ =\ -50\ mV$, a reset potential of $V_{reset}\ =\ -60\ mV$, a membrane capacitance of $C_m\ =\ 0.5\ nF$ for pyramidal cells and $C_m\ =\ 0.2\ nF$ for interneurons, a membrane leak conductance of $g_L\ =\ 25\ nS$ for pyramidal cells and 20 nS for interneurons, and a refractory period of $\tau_{ref}\ =\ 2\ ms$ for pyramidal cells and 1 ms for interneurons. The corresponding membrane time constants were $\tau_{ref}\ =\ \frac{C_m}{g_L}\ =\ 20\ ms$ for excitatory cells and 10 ms for interneurons, as reported by McCormick et al. (1985). When the membrane potential of a cell is below the threshold, the membrane potential $V(t)$,

$$C_m \frac{dV(t)}{dt}\ =\ -g_L\left(V\left(t\right)-\ V_L\right)-\ I_{syn}\left(t\right),$$

The rate of membrane potential change differs based on the difference between the current $V(t)$ and V_L to which the potential naturally returns when there are no synaptic inputs. The total current flowing into the cell owing to all synapses is represented as $I_{syn}\left(t\right)$.

2.5.2. Synapses

The network comprises connections between pyramidal cells and interneurons (**Figure 2A**), which receive recurrent EPSCs via AMPA and NMDA receptors. It receives inputs from two sources: right and left and background noise. NMDA receptors receive inputs only from the local network, whereas AMPA receptors receive external inputs.

$$I_{syn}\left(t\right)\ =\ I_{ext,\ AMPA}\left(t\right)\ +\ I_{rec,\ AMPA}\left(t\right)\ +\ I_{rec,\ NMDA}\left(t\right)\ +\ I_{rec,\ GABA}\left(t\right)$$

where

$$I_{ext,AMPA}\left(t\right)\ =\ g_{ext,\ AMPA}\left(V\left(t\right)-\ V_E\right)\ s^{ext,AMPA}(t)$$

$$I_{rec,AMPA}\left(t\right)\ =\ g_{ext,\ AMPA}\left(V\left(t\right)-\ V_E\right)\sum_{j=1}^{C_1} w_j s_j^{AMPA}(t)$$

$$I_{rec,NMDA}\left(t\right)\ =\ \frac{g_{NMDA}\left(V\left(t\right)-\ V_E\right)}{\left(1+[Mg^{2+}]\exp\left(-\frac{0.062V(t)}{3.57}\right)\right.}\sum_{j=1}^{C_E} w_j s_j^{NMDA}(t)$$

$$I_{rec,GABA}\left(t\right)\ =\ g_{GABA}\left(V\left(t\right)-\ V_I\right)\sum_{j=1}^{C_1} s_j^{GABA}(t)$$

The V_E and V_I represent the membrane potentials (MPs), with $V_E\ =\ 0\ mV$ and $V_I\ =\ -70\ mV$. The dimensionless weight w_j represents the structured excitatory recurrent connections. The sum over j represents the sum of all synapses connected to the presynaptic neuron j in the local network. In this model, the NMDA currents were dependent on the extracellular magnesium concentration, $\left[Mg^{2+}\right]\ =\ 11\ mM$.

The timescales of the different synaptic inputs are described as follows. The variables that control the opening and closing of channels—known as gating variables (s)—are described as follows: The AMPA channels, both external and recurrent, are described by

$$\frac{ds_j^{AMPA}(t)}{dt}\ =\ -\frac{s_j^{AMPA}(t)}{\tau_{AMPA}}+\sum_k \delta(t-t_j^k)$$

The time required for AMPA currents to decrease is represented as $\tau_{AMPA}\ =\ 2\ ms$ (Hestrin et al., 1990; Spruston et al., 1995). The sum of k represents the sum of spikes emitted by presynaptic neuron j. In the case of external AMPA currents, the spikes are emitted according to a Poisson process with a rate of $\vartheta_{ext}\ =\ 2.4$ kHz independently for each cell. NMDA channels are described by

$$\frac{ds_j^{NMDA}(t)}{dt}\ =\ -\frac{s_j^{NMDA}\left(t\right)}{\tau_{NMDA,decay}}+\alpha x_j\left(t\right)\ \left(1-s_j^{NMDA}\left(t\right)\right)$$

$$\frac{dx_j(t)}{dt}\ =\ -\frac{x_j(t)}{\tau_{NMDA,rise}}+\sum_k \delta(t-t_j^k)$$

where the decay time of the NMDA currents is set to $\tau_{NMDA,decay}\ =\ 100\ ms$, the rise time constant is set to $\tau_{NMDA,rise}\ =\ 2\ ms$ and the amplitude of the NMDA current is set to $\alpha\ =\ 0.5\ ms^{-1}$. The equation governing the GABA synaptic variable can be expressed as follows

$$\frac{ds_j^{GABA}(t)}{dt}\ =\ -\frac{s_j^{GABA}(t)}{\tau_{GABA}}+\sum_k \delta(t-t_j^k)$$

The decay time constant of GABA currents is represented as $\tau_{\mathrm{GABA}}\ =\ 5$ ms (Salin and Prince, 1996; Xiang et al., 1998). All synapses had a latency of 5 ms. In the $N\ =\ 480$ neuron network, the following values were used for the recurrent synaptic conductance (in nS): for pyramidal cells, $g_{\mathrm{ext,AMPA}}\ =\ 2.1$, $g_{\mathrm{rec,AMPA}}\ =\ 0.5$, $g_{\mathrm{NMDA}}\ =\ 0.165$, and $g_{\mathrm{GABA}}\ =\ 1.3$; for interneurons, $g_{\mathrm{ext,AMPA}}\ =\ 1.62$, $g_{\mathrm{rec,AMPA}}\ =\ 0.04$, $g_{\mathrm{NMDA}}\ =\ 0.13$ and $g_{\mathrm{GABA}}\ =\ 1.0$. These synaptic conductances are roughly similar to those measured in experiments (Destexhe et al., 1998). Three features are noteworthy: First, recurrent excitation is mostly mediated by NMDA receptors (Wang, 1999, 2001); second, the network is overall dominated by recurrent inhibition (Amit and Brunel, 1997; Brunel and Wang, 2001); third, neurons receive a large amount of stochastic background inputs.

2.5.3. Structure of recurrent excitatory connections between pyramidal cells

Every neuron receives inputs from all the other neurons, but the strength of these connections is organized in a specific manner. Because of the Hebbian rule, which states that neurons that fire together frequently are more likely to have stronger connections than other neurons, groups of neurons that respond to similar external sensory inputs are likely to have "potentiated" synapses. Therefore, we set the strength of the neurons in the same group as $w_j = w_+ > 1$ compared to the baseline with a synaptic strength of $w_j = 1$. These neurons tend to be involved in the making of similar decisions. Unless otherwise stated, we used $w_+ = 1.9$. We varied the value of w_+ to study the effects of recurrent synaptic strength. The strength of synaptic "depression" between two selective populations, and from a nonselective population to a selective one, is represented by a value of w_-, which is less than 1. By contrast, the connections between other populations have a value of w_j equal to 1. In the model, the overall recurrent excitatory synaptic drive in the spontaneous state remains constant as w_+ is varied (Amit and Brunel, 1997) by setting

$$w_- = 1 - \frac{f(w_+ - 1)}{(1 - f)}$$

Additionally, synaptic efficacy remained fixed throughout the simulation, assuming that the overall influence of recurrent excitatory synapses during spontaneous activity remained unchanged when the value of w_+ was altered (Amit and Brunel, 1997). The strengths of the synapses were maintained constant throughout the simulation. The population firing rates r_A and r_B were calculated by counting the total number of spikes in each of the two neural groups during a time window of 20 *ms*. The spike count was then divided by the number of neurons and the length of the time window.

2.5.4. Simulations

Computer-based simulations were performed on a MacBook Pro workstation, utilizing a customized version of the RK2 method [as described in Hansel et al. (1998) and Shelley and Tao (2001)] for the numerical calculation of the equations that govern the behavior of all cells and synapses. The time increment used in the integration process was set as 0.02 *ms*. The computer simulation was conducted using Python code, which is freely available online[1] (Wong and Wang, 2006; Gerstner et al., 2014).

3. Results

The resting membrane potential (RMP) levels in the brain are influenced not only by the behavioral state of the animal, but also by the specific layer within a cortical column (Crochet and Petersen, 2006; Crochet et al., 2011; Poulet et al., 2012; Eggermann et al., 2014). To investigate the possibility of these differences in RMPs in areas related to cognitive tasks, we performed whole-cell recording in the area of prefrontal cortex (n = 13, 1.0 AP, ±0.5 ML from bregma, −0.5 DV from the brain surface) and posterior parietal cortical area (n = 19, −2.0 AP, ±1.5 ML from bregma, −0.5 DV from the brain surface) in mice. We measured the MPs of neurons in these areas. In the present study, the levels of membrane potential of PFC were generally 10 mV higher than those of PPC (PPC = 84.29 ± 1.52 mV, PFC = 76.12 ± 0.89 mV, $p = 0.001$) (**Figure 1**). Except the whole cell capacitance our experimental findings revealed notable distinctions between the cells of prefrontal cortex (PFC) neurons and posterior parietal cortex (PPC) neurons. While both regions displayed similar values of the whole cell capacitance, with PPC neurons at 39.61 ± 3.23 pF and PFC neurons at 40.05 ± 2.96 pF, the rheobase values for PFC neurons were lower compared to those of PPC neurons (115.625 ± 16.90 pA and 213.15 ± 13.70 pA, respectively). Also, the voltage changes required to trigger action potentials were also markedly different between the two regions (47.85 ± 1.75 mV for PPC and 36.87 ± 1.83 mV for PFC), and input resistance was found to be higher in PFC neurons (97.92 ± 6.47 MΩ) compared to PPC neurons (72.53 ± 3.96 MΩ).

We used a SNN introduced in the decision-making process (Wang, 2002). The most distinctive characteristic of this model is that we can introduce synaptic transmission dynamics into the model and monitor their behavior during the decision-making process. This model successfully describes and mimics single-cell neural activities during cognitive tasks related to working and decision making (Goldman-Rakic, 1995; Shadlen and Newsome, 1996). This model assumes two types of sensory information (external inputs to the network). Once a specific type of information for decision-making reaches a specific group of related population in the neural network, neurons in the group starts increasing their firing rates while exciting the neurons in the same group through recurrent synaptic connections among neurons in the group. This leads to the winner-take-all phenomenon (Wang, 2002), in which a group of neurons related to a type of choice keeps increasing their firing rates, while the other group of pyramidal neurons for the other alternative choice suppresses activities through a group of inhibitory neurons that are connected to both groups of pyramidal neurons (**Figure 2**). A theoretical study reported that the most distinct difference between the PPC and PFC is recurrent synaptic structure (Murray et al., 2017). This difference in the level of connections of recurrent structure that connect neurons in the same group for a type of decision was solely able to explain the specific neuronal network dynamics shown in the experimental studies. They were able to show that stronger recurrent structure causes a faster increase in the population firing rate of a neural network, indicating that the population firing rate of the neural network in the PFC with higher recurrent synaptic strengths increases faster than that in the PPC, which possesses lower synaptic strengths among neurons with the same type of preferred decision cues.

As suggested by Murray et al. (2017), a neural network with stronger recurrent synapses showed faster ramping up of population dynamics (**Figure 3**). When w_+ is lower than 1.7, the neural network was not able to hold persistent activities, which is an essential feature for the PPC or PFC for required cognitive functions, such as working memory. Therefore, we set a range of values for w_+ for the analysis in this study from 1.7 to 2.2 (**Supplementary Figure 1**). The value of 2.2 is the limit at which the network shows the highest reasonable population firing rate, as shown in the experimental data. In previous experiments, firing

1 https://github.com/EPFL-LCN/neuronaldynamics-exercises

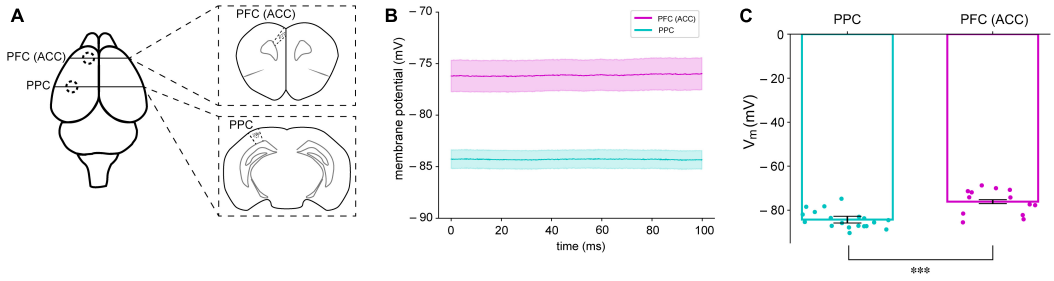

FIGURE 1
Different membrane potentials (MPs) in the PFC and PPC of mice. **(A)** The PFC and PPC regions where brain slices were obtained for whole-cell recording **(B)** Averaged resting membrane potentials (RMPs) of neurons in the PFC (magenta) and PPC (cyan) in mice. The shaded areas indicate standard error of mean (SEM) **(C)** Summary of RMPs in PPC (n = 19) and PFC (n = 13). ***$P < 0.05$.

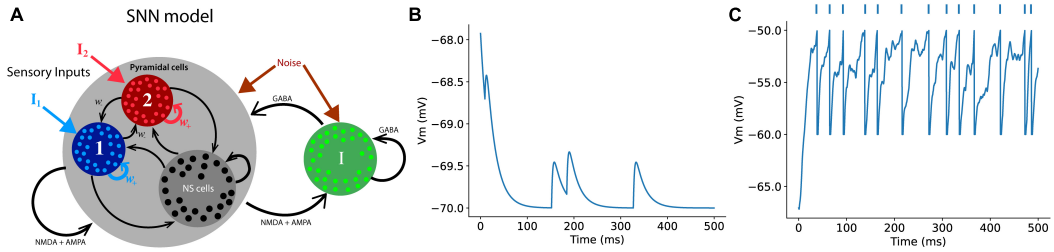

FIGURE 2
Schematics of a spiking neural network (SNN) **(A)** The SNN model in this study contains a total of 384 excitatory (pyramidal cells) and 96 inhibitory neurons. Each group of a chosen type comprises 96 neurons that specifically responds either right or left external sensory inputs, and the rest of excitatory neurons are non-specific (NS cells) that have no preferred choice type. Each neuron in the model receives three types of synaptic inputs (AMPA, GABA, and NMDA) **(B)** An example of the RMPs of a neuron that receives AMPA inputs from presynaptic neurons in the network. **(C)** When the post-synaptic neurons receive enough number of synaptic inputs, the neuron discharges an action potential, the RMP returns to the reset voltage set in the model (−60 mV in this case). The dots on the top of the plot represent spike events.

rates generally did not exceed 100 spikes/s (Shadlen and Newsome, 1996, 2001; Roitman and Shadlen, 2002).

Because we found distinctively different levels of base membrane potential, we applied the values found in our experiment to the neural network model for the decision-making process (**Figures 4A, B**). We chose the RMP as a primary variable for our modeling parameters because it exhibited both significant differences between the PPC and PFC and offered a straightforward interpretation while monitoring the modeling results. To our surprise, altering the RMP had a notable impact on the behaviors of the neural network. The neural network with a lower base membrane potential showed longer durations of ramping than the network with a higher base membrane potential (**Figures 4C, D**). This finding emphasizes the influential role of RMP in shaping the dynamics and functioning of the modeled neural system.

We subsequently investigated how reaction time is affected by either recurrent synaptic strength or RMPs levels (**Figure 5A**). As we studied in **Figure 3**, the reasonable range of synaptic strength from w_+ = 1.7–2.2, since persistent activities during the delay period start appearing when the recurrent structure value is set to w_+ = 1.7. At w_+ = 2.2, the firing rate of the population was close to 100 spikes/s. A firing rate of 100 spikes/s is considered biologically feasible. The difference between the reaction time resulted from the neural networks with the values of w_+ = 1.7 and w_+ = 2.2 (40 *ms*) is less significant than the difference in the reactions times of the neural networks with different resting membrane potential levels between RMP = 77.5 *mV* and 71.5 *mV* (180 *ms*) with the same recurrent synaptic strengths w_+ = 1.8 (**Figures 5B, C**). Therefore, we can conclude that for neural networks to have more distinctive functions through neural network dynamics, such as more PPC-like or PFC-like functions, the differences in the membrane potential can be critical.

To track the mechanism of higher membrane potential values, we built a single neuron model with various types of synaptic inputs to a single cell (**Figure 6A**). As a neuron in a noisy neural network constantly receives synaptic inputs from other neurons in the network, the single neuron in this model receives 1,000 excitatory and 250 inhibitory synaptic inputs that fire randomly following the Poisson process with a mean firing rate of 10 Hz. In this model, the mean frequency and strength of the NMDA synaptic inputs were fixed remained constant while the time constants of the synaptic transmission were varied to examine the impact of slow NMDA inputs to the MPs of the single neuron. This single neuron exhibits three types of synaptic transmission: AMPA, GABA, and NMDA, with different synaptic time scales. Previous studies have reported that slow synaptic transmission in the PPC and PFC areas is an essential factor that induces persistent working memory (Tsukada et al., 2005). It has also been suggested that NMDA receptor be the main source of this slow synaptic current to neurons in the PPC and PFC (Wang, 1999, 2002). Hence, we built a single neuron model to control the amount of NMDA synaptic inputs to the neuron by changing the synaptic strengths

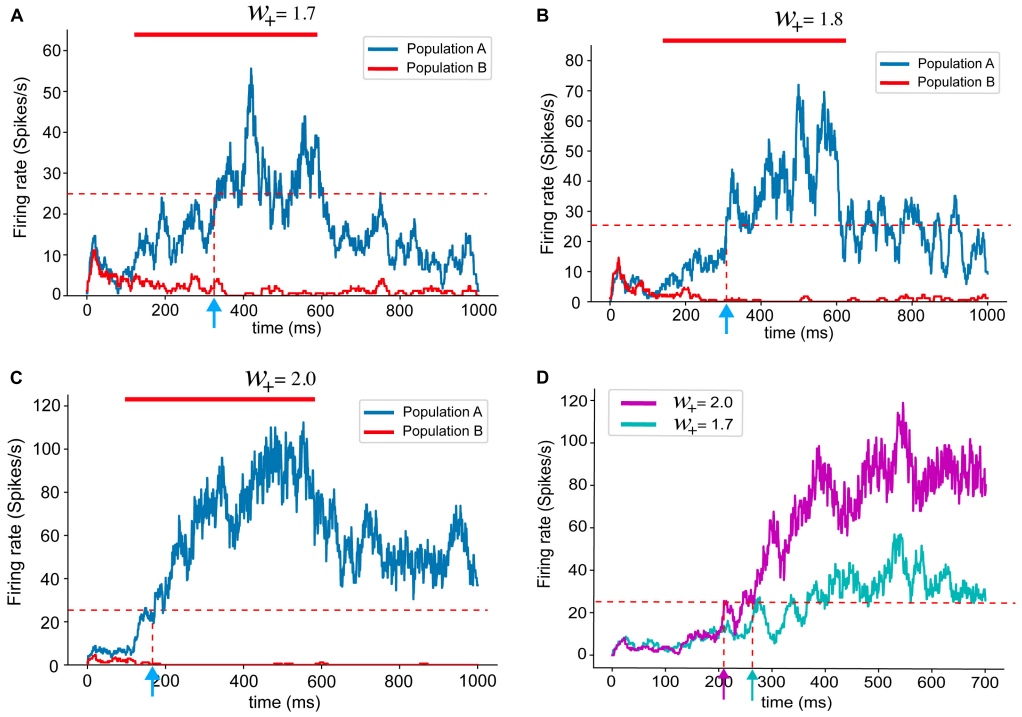

FIGURE 3
Population firing rates with different recurrent synaptic strengths **(A–C)**. The red bar marks stimulus presentation. As introduced in the previous study (Murray et al., 2017), the population firing rates obtained from spiking neural network models shows shorter reaction times with stronger recurrent synaptic connections. **(D)** Overlapped population firing rates of networks with w_+ 2.0 (magenta) and w_+ = 1.7 (cyan). Stronger recurrent synaptic connections yield higher population firing rate and shorter reaction time.

of the NMDA inputs. One of the most distinctive characteristics of synaptic transmission mediated by NMDA receptors is summations and saturation (Hestrin et al., 1990). The single-cell model shows that NMDAR-mediated EPSCs with a longer time scale saturate once a sufficient number of incoming presynaptic spikes arrive (**Figure 6B**). **Figures 6B, C** show the lifted RMPs with a higher NMDA input to the post-synaptic neuron. In **Figure 6C**, the time constant of NMDAR-mediated EPSCs was shortened from 100 *ms* (magenta and cyan) to 2 *ms* (red and blue). RMP levels significantly differ according to recurrent synaptic strength at 100 *ms* of the time constant of NMDAR-mediated EPSCs. The difference in the levels of RMPs, however, with 2 *ms* of the time scale of incoming EPSCs (no NMDAR-mediated EPSCs) was visibly reduced. It appears that an increase in the strength of recurrent synaptic inputs does not lead to a membrane potential increase if the synaptic time constant is short (e.g., 2 *ms*, as in the case of AMPA). These findings suggest that the slow synaptic input current, likely mediated by NMDA receptors and characterized by a longer synaptic time constant of approximately 100 *ms*, is the primary factor responsible for the increase in RMPs. Taken together, the modeling results reveal a highly possible mechanism of higher membrane potential levels in a higher cortical area, the PFC.

4. Discussion

In this study, we introduced the importance of elevated RMPs based on new observations of different levels of RMPs in the PFC and PPC. From our experimental data of whole-cell recording, we tracked a possible mechanism for the lifted membrane potential in the PFC. To our knowledge, this is the first study to report that membrane potential levels are generally different in the areas of PPC and PFC. These two areas have been studied with respect to decision-making and working memory, and the mechanistic processes at the circuit level have also been widely studied. Based on this knowledge, we investigated how these physiological differences affect the neural network dynamics that elicit the cognitive functions generated in these two areas.

We showed that the different levels of MPs of neurons in the network can affect neuronal network dynamics, eliciting desired cognitive functions (slow and fast ramping up dynamics) in the PPC and PFC, respectively. When the MP levels were set to the value that we found in our whole-cell recording experiment, the network showed similar population firing patterns in the PPC and PFC, as shown in *in vivo* experiments (Hanks et al., 2015). Our study is an example of using experimental data, theoretical background knowledge, and simulation results acquired from a neural network model to investigate the reasons for physiological phenomena and how these phenomena affect neural activities at the network level. A theoretical study has suggested that distinct recurrent synaptic structures in the neural networks of the PPC and PFC give rise to unique population dynamics that are essential for specific cognitive behaviors (Murray et al., 2017). Since the previous study used a population firing rate-based model, there were limitations in monitoring single-cell properties in the population that can be altered by synaptic strengths,

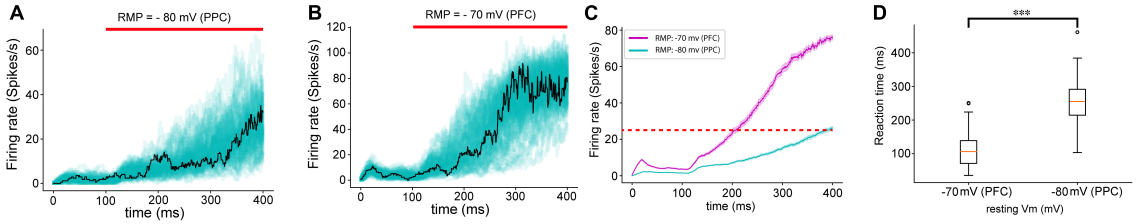

FIGURE 4
Neural network dynamics (reaction time) changed by different levels of MPs. **(A)** Overlapped population firing rates of 100 trials with the RMPs found in PPC (−80 mV) and **(B)** in PFC (−70 mV). The red bar indicates external sensory input stimulation applied. The solid black line represents the population firing rate with a median reaction time value. **(C)** Averaged population rate (solid lines) of 100 trials with SEM in shaded area. **(D)** Boxplot of reaction time during which the population firing rate of the neural network reaches 25 Hz from the stimulation onset. The population firing patterns of the neural networks with lower (PPC) and higher (PFC) MPs set with values found in our experiment resemble the firing patterns revealed by the experiment data and the results introduced in a previous study (Murray et al., 2017). ***$P < 0.05$.

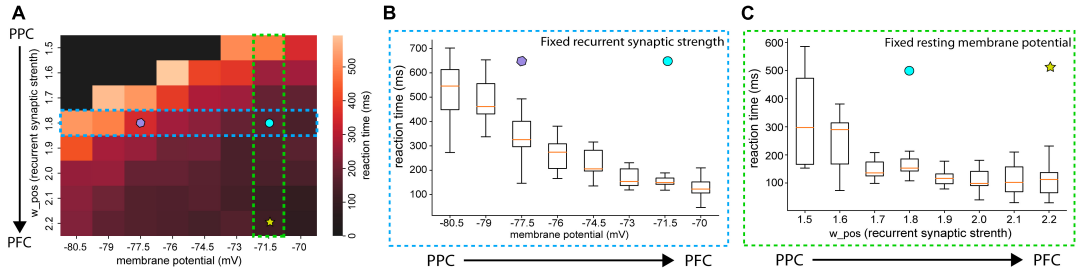

FIGURE 5
Averaged reaction time with various RMPs and recurrent synaptic strengths **(A)** heatmap of reactions times. The color of each cell indicates the averaged reaction time of 10 trials. The black-colored cell indicates that the population firing rate of the neural network did not pass 25 Hz in any of those 10 trials. **(B)** Boxplot of reaction time as RMPs set in the neural networks increase with the fixed recurrent synaptic strength (w_+ 1.8). **(C)** Box plot of the reaction time as recurrent synaptic strength set in the neural networks increase with the resting membrane potential (RMP = −71.5 mV). The difference in reaction times between the networks of RMP = −77.5 mV (purple polygon) and RMP = −71.5 mV (cyan circle) in **(B)** is greater than the one between w_+ = 1.8 (cyan circle) and w_+ 2.2 (yellow star).

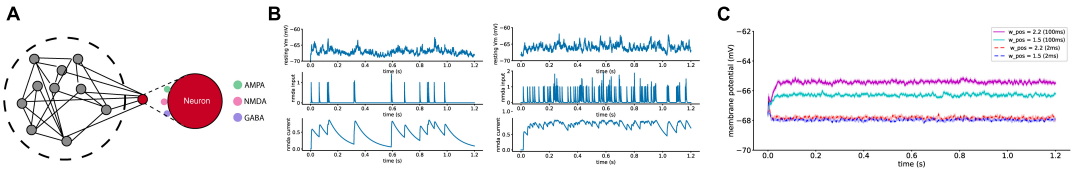

FIGURE 6
Single-cell modeling to mimic the whole-cell recording session. **(A)** The schematic of single-cell model with three major synaptic inputs of AMPA, GABA, and NMDA. **(B)** The effect of NMDA synaptic inputs to the RMP with lower (left) and higher (right) frequency. One of the most distinctive features of NMDA synaptic inputs is that the level of synaptic current saturate once enough number of synaptic inputs occur. **(C)** In this model, the mean frequency and strength of the NMDA synaptic inputs remained constant, while the time constants of synaptic transmission were varied. Increasing the strength of recurrent synapses led to an increase in (RMP) in the recipient neuron, but this effect was observed only with slow NMDA synaptic transmission inputs (100 *ms*) and not with fast inputs (20 *ms*). Averaged RMPs (solid lines) of 100 trials with the SEM in the shaded area.

including the RMP levels. The novelty of this study lies in the application of the RMPs values found in our experiment to the neuronal network model. Population firing rates acquired from our model simulations applying RMPs levels of neurons in the PPC and PFC showed similar patterns of population firing rates to those introduced in the theoretical study, indicating the possibility that stronger recurrent synaptic strengths in the PFC might have contributed to the elevated RMPs of neurons in that area.

Using the modeling toolkit, it is possible to modify various synaptic properties to study how new experimental findings can affect neural network dynamics, thereby elucidating the link between animal behaviors and neural network dynamics altered by changes in synaptic functional properties.

In the present study, we introduced a novel method using an available toolkit for neural network modeling. We applied the detailed parameters found in our experiments. This approach may enable researchers to investigate how functional modifications in synaptic transmission can affect neural dynamics, resulting in notable changes in animal behavior.

4.1. Reason for the lifted RMP: NMDA receptors as a contributor for the lifted resting membrane potential in the PFC area

Generally, RMP is closely related to excitability of neurons since it establishes the amount of input current required to reach the threshold for generating an action potential. The importance of appropriate levels of membrane potential in different regions for various functions has been widely studied (Kadir et al., 2018). RMP levels can be influenced by several factors, including the activity of specific ion channels, such as HCN and Kv4.2 (Hoffman et al., 1997; George et al., 2009; Eggermann et al., 2014). Factors such as the distribution of ion channels or pumps embedded in their cell membranes, as well as physical properties including membrane and axial resistance and membrane capacitance, could potentially contribute to these variations in RMP. For example, our observations revealed that the input resistance of neurons in the PFC was significantly higher compared to those in the PPC. This difference in input resistance may have played a role in the higher RMPs observed in the PFC.

Neuromodulators also alter RMPs, affecting cognitive states such as attention, arousal, and stress response by changing the responsiveness of a neuron to synaptic inputs. Noradrenaline and serotonin, for example, increase inward current to counteract the hyperpolarizing effects of potassium currents to maintain a neuron's RMP for generating action potentials with appropriate synaptic inputs (Pape and McCormick, 1989). In our study, however, the RMP levels were measured in the brain slices of the PPC and PFC areas during a resting state, without the presence of specific input neuromodulators or apparent stimulation. Thus, the influence of other factors, such as specific ion channels or neuromodulators, on the measured RMP levels was likely minimal. Instead, we hypothesized that the distinct morphological differences between the PPC and PFC areas, specifically in the basal dendrites of pyramidal cells, may provide a more plausible explanation for the observed variations in RMPs (González-Burgos et al., 2019).

González-Burgos et al. (2019) has found that in comparison to the posterior parietal cortex (PPC), the prefrontal cortex (PFC) exhibited significantly larger basal dendrites, with a total length approximately 54% longer and a convex hull volume approximately 43% larger. According to their study, the researchers found that the total number of basal dendritic spines per pyramidal neuron was estimated to be 89% higher in the PFC compared to the PPC, based on mean spine density and total basal dendrite length. These cortex basal dendrites, especially in rodents, display NMDA spikes that are known to contribute recurrent excitation (Markram et al., 1997; Lisman et al., 1998; Nevian et al., 2007; Gökçe et al., 2016). These studies suggest that the stronger recurrent connections observed in the prefrontal cortex (PFC) could involve NMDA spike-mediated connections. The NMDA spikes may have contributed to higher resting membrane potential. In our study, we tested the hypothesis that synaptic time scales can affect the resting membrane potential (RMP) of neurons by comparing the changes in RMPs of two neurons only with different time scales (100 *ms* for NMDA-like and 2 *ms* for AMPA-like) in a setup where neurons receive inputs stochastically from presynaptic neurons, as in the brain slice experiment setup.

In a theoretical study, Murray et al. (2017) suggested that the recurrent structure is a key element that induces differences in neural network dynamics for optimal performance in the PPC and PFC. However, the study did not identify the components of the recurrent structure that may have contributed the most to distinctive neural network dynamics. Our study suggests that a possible component of the recurrent structure is NMDAR-mediated synaptic transmission, especially with a longer time constant.

Our modeling simulations showed that slow post-synaptic input through NMDA receptors can elevate RMP levels, while shorter synaptic transmissions, such as AMPA, have only transient impacts on the RMPs and affect them less. An anatomical study identified more NMDA synaptic connections in the PFC than in the PPC. González-Burgos et al. (2019) has found that there are more basal dendrites that receive NMDA spikes in the PFC than in the PPC in non-human primates. Based on their study, along with the simulation results in our study, the lifted level of membrane potential may have been due to the increased number of synaptic boutons in the PFC area rather than the number of AMPA receptors.

However, another study showed that the time constant of NMDAR-mediated synaptic transmission is more important than the number of NMDA receptors itself (Wang et al., 2008). This study found that even though the ratios of NMDA/AMPA receptors were similar in the PFC and V1 of rats, NMDAR-mediated synaptic transmission was much slower in the PFC than in V1 due to the higher expression of NR2B in the PFC. NR2B is also related to long-term potentiation and tends to decrease the extent of the expression as an animal ages (Cui et al., 2013). Although a comparison of NR2B expression in the PPC and PFC has not been elucidated, it is expected that NR2B might be expressed less in the PPC than in the PFC, based on the results of our experiment and modeling simulation. A study reported that inactivation of NMDA receptors in the PPC of rats did not have a major impact on the ability of the animals to perform working memory tasks (Goard et al., 2016; Scott et al., 2019). Taken together, it seems that more NMDAR-mediated synaptic transmissions in the PFC lift the RMPs of the PFC by slow synaptic transmission through NR2B receptors. Therefore, blocking NR2B receptors may reduce the RMPs levels.

Furthermore, there is extensive recognition that animals exhibiting schizophrenia (SZ) display impaired working memory (Eryilmaz et al., 2016). The dysfunction in maintaining population activities for working memory in SZ may be linked to NMDAR-mediated synaptic transmission, as suggested by the NMDAR hypofunction hypothesis (Amit et al., 1983). This hypothesis, developed in the 1980s, emerged from observations that administering NMDAR antagonists to healthy individuals could reproduce a broad range of positive, negative, and cognitive symptoms associated with schizophrenia (Krystal et al., 1994; Lee and Zhou, 2019). In the context of SZ models, this suggests that even with numerous incoming inputs from other neurons in the network, a deficient number of NMDA receptors can impede the adequate increase in RMPs necessary to sustain persistent activities for working memory. Moreover, variations in MPs in this study were observed in slice experiments. Conducting *in vivo* whole-cell recordings in the PFC and PPC during decision-making tasks will provide a deeper understanding of the relationship between different MP levels and distinct network dynamics in these regions.

4.2. Lifted membrane potential and neural network dynamics

According to the theoretical study mentioned above, the PPC with relatively weaker recurrent synaptic connections provides computational advantages when the neural network accumulates evidence by reducing the error rates in discrimination between choices, forming a weak network attractor. However, the PFC with a higher recurrent synaptic structure is more robust to distractors. Ramping up quickly in the population dynamics of the PFC area may have advantages in holding up choices (working memory), but changing the decision becomes difficult if a wrong decision is made. Therefore, slow ramping up in the PPC and a faster increase in the population firing rate in the PFC are suggested to be advantageous for performing cognitive tasks with fewer errors and more robustness to distractors.

Using the SNN model in this study, our simulation results verified that higher recurrent synaptic strength, as suggested by Murray et al. (2017), gives rise to more PFC-like neural dynamics, whereas weaker connections make the network behave more like the population neural activities in PPC. However, unlike the study that used the rate-model to describe neural behaviors (Murray et al., 2017), we used the SNN model to apply distinctive MP levels in the PPC (lower) and PFC (higher).

In addition, we showed that in a reasonable range of w_+, which was determined by the general firing rates (∼50 spikes/s) shown in the network (Chafee and Goldman-Rakic, 1998), the levels of MP can affect neuronal network dynamics. Our study introduces the possibility that the lifted MP levels can be crucial in giving rise to distinctive neural network dynamics in the areas of the PPC and PFC, implying that the lifted MPs of neurons in these areas could not just be epiphenomenal, but necessary for each area to have optimized performance in cognitive tasks. For example, with the same number of synaptic transmissions of either AMPA or NMDA, more time for synaptic input integration is needed to reach an action potential threshold if the MP is lower. This delayed time may be the reason why neurons in the PPC gradually increase their firing rates while accumulating more evidence than neurons in the PFC. Likewise, the elevated RMPs of neurons in the PFC, inducing shorter distances from RMPs to the firing threshold, may enable them to encode incoming evidence more categorically than the PPC, since the same number of AMDAR- or NMDAR-mediated synaptic inputs will more promptly increase the firing rate of a single cell, which results in a rapid increase in the population firing rate of the PFC neural network. This relatively shorter time to generate action potentials may contribute to the physiological mechanism that helps the PFC network be more robust to distractions and more likely to induce errors in making decisions.

We propose that the lower and higher RMP levels in the PPC and PFC, respectively, may be a necessary condition for each area to give rise to desirable cognitive functions, such as gradual evidence collection and attentional saliency for PPC and robustness of persistent activities (working memory) and filtering of distractors for PFC. Therefore, it is reasonable to conclude that stronger recurrent structure introduced in the previous study (Murray et al., 2017), which our study suggests, are derived from a greater number of NMDA receptors with slow synaptic transmissions that lift the RMPs. The increased RMPs by NMDAR-mediated synaptic transmission may, in turn, contribute to a faster ramping up in the PFC area relative to the PPC area.

Data availability statement

The original contributions presented in this study are included in this article/**Supplementary material**, further inquiries can be directed to the corresponding author.

Ethics statement

The animal study was reviewed and approved by the Animal Experiment Ethics Committee (approval no. IACUC-20-00007) of the Korea Brain Research Institute (KBRI).

Author contributions

MY carried out all the computer simulations and analysis of simulation data, and co-wrote the manuscript. Y-SY performed whole-cell recording. J-CR designed whole-cell recording and contributed to all aspects of this project in interactions with JC and MY. JC designed the research, worked with the other authors throughout the project, and co-wrote the manuscript. All authors contributed to the article and approved the submitted version.

Funding

This research was supported by the KBRI basic research program through Korea Brain Research Institute funded by the Ministry of Science and ICT (22-BR-01-01).

Conflict of interest

The authors declare that the research was conducted in the absence of any commercial or financial relationships that could be construed as a potential conflict of interest.

Publisher's note

Supplementary material

The Supplementary Material for this article can be found online at: https://www.frontiersin.org/articles/10.3389/fncel.2023.1153970/full#supplementary-material

References

Amit, D., and Brunel, N. (1997). Model of global spontaneous activity and local structured activity during delay periods in the cerebral cortex. *Cereb. Cortex* 7, 237–252. doi: 10.1093/cercor/7.3.237

Amit, D., Brunel, N. A., and Berry, S. C. (1983). The dissociative anaesthetics, ketamine and phencyclidine, selectively reduce excitation of central mammalian neurones by N-methyl-aspartate. *Br. J. Pharmacol.* 79, 565–575. doi: 10.1111/j.1476-5381.1983.tb11031.x

Braitenberg, V., and Schüz, A. (1998). *Cortex: Statistics and geometry of neuronal connectivity*. Berlin: Springer.

Brunel, N., and Wang, X. (2001). Effects of neuromodulation in a cortical network model of object working memory dominated by recurrent inhibition. *J. Comput. Neurosci.* 11, 63–85. doi: 10.1023/a:1011204814320

Chafee, M., and Goldman-Rakic, P. (1998). Matching patterns of activity in primate prefrontal area 8a and parietal area 7ip neurons during a spatial working memory task. *J. Neurophysiol.* 79, 2919–2940. doi: 10.1152/jn.1998.79.6.2919

Constantinidis, C., and Steinmetz, M. (1996). Neuronal activity in posterior parietal area 7a during the delay periods of a spatial memory task. *J. Neurophysiol.* 76, 1352–1355. doi: 10.1152/jn.1996.76.2.1352

Crochet, S., and Petersen, C. (2006). Correlating whisker behavior with membrane potential in barrel cortex of awake mice. *Nat. Neurosci.* 9, 608–610. doi: 10.1038/nn1690

Crochet, S., Poulet, J., Kremer, Y., and Petersen, C. (2011). Synaptic mechanisms underlying sparse coding of active touch. *Neuron* 69, 1160–1175. doi: 10.1016/j.neuron.2011.02.022

Cui, Z., Feng, R., Jacobs, S., Duan, Y., Wang, H., Cao, X., et al. (2013). Increased NR2A:NR2B ratio compresses long-term depression range and constrains long-term memory. *Sci. Rep.* 3:1036. doi: 10.1038/srep01036

Destexhe, A., Zachary, M., and Sejnowski, T. (1998). *Methods in neuronal modelling, from ions to networks kinetic models of synaptic transmission*. Cambridge, MA: MIT Press.

di Pellegrino, G., and Wise, S. (1993). Effects of attention on visuomotor activity in the premotor and prefrontal cortex of a primate. *Somatosens Mot. Res.* 10, 245–262. doi: 10.3109/08990229309028835

Eggermann, E., Kremer, Y., Crochet, S., and Petersen, C. (2014). Cholinergic signals in mouse barrel cortex during active whisker sensing. *Cell Rep.* 9, 1654–1660. doi: 10.1016/j.celrep.2014.11.005

Eryilmaz, H., Tanner, A., Ho, N., Nitenson, A., Silverstein, N., Petruzzi, L., et al. (2016). Disrupted working memory circuitry in schizophrenia: Disentangling fMRI markers of core pathology vs other aspects of impaired performance. *Neuropsychopharmacology* 41, 2411–2420. doi: 10.1038/npp.2016.55

George, M. S., Abbott, L. F., and Siegelbaum, S. A. (2009). HCN hyperpolarization-activated cation channels inhibit EPSPs by interactions with M-type K^+ channels. *Nat. Neurosci.* 12, 577–584.

Gerstner, W., Kistler, W. M., Naud, R., and Paninski, L. (2014). *Neuronal dynamics: From single neurons to networks and models of cognition*. Cambridge, MA: Cambridge University Press.

Goard, M., Pho, G., Woodson, J., and Sur, M. (2016). Distinct roles of visual, parietal, and frontal motor cortices in memory-guided sensorimotor decisions. *Elife* 5:e13764. doi: 10.7554/eLife.13764

Gökçe, O., Bonhoeffer, T., and Scheuss, V. (2016). Clusters of synaptic inputs on dendrites of layer 5 pyramidal cells in mouse visual cortex. *Elife* 5:e09222. doi: 10.7554/eLife.09222

Goldman-Rakic, P. (1995). Cellular basis of working memory. *Neuron* 14, 477–485. doi: 10.1016/0896-6273(95)90304-6

González-Burgos, G., Miyamae, T., Krimer, Y., Gulchina, Y., Pafundo, D., Krimer, O., et al. (2019). Distinct properties of layer 3 pyramidal neurons from prefrontal and parietal areas of the monkey neocortex. *J. Neurosci.* 39, 7277–7290. doi: 10.1523/JNEUROSCI.1210-19.2019

Hanks, T., Kopec, C., Brunton, B., Duan, C., Erlich, J., and Brody, C. (2015). Distinct relationships of parietal and prefrontal cortices to evidence accumulation. *Nature* 520, 220–223. doi: 10.1038/nature14066

Hansel, D., Mato, G., Meunier, C., and Neltner, L. (1998). On numerical simulations of integrate-and-fire neural networks. *Neural Comput.* 10, 467–483. doi: 10.1162/089976698300017845

Hestrin, S., Sah, P., and Nicoll, R. (1990). Mechanisms generating the time course of dual component excitatory synaptic currents recorded in hippocampal slices. *Neuron* 5, 247–253. doi: 10.1016/0896-6273(90)90162-9

Hoffman, D. A., Magee, J. C., Colbert, C. M., and Johnston, D. (1997). K^+ channel regulation of signal propagation in dendrites of hippocampal pyramidal neurons. *Nature* 387, 869–875. doi: 10.1038/43119

Kadir, L. A., Stacey, M., and Barrett-Jolley R. (2018). Emerging roles of the membrane potential: Action beyond the action potential. *Front. Physiol.* 9:1661. doi: 10.3389/fphys.2018.01661

Krystal, J., Karper, L., Seibyl, J., Freeman, G., Delaney, R., Bremner, J., et al. (1994). Subanesthetic effects of the noncompetitive NMDA antagonist, ketamine, in humans. Psychotomimetic, perceptual, cognitive, and neuroendocrine responses. *Arch. Gen. Psychiatry* 51, 199–214. doi: 10.1001/archpsyc.1994.03950030035004

Lee, G., and Zhou, Y. (2019). NMDAR hypofunction animal models of schizophrenia. *Front. Mol. Neurosci.* 12:185. doi: 10.3389/fnmol.2019.00185

Lisman, J., Fellous, J., and Wang, X. J. (1998). A role for NMDA-receptor channels in working memory. *Nat. Neurosci.* 1, 273–275. doi: 10.1038/1086

Markram, H., Lübke, J., Frotscher, M., and Sakmann, B. (1997). Regulation of synaptic efficacy by coincidence of postsynaptic APs and EPSPs. *Science* 275, 213–215. doi: 10.1126/science.275.5297.213

McCormick, D. A., Connors, B. W., Lighthall, J. W., and Prince, D. A. (1985). Comparative electrophysiology of pyramidal and sparsely spiny stellate neurons of the neocortex. *J. Neurophysiol.* 54, 782–806. doi: 10.1152/jn.1985.54.4.782

Murray, J., Jaramillo, J., and Wang, X. (2017). Working memory and decision-making in a frontoparietal circuit model. *J. Neurosci.* 37, 12167–12186. doi: 10.1523/JNEUROSCI.0343-17.2017

Nevian, T., Larkum, M., Polsky, A., and Schiller, J. (2007). Properties of basal dendrites of layer 5 pyramidal neurons: A direct patch-clamp recording study. *Nat. Neurosci.* 10, 206–214. doi: 10.1038/nn1826

Pape, H. C., and McCormick, D. A. (1989). Noradrenaline and serotonin selectively modulate thalamic burst firing by enhancing a hyperpolarization-activated cation current. *Nature* 340, 715–718. doi: 10.1038/340715a0

Poulet, J., Fernandez, L., Crochet, S., and Petersen, C. (2012). Thalamic control of cortical states. *Nat. Neurosci.* 15, 370–372. doi: 10.1038/nn.3035

Qi, X., Katsuki, F., Meyer, T., Rawley, J., Zhou, X., Douglas, K., et al. (2010). Comparison of neural activity related to working memory in primate dorsolateral prefrontal and posterior parietal cortex. *Front. Syst. Neurosci.* 4:12. doi: 10.3389/fnsys.2010.00012

Roitman, J., and Shadlen, M. (2002). Response of neurons in the lateral intraparietal area during a combined visual discrimination reaction time task. *J. Neurosci.* 22, 9475–9489. doi: 10.1523/JNEUROSCI.22-21-09475.2002

Salin, P., and Prince, D. (1996). Spontaneous GABAA receptor-mediated inhibitory currents in adult rat somatosensory cortex. *J. Neurophysiol.* 75, 1573–1588. doi: 10.1152/jn.1996.75.4.1573

Scott, G., Roebuck, A., Greba, Q., and Howland, J. (2019). Performance of the trial-unique, delayed non-matching-to-location (TUNL) task depends on AMPA/Kainate, but not NMDA, ionotropic glutamate receptors in the rat posterior parietal cortex. *Neurobiol. Learn. Mem.* 159, 16–23. doi: 10.1016/j.nlm.2019.02.001

Shadlen, M., and Newsome, W. (1996). Motion perception: Seeing and deciding. *Proc. Natl. Acad. Sci. U. S. A.* 93, 628–633. doi: 10.1073/pnas.93.2.628

Shadlen, M., and Newsome, W. (2001). Neural basis of a perceptual decision in the parietal cortex (area LIP) of the rhesus monkey. *J. Neurophysiol.* 86, 1916–1936. doi: 10.1152/jn.2001.86.4.1916

Shelley, M. J., and Tao, L. (2001). Efficient and accurate time-stepping schemes for integrate-and-fire neuronal networks. *J. Comput. Neurosci.* 11, 111–119. doi: 10.1023/A:1012885314187

Spruston, N., Jonas, P., and Sakmann, B. (1995). Dendritic glutamate receptor channels in rat hippocampal CA3 and CA1 pyramidal neurons. *J. Physiol.* 482, 325–352. doi: 10.1113/jphysiol.1995.sp020521

Tsukada, H., Nishiyama, S., Fukumoto, D., Sato, K., Kakiuchi, T., and Domino, E. (2005). Chronic NMDA antagonism impairs working memory, decreases extracellular dopamine, and increases D1 receptor binding in prefrontal cortex of conscious monkeys. *Neuropsychopharmacology* 30, 1861–1869. doi: 10.1038/sj.npp.1300732

Tuckwell, H. C. (1988). *1 Introduction to Theoretical Neurobiology: Volume 1: Linear Cable Theory and Dendritic Structure*. Cambridge, MA: Cambridge University Press.

Wang, H., Stradtman, G., Wang, X., and Gao, W. J. (2008). A specialized NMDA receptor function in layer 5 recurrent microcircuitry of the adult rat prefrontal cortex. *Proc. Natl. Acad. Sci. U. S. A.* 105, 16791–16796. doi: 10.1073/pnas.0804318105

Wang, X. (1999). Synaptic basis of cortical persistent activity: The importance of NMDA receptors to working memory. *J. Neurosci.* 19, 9587–9603. doi: 10.1523/JNEUROSCI.19-21-09587.1999

Wang, X. (2001). Synaptic reverberation underlying mnemonic persistent activity. *Trends Neurosci.* 24, 455–463. doi: 10.1016/s0166-2236(00)01868-3

Wang, X.-J. (2002). Probabilistic decision making by slow reverberation in cortical circuits. *Neuron* 36, 955–968. doi: 10.1016/s0896-6273(02)01092-9

Wong, K., and Wang, X. J. (2006). A recurrent network mechanism of time integration in perceptual decisions. *J. Neurosci.* 26, 1314–1328. doi: 10.1523/JNEUROSCI.3733-05.2006

Xiang, Z., Huguenard, J., and Prince, D. A. (1998). GABAA receptor-mediated currents in interneurons and pyramidal cells of rat visual cortex. *J. Physiol.* 506, 715–730. doi: 10.1111/j.1469-7793.1998.715bv.x

frontiers | Frontiers in Cellular Neuroscience

TYPE Original Research
PUBLISHED 17 July 2023
DOI 10.3389/fncel.2023.1232541

OPEN ACCESS

EDITED BY
Jacopo Lamanna,
Vita-Salute San Raffaele University, Italy

REVIEWED BY
Eric Hanse,
University of Gothenburg, Sweden
Igor Delvendahl,
University of Zurich, Switzerland

*CORRESPONDENCE
Helmut W. Kessels
✉ h.w.h.g.kessels@uva.nl

RECEIVED 31 May 2023
ACCEPTED 30 June 2023
PUBLISHED 17 July 2023

CITATION
Lumeij LB, van Huijstee AN, Cappaert NLM and Kessels HW (2023) Variance analysis as a method to predict the locus of plasticity at populations of non-uniform synapses. *Front. Cell. Neurosci.* 17:1232541. doi: 10.3389/fncel.2023.1232541

Variance analysis as a method to predict the locus of plasticity at populations of non-uniform synapses

Lucas B. Lumeij, Aile N. van Huijstee, Natalie L. M. Cappaert and Helmut W. Kessels*

Cellular and Computational Neuroscience, Swammerdam Institute for Life Sciences, Amsterdam Neuroscience, University of Amsterdam, Amsterdam, Netherlands

Our knowledge on synaptic transmission in the central nervous system has often been obtained by evoking synaptic responses to populations of synapses. Analysis of the variance in synaptic responses can be applied as a method to predict whether a change in synaptic responses is a consequence of altered presynaptic neurotransmitter release or postsynaptic receptors. However, variance analysis is based on binomial statistics, which assumes that synapses are uniform. In reality, synapses are far from uniform, which questions the reliability of variance analysis when applying this method to populations of synapses. To address this, we used an *in silico* model for evoked synaptic responses and compared variance analysis outcomes between populations of uniform versus non-uniform synapses. This simulation revealed that variance analysis produces similar results irrespectively of the grade of uniformity of synapses. We put this variance analysis to the test with an electrophysiology experiment using a model system for which the loci of plasticity are well established: the effect of amyloid-β on synapses. Variance analysis correctly predicted that postsynaptically produced amyloid-β triggered predominantly a loss of synapses and a minor reduction of postsynaptic currents in remaining synapses with little effect on presynaptic release probability. We propose that variance analysis can be reliably used to predict the locus of synaptic changes for populations of non-uniform synapses.

KEYWORDS

synapse, hippocampus, variance, uniformity, amyloid–beta, excitatory postsynaptic current (EPSC)

Introduction

Synaptic plasticity is a crucial mechanism for the brain to adapt behavior based on experience (Kessels and Malinow, 2009). Specifically, strengthening and weakening of hippocampal synapses play a pivotal role in memory formation and forgetting (Martin et al., 2000). However, when a change in synaptic strength occurs, it is often unknown what the underlying mechanism and locus of that change is, e.g., whether this change is either presynaptic or postsynaptic.

The efficacy of synaptic communication is determined by three main parameters: the number of functional vesicle release sites (N), the probability of presynaptic vesicle release per release site (P_r) and the postsynaptic response size to the release of a single vesicle of neurotransmitter (i.e., a quantum), which is called the quantal size (Q) (Korn and Faber, 1991). In the central nervous system, neurotransmitter is released stochastically, leading to fluctuations in postsynaptic responses that roughly follow a binomial distribution when axon bundles are repeatedly stimulated (Korn and Faber, 1991). Quantal analysis on the variance in synaptic responses can be used to predict changes in N, P_r, and Q (Del Castillo and Katz, 1954). If one assumes a binomial distribution, the mean amplitude of postsynaptic responses (μ) and its variance (σ^2) can be calculated using the following equations:

$$\mu = N\, P_r\, Q \tag{1}$$

$$\sigma^2 = N\, P_r\, (1 - P_r)\, Q^2 \tag{2}$$

To dissect which of these three parameters is affected when synaptic changes occur, simple indices can be derived from these equations. Firstly, the inverse square of the coefficient of variation ($1/CV^2$) is revealing, because it is independent of Q (Bekkers and Stevens, 1990; Malinow and Tsien, 1990; Redman, 1990):

$$\frac{1}{CV^2} = \frac{\mu^2}{\sigma^2} = \frac{N\, P_r}{1 - P_r} \tag{3}$$

The $1/CV^2$ has been used extensively to predict whether a synaptic change was presynaptic (P_r) or postsynaptic (Q) in origin, provided that the number of functional release sites (N) stays constant within an experiment (Bekkers and Stevens, 1990; Malinow and Tsien, 1990). The variance-to-mean ratio (VMR) is a useful index to further dissect the synaptic loci, because it is independent of N (Lupica et al., 1992; van Huijstee and Kessels, 2020):

$$VMR = \frac{\sigma^2}{\mu} = (1 - P_r)\, Q \tag{4}$$

Applying the combination of $1/CV^2$ and VMR on evoked synaptic responses has been validated as a method to decipher the contributions of N, P_r, and Q to a change in synaptic strength (van Huijstee and Kessels, 2020; Hogrefe et al., 2022).

There are a number of assumptions underlying a binomial release model (Brock et al., 2020), of which the first two are largely met at central synapses. Firstly, variance analysis assumes that at most one quantum is released at each functional release site per action potential. Most central synapses indeed release at most one vesicle per action potential, although multivesicular release within a single synapse, and even within a single active zone, can occur at central synapses (Korn and Faber, 1991; Quastel, 1997; Oertner et al., 2002; Conti and Lisman, 2003; Jensen et al., 2019; Maschi and Klyachko, 2020; Dürst et al., 2022). Therefore, in situations where multivesicular release is prevalent, one should regard N as the number of functional release sites rather than the number of synapses. A second assumption is that the release of a vesicle happens independently from other release sites, meaning that released quanta summate linearly. This assumption appears to be largely true, since release sites are considered to act autonomously (Ventura and Harris, 1999; Oertner et al., 2002; Christie and Jahr, 2006; Dürst et al., 2022).

However, the assumption related to variance analysis that is clearly not met is that P_r and Q are uniform across synapses. In fact, previous studies reported a large variety in P_r between release sites (Hessler et al., 1993; Rosenmund et al., 1993; Dobrunz and Stevens, 1997; Oertner et al., 2002; Dürst et al., 2022). Similarly, the postsynaptic response (Q) to each released vesicle varies between release sites, as Q depends on receptor density and receptor conductance (Dobrunz and Stevens, 1997; Hanse and Gustafsson, 2001), although the amount of neurotransmitter released per vesicle is thought to be relatively uniform (Rost et al., 2015; Dürst et al., 2022). Based on these considerations, we questioned whether this non-uniform distribution of P_r and Q would cause extra variance to the synaptic responses, making variance analysis potentially unreliable for predicting changes at populations of synapses.

In this study we aimed to test the effects of a non-uniform distribution of P_r and Q in populations of synapses on the outcome parameters of variance analysis (i.e., $1/CV^2$ and VMR). We did this by simulating whole-cell patch clamp experiments, to study the variance in evoked excitatory postsynaptic currents (EPSCs) in a controlled manner. Comparing uniform and non-uniform input parameters N, P_r, and Q *in silico* and testing their effects on μ, $1/CV^2$, and VMR, allows us to assess the importance of the assumption that synaptic populations should be uniform when conducting variance analysis. To validate our model, we compared the outcomes of our *in silico* model with an actual patch clamp experiment on AMPA receptor (AMPAR) currents in hippocampal CA1 pyramidal neurons receiving Schaffer collateral input from CA3 neurons (i.e., Sc-CA1 synapses) (Kessels et al., 2013). In these experiments, we studied the effect of the expression of the amyloid precursor protein (APP) on the AMPAR EPSCs in CA1 neurons in organotypic hippocampal rat slices. Dual recordings from pairs of APP-expressing and control neurons were used to assess the effects of the overproduction of amyloid-β (Aβ), an important protein in the pathogenesis of Alzheimer's disease, on synaptic transmission (Selkoe, 2002). Multiple studies that used this model system show that the production of Aβ oligomers reduces synaptic transmission onto CA1 neurons (Kamenetz et al., 2003; Hsieh et al., 2006; Kessels et al., 2010, 2013; Knafo et al., 2016; Reinders et al., 2016). We tested whether variance analysis can be used to make a prediction about the contributions of changes in N, P_r, and/or Q that cause this decrease in EPSC amplitude. Together, this study provides more insight into the strengths and limitations of variance analysis and shows its merit when predicting pre- and postsynaptic plasticity in the hippocampus and possibly in central synapses overall.

Materials and methods

Electrophysiology

Organotypic hippocampal slices were prepared, as previously described, from P6-7 female and male Sprague Dawley rats and kept in culture for 6–13 days (Stoppini et al., 1991; Kessels et al., 2013). APP_{CT100} was sparsely expressed using Sindbis viral vectors that were injected into CA1 20–30 h before recording. Sparse expression is relevant to avoid immune responses to viral

particles (Uyaniker et al., 2019) and to ensure that the majority of synapses from control neurons are sufficiently separated from Aβ-producing neurons (Wei et al., 2010). On the day of recording a cut was made between CA3 and CA1 to prevent stimulus-induced bursting. Whole-cell recordings were obtained simultaneously from neighboring uninfected and infected CA1 neurons; infected neurons were identified by fluorescence using co-expression of GFP. Two stimulating electrodes were placed 100 μm apart laterally and 200 μm in opposite directions (e.g., 100 and 300 μm) along the apical dendrite in the stratum radiatum (**Figure 5A**). For the recordings 3- to 5-MΩ pipettes were used containing internal solution of 115 mM cesium methanesulfonate, 20 mM CsCl, 10 mM Hepes, 2.5 mM $MgCl_2$, 4 mM Na_2ATP, 0.4 mM Na_3GTP, 10 mM sodium phosphocreatine (Sigma), and 0.6 mM EGTA (Amresco), at pH 7.25. During recording, slices were perfused with artificial cerebrospinal fluid containing 119 mM NaCl, 2.5 mM KCl, 26 mM $NaHCO_3$, 1mM NaH_2PO_4, and 11 mM glucose (pH 7.4), and gassed with 5% CO2/95% O_2 at 27 °C with 4 mM $MgCl_2$, 4 mM $CaCl_2$, 4 μM 2-chloroadenosine (Sigma), and 100 μM picrotoxin (Sigma). During each recording, neurons received input from the two stimulating electrodes, sweeps from each individual electrode were 3 s apart. The resulting EPSCs were averaged and count as $n = 1$. AMPAR EPSCs were measured as peak inward currents at −60 mV.

In silico simulation

Evoked whole-cell patch clamp experiments were simulated using MATLAB 2021a. To match the electrophysiological data, experimental groups always consisted of 27 *in silico* neurons. In these simulations, populations of neurons were given values for N, P_r, and Q. The number of synapses (N) differed between 5 and 25, depending on the experiment. Each synapse was assigned a release probability (P_r) between 0 and 1. In a uniform population all synapses had the same P_r, but in a non-uniform population, synapses were randomly assigned a value drawn from a beta distribution with a specific mean P_r and corresponding standard deviation (SD). An example of randomly drawn P_r values within such a distribution is depicted in **Supplementary Figure 1** (i.e., 27 neurons with 15 synapses each). Regarding quantal response size (Q), each synapse was given a value between 5 and 25 pA, depending on the experiment. Again, in uniform populations Q was the same for each synapse, but in non-uniform populations Q was attributed randomly per synapse from the distribution in the Pearson system with mean, standard deviation, skewness (between 0.75 and 1) and kurtosis (4). An exemplar distribution of randomly drawn Q values for one experiment is depicted in **Supplementary Figure 1** (i.e., 27 neurons with 15 synapses each).

Each simulated experiment consisted of 48 sweeps, based on the average number of sweeps used in the electrophysiological experiments (**Figure 5A**). Each sweep meant the stimulation of one population of synapses that was activated. However, to mimic the stochastic process of neurotransmitter release, a go/no go value was randomly drawn from a uniform distribution in the interval (0,1) for each synapse for each sweep. If this go/no go value was equal to or lower than the P_r of that synapse a "vesicle was released" and the EPSC amplitude of that synapse would be equal to its Q. If the go/no go value would lead to no release, the EPSC amplitude of that synapse would be 0. Per sweep, the currents of all the synapses in which release took place were summated giving the total EPSC amplitude of that sweep. Per neuron/recording this was done 48 times (i.e., nr. of sweeps), leading to a mean EPSC amplitude and its variance per neuron.

Variance analysis

For the electrophysiological recordings, variance analysis was performed on the mean EPSC amplitudes and variance of responses to 30–80 sweeps, on average 48 sweeps, per neuron. For the *in silico* neurons, 48 sweeps were used. The EPSC amplitudes per sweep and variance per neuron were used to calculate their mean EPSC amplitude, $1/CV^2$ and VMR (equations 2 and 3). These three values were averaged over 27 neurons per group and compared between conditions. Note that multiplying $1/CV^2$ with VMR per neuron leads to its μ value. As a consequence, $1/CV^2$ and VMR are negatively correlated for both simulated and recorded neurons (**Supplementary Figure 2**).

Statistics

Multiple *t*-tests with a Holm-Šídák correction were performed on log_2-normalized data to test whether they differed significantly from 0 or if there were differences between groups. One-way ANOVAs were used to test if there were differences between multiple groups. Paired *t*-tests were used to detect differences between two groups in the electrophysiological experiments and unpaired *t*-tests were used for two-group comparisons in the *in silico* experiments. For all experiments, $p < 0.05$ was considered significant.

Results

Variance analysis outcomes are similar between uniform and non-uniform populations of *in silico* synapses

To examine whether a uniform versus a non-uniform input variable distribution (N, P_r and Q) would lead to different outcomes in variance analysis output (i.e., μ, $1/CV^2$ and VMR), we simulated whole-cell electrophysiological experiments in which excitatory postsynaptic currents are determined by stimulating a population of 27 neurons. In this simulation, for each *in silico* neuron 15 synapses were stimulated ($N = 15$). Release was set to be univesicular, indicating that in this model N represents the number of release sites and also the number of synapses. These *in silico* synapses had physiological values for the mean and standard deviation of the release probability ($P_r = 0.3 \pm 0.15$) and quantal size ($Q = 15 \pm 4.5$ pA) based on previous literature for Sc-CA1 hippocampal synapses that receive Schaffer collateral input (Hessler et al., 1993; Rosenmund et al., 1993; Dobrunz and Stevens, 1997; Hanse and Gustafsson, 2001; Oertner et al., 2002).

10.3389/fncel.2023.1232541

In the non-uniform distributions, P_r ranged from 0.04 to 0.81 and Q values ranged from and 6 to 28 pA (Supplementary Figure 1). We used these values to design four populations with the same N, mean P_r and mean Q, but with different distributions for P_r and Q.

In the first population, all 15 synapses were uniform having an identical P_r and Q (Figure 1A; P_r = 0.3 ± 0; Q = 15 ± 0 pA). In the second set of *in silico* experiments, we tested groups of 15 synapses per neuron that varied in P_r but with Q uniform (Figure 1B; Pr = 0.3 ± 0.15; Q = 15 ± 0 pA). The third experiment used 15 synapses with uniform P_r and with different values for Q (Figure 1C; P_r = 0.3 ± 0; Q = 15 ± 4.5 pA). In the fourth experiment both P_r and Q were non-uniform in the 15 synapses (Figure 1D; P_r = 0.3 ± 0.15; Q = 15 ± 4.5 pA). Because the N of each neuron and the P_r and Q of the synapses were on average the same in all four experiments, the average EPSC amplitudes were also highly similar to each other (Figures 1A–D). We calculated the $1/CV^2$ and VMR values for the 4 populations to assess whether the uniformity of the input variables affect the output (Figures 1A–D). We make a distinction between "predicted values" (i.e., $1/CV^2$ and VMR) that result from variance analysis, and "expected values" that are calculated by input variables N, P_r and Q in equations 1, 3 and 4. Normalizing the predicted values of $1/CV^2$ and VMR to their expected values showed that the prediction did not deviate significantly from the expected outcome for both the uniform and non-uniform populations of *in silico* synapses (Figure 1E). More importantly, these normalized values gave similar values when comparing between the four *in silico* experiments (Figure 1E). Furthermore, changing the distribution further by using either smaller or larger values as standard deviation for P_r and Q also did not affect the average EPSC amplitude, $1/CV^2$ or VMR significantly (Supplementary Figure 3). These data indicate that the uniformity of a population of synapses did not affect the outcomes of variance analysis.

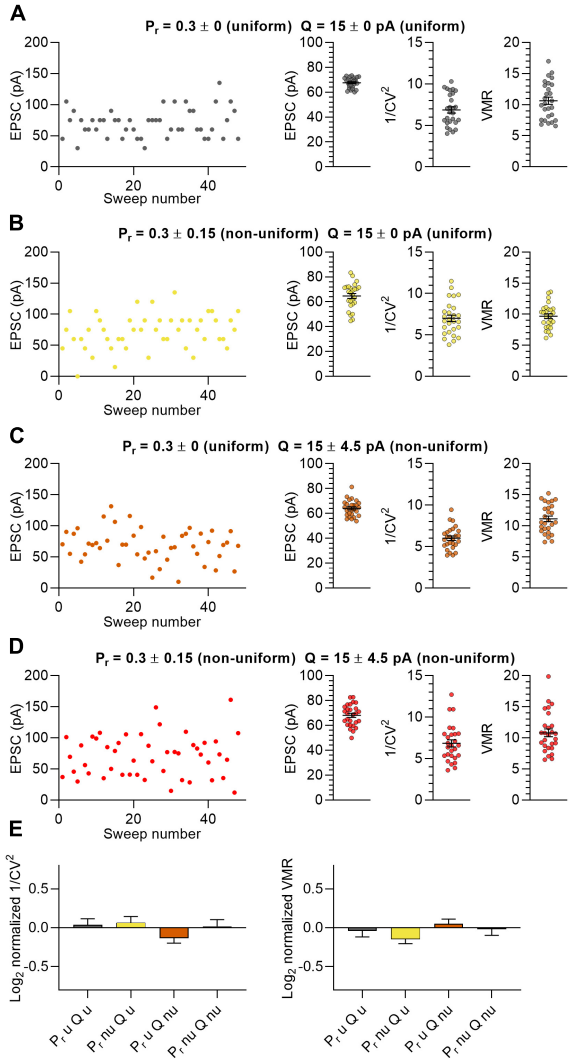

FIGURE 1
Non-uniform *in silico* populations of synapses do not affect variance analysis outcomes. **(A–D)** Left panel: example traces of summated EPSC amplitudes of 15 stimulated synapses per sweep of one *in silico* neuron. Right panels: average EPSC, $1/CV^2$ and VMR (n = 27 neurons). **(A)** Both P_r (0.3 ± 0) and Q (15 ± 0 pA) uniform across synapses (grey). **(B)** P_r (0.3 ± 0.15) non-uniform and Q uniform (15 ± 0 pA) across synapses (yellow). **(C)** P_r (0.3 ± 0) uniform and Q (15 ± 4.5 pA) non-uniform across synapses (orange). **(D)** Both P_r (0.3 ± 0.15) and Q (15 ± 4.5 pA) non-uniform across synapses (red). **(E)** Log_2 values of $1/CV^2$ and VMR for all four conditions normalized to their expected values. Statistics: normalized values were compared to 0 using multiple t-tests with a Holm-Šídák correction and to each other by one-way ANOVAs. Error bars indicate SEM.

Variance analysis correctly predicts changes in N, p_r, and Q in both uniform and non-uniform populations of *in silico* synapses

In the previous experiment, we simulated synaptic responses upon stimulation of 15 Sc-CA1 synapses per neuron. It may be possible that when stimulating a lower number of synapses, differences in variance between uniform and non-uniform populations of synapses become more apparent. To examine the effect of changing the number of synapses, we chose different numbers for N ranging from 5 to 25 with P_r (0.3) and Q (15 pA) kept constant (Figure 2). We compared synapses that were uniform in both P_r (0.3 ± 0) and Q (15 ± 0 pA) or non-uniform in both P_r (0.3 ± 0.15) and Q (15 ± 4.5 pA). The mean EPSC and $1/CV^2$ changed linearly with a change in N (Figures 2A, B), whereas the VMR was not affected by changes in N (Figure 2C), indicating that changing N has the expected effects on the variance analysis parameters in both uniform and non-uniform populations of synapses. The values for average EPSC amplitude, $1/CV^2$ and VMR normalized to their expected values showed that the uniform and the non-uniform populations did not deviate from each other (Figures 2A–C), indicating the number of stimulated synapses does not influence the reliability of variance analysis.

It was previously suggested that variance analysis outcomes for non-uniform populations of synapses would deviate more from expected values at high release probability than at low release probabilities (Silver et al., 1998). We therefore asked whether variance analysis comparisons between uniform and non-uniform populations of synapses depend on average release probability. The effects of changes in release probability were assessed by

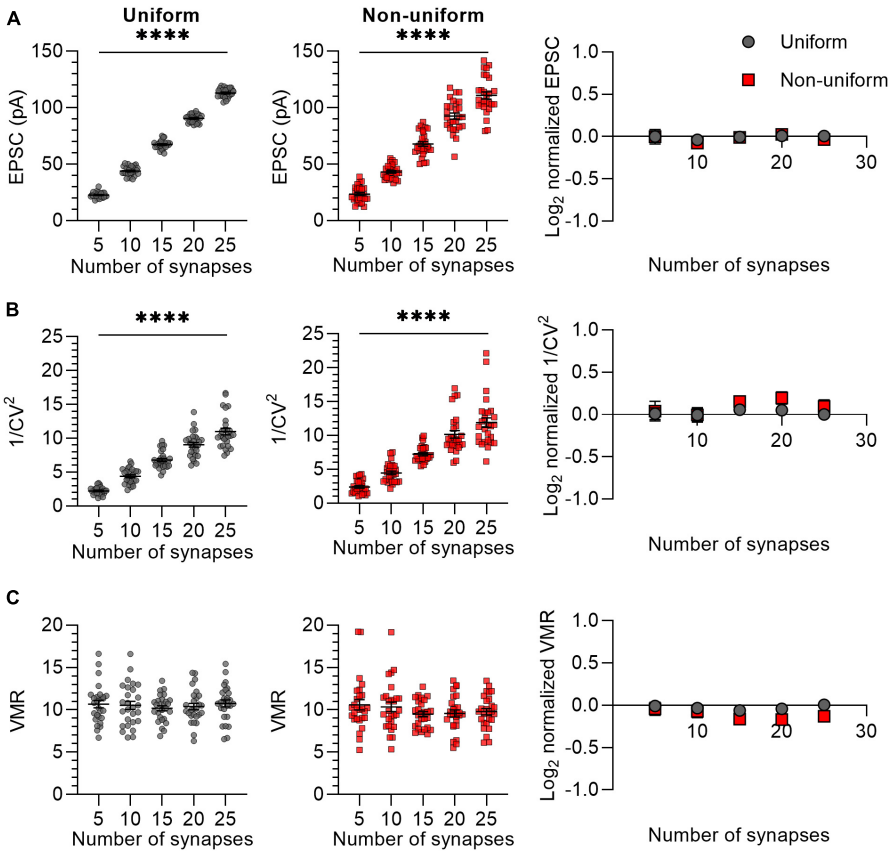

FIGURE 2
Changes in N lead to similar variance analysis outcomes in both uniform and non-uniform *in silico* populations of synapses. **(A–C)** Left panels: effects of changes in number of synapses (N) on average EPSC **(A)**, $1/CV^2$ **(B)**, and VMR **(C)** in uniform (grey circles) and non-uniform (red squares) populations. Right panel: average $\log_2$ values of EPSC **(A)**, $1/CV^2$ **(B)**, and VMR **(C)** normalized to expected values of uniform (grey circles) and non-uniform populations (red squares). For uniform populations $P_r = 0.3 \pm 0$ and $Q = 15 \pm 0$ pA; for non-uniform populations $P_r = 0.3 \pm 0.15$ and $Q = 15 \pm 4.5$ pA ($n = 27$). Statistics: effect of number of synapses on average EPSC, $1/CV^2$ and VMR values (left panels) were tested using one-way ANOVAs. Normalized values were compared to 0 and between uniform and non-uniform using multiple *t*-tests with a Holm-Šídák correction. Error bars indicate SEM; $^{****}p < 0.0001$.

selecting five values for P_r ranging from 0.2 to 0.8 (Figure 3). Note that we avoided including *in silico* synapses with a P_r lower than 0 or higher than 1 by setting the standard deviation for non-uniform populations to 0.14 instead of 0.15 for $P_r = 0.2$ and 0.8. In accordance with the prediction, the mean EPSC increased proportionally with an increase in P_r for both uniform and non-uniform groups of synapses (Figure 3A). However, only for a low average release probability ($P_r = 0.2$), the average EPSC amplitude was significantly lower for non-uniform synapses compared with uniform synapses ($p = 0.001$; Figure 3A). This result was unexpected, since the average EPSC should be similar when average N, P_r and Q are the same. Repeating this *in silico* experiment did give similar average EPSC amplitudes for changes at $P_r = 0.2$ ($p = 0.924$; Supplementary Figure 4) and for all other outcome values, which supports the notion that statistical differences can be based on chance. Nevertheless, irrespectively of having obtained a significant difference in EPSC amplitude at average $P_r = 0.2$, $1/CV^2$ increased exponentially with an increase in P_r without differences between the uniform and non-uniform populations of synapses (Figure 3B). In addition, increases in P_r lead to the expected linear decrease in VMR and also here no differences were found between uniform and non-uniform populations (Figure 3C). This simulation indicates that changes in average P_r resulted in expected changes in $1/CV^2$ and VMR in both uniform and in non-uniform populations of *in silico* synapses.

We next selectively varied the quantal response size by varying the Q from 5 to 25 pA in steps of 5 pA, with a standard deviation of 0 (uniform) or 4.5 (non-uniform) (Figure 4). We chose these values of average Q (15 pA) and standard deviation (4.5 pA) based on previous literature (Dobrunz and Stevens, 1997; Hanse and Gustafsson, 2001). To prevent the inclusion of synapses with negative values for Q, in the non-uniform populations the SD for the lowest value ($Q = 5$ pA) was set to 2.5 instead of 4.5. The average EPSC of synaptic responses increased proportionally with an increase in Q and did not differ between uniform and non-uniform populations for any of the Q values (Figure 4A). The $1/CV^2$ is expected to be independent of Q, which was indeed reflected by variance analysis of both uniform and non-uniform populations of synapses (Figure 4B). VMR values increased linearly with Q and similarly for uniform and non-uniform populations of *in silico* synapses (Figure 4C), which is in line with the expectation that changes in Q are reflected in altered VMR values.

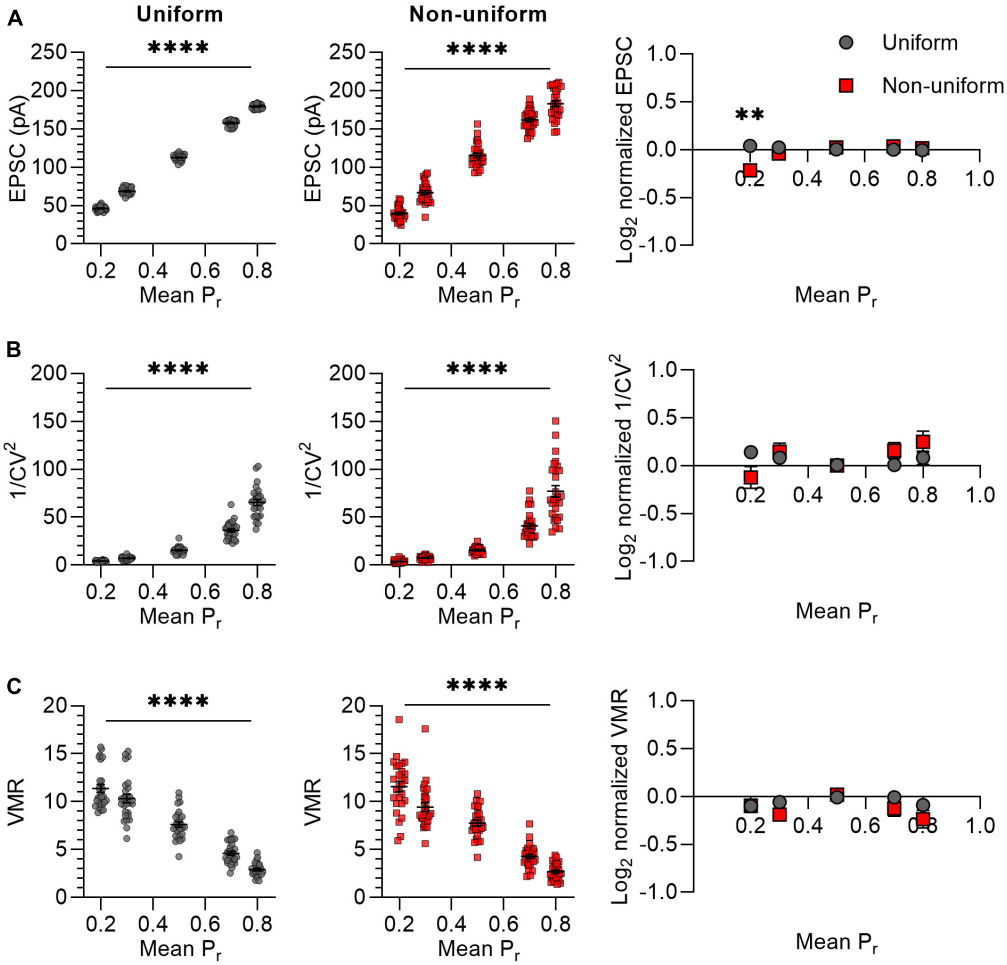

FIGURE 3
Changes in P_r lead to similar variance analysis outcomes in both uniform and non-uniform *in silico* populations of synapses. **(A–C)** Left panels: effects of changes in release probability (P_r) on average EPSC **(A)**, 1/CV^2 **(B)**, and VMR **(C)** in uniform (grey circles) and non-uniform (red squares) populations. Right panel: average $\log_2$ values of EPSC **(A)**, 1/CV^2 **(B)**, and VMR **(C)** normalized to expected values of uniform (grey circles) and non-uniform populations (red squares). For all populations $N = 15$ and $Q = 15$ pA; in uniform populations SDs of P_r and Q were 0; in non-uniform populations SDs of P_r were 0.15 (0.14 for $P_r = 0.2$ and 0.8) and SDs of Q were 4.5 pA ($n = 27$). Statistics: effect of release probability on average EPSC, 1/CV^2 and VMR values (left panels) were tested using one-way ANOVAs. Normalized values were compared to 0 and between uniform and non-uniform using multiple *t*-tests with a Holm-Šídák correction. Error bars indicate SEM; $^{**}p < 0.01$, $^{****}p < 0.0001$.

Combined, these results indicate that variance analysis correctly predicts changes in N, P_r and Q for non-uniform groups of *in silico* synapses.

Validation of variance analysis to predict effects of amyloid-β on synapses

To validate variance analysis as a predictor for the locus of synaptic plasticity, we previously demonstrated in electrophysiological experiments that changing a single parameter, i.e. either N, P_r or Q individually, resulted in the expected changes in 1/CV^2 and VMR (van Huijstee and Kessels, 2020). To further investigate the value of variance analysis in a more complex situation where potentially more than one parameter may be altered, we compared our *in silico* model to a previously published *ex vivo* whole-cell patch clamp experiment in which synaptic transmission is affected by the production of Aβ (Kessels et al., 2013). To induce elevated Aβ levels in CA1 pyramidal neurons, organotypic hippocampal slices were injected with viral vectors expressing APP_{CT100}, the β-secretase product of APP and substrate for Aβ after γ-secretase cleavage. Dual whole-cell recordings from pairs of neighboring uninfected and infected neurons were performed, and AMPAR currents at Sc-CA1 synapses were evoked by stimulating the same axonal input to both neurons. Excitatory transmission was on average 47% lower in APP_{CT100}-infected CA1 neurons compared with their neighboring control neurons ($p < 0.0001$; Figure 5A). We subsequently tested whether variance analysis could predict a synaptic locus of the observed synaptic depression. We found that the 1/CV^2 decreased significantly in these recordings by 40% ($p = 0.0056$; Figure 5A). The VMR also tended to decrease by on average 23%, but did not reach statistical significance ($p = 0.058$; Figure 5A).

To further entangle the prediction for a synaptic locus, we reproduced the 47% decrease of the EPSC amplitude *in silico* by lowering N, P_r and Q separately by ~47% (Figures 5B–D). In these

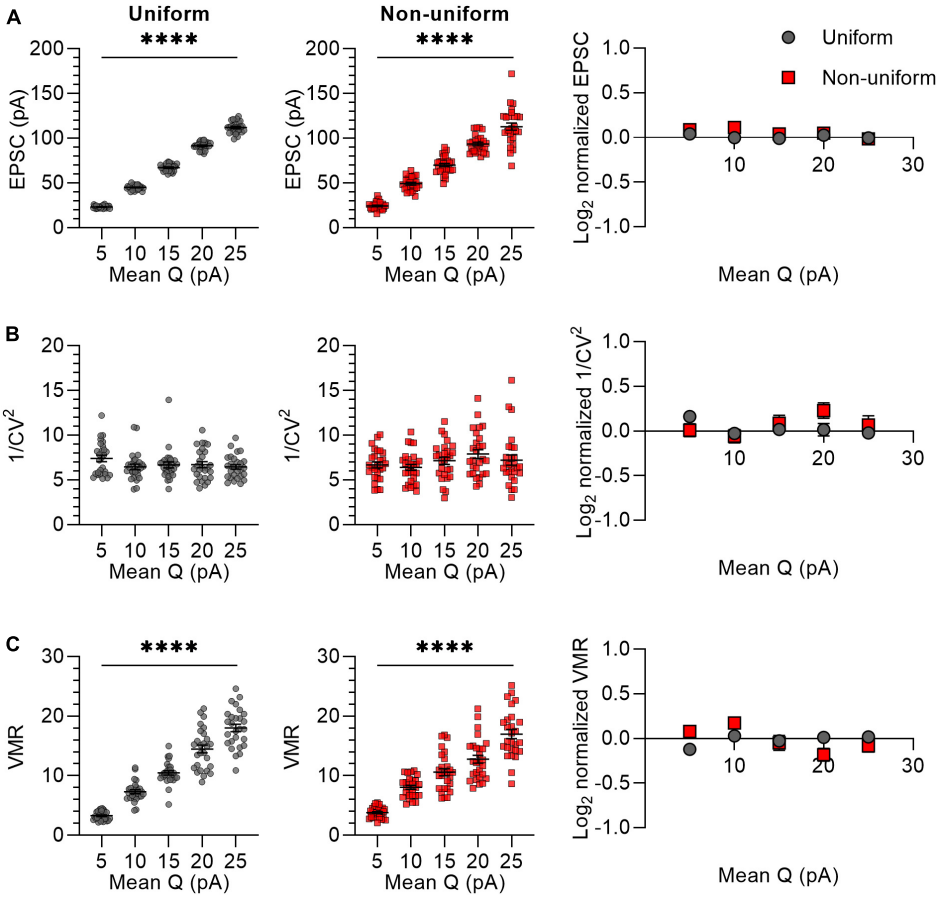

FIGURE 4
Changes in Q lead to similar variance analysis outcomes in both uniform and non-uniform *in silico* populations of synapses. **(A–C)** Left panels: effects of changes in quantal size (Q) on average EPSC **(A)**, $1/CV^2$ **(B)**, and VMR **(C)** in uniform (grey circles) and non-uniform (red squares) populations. Right panel: average $\log_2$ values of EPSC **(A)**, $1/CV^2$ **(B)**, and VMR **(C)** normalized to expected values of uniform (grey circles) and non-uniform (red squares) populations. For all populations $N = 15$ and $P_r = 0.3$; in uniform populations SDs of Pr and Q were 0; in non-uniform populations SDs of P_r were 0.15 and SDs of Q were 4.5 pA (2.5 pA for $Q = 5$ pA) ($n = 27$). Statistics: effect of quantal size on average EPSC, $1/CV^2$ and VMR values (left panels) were tested using one-way ANOVAs. Normalized values were compared to 0 and between uniform and non-uniform using multiple *t*-tests with a Holm-Šídák correction. Error bars indicate SEM; $^{****}p < 0.0001$.

experiments, we attempted to use values for N, P_r, and Q that would match the electrophysiological experiments in organotypic slices of the rat hippocampus. An important factor here is that the *ex vivo* slice recordings were conducted with 4 mM extracellular Ca^{2+} and P_r is known to depend strongly on extracellular Ca^{2+} concentration (Dodge and Rahamimoff, 1967; Rosenmund et al., 1993; Dobrunz and Stevens, 1997; Oertner et al., 2002). To estimate P_r in our *in silico* experiments, we used the VMR of the uninfected neurons (**Figure 5A**) and assumed that Q was on average 15 pA, since Q is not affected by changing Ca^{2+} concentrations when Mg^{2+} levels are kept high at 4 mM (Hardingham et al., 2006). By using this VMR (8.13) and Q (15 pA) in equation 4, we calculated a P_r of ∼0.46. This value is approximately in line with the relationship between Ca^{2+} concentration and P_r reported in literature (Rosenmund et al., 1993; Dobrunz and Stevens, 1997; Oertner et al., 2002). A factor that was considered to influence variance analysis when comparing EPSC recordings with *in silico* results is random electrical noise. When we included noise with a bandwidth of 10 pA to the *in silico* model by adding a random value between +5 pA and −5 pA to the amplitude generated by each sweep, the $1/CV^2$ and VMR values are minimally affected except for recordings with low average EPSC amplitudes (**Supplementary Figure 5**).

To simulate a loss of functional synapses as the cause of ∼47% decrease in EPSC, we analyzed the effect of lowering N from 10 to 5 synapses per neuron, which resulted in a 43% decrease in the $1/CV^2$ while the VMR remained unchanged (**Figure 5B**). Decreasing P_r from 0.46 ± 0.23 to 0.24 ± 0.15 to achieve a 47% decrease in EPSC amplitude led to a 65% decrease in $1/CV^2$ and a 49% increase in VMR (**Figure 5C**), which particularly for VMR does not match experimental results. When decreasing Q by 47% from 15 to 7.96 pA, we found that $1/CV^2$ decreased by 20% and VMR decreased by 33% (**Figure 5D**). This result is partially in line with expectation, since the significant change in $1/CV^2$ ($p = 0.029$) unexpectedly predicts a decrease in N or P_r. An advantage of *in silico* experiments over electrophysiology experiments is that they can be effortlessly repeated many times. To assess the probability of finding statistically significant differences, we ran experiments of **Figures 5B–D** and subsequent statistics for each parameter (EPSC, $1/CV^2$, VMR) 1,000 times. Whereas

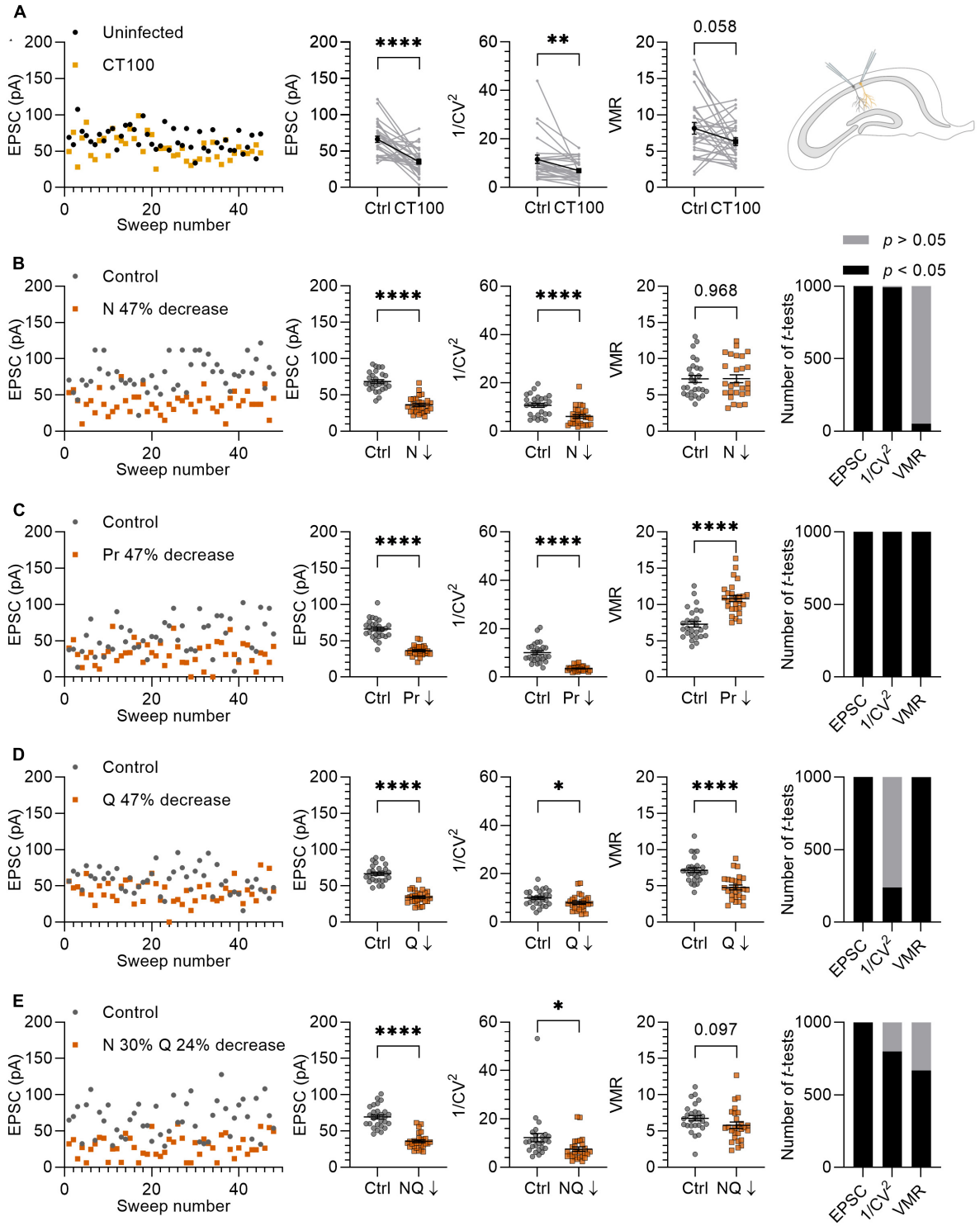

FIGURE 5

Variance analysis predicts the effects of Aβ on synapses. **(A)** Left panel: example traces of EPSCs from uninfected neuron (black circles) and infected neighboring neuron expressing APP_{CT100} (yellow squares). Middle panels: with averages of EPSC, $1/CV^2$ and VMR in uninfected neurons and their neighboring APP_{CT100}-infected neurons. Right panel: schematic representation of two CA1 neurons (uninfected and infected) that are recorded simultaneously. **(B–E)** Left panel: example traces of *in silico* control neuron (grey circles; $N = 10$, $P_r = 0.46 \pm 0.23$, $Q = 15 \pm 4.5$ pA) and test neuron in which N, P_r, and Q are changed to achieve a ~47% reduction in EPSC amplitude (orange squares). Middle panels: averages of EPSC, $1/CV^2$ and VMR between control and test neurons ($n = 27$). Right panel: simulations were run 1,000 times and differences in EPSC, $1/CV^2$ and VMR were assessed using *t*-tests and checked for statistical significance. **(B)** N is reduced by ~47% ($N = 5$); P_r and Q are unchanged compared to control. **(C)** P_r is reduced by 47% ($P_r = 0.24 \pm 0.15$); N and Q are unchanged compared to control. **(D)** Q is reduced by 47% ($Q = 7.95 \pm 4.5$ pA); N and P_r are unchanged compared to control. **(E)** N is decreased by 30% ($N = 7$) and Q is decreased by 24% ($Q = 11.36 \pm 4.5$ pA), P_r is unchanged compared to the control. Statistics: paired *t*-test **(A)**; unpaired *t*-test **(B–D)**. Error bars indicate SEM; $^*p < 0.05$; $^{**}p < 0.01$, $^{****}p < 0.0001$.

comparisons were either statistically significant or non-significant in nearly all repetitions for **Figures 5B, C**, the change in $1/CV^2$ upon a decrease in Q reached significance in only 239 out of 1,000 repetitions (**Figure 5D**). In conclusion, this variance analysis predicts that APP_{CT100} expression predominantly causes a loss of functional release sites, with possibly also a contribution of a decrease in quantal size at remaining functional release sites, and little change in presynaptic release probability.

For a more tailored reproduction, we based our *in silico* parameters on previous findings in similar models to the experiment described here (Kessels et al., 2013). APP and APP_{CT100} expression consistently cause a ∼30% spine loss in CA1 dendrites across different studies (Hsieh et al., 2006; Kessels et al., 2010; Reinders et al., 2016). APP expression was reported not to affect presynaptic release probability in Sc-CA1 synapses, shown by an absence of change in paired-pulse facilitation (Kamenetz et al., 2003). There is also evidence that APP expression causes AMPAR removal in remaining Sc-CA1 synapses. Specifically, a ∼25% spine surface reduction of GluA1-expressing AMPARs was found (Hsieh et al., 2006), which predominantly contribute to AMPAR currents (Renner et al., 2017). This observation indicates a decrease in Q in the remaining synapses that did not undergo spine loss. Based on these findings we decided to decrease N by 30% (from 10 to 7 synapses) and cover the remaining EPSC amplitude reduction by lowering Q by 24% (from 15 to 11.36 ± 4.5 pA) (**Figure 5E**). With these manipulations, $1/CV^2$ decreased significantly by 39% ($p = 0.019$) and VMR decreased by 15%, without reaching statistical significance ($p = 0.097$). Repeating this *in silico* experiment a 1,000 times, $1/CV^2$ lowered significantly in 798/1,000 repetitions and the VMR lowered significantly in 667/1,000 repetitions (**Figure 5E**). These results obtained by *in silico* simulations approach the biological electrophysiology data (**Figure 5A**), demonstrating the validity of variance analysis for predicting the locus of synaptic changes.

Discussion

We show that a non-uniform distribution of release probability and postsynaptic response size in a population of synapses does not affect the outcomes of variance analysis. Testing this assumption is relevant because uniformity is implausible for any population of central synapses (Hessler et al., 1993; Rosenmund et al., 1993; Dobrunz and Stevens, 1997; Hanse and Gustafsson, 2001; Oertner et al., 2002; Dürst et al., 2022). Therefore, non-uniform populations would violate the binomial release model. We intuitively anticipated observing larger variance in synaptic responses for non-uniform populations of synapses in comparison to uniform synapses, thus the model requiring a multinomial instead of a binomial fit. Previous studies used elegant mathematical solutions by incorporating intrasynaptic and intersynaptic quantal variance of P_r and Q, thereby incorporating a multinomial model and extending equations for variance analysis (Frerking and Wilson, 1996; Silver et al., 1998). However, our simulation shows that incorporating these factors into the equations is in practice not necessary and that simple indices for $1/CV^2$ and VMR do comply with non-uniform populations of synapses. Therefore, the use of binomial statistics and $1/CV^2$ and VMR to predict the synaptic locus of plasticity is justified in the physiological context of hippocampal synapses. Importantly, our model to test the effects of non-uniformity was validated by testing effects of changes in N, P_r, and Q on variance analysis output parameters, as these output parameters did not deviate from the expected outcomes in either the uniform or the non-uniform populations. Note that non-uniform populations of *in silico* synapses show a larger range in outcomes for EPSC amplitude compared with uniform populations, without seeing this larger spread for $1/CV^2$ and VMR. This indicates that non-uniformity does lead to a larger variability in results for EPSCs, but that the change in variance relative to EPSC amplitude (i.e., $1/CV^2$ and VMR) remains largely unchanged in non-uniform versus uniform populations.

We argue that variance analysis can be used to predict whether a change in synaptic strength is of pre- or postsynaptic origin, and our *in silico* model may be used to help making such predictions. In our simulation, we programmed synapses to release maximally one vesicle per *in silico* synapse. The majority of CA1 synapses in reality contain multiple vesicle docking sites per synapse, which are potential release sites that operate independently (Schikorski and Stevens, 1997; Rudolph et al., 2015; Pulido and Marty, 2017; Sakamoto et al., 2018). As long as the release probability is sufficiently low that maximally one docked vesicle is released in response to a single action potential, N represents both the number of active release sites as well as the number of active synapses. However, predominantly at large synapses that have many docked vesicles and under conditions that allow high release probabilities, multivesicular release can occur at CA1 synapses (Oertner et al., 2002; Conti and Lisman, 2003; Jensen et al., 2019; Dürst et al., 2022). In addition, in many other types of synapses multivesicular release may be more common than previously thought (Rudolph et al., 2015). For instance, a recent study that used a combination of electron microscopy and variance analysis of electrophysiological recordings demonstrates that in the mouse neocortex the number of release sites appeared to be at least 2.7-fold higher than the number of anatomical synapses (Holler et al., 2021). Therefore, when applying variance analysis on groups of synapses that may have multivesicular release, a decrease in N may not necessarily predict a loss or silencing of synapses (Isaac et al., 1995; Liao et al., 1995; Kerchner and Nicoll, 2008) but instead should be interpreted as presynaptic inactivation of vesicle release sites or postsynaptic silencing of active zones. Another potential factor of caution in interpreting variance analysis data is whether Q solely represents postsynaptic changes or also presynaptic changes. There is evidence that the amount of neurotransmitter stored in vesicles can vary slightly (Hanse and Gustafsson, 2001; Wu et al., 2007; Goh et al., 2011; Takamori, 2016). However, vesicles that are not completely filled have much lower release probabilities (Rost et al., 2015), suggesting that the relationship between the amount of neurotransmitter in a vesicle and its release probability can be a mechanism that ensures quantal uniformity (Rost et al., 2015; Dürst et al., 2022). These studies imply that when variance analysis predicts a change in Q, this can most likely be attributed to postsynaptic plasticity.

As an example to assess the predictive value of variance analysis, we applied it to an experiment that has been used to study the effects of Aβ on synapses. In this model system,

CA1 neurons in rat organotypic slices that acutely overproduce APP or APP_{CT100} show reduced synaptic plasticity and a loss of ∼30% of spines at their apical dendrites (Hsieh et al., 2006; Kessels et al., 2010; Wei et al., 2010; Reinders et al., 2016). The remaining synapses in APP_{CT100}-expressing CA1 neurons have reduced AMPAR levels, with a substantial loss of GluA3-containing AMPARs and to a lesser extent GluA1-containing ones are removed from synapses (Hsieh et al., 2006). Because GluA3-containing AMPARs contribute little to synaptic currents of CA1 neurons under basal conditions (Renner et al., 2017), the removal of 25% of GluA1-containing AMPARs will predominantly cause a reduced synaptic transmission in these neurons. Although Aβ can affect presynaptic release (Barthet and Mulle, 2020), in this model system release probability is not affected (Kamenetz et al., 2003), likely because APP_{CT100} is only acutely produced at the postsynaptic neuron and not presynaptically. The outcomes of variance analysis in our electrophysiological recordings of APP_{CT100}-expressing CA1 neurons are in line with these previous observations. Moreover, if we mimic these effects by reducing N and Q in the *in silico* model, the variance analysis parameters closely match the changes caused by Aβ overproduction in the electrophysiological data. We note that Aβ overproduction appears to mainly target smaller spines, because PSD-95, a prominent synaptic scaffolding protein that is relatively more enriched at large synapses, protects synapses from Aβ (Dore et al., 2021). As a consequence, Aβ overproduction would also change the distribution of P_r and/or Q. Yet, as we demonstrate in this study, such a change in distribution does not affect variance analysis results.

We here propose that variance analysis using both $1/CV^2$ and VMR can have a predictive value to assess how a change in synaptic transmission has occurred. Although we here show that variance analysis results are independent of the uniformity of synapses, we remain cautious for using variance analysis to predict absolute values of N, P_r, or Q. Instead we advocate this method as a useful tool to predict whether a change in synaptic transmission is caused by a change in N, P_r, and/or Q (van Huijstee and Kessels, 2020). As such, variance analysis can be reliably used as a simple and effective tool to characterize synaptic changes identified in evoked electrophysiological recordings to give direction in further experiments to measure parameters of synaptic plasticity more directly and in a quantitative manner.

Data availability statement

The raw data supporting the conclusions of this article will be made available by the authors, without undue reservation.

Ethics statement

The animal study was reviewed and approved by the Animal Experiment Committee, Swammerdam Institute for Life Sciences, University of Amsterdam.

Author contributions

LL and HK conceptualized the project. LL and AH performed experiments and data analysis. NC wrote the code for the *in silico* model. LL, NC, and HK wrote the manuscript. HK supervised and acquired funding. All authors approved the final manuscript.

Funding

This work was supported by Alzheimer Nederland (WE.03-2020-06) and the Dutch Brain Foundation (Hersenstichting; project DR-2018-00252).

Conflict of interest

The authors declare that the research was conducted in the absence of any commercial or financial relationships that could be construed as a potential conflict of interest.

Publisher's note

Supplementary material

The Supplementary Material for this article can be found online at: https://www.frontiersin.org/articles/10.3389/fncel.2023.1232541/full#supplementary-material

References

Barthet, G., and Mulle, C. (2020). Presynaptic failure in Alzheimer's disease. *Prog. Neurobiol.* 194:101801. doi: 10.1016/j.pneurobio.2020.101801

Bekkers, J. M., and Stevens, C. F. (1990). Presynaptic mechanism for long-term potentiation in the hippocampus. *Nature* 346, 724–729. doi: 10.1038/346724a0

Brock, J. A., Thomazeau, A., Watanabe, A., Li, S. S. Y., and Sjöström, P. J. (2020). A practical guide to using CV analysis for determining the locus of synaptic plasticity. *Front. Synaptic Neurosci.* 12:11. doi: 10.3389/fnsyn.2020.00011

Christie, J. M., and Jahr, C. E. (2006). Multivesicular release at Schaffer collateral-CA1 hippocampal synapses. *J. Neurosci.* 26, 210–216. doi: 10.1523/JNEUROSCI.4307-05.2006

Conti, R., and Lisman, J. (2003). The high variance of AMPA receptor-and NMDA receptor-mediated responses at single hippocampal synapses: Evidence for multiquantal release. *Proc. Natl. Acad. Sci. U.S.A.* 100, 4885–4890.

Del Castillo, J., and Katz, B. (1954). Quantal components of the end-plate potential. *J. Physiol.* 124, 560–573. doi: 10.1113/jphysiol.1954.sp005129

Dobrunz, L. E., and Stevens, C. F. (1997). Heterogeneity of release probability, facilitation, and depletion at central synapses. *Neuron* 18, 995–1008.

Dodge, F. A., and Rahamimoff, R. (1967). Co-operative action of calcium ions in transmitter release at the neuromuscular junction. *J. Physiol.* 193, 419–432. doi: 10.1113/jphysiol.1967.sp008367

Dore, K., Carrico, Z., Alfonso, S., Marino, M., Koymans, K., Kessels, H. W., et al. (2021). PSD-95 protects synapses from β-amyloid. *Cell Rep.* 35:109194. doi: 10.1016/j.celrep.2021.109194

Dürst, C. D., Wiegert, J. S., Schulze, C., Helassa, N., Török, K., and Oertner, T. G. (2022). Vesicular release probability sets the strength of individual Schaffer collateral synapses. *Nat. Commun.* 13:6126. doi: 10.1038/s41467-022-33565-6

Frerking, M., and Wilson, M. (1996). Effects of variance in mini amplitude on stimulus-evoked release: A comparison of two models. *Biophys. J.* 70, 2078–2091. doi: 10.1016/S0006-3495(96)79774-6

Goh, G. Y., Huang, H., Ullman, J., Borre, L., Hnasko, T. S., Trussell, L. O., et al. (2011). Presynaptic regulation of quantal size: K+/H+ exchange stimulates vesicular glutamate transport. *Nat. Neurosci.* 14, 1285–1292. doi: 10.1038/nn.2898

Hanse, E., and Gustafsson, B. (2001). Quantal variability at glutamatergic synapses in area CA1 of the rat neonatal hippocampus. *J. Physiol.* 531, 467–480. doi: 10.1111/j.1469-7793.2001.0467i.x

Hardingham, N. R., Bannister, N. J., Read, J. C. A., Fox, K. D., Hardingham, G. E., and Jack, J. J. B. (2006). Extracellular calcium regulates postsynaptic efficacy through group 1 metabotropic glutamate receptors. *J. Neurosci.* 26, 6337–6345. doi: 10.1523/JNEUROSCI.5128-05.2006

Hessler, N. A., Shirke, A. M., and Malinow, R. (1993). The probability of transmitter release at a mammalian central synapse. *Nature* 366, 569–572. doi: 10.1038/366569a0

Hogrefe, N., Blom, S. M., Valentinova, K., Ntamati, N. R., Jonker, L. J. E., Nevian, N. E., et al. (2022). Long-lasting, pathway-specific impairment of a novel form of spike-timing-dependent long-term depression by neuropathic pain in the anterior cingulate cortex. *J. Neurosci.* 42, 2166–2179. doi: 10.1523/JNEUROSCI.0326-21.2022

Holler, S., Köstinger, G., Martin, K. A. C., Schuhknecht, G. F. P., and Stratford, K. J. (2021). Structure and function of a neocortical synapse. *Nature* 591, 111–116. doi: 10.1038/s41586-020-03134-2

Hsieh, H., Boehm, J., Sato, C., Iwatsubo, T., Tomita, T., Sisodia, S., et al. (2006). AMPAR removal underlies Aβ-induced synaptic depression and dendritic spine loss. *Neuron* 52, 831–843. doi: 10.1016/j.neuron.2006.10.035

Isaac, J. T. R., Nicoll, R. A., and Malenka, R. C. (1995). Evidence for silent synapses: Implications for the expression of LTP. *Neuron* 15, 427–434. doi: 10.1016/0896-6273(95)90046-2

Jensen, T. P., Zheng, K., Cole, N., Marvin, J. S., Looger, L. L., and Rusakov, D. A. (2019). Multiplex imaging relates quantal glutamate release to presynaptic Ca2+ homeostasis at multiple synapses in situ. *Nat. Commun.* 10:1414. doi: 10.1038/s41467-019-09216-8

Kamenetz, F., Tomita, T., Hsieh, H., Seabrook, G., Borchelt, D., Iwatsubo, T., et al. (2003). APP processing and synaptic function. *Neuron* 37, 925–937. doi: 10.1016/S0896-6273(03)00124-7

Kerchner, G. A., and Nicoll, R. A. (2008). Silent synapses and the emergence of a postsynaptic mechanism for LTP. *Nat. Rev. Neurosci.* 9, 813–825. doi: 10.1038/nrn2501

Kessels, H. W., and Malinow, R. (2009). Synaptic AMPA receptor plasticity and behavior. *Neuron* 61, 340–350. doi: 10.1016/j.neuron.2009.01.015

Kessels, H. W., Nabavi, S., and Malinow, R. (2013). Metabotropic NMDA receptor function is required for β-amyloid-induced synaptic depression. *Proc. Natl. Acad. Sci. U.S.A.* 110, 4033–4038. doi: 10.1073/pnas.1219605110

Kessels, H. W., Nguyen, L. N., Nabavi, S., and Malinow, R. (2010). The prion protein as a receptor for amyloid-beta. *Nature* 466, E3–E4; discussion E4–5. doi: 10.1038/nature09217

Knafo, S., Sánchez-Puelles, C., Palomer, E., Delgado, I., Draffin, J. E., Mingo, J., et al. (2016). PTEN recruitment controls synaptic and cognitive function in Alzheimer's models. *Nat. Neurosci.* 19, 443–453. doi: 10.1038/nn.4225

Korn, H., and Faber, D. S. (1991). Quantal analysis and synaptic efficacy in the CNS. *Trends Neurosci.* 14, 439–445. doi: 10.1016/0166-2236(91)90042-S

Liao, D., Hessler, N. A., and Malinow, R. (1995). Activation of postsynaptically silent synapses during pairing-induced LTP in CA1 region of hippocampal slice. *Nature* 375, 400–404. doi: 10.1038/375400a0

Lupica, C. R., Proctor, W. R., and Dunwiddie, T. V. (1992). Presynaptic inhibition of excitatory synaptic transmission by adenosine in rat hippocampus: Analysis of unitary EPSP variance measured by whole-cell recording. *J. Neurosci.* 12, 3753–3764. doi: 10.1523/JNEUROSCI.12-10-03753.1992

Malinow, R., and Tsien, R. W. (1990). Presynaptic enhancement shown by whole-cell recordings of long-term potentiation in hippocampal slices. *Nature* 346, 177–180. doi: 10.1038/346177a0

Martin, S. J., Grimwood, P. D., and Morris, R. G. (2000). Synaptic plasticity and memory: An evaluation of the hypothesis. *Annu. Rev. Neurosci.* 23, 649–711. doi: 10.1146/annurev.neuro.23.1.649

Maschi, D., and Klyachko, V. A. (2020). Spatiotemporal dynamics of multi-vesicular release is determined by heterogeneity of release sites within central synapses. *Elife* 9:e55210. doi: 10.7554/eLife.55210

Oertner, T. G., Sabatini, B. L., Nimchinsky, E. A., and Svoboda, K. (2002). Facilitation at single synapses probed with optical quantal analysis. *Nat. Neurosci.* 5, 657–664. doi: 10.1038/nn867

Pulido, C., and Marty, A. (2017). Quantal fluctuations in central mammalian synapses: Functional role of vesicular docking sites. *Physiol. Rev.* 97, 1403–1430. doi: 10.1152/physrev.00032.2016

Quastel, D. M. (1997). The binomial model in fluctuation analysis of quantal neurotransmitter release. *Biophys. J.* 72, 728–753. doi: 10.1016/s0006-3495(97)78709-5

Redman, S. (1990). Quantal analysis of synaptic potentials in neurons of the central nervous system. *Physiol. Rev.* 70, 165–198. doi: 10.1152/physrev.1990.70.1.165

Reinders, N. R., Pao, Y., Renner, M. C., Da Silva-Matos, C. M., Lodder, T. R., Malinow, R., et al. (2016). Amyloid-β effects on synapses and memory require AMPA receptor subunit GluA3. *Proc. Natl. Acad. Sci. U.S.A.* 113, E6526–E6534. doi: 10.1073/pnas.1614249113

Renner, M. C., Albers, E. H., Gutierrez-Castellanos, N., Reinders, N. R., van Huijstee, A. N., Xiong, H., et al. (2017). Synaptic plasticity through activation of GluA3-containing AMPA-receptors. *Elife* 6:e25462. doi: 10.7554/eLife.25462

Rosenmund, C., Clements, J. D., and Westbrook, G. L. (1993). Nonuniform probability of glutamate release at a hippocampal synapse. *Science* 262, 754–757. doi: 10.1126/science.7901909

Rost, B. R., Schneider, F., Grauel, M. K., Wozny, C., Bentz, C., Blessing, A., et al. (2015). Optogenetic acidification of synaptic vesicles and lysosomes. *Nat. Neurosci.* 18, 1845–1852. doi: 10.1038/nn.4161

Rudolph, S., Tsai, M.-C., von Gersdorff, H., and Wadiche, J. I. (2015). The ubiquitous nature of multivesicular release. *Trends Neurosci.* 38, 428–438. doi: 10.1016/j.tins.2015.05.008

Sakamoto, H., Ariyoshi, T., Kimpara, N., Sugao, K., Taiko, I., Takikawa, K., et al. (2018). Synaptic weight set by Munc13-1 supramolecular assemblies. *Nat. Neurosci.* 21, 41–55. doi: 10.1038/s41593-017-0041-9

Schikorski, T., and Stevens, C. F. (1997). Quantitative ultrastructural analysis of hippocampal excitatory synapses. *J. Neurosci.* 17, 5858–5867.

Selkoe, D. J. (2002). Alzheimer's disease is a synaptic failure. *Science (1979)* 298, 789–791. doi: 10.1126/science.1074069

Silver, R. A., Momiyama, A., and Cull-Candy, S. G. (1998). Locus of frequency-dependent depression identified with multiple-probability fluctuation analysis at rat climbing fibre - Purkinje cell synapses. *J. Physiol.* 510, 881–902. doi: 10.1111/j.1469-7793.1998.881bj.x

Stoppini, L., Buchs, P.-A., and Muller, D. (1991). A simple method for organotypic cultures of nervous tissue. *J. Neurosci. Methods* 37, 173–182.

Takamori, S. (2016). Presynaptic molecular determinants of quantal size. *Front. Synaptic Neurosci.* 8:2. doi: 10.3389/fnsyn.2016.00002

Uyaniker, S., van der Spek, S. J. F., Reinders, N. R., Xiong, H., Li, K. W., Bossers, K., et al. (2019). The effects of sindbis viral vectors on neuronal function. *Front. Cell. Neurosci.* 13:362. doi: 10.3389/fncel.2019.00362

van Huijstee, A. N., and Kessels, H. W. (2020). Variance analysis as a tool to predict the mechanism underlying synaptic plasticity. *J. Neurosci. Methods* 331:108526. doi: 10.1016/j.jneumeth.2019.108526

Ventura, R., and Harris, K. M. (1999). Three-dimensional relationships between hippocampal synapses and astrocytes. *J. Neurosci.* 19, 6897–6906. doi: 10.1523/JNEUROSCI.19-16-06897.1999

Wei, W., Nguyen, L. N., Kessels, H. W., Hagiwara, H., Sisodia, S., and Malinow, R. (2010). Amyloid beta from axons and dendrites reduces local spine number and plasticity. *Nat. Neurosci.* 13, 190–196. doi: 10.1038/nn.2476

Wu, X.-S., Xue, L., Mohan, R., Paradiso, K., Gillis, K. D., and Wu, L.-G. (2007). The origin of quantal size variation: Vesicular glutamate concentration plays a significant role. *J. Neurosci.* 27, 3046–3056. doi: 10.1523/JNEUROSCI.4415-06.2007

frontiers | Frontiers in Cellular Neuroscience

TYPE Original Research
PUBLISHED 20 July 2023
DOI 10.3389/fncel.2023.1221147

OPEN ACCESS

EDITED BY
Jacopo Lamanna,
Vita-Salute San Raffaele University, Italy

REVIEWED BY
Jonathan S. Marvin,
Janelia Research Campus, United States
Roman A. Romanov,
Medical University of Vienna, Austria

*CORRESPONDENCE
Andreas Toft Sørensen
✉ andreass@sund.ku.dk

†These authors have contributed equally to this work and share first authorship

RECEIVED 11 May 2023
ACCEPTED 06 July 2023
PUBLISHED 20 July 2023

CITATION
Christensen EK, Konomi-Pilkati A, Rombach J, Comaposada-Baro R, Wang H, Li Y and Sørensen AT (2023) Detection of endogenous NPY release determined by novel GRAB sensor in cultured cortical neurons. *Front. Cell. Neurosci.* 17:1221147. doi: 10.3389/fncel.2023.1221147

Detection of endogenous NPY release determined by novel GRAB sensor in cultured cortical neurons

Emma Kragelund Christensen[1†], Ainoa Konomi-Pilkati[1†], Joscha Rombach[1], Raquel Comaposada-Baro[1], Huan Wang[2,3], Yulong Li[2,3] and Andreas Toft Sørensen[1*]

[1]Molecular Neuropharmacology and Genetics Laboratory, Department of Neuroscience, Faculty of Health and Medical Sciences, University of Copenhagen, Copenhagen, Denmark, [2]State Key Laboratory of Membrane Biology, Peking University School of Life Sciences, Beijing, China, [3]PKU-IDG/McGovern Institute for Brain Research, Beijing, China

Neuropeptide Y (NPY) is an abundantly expressed peptide in the nervous system. Its widespread distribution along with its receptors, both centrally and peripherally, indicates its broad functions in numerous biological processes. However, the low endogenous concentration and diffuse distribution of NPY make it challenging to study its actions and dynamics directly and comprehensively. Studies on the role of NPY have primarily been limited to exogenous application, transgene expression, or knock-out in biological systems, which are often combined with pharmacological probes to delineate the involvement of specific NPY receptors. Therefore, to better understand the function of NPY in time and space, direct visualization of the real-time dynamics of endogenous NPY is a valuable and desired tool. Using the first-generation and newly developed intensiometric green fluorescent G-protein-coupled NPY sensor (GRAB NPY1.0), we, for the first time, demonstrate and characterize the direct detection of endogenously released NPY in cultured cortical neurons. A dose-dependent fluorescent signal was observed upon exogenous NPY application in nearly all recorded neurons. Pharmacologically evoked neuronal activity induced a significant increase in fluorescent signal in 32% of neurons, reflecting the release of NPY, despite only 3% of all neurons containing NPY. The remaining pool of neurons expressing the sensor were either non-responsive or displayed a notable decline in the fluorescent signal. Such decline in fluorescent signal was not rescued in cortical cultures transduced with an NPY overexpression vector, where 88% of the neurons were NPY-positive. Overexpression of NPY did, however, result in sensor signals that were more readily distinguishable. This may suggest that biological factors, such as subtle changes in intracellular pH, could interfere with the fluorescent signal, and thereby underestimate the release of endogenous NPY when using this new sensor in its present configuration.

However, the development of next-generation NPY GRAB sensor technology is expected soon, and will eventually enable much-wanted studies on endogenous NPY release dynamics in both cultured and intact biological systems.

KEYWORDS

NPY, GRAB sensor, biosensor, NPY release, neuropeptides, neuronal cultures, genetically encoded fluorescent sensor

Introduction

Today, there are approximately 100 known neuropeptides. They are synthesized and released from neurons, and almost all of them bind to G-protein coupled receptors (GPCR). Not only are they key actors on both neuronal and non-neuronal cells and act in an extensive range of biological functions in the central nervous system (CNS), but they may also serve as endocrine signaling agents that can act on organs outside the CNS (Burbach, 2011; van den Pol, 2012). Moreover, expression levels of neuropeptides are altered in many disease conditions and are thought to be directly involved in several neurological conditions. Despite the existence of a variety of available techniques and tools, there are still limitations in monitoring extracellular dynamics of neurotransmitters at physiological levels with good spatial and temporal resolution, particularly when it comes to neuropeptides (Patriarchi et al., 2018; Sun et al., 2020). Techniques that can directly visualize or monitor endogenous neuropeptide function and dynamics *ex vivo* or *in vivo* are almost non-existent.

Neuropeptide Y (NPY) was discovered back in 1982 (Tatemoto et al., 1982), but the multiple biological actions of neuropeptide Y (NPY), the circumstances under which endogenous NPY is released, and its dynamics within biological systems remain largely incompletely understood. This can be attributed to the fact that NPY, along with neuropeptides in general, is challenging to study. The challenges arise due to a common set of characteristics for neuropeptides, such as low endogenous concentrations, acting on cell surface receptors over a relatively large distance, diffuse degradation patterns, a large number of isoforms (DeLaney et al., 2018), and pronounced adsorption to surfaces (Kendrick, 1990; Kristensen et al., 2015). Moreover, since neuropeptides, including NPY, positively or negatively modulate the activity of co-released neurotransmitters, they are best understood regarding their influence on other neurotransmitter systems (Hirsch and Zukowska, 2012; Nusbaum et al., 2017). Hence, the present understanding of neuropeptide dynamics is, to a large extent, extrapolated from measures of how they modulate other neurotransmitter signaling systems, and not by directly probing the neuropeptides themselves. Owing to these technical obstacles, "*the question of neuropeptide signaling has since the discovery of neuropeptides largely faded from view with a few exceptions*" to quote Nobel Prize laureate Thomas C. Südhof (Südhof, 2017).

The prevailing techniques used to determine how NPY affects synaptic transmission are electrophysiological and typically rely on observing the effect of exogenous NPY on glutamatergic transmission (El Bahh et al., 2002; Li et al., 2017). Such indirect measurement provides high temporal resolution at the expense of poor spatial resolution because it is typically limited to recording at the single-cell or local field level. Determining the effect of endogenous NPY actions is more demanding. This can be achieved by using pharmacological probes targeting NPY receptors or exploiting NPY-system knock-out models, but again the readout is indirect and typically relies on glutamatergic transmission (Lin et al., 2004; Shiozaki et al., 2020; Cattaneo et al., 2021). To visualize the release and dynamics of NPY directly, one option is to fluorescently tag the peptide. However, peptide tagging only allows the detection of transgene NPY as it is introduced by transgene gene expression (Hoogstraaten et al., 2020). An alternative technique used to investigate endogenous NPY dynamics is microdialysis, but this also exhibits limitations. Microdialysis suffers from poor temporal resolution and is spatially limited to the probe size (Kennedy, 2013), but more importantly, the adhesive nature of NPY has made this technique notably inaccurate to measure the levels of NPY (Kendrick, 1990; Lambert et al., 1994). Altogether, these technical circumstances showcase that progress in NPY research is functionally limited by the scientific tools available.

Recent advanced technologies relying on fluorescent-based imaging using biosensors, such as the G-protein-coupled receptor (GPCR) activation-based sensors (GRAB sensors), represent a compelling breakthrough, including for NPY research. GRAB sensors are genetically encoded GPCRs tethered to a confirmation-sensitive circular-permuted EGFP (cpEGFP) that enables a ligand-binding dependent change in fluorescence intensity (Nasu et al., 2021; Wang et al., 2022; Wu et al., 2022b). GRAB sensors are highly ligand-specific and display rapid activation kinetics, thereby providing excellent spatiotemporal resolution for studying neurotransmitters or neuromodulators, such as NPY (Patriarchi et al., 2018; Sun et al., 2020; Wu et al., 2022a). The GPCR used for the recently developed NPY GRAB sensor (GRAB NPY1.0) is the NPY receptor type 1 (Y1 receptor) (Wang et al., 2022). The Y1 receptor is one of the most abundant Y-receptors in the brain of humans, rats, and mice (Sperk et al., 2007; Tasan et al., 2016). One property characterizing the Y1 receptor is that it requires the full-length NPY (1–36) for activation and that it rapidly loses affinity toward truncated variants (Larhammar and Salaneck, 2004), such as NPY3-36 that also binds to Y2 and Y5 receptors (Abid et al., 2009). Hence, the GRAB NPY1.0 sensor based on the Y1 receptor scaffold is tuned for studying the release of full-length NPY.

Until now, the current GRAB NPY1.0 sensor has been characterized in HEK293T cells and rat primary cortical neurons. The sensor displays high selectivity toward NPY and not to other neuropeptides (CRF, NTS, SST, CCK, and VIP) and classical neurotransmitters (glutamate, GABA, dopamine, acetylcholine) tested. Moreover, changes in the fluorescent signal are blocked

upon application of BIBO, a specific Y1 receptor antagonist (Wang et al., 2022). Since these initial characterizations were exclusively done using exogenous applied NPY, we here investigated whether the sensor is capable of detecting the release of endogenous NPY in cultured cortical neurons obtained from mice. We transduced the cultures with an adeno-associated viral (AAV) vector expressing the GRAB NPY1.0 sensor and performed live-imaging experiments. To evoke neuronal activity, we used either a pharmacological or chemical protocol. The studies were further complemented in combination with an AAV vector expressing full-length NPY as well as employing the red-shifted calcium sensor, sRGECO.

Materials and methods

Neuronal cell cultures

Culturing of glia cells for co-culture

Neurons were co-cultured on a glial monolayer. Stocks of glial cells were prepared by isolating glial cells from 1-day-old (P1) rat cortices (male and female, randomly selected). The dissociated cells were seeded in DMEM with HEPES "1965" media (Gibco, Scotland, #52100-039) containing 11% FBS, and 0.3% penicillin-streptomycin (P/S; Sigma-Aldrich, Germany, #P0781) and grown at 37°C in a humidified incubator with 10% CO_2. When the seeded glia had reached a ∼80% confluency, the glia cells were plated on 25 mm or 18 mm coverslips coated with poly-D-lysine (Sigma-Aldrich, Germany, #2796-99-4) and laminin (Sigma-Aldrich, Germany, #L2020) and allowed to form a monolayer before seeding the neurons. If necessary, FDU (Sigma-Aldrich, Germany, #F0503) was added to the glia cultures to avoid overgrowth. The day before seeding the neurons to the glial monolayer, the media was changed to Neurobasal A media (Thermofisher, #10888022) containing 1% Glutamax (Gibco, Scotland, #35050061), 2% B-27 Plus (Thermofisher, #A3582801), and 0.1% P/S.

Culturing of primary neurons

Cortex was isolated from postnatal day 1–2 (P1-P2) mice (C57Bl/6, Charles River, Germany), and the meninges were removed in ice-cold dissection media containing 10% 10xHBSS (Gibco, Scotland, #14065056), 1% P/S, 1% sodium pyruvate (Gibco, Scotland, #11360070), 1% 1M HEPES (Gibco, Scotland), and 1.2% 45% glucose (Sigma-Aldrich, Germany). The cortices were cut into smaller pieces and incubated for 20–30 min at 37°C in papain solution containing 20 units/mL papain (Worthington Biochemical, #LS003126), 1mM L-cysteine (Sigma-Aldrich, Germany, #C7352), 1.9 mM CaCl2 (Sigma-Aldrich, Germany), 0.5 mM Kynurenic acid (Sigma-Aldrich, Germany, #K3375), pH adjusted to 7.4 with HCl and oxygenated with 95% O2 and 5% CO_2. After incubation, the tissue was washed 3 times with Neurobasal A media and carefully triturated 3–5 times with a glass Pasteur pipette with a fire-polished tip. The dissociated cortical neurons were plated at a density of 100,000 or 150,000 cells/well onto the glia monolayered 18- or 25-mm coverslips, respectively, and grown in Neurobasal A media containing 1% Glutamax, 2% B-27, and 0.1% P/S. The day after seeding the neurons, half of the media was changed to remove any cell debris. Every 3–4 days, 1/4 of the media in the wells was removed and replaced with double of the removed volume of fresh neuronal media. The use of experimental animals was conducted in concordance with the Danish Research Ethical Committee for Experimental Animals (ethical permit #2017-15-0202-00092; PI: Andreas Toft Sørensen).

Viral vectors and transduction

The following AAV vectors were used for experiments: GRAB NPY1.0 sensor (AAV2/9-hSyn-GRAB_NPY1.0; 6E+12−4.7E+13 vg/ml, 1 μL/well); sRGECO calcium sensor (AAV2/8-Ef1a-sRGECO-WPRE; Addgene plasmid #137125; RRID:Addgene_137125; 2.2E+13 vg/ml, 0.2 μL/well) (Fenno et al., 2020); NPY1-36 vector (AAV2/8-hSyn-PreproNPY-WPREpA; full-length peptide incl. CPON; produced in-house; 7.8E+12 vg/ml, 0.5 μL/well) (Soud et al., 2019). Primary cultures were transduced after 2–3 DIV and given <14 days to assure robust expression before being used for live-cell imaging.

Immunocytochemistry

For immunocytochemistry (ICC) staining, neurons were fixed in 2% PFA for 15 min at room temperature. The coverslips were washed three times with 7.5 mM glycine (Sigma-Aldrich, Germany) in 1xPBS to block unreacted aldehydes following a single wash in 1xPBS and stored in 1xPBS at 4°C until ICC was performed. Coverslips were transferred to a humidifying chamber and washed three times with 1xPBS before being incubated in blocking buffer containing 5% goat serum, and 0.25% Triton X-100 for 30–45 min. The coverslips were then incubated with rabbit anti-NPY antibodies recognizing the C-terminal region of full-length NPY (1:1000; N9528, Sigma-Aldrich, Germany) and chicken anti-MAP2 (1:500, Ab5392, Abcam) in 5% goat serum + 0.25% Triton X-100 (Sigma-Aldrich, Germany, #93443) at 4°C overnight. The following day, the coverslips were washed four times with 1xPBS for 5 min before incubating with the secondary antibodies (1:500; goat anti-rabbit, Alexa 568 and goat-anti chicken, Alexa 488; Invitrogen) for 1 h at room temperature in 5% goat serum + 0.25% Triton X-100 excluded from light exposure. Next, the coverslips were washed three times with 1xPBS for 5 min, mounted on slides with DAPI Fluoromount-G (SouthernBiotech, #0100-20), and allowed to dry overnight. The stained coverslips were stored at 4°C excluded from light exposure.

Fluorescent live-cell imaging

Neurons were continuously perfused with artificial cerebrospinal fluid (aCSF) [120 mM NaCl, 5 mM KCl, 2 mM CaCl2, 2 mM MgCl2, 25 mM HEPES, and 30 mM D-glucose] at pH 7.4 and 32°C for all live imaging experiments. An RC-21BDW microscope flow chamber (Warner Instruments, Hamden, CT, USA) was used to hold the coverslips and to apply a flow of different aCSF and drug buffers during imaging at 20× with a Nikon Eclipse Ti microscope connected to two EM-CCD cameras (iXon3 897, Andor). A NIS-Elements software (Nikon, Tokyo, Japan) was used for recordings. GRAB NPY1.0 and sRGECO biosensors were excited with 488 nm and 561 nm laser lines (LED sapphire laser; Coherent Inc., Santa Clara, CA, USA),

respectively. For the 488 nm LED laser excitation, a 491 nm mirror, and a 475/35 nm band-pass filter were used, while a 525/50 nm band-pass filter (AHF Analysentechnik, Tübingen-Pfrondorf, Germany) was used to detect emitted light. For the 561 nm LED laser excitation, a 561 nm mirror, and a 560/40 nm band-pass filter were used, while a 630/75 nm band-pass filter (AHF Analysentechnik, Tübingen-Pfrondorf, Germany) was used to detect emitted light. The collected images were recorded either at a frame rate of 1 frame/second when recording GRAB NPY1.0 alone or 4 frames/second when the sRGECO signal was also recorded. All recordings were performed using epifluorescence microscopy.

Epifluorescence imaging was conducted under constant slow perfusion of aCSF buffers at a flow rate of approximately 1 ml/min. To induce neuronal activity, bicuculline (Bic; 50 μM; 14340, Sigma-Aldrich, Germany; dissolved in DMSO) and 4-aminopyridine (4-AP; 250 μM; 275875, Sigma-Aldrich, Germany; dissolved in Milli-Q water) was added together with aCSF, which was carefully measured after adding the compounds to confirm a pH of 7.4. Bic is a classical competitive $GABA_A$ antagonist, which increases the excitatory responses by disinhibiting neuronal signaling, whereas 4-AP is a non-selective antagonist of voltage-gated potassium (Kv) channels. Potassium chloride (KCl; 60 mM; SLCG7350; Sigma-Aldrich, Germany) in aCSF was used as an alternative stimulation method. The Y1 receptor antagonist BIBO3304 (1 μM; SML2094, Sigma Aldrich, Germany; dissolved in DMSO) and NPY (NPY1-36; 0.3, 1, 30, 1000 nM; Schafer-N, Denmark; dissolved in DMSO) were used to confirming the function of the GRAB NPY1.0 sensor. 1% bovine serum albumin (BSA) was added to all NPY-containing buffers to minimize the adsorption of NPY to surfaces. Dissolved NPY were stored in low protein binding tubes (Eppendorf Protein LoBind tubes, Sigma-Aldrich, Germany). All drugs were applied as indicated in the figures.

Data analysis and statistics

Fiji-ImageJ 1.53r software (NIH) was used for analyzing the time-lapse files from live-cell imaging of the primary cultures. Regions of interest (ROIs) were manually drawn around the neuronal somas and the plugin Time Series Analyzer V3 was used to calculate the mean intensity of the ROIs in all frames. Moreover, the intensity of two background ROIs was calculated per video. In Excel, the given ROI values were subtracted from the average value of the two background ROIs to obtain the F-values. The change in fluorescence intensity (ΔF/F0) was calculated as (F–F_baseline)/F_baseline. For videos with moving neurons, the plugin Template Matching was used to align each frame of the stack to a template frame. For all quantifications, the mean ΔF/F0 for the entire interval of the specific compound application was calculated. For the raw fluorescence images from ICC or live-cell imaging, a false color has been added for illustrative purposes. For representative images of live-cell recordings, the background was subtracted from all images, and the Image Calculator in ImageJ was used to create the final representative images of the change in fluorescence intensity. The pseudocolor images were created using the ImageJ LUT editor plugin. Identical brightness and contrast conditions were set for all images to be compared. Image scale bars were calibrated and applied in ImageJ as well. Sample sizes are indicated in the figures, and sample size calculations were not determined before the study. All GRAB NPY1.0 transduced neurons that could be identified visually by the experimenter at baseline conditions, before applying any further reagents to aCSF, were included in the analysis. A z-project was performed on the baseline frames for each recording to properly visualize and delineate a ROI around the soma of each neuron.

The ICC analysis was performed using a LSM 700 microscope to acquire 10 images from each coverslip at a 10X magnification. 3 coverslips from each condition were used for the analysis. The number of MAP2 and NPY positive neurons was counted manually in ImageJ.

Heatmaps were generated and clustering analysis was performed in R (version 4.0.4) using RStudio (version 2022.12.0). Data were grouped and averaged into time bins to combine datasets with different frame intervals. The data were combined into a matrix with rows representing neurons and columns representing bins. The matrix rows were seriated using the ARSA method in the R package seriation (version 1.4.0). Heatmaps were created from the seriated matrices using the Heatmap function from the Complexheatmap package (version 2.12.1). For Cluster analysis, the dimensionality of the matrices was reduced by principal component analysis (PCA) using the prcomp function. Clustering within the PCA space was performed using the tsclust function from the R package dtwclust (version 5.5.12) with Euclidean distances. The number of clusters was defined using the elbow method with the kmeans clustering, from the stats package (version 4.2.1).

The rest of the graphical and statistical analyses were performed using GraphPad Prism version 9 (GraphPad Software, LLC). EC50 analysis was made using the log(agonist) vs. response (three parameters) non-linear fit. Neurons presenting negative values were discarded from the EC50 analysis. One-way analysis of variance (ANOVA) followed by Tukey's multiple comparison test, one-way ANOVA followed by Dunnett's multiple comparisons, two-tailed *t*-test, Mann-Whitney test, and paired Wilcoxon paired *t*-test were performed. All comparisons were two-sided and statistical significance was defined as $^{*}p < 0.05$, $^{**}p < 0.01$, $^{***}p < 0.001$, $^{****}p < 0.0001$, ns (non-significant) $p > 0.05$.

Results

Imaging NPY responses in cultured cortical neurons using the GRAB NPY1.0 sensor

To use the GRAB NPY1.0 sensor, mouse-cultured cortical neurons were transduced with an AAV vector expressing the sensor under the control of the pan-neuronal human synapsin promoter (**Figure 1A**). Such a setup gives rise to exclusive neuronal expression while avoiding glial cell expression in the co-culture. The GRAB NPY1.0 sensor is composed of two basic units: the NPY Y1 receptor and the cpEGFP, serving as the ligand-sensing unit and reporter module, respectively. When the ligand binds, the EGFP fluorescent intensity increases enabling intensiometric readouts (**Figure 1A**). When assessing the cultures 2 weeks after transduction, sensor expression was found to be

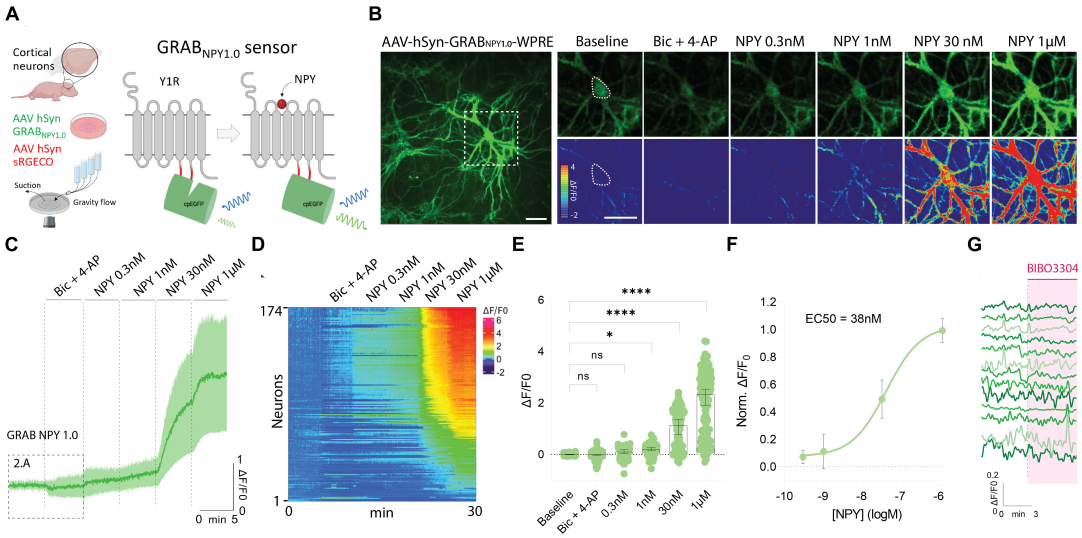

FIGURE 1
GRAB NPY1.0 sensor imaging in cultured cortical neurons during exogenous NPY application. **(A)** A schematic diagram of the basic experimental setup and principles behind the GRAB NPY1.0 sensor design. Y1R, Neuropeptide Y receptor type 1. **(B)** Left: Representative fluorescence image of GRAB NPY1.0 sensor expression during 1 µM NPY application. Scale bar, 50 µm. Right: Magnification of left image (see dotted square). The upper panels show GRAB NPY1.0 signal background subtracted during baseline, Bic + 4-AP conditions, and at different concentrations of exogenous NPY1-36. The lower panels show the corresponding scaled pseudocolor images. Scale bar, 50 µm. **(C)** Time course of GRAB NPY1.0 fluorescence presented as average (mean ± SD) ΔF/F0 trace in cortical cultures; Bic + 4-AP and different concentrations of NPY1-36 were applied where indicated. *n* = 142 neurons from 5 different coverslips. **(D)** Heatmap representation of all neurons exposed to Bic + 4-AP followed by different concentrations of applied exogenous NPY. *n* = 174 neurons from 9 different coverslips. **(E)** Quantification of mean fluorescence (ΔF/F0) at baseline, during Bic + 4-AP conditions, and different concentrations of NPY1-36. Each point represents the mean response per single neuron. *n* = 174 neurons from 9 different coverslips. Median and 95% CI are shown **(F)** normalized dose-response curve of cortical neurons expressing GRAB NPY1.0 in response to NPY. *n* = 130 neurons from 5 different coverslips. Mean and SD is shown. **(G)** Representative traces upon application of BIBO3304 to the baseline. *n* = 90 neurons from 2 different coverslips. The data in panel **(E)** were analyzed using a one-way ANOVA followed by Dunnett's multiple comparisons. ****$p < 0.0001$, *$p < 0.05$, ns (non-significant) $p > 0.05$.

widely distributed throughout the neuronal body, including the soma and neurites (Figure 1B). All neurons whose soma could be identified based on their baseline GRAB NPY1.0 fluorescent signal were selected for the analysis, independent of changes in fluorescent signal upon subsequent manipulations. Because the release of neuropeptides from large dense-core vesicles is largely facilitated by high-frequency neuronal activity, a pharmacological combination of bicuculline (Bic) and 4-Aminopyridine (4-AP) was applied together with aCSF in the flow chamber following a baseline recording. Next, in the absence of Bic + 4-AP, exogenous NPY was applied at increasing concentrations (Figure 1B). A dose-dependent response was measured here, displaying a half-maximal effective concentration in the nanomolar range (Figures 1C–F). However, 8 out of 174 neurons expressing the GRAB NPY1.0 sensor remained unresponsive, even when exposed to 1 µM of exogenous NPY (Figures 1D, E). When applying BIBO3304, an NPY Y1 receptor antagonist that blocks the GRAB NPY1.0 sensors (Wang et al., 2022), at baseline conditions, the fluorescence signaling remained unchanged (Figure 1G), suggesting no constitutive release of endogenous NPY.

Interestingly, the responses observed during Bic + 4-AP application were more diverse (Figures 2A–G). While approximately 32% of the neurons displayed an apparent increase in fluorescence intensity, suggesting the release of endogenous NPY, a fraction of neurons did not change their baseline fluorescence, while the remaining neurons surprisingly displayed a drop in fluorescent signal (Figures 2A–G). As a direct consequence, the average signal measured during Bic + 4-AP application from 351 individual neurons was statistically lower than their baseline fluorescence (Figure 2C).

Next, we tested another stimulation paradigm, applying 60 mM KCl to depolarize the neurons (Figures 2B–D). Similar to the Bic + 4-AP conditions, we observed increases and decreases in signal as well as non-responders from a total of 93 neurons recorded. This indicates that the differential responses were not exclusively related to the Bic + 4-AP application itself. Moreover, when directly comparing these two conditions, the average response was statistically lower for the KCl experiments (Figure 2C). However, a paired comparison of responses from neurons exposed to both Bic + 4-AP and KCl with an in-between washout period showed no statistical difference between the two conditions (Figure 2D). When further correlating the fluorescent intensity changes induced by these two conditions, individual neurons tended to respond similarly (Figure 2D), but this did not correlate with their response to exogenous NPY (Figure 2D). Because the GRAB NPY1.0 sensor apparently can get brighter or dimmer (Figure 2E), we additionally examined whether neighboring neurons, considering their profound interconnectivity within cultures, would display similar response patterns. Neurons within the same field of view could indeed respond as independent actors during both Bic + 4-AP and KCl conditions (Figure 2F), but tight clusters of neurons could also display a more uniform response (Figure 2G).

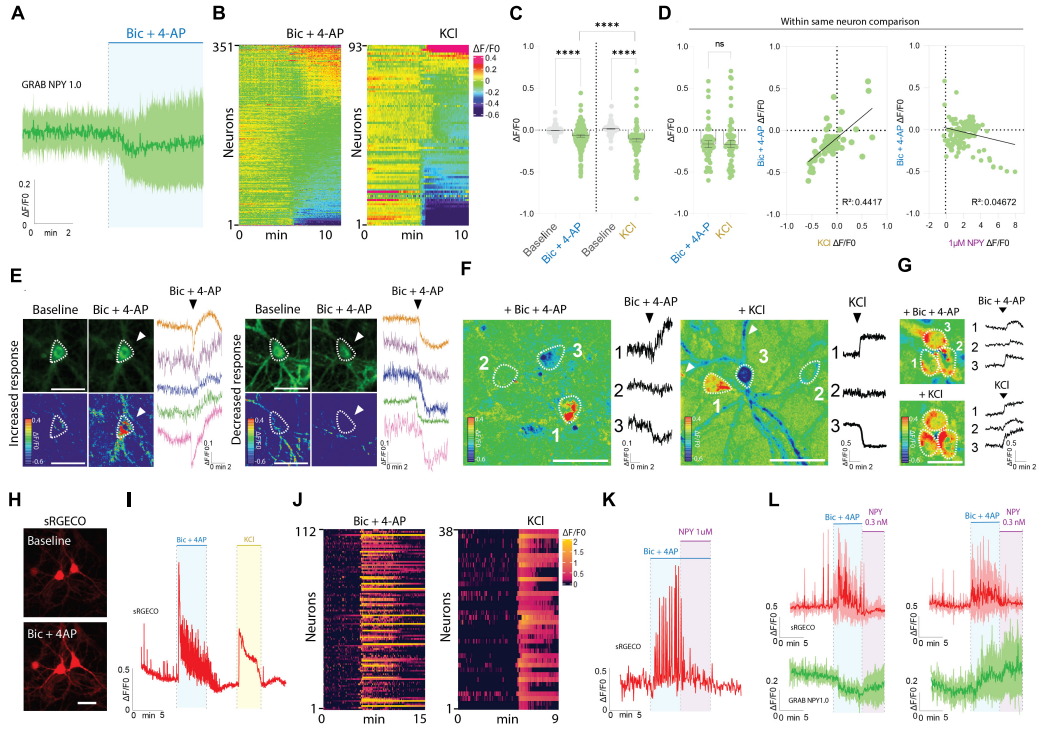

FIGURE 2
GRAB NPY1.0 sensor imaging in cortical cultures during conditions of enhanced neuronal excitability. **(A)** Magnification of the traces during Bic + 4-AP conditions shown in Figure 1C. **(B)** Heatmap representation of all neurons exposed to Bic + 4-AP, *n* = 351 from 29 different coverslips, and KCl, *n* = 93 from 5 different coverslips. **(C)** Quantification of mean fluorescent response to Bic + 4-AP and KCl stimulation of GRAB NPY1.0 expressing cortical neurons paired-compared to their corresponding baselines and non-paired between the two conditions. *n* = 351 neurons from 9 different coverslips and *n* = 93 from 5 different coverslips, respectively. **(D)** On the left, quantification and comparison between the fluorescent response (ΔF/F0) upon application of Bic + 4-AP and KCl performed in the same neuron. Middle panel, a correlation of the Bic + 4-AP and KCl responses, *n* = 56 neurons from 2 different coverslips, and right panel, a correlation between Bic + 4-AP response and NPY (1 μM) sensitivity. Median and 95% CI is shown. **(E)** Representative GRAB NPY1.0 time series images and their corresponding calibrated pseudocolored images during baseline, Bic + 4-AP conditions together with representative ΔF/F0 traces. On the left, examples of increased signal upon Bic + 4-AP application, and on the right examples of decreased fluorescence. Dotted lines indicate ROIs measured, and arrows point to the responses to Bic + 4-AP. Scale bar 50 μm. **(F)** Calibrated pseudocolored images with no background subtraction for better visualization together with ΔF/F0 traces corresponding to the outlined ROIs on the images. Showing examples of increased (1), no response (2), and decreased (3) signals in the same field of view during Bic + 4-AP (left) or KCl (right) conditions. White arrows point to the processes of the responding neurons. Scale bar 50 μm. **(G)** Calibrated pseudocolored images together with corresponding ΔF/F0 traces showing increasing responses of the same group of neurons to Bic + 4-AP or KCl. An in-between washout between the two applications was performed. The pseudocolored images are shown with no background subtraction. ΔF/F0 traces are corresponding to the outlined ROIs shown as a dotted line on the images. Scale bar 50 μm. **(H)** Representative images of sRGECO signal during baseline and Bic + 4-AP conditions. **(I)** Representative trace of sRGECO signal comparing Bic + 4-AP to KCl stimulation. **(J)** Heatmap representation of all sRGECO responses during Bic + 4-AP, *n* = 112 from 9 different coverslips, or KCl, *n* = 38 from 3 different coverslips. **(K)** Representative trace of sRGECO signal upon Bic + 4-AP application alone and together with NPY. **(L)** Time course of GRAB NPY1.0 and sRGECO fluorescence during Bic + 4-AP conditions of neurons co-expressing both sensors presented as average (mean ± SD) ΔF/F0 traces. sRGECO and GRAB NPY1.0 average responses during decreasing (left) and increasing (right) GRAB NPY1.0 signal upon Bic + 4-AP application. *n* = 69 from 8 different coverslips. The data in panel **(C)** were analyzed using a Wilcoxon paired *t*-test when comparing to baseline, and Bic + 4-AP and KCl comparison was evaluated by the Mann–Whitney test. Data in panel **(D)** was analyzed using a paired Wilcoxon paired *t*-test. ****$p < 0.0001$, ns (non-significant) $p > 0.05$.

To gain better insight into the pharmacological protocols, that can induce a rise or decrease in fluorescent signaling (Figures 2B, E–G), we next expressed the red-shifted cytoplasmic calcium sensor sRGECO (Fenno et al., 2020) to confirm that the application of the Bic and 4-AP cocktail indeed evoked high-frequency activity in cultured cortical neurons. As expected, fluorescent spikes were substantially increased (Figures 2H–L), providing a functional visualization and confirmation of induced high-frequency neuronal activity. Furthermore, the calcium response induced by either Bic + 4-AP or KCl appeared equally potent (Figure 2I). Adding exogenous NPY to the primary cultures during continuous Bic + 4-AP perfusion, on the other hand, gave rise to a marked decrease in sRGECO fluorescent signal, reflecting suppression of neuronal activity (Figure 2K) in agreement with existing literature on NPY's role in suppressing glutamatergic transmission (Qian et al., 1997; Acuna-Goycolea et al., 2005). Subsidiary experiments examining individual neurons co-transduced with both sensors further substantiated that elevated neuronal activity can give rise to both a raise or decrease in GRAB NPY1.0 fluorescence (Figure 2L).

Taken together, these data demonstrate that the GRAB NPY1.0 sensor is readily responding to increasing dosing of exogenous applied NPY. However, during conditions of enhanced neuronal activity, as confirmed by calcium signaling, the fluorescent response in GRAB NPY1.0 expressing neurons is not equally consistent. While a fraction of neurons increased their signaling, indicating

the release of endogenous NPY, the average signaling in neuronal cultures was significantly lower as compared to their baseline fluorescence (Figure 1I).

Detection of NPY release in cortical cultures overexpressing NPY

In the next series of experiments, immunocytochemistry (ICC) was performed to validate the presence of NPY-positive neurons in naive cortical cultures, processed in parallel with cultures transduced with an AAV vector containing an expression cassette encoding full-length NPY (i.e., pre-pro-NPY) (Figures 3A, B). MAP2 staining was used as a neuronal marker and DAPI as a nuclear counterstain. Based on these stainings, 2.9% of neurons in naive cultures were found to be NPY-positive (Figures 3B, C), which is consistent with previous findings showing that an estimate of 1–2% of neurons in the cerebral cortex are NPY-positive (Aoki and Pickel, 1989). For cortical cultures transduced with the AAV vector expressing NPY, 88% of the neurons were found to be NPY-positive (Figures 3B, C).

Considering the limited number of NPY-positive neurons, including the variability in fluorescent signaling seen in previous naive cultures, we next asked whether Bic + 4-AP application could enhance transgene NPY release and, hence, be more readily detectable by the GRAB NPY1.0 sensor. Previously, transgene NPY, encoded by different viral expression systems, has been shown to be released from neurons during high-frequency neuronal activity (Sørensen et al., 2008; Hoogstraaten et al., 2020). To address the question, cultured cortical neurons were co-transduced with AAV-NPY and AAV-GRAB NPY1.0 vectors. When applying Bic + 4-AP to the cultures, a similar divergence in the sensor signaling was observed. While a portion of neurons displayed an increase others showed a decrease in fluorescence intensity (Figures 3D, E, H). Due to this variation, the overall fluorescent change was not statistically different from baseline values (Figure 3F). When further adding BIBO3304, a significant drop in fluorescence was observed (Figures 3D–F). This may suggest that transgene NPY was indeed released under the present conditions, but we cannot rule out the contribution of released endogenous NPY in addition to transgene NPY. When directly comparing the intensity changes in fluorescence between endogenous NPY and transgene NPY conditions during Bic + 4-AP application, the mean signal was significantly higher for the transgene NPY condition (Figure 3G). Also, in individual neurons displaying a noticeable increase in fluorescent signaling during Bic + 4-AP conditions and blocked by BIBO3304 application (Figure 3H), it appeared that such responses were more robust as compared to neurons responding equivalent in the naïve conditions (Figure 2E). We finally confirmed that high-frequency activity induced by Bic + 4-AP application was not *per se* affected by applying BIBO3304 to the cultures (Figure 3I).

A subset of neurons expressing the GRAB NPY1.0 detects the release of endogenous NPY

Because of the variability observed in the GRAB NPY1.0 sensor responses upon Bic + 4-AP conditions, we conducted a principal component analysis and subsequent clustering of the datasets. We used similar clustering parameters to cluster the datasets obtained from naïve and transduced cultures to compare the responses. Three different clusters were defined, dividing both naïve and transgene datasets into decreased (cluster A), no response (cluster B), and increased (cluster C) signals upon Bic + 4-AP application (Figure 4A). As seen from the standard deviations of the mean fluorescent traces of each cluster (Figure 4A), the clusters obtained from naïve cultures, reflecting endogenous NPY, were more overlapping than those from transgene NPY conditions. This arrangement of clusters was further visualized by plotting the two first principal components in a scatter plot (Figure 4B). From this, 57.4% of the variance could be explained for the naïve clusters, whereas 75.1% of the variance could be explained for the transgene clustering. This indicates that the data obtained from the NPY overexpression experiments were more robustly separated into defined clusters as compared to the naïve dataset. No statistical difference was observed for cluster A when comparing fluorescent signals between naïve and transgene conditions (Figure 4C). This indicates that overexpression of NPY does not affect the decreased fluorescent signaling. However, for cluster C, the signal from the transgene condition was statistically higher (Figure 4C), indicating that a higher release of NPY can be detected in the cultures overexpressing NPY. The non-responding cluster (B) also displayed a higher signal upon Bic + 4-AP application in the transgene cultures (Figure 4C), suggesting that transgene NPY release may also be detected in this cluster. The distribution of neurons among the clusters was consistent between the endogenous and transgene experiments. The majority of neurons were classified as non-responders (Cluster B; 48.12 and 47.62%, respectively), followed by increased responders (Cluster C; 31.49% and 35.71%, respectively), and decreased responders (Cluster A; 20.41% and 16.67%, respectively), which were equally distributed between experimental conditions (Figure 4D).

Finally, we assessed how the different clusters from the transgene experiment responded to BIBO3304 application during the Bic + 4-AP conditions. Cluster A was not affected by the BIBO3304 application, while signals were significantly reduced in clusters B and C (Figures 4E, F). This further confirms that the release of transgene NPY is provoked during heightened neuronal activity and hence detectable by the GRAB NPY1.0 sensor. The decrease upon BIBO3304 application seen for the "non-responders" cluster also points out that any NPY-induced signals may be masked by activity-induced quenching of fluorescence.

Discussion

Genetically encoded fluorescent sensors are increasingly popular tools in neuroscience for investigating fundamental questions. GPCR-based biosensors are unique in their ability to directly and continuously measure the real-time dynamics of specific signaling molecules in cell cultures, tissue slices, and living animals. With a temporal resolution down to the millisecond range and a low signal-to-noise ratio, these biosensors are designed to monitor molecular dynamics at a range of physiological relevance. However, they do not provide information about the actual signaling of endogenous receptors (Jing et al., 2019; Wu et al., 2022b). As biosensors are genetically encoded, including

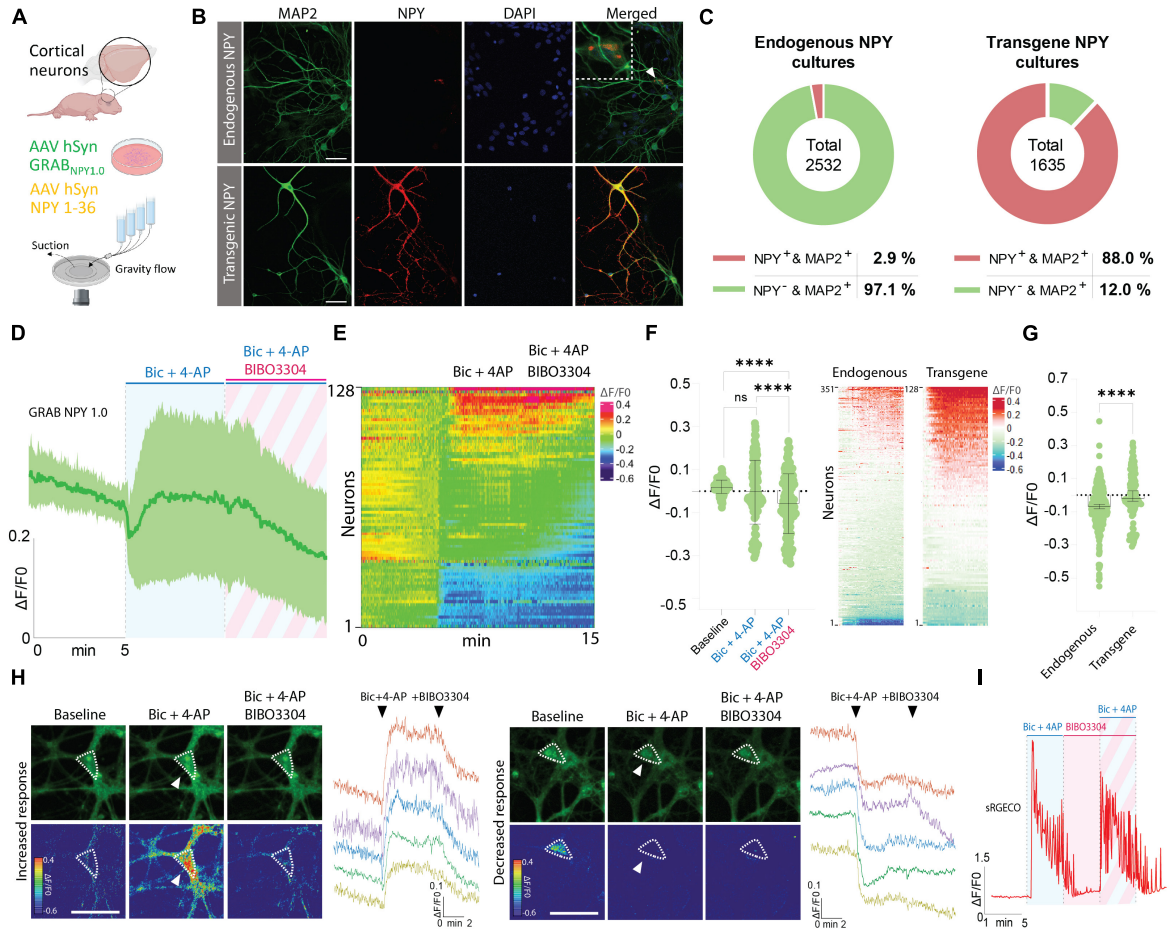

FIGURE 3
Determination of NPY-positive neurons in neuronal cultures and GRAB NPY1.0 fluorescent signaling in cultures overexpressing NPY. **(A)** Graphical representation of the experimental design. **(B)** Representative examples of ICC stainings of NPY-positive neurons in naïve and NPY transgene cultures. Scale bar 50 μm. **(C)** Percentage of NPY-positive neurons in neuronal cultures. *n* = 2,532 from 3 coverslips for endogenous NPY cultures and 1,635 from 3 coverslips for transgene NPY cultures. **(D)** Time course of GRAB NPY1.0 fluorescence presented as average (mean ± SD) ΔF/F0 trace in NPY transgene cortical cultures. **(E)** Heatmap representation of data shown in panel **(C)**. **(F)** Quantification of mean fluorescence (ΔF/F0) at baseline, Bic + 4-AP, and Bic + 4-AP + BIBO3304 application. Each circle represents the mean response per single neuron. Mean and SD is shown. **(G)** Response of NPY endogenous vs. transgene cultures to Bic + 4-AP. On the left color-simplified heatmaps showing only the Bic + 4-AP response from both conditions. Data shown in **Figures 2B**, **3E**. On the right, average response quantification of both conditions. Data shown in **Figures 2C**, **3F**. Median and 95% CI are shown. **(H)** Representative GRAB NPY1.0 time series images and their corresponding calibrated pseudocolored images during baseline, Bic + 4-AP, and Bic + 4-AP + BIBO3304 conditions. On the left, an example of increased signal upon Bic + 4-AP application, and on the right an example of decreased fluorescence. Dotted lines indicate ROIs measured, and arrows point to the responses to Bic + 4-AP. Scale bar 50 μm. **(I)** Representative trace of sRGECO signal during Bic + 4-AP application before and after incubation with the Y1R antagonist BIBO3304. For panels **(D–F)** *n* = 128 neurons from 6 coverslips. The data in panel **(F)** was analyzed using a one-way ANOVA followed by Tukey's multiple comparisons test with a single pooled variance. ****$p < 0.0001$, ns (non-significant). Data in panel **(G)** was analyzed using a Mann–Whitney test. ****$p < 0.0001$.

the GRAB sensor family, they have a major advantage in being non-invasive. The coding DNA can be delivered easily into cells using viral vectors or by simple transfection, and selective spatial distribution can be achieved by using cell-type specific promoters or Cre-reporter mouse lines, making the sensors highly versatile. Consequently, biosensors have become an indispensable tool in modern brain research due to their broad use (Dong et al., 2022).

Here, we report on the usage of the GRAB NPY1.0 sensor in mouse-cultured cortical neurons and address the question: can the sensor detect the release of endogenous NPY? This sensor, recently developed in the Yulong Li laboratory, Peking University of China, is one of six neuropeptide-based GRAB sensors engineered for detecting either SST, CCK, CRF, NTS, VIP or NPY (Wang et al., 2022). While it was shown that the SST, CCK, and CRF sensors can detect endogenously released neuropeptides (Wang et al., 2022), similar information is lacking on the NPY1.0 sensor. In our setup, we tested the NPY1.0 sensor in mouse cortical cultures, where nearly 3% of the neurons were found to be NPY-positive. The average fluorescent signal robustly increased upon application of exogenous NPY, displaying an estimated EC50 value of 38 nM (**Figure 1F**). This responsiveness is comparable to that obtained from HEK293T cells stably expressing the NPY1.0 sensor (EC50: 40 nM). However, it is considerably higher than the EC50 value of 0.7 nM reported from rat cortical neurons transduced by a similar AAV9 vector, also harboring the human synapsin promoter used here (Wang et al., 2022). At baseline condition, perfusion with the Y1 receptors antagonist, BIBO3304, did not change the GRAB NPY1.0 output (**Figure 1G**). This can be interpreted

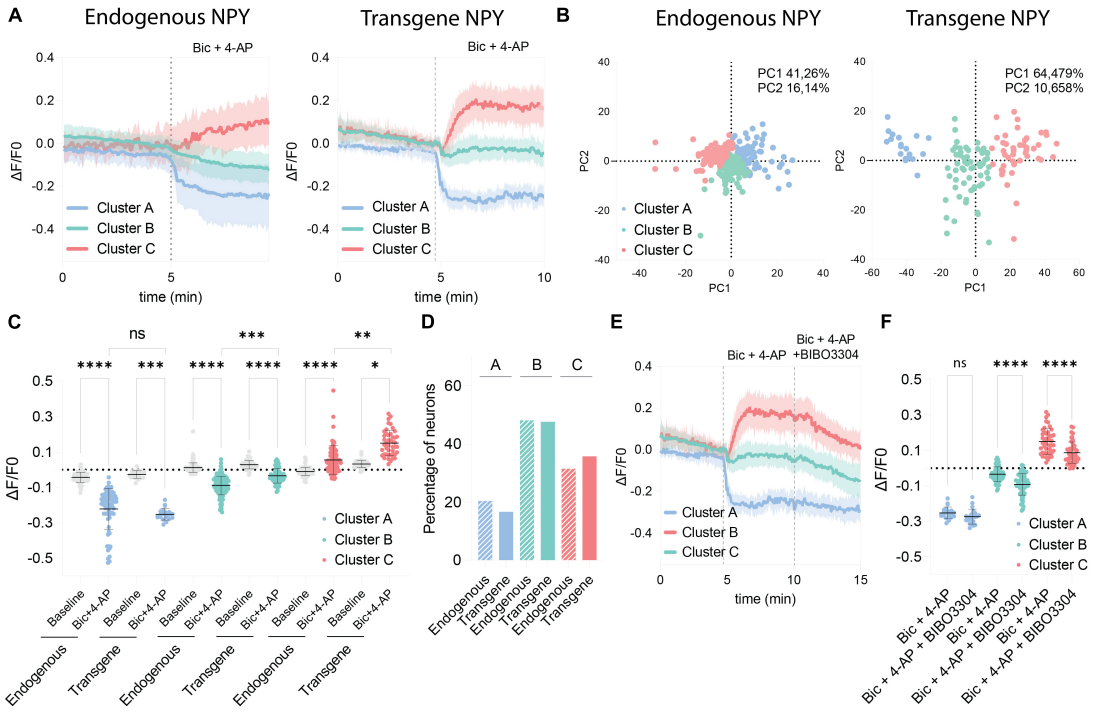

FIGURE 4
Comparison of clustered GRAB NPY1.0 signals between the endogenous and transgene NPY cultures. **(A)** Mean ΔF/F0 traces of the clustered response to Bic + 4-AP in each culture condition previously shown in **Figures 1**, **2**. *n* = 351 and *n* = 128, respectively. The shaded area corresponds to SD. **(B)** Scatterplots from the principal component analysis showing the variance explained by the clustering for both culturing conditions. **(C)** Quantification of the average ΔF/F0 signal during baseline and upon Bic + 4-AP application for each cluster from the endogenous and transgene cultures. Median and 95% CI are shown. **(D)** Bar graph showing the percentage of neurons found in each cluster. **(E)** Mean clustered traces from transgene cultures shown in panel **(A)** together with the BIBO3304 inhibition. **(F)** Quantification of the mean signal during Bic + 4-AP and Bic + 4-AP + BIBO3304 application for each of the transgene clusters shown in panel **(E)**. Mean and SD is shown. The data in panel **(C)** were analyzed using a Kruskal–Wallis test followed by Dunnett's multiple comparisons. The data in panel **(F)** was analyzed by one-way ANOVA with Geisser-Greenhouse correction ****$p < 0.0001$, ***$p < 0.001$, **$p < 0.01$, *$p < 0.05$, ns (non-significant) $p > 0.05$.

in two ways; endogenous NPY is not released during these conditions, or the overexpressed sensor is not constitutively active. Intriguingly, although the wild-type NPY Y1 receptor is reported not to be constitutively active (Chee et al., 2008), the cpEGFP reporter module of the GRAB NPY sensor is inserted in the third intracellular loop of the Y1 receptor that stabilizes its inactive state. Nonetheless, our data do not suggest that the inactive state is perturbed.

To promote the release of endogenous NPY, we used either Bic + 4-AP or KCl to enhance the level of excitability. Based on sRGECO signaling, the former gave rise to high-frequency neuronal activity while the latter resulted in sustained depolarization (**Figures 2H–L**). We chose such protocols because NPY release occurs most prominently during high-frequency neuronal activity (Hirsch and Zukowska, 2012; Li et al., 2017), although it may also happen upon single stimulation or spontaneously (Tu et al., 2005; Li et al., 2017). During Bic + 4-AP or KCl conditions, the largest fraction of neurons did not show an increase in fluorescence. As neighboring neurons could display contrasting patterns of GRAB NPY1.0 fluorescence, this particular outcome did not appear to be attributed by any spatial factors (**Figures 2F, G**).

However, about 32 and 36% of the cells across the two experimental conditions, respectively, did display an increased signal intensity. This increase was significantly reduced by the Y1R antagonist, BIBO3304, which blocked the sensor (**Figures 4E, F**). These findings suggest that both endogenous and transgene NPY release can be measured by the sensor. However, as outlined further below, certain circumstances can affect the fluorescent signal, which may hinder accurate readouts.

Determining NPY release of individual neurons in cultures is prone to masking since an apparent quenching of the signal was not rescued in NPY overexpressing cultures despite the overall fluorescent signal being higher (**Figure 3G**). Hereby the actual true signal may be underestimated. The lack of signal response, even for the minor fraction of neurons exposed to high concentrations of exogenous NPY could be due to several reasons. First, and considered the most important, we selected cells based on their basal fluorescent signals. This signal was in many cases weak, implying that neurons expressing the sensor to a low amount were also included in this study. However, to provide a comprehensive characterization of the sensor, even low-expressing neurons were not excluded from the analysis. In addition, being a membrane-expressed sensor, the highest fluorescent output comes from the perimeter of the soma compared to within the center, as some membrane signals from the top and bottom of the soma can be detected since we imaged using an epifluorescence microscope. Therefore, this can affect the average signal calculated as the ROIs are drawn around the entire soma of the neuron and not only

the membrane part. Moreover, the quantification of the fluorescent signal in this study was based on the mean value obtained across the entire time interval where each compound was applied and not only from the highest response. Therefore, the endogenous signal during increased neuronal activity often increased until a peak value (**Figure 2E**), while the mean value would be lower. Similar reflections can be made on the exogenous applied NPY, where we measured mean values, while the previous study characterizing the NPY1.0 sensor reported peak fluorescence (Wang et al., 2022).

Why does the fluorescent signal sometimes become lower in some cells? The fluorophore must be stable in the cellular microenvironment to sustain the fluorescent signal. In neuronal cultures, factors such as pH (Baird et al., 1999), oxygen, and temperature (Buckley et al., 2015; Kostyuk et al., 2019) have all been shown to affect the optical properties of the fluorophore. Particularly circular permutations, which make the fluorophore prone to acid-quenching (Baird et al., 1999). Of notice, it has been reported that excitatory synaptic activity, including seizure-like activity (Siesjö et al., 1985; Xiong et al., 2000; Raimondo et al., 2012), pharmacological glutamate receptor activation (Irwin et al., 1994), and membrane depolarizations (Hartley and Dubinsky, 1993; Zhan et al., 1998; Svichar et al., 2011), can induce transient pH variations intracellularly, but also extracellularly. Elevated K^+ can likewise lead to an acid shift in cytosolic pH (Hartley and Dubinsky, 1993; Zhan et al., 1998; Svichar et al., 2011). We, therefore, speculate that the lack or drop in fluorescent signal could be caused by fluctuations in pH as a direct consequence of high neuronal activity.

Despite its caveats, the novel GRAB NPY1.0 represents a promising step toward advancing NPY research. Similar to genetically encoded calcium sensors, which have been optimized iteratively since the development of the first generation (Tian et al., 2012), improved variants of GRAB NPY sensors are likely to be introduced soon. For this, important elements need to be considered: a large dynamic range without compromising the sensitivity of the sensor to low ligand concentrations, selectivity, fluorescent brightness, membrane trafficking, and stabilization of the sensor. Such optimizations are a cumbersome process and mostly done by trial and error, leaving a large number of possible sequence alterations to be tested. It also needs to be determined whether overexpression of the GRAB NPY in different cell types will result in similar outcomes.

In this study, we illustrate how the development of new scientific tools can open up new scientific frontiers to be explored. Until now, it has not been possible to directly measure the endogenous release of NPY from neurons. Nevertheless, with the arrival of the novel GRAB NPY1.0 sensor, we have been able to monitor NPY release at the single-cell level. However, there is no progress without struggle. This study also pinpoints a limitation of the GRAB NPY1.0 sensor, at least in neuronal cultures, and further emphasizes the necessity of carefully characterizing new research tools before using them more broadly. To use a GRAB NPY sensor effectively in experimental settings, it may require further optimization and experimental protocols should be designed with its limitations in mind. It can be speculated whether the implementation of the GRAB NPY1.0 sensor in fiber photometry *in vivo* settings might have better potential as the output is not based on the signal from a single neuron but rather a pool of neurons. Nevertheless, the GRAB NPY1.0 sensor is a great example of the importance of research tool development in the continuous flow of science, as it brings us one step in the direction of changing the field of NPY research by presenting potential advantages over existing tools. Lastly, to quote another Nobel Laureate Sydney Brenner "*Progress depends on the interplay of techniques, discoveries, and ideas, probably in that order of decreasing importance*" (Brenner, 2002).

Data availability statement

The original contributions presented in this study are included in this article, further inquiries can be directed to the corresponding author.

Ethics statement

The animal study was reviewed and approved by the Danish Research Ethical Committee for Experimental Animals (ethical permit 2017-15-0202-00092; PI: AS).

Author contributions

EC performed the experiments, completed the immunocytochemistry, did data analysis, and assisted with figure layouts. AKP contributed with neuronal culture assistance and expertise, assisted with the technical setup, did data analysis, and provided figure layouts. JR assisted with scripts used for data analysis. RC-B contributed with neuronal culture work and immunocytochemistry imaging. HW and YL developed and provided the GRAB NPY1.0 sensor. AS designed and supervised the project. EC, AKP, and AS wrote the manuscript. All authors reviewed and critically evaluated the manuscript.

Funding

This work was supported by Lundbeck Foundation grant R346-2020-1793 (AS) and Independent Research Fund Denmark grant 2034-00306B (AS).

Acknowledgments

We acknowledge the Core Facility for Integrated Microscopy, Faculty of Health and Medical Sciences, University of Copenhagen. Graphical illustrations were created with Biorender.com.

Conflict of interest

YL and HW have filed a patent application on the GRAB sensor (international patent PCT/CN2018/107533).

The remaining authors declare that the research was conducted in the absence of any commercial or financial relationships that could be construed as a potential conflict of interest.

Publisher's note

References

Abid, K., Rochat, B., Lassahn, P. G., Stöcklin, R., Michalet, S., Brakch, N., et al. (2009). Kinetic study of neuropeptide Y (NPY) proteolysis in blood and identification of NPY3-35: A new peptide generated by plasma kallikrein. *J. Biol. Chem.* 284, 24715–24724. doi: 10.1074/jbc.M109.035253

Acuna-Goycolea, C., Tamamaki, N., Yanagawa, Y., Obata, K., and van den Pol, A. N. (2005). Mechanisms of neuropeptide Y, peptide YY, and pancreatic polypeptide inhibition of identified green fluorescent protein-expressing GABA neurons in the hypothalamic neuroendocrine arcuate nucleus. *J. Neurosci.* 25, 7406–7419. doi: 10.1523/jneurosci.1008-05.2005

Aoki, C., and Pickel, V. M. (1989). Neuropeptide Y in the cerebral cortex and the caudate-putamen nuclei: Ultrastructural basis for interactions with GABAergic and non-GABAergic neurons. *J. Neurosci.* 9, 4333–4354. doi: 10.1523/jneurosci.09-12-04333.1989

Baird, G. S., Zacharias, D. A., and Tsien, R. Y. (1999). Circular permutation and receptor insertion within green fluorescent proteins. *Proc. Natl. Acad. Sci. U.S.A.* 96, 11241–11246. doi: 10.1073/pnas.96.20.11241

Brenner, S. (2002). Life sentences: Detective rummage investigates. *Genome Biol.* 3, comment1013.1–comment1013.2. doi: 10.1186/gb-2002-3-9-comment1013

Buckley, A. M., Petersen, J., Roe, A. J., Douce, G. R., and Christie, J. M. (2015). LOV-based reporters for fluorescence imaging. *Curr. Opin. Chem. Biol.* 27, 39–45. doi: 10.1016/j.cbpa.2015.05.011

Burbach, J. P. (2011). What are neuropeptides? *Methods Mol. Biol.* 789, 1–36. doi: 10.1007/978-1-61779-310-3_1

Cattaneo, S., Verlengia, G., Marino, P., Simonato, M., and Bettegazzi, B. (2021). NPY and gene therapy for epilepsy: How, when,. . . and Y. *Front. Mol. Neurosci.* 13:608001. doi: 10.3389/fnmol.2020.608001

Chee, M. J., Mörl, K., Lindner, D., Merten, N., Zamponi, G. W., Light, P. E., et al. (2008). The third intracellular loop stabilizes the inactive state of the neuropeptide Y1 receptor. *J. Biol. Chem.* 283, 33337–33346. doi: 10.1074/jbc.M804671200

DeLaney, K., Buchberger, A. R., Atkinson, L., Gründer, S., Mousley, A., and Li, L. (2018). New techniques, applications and perspectives in neuropeptide research. *J. Exp. Biol.* 221, 1–45. doi: 10.1242/jeb.151167

Dong, C., Zheng, Y., Long-Iyer, K., Wright, E. C., Li, Y., and Tian, L. (2022). Fluorescence imaging of neural activity, neurochemical dynamics, and drug-specific receptor conformation with genetically encoded sensors. *Annu. Rev. Neurosci.* 45, 273–294. doi: 10.1146/annurev-neuro-110520-031137

El Bahh, B., Cao, J. Q., Beck-Sickinger, A. G., and Colmers, W. F. (2002). Blockade of neuropeptide Y(2) receptors and suppression of NPY's anti-epileptic actions in the rat hippocampal slice by BIIE0246. *Br. J. Pharmacol.* 136, 502–509. doi: 10.1038/sj.bjp.0704751

Fenno, L. E., Ramakrishnan, C., Kim, Y. S., Evans, K. E., Lo, M., Vesuna, S., et al. (2020). Comprehensive dual- and triple-feature intersectional single-vector delivery of diverse functional payloads to cells of behaving mammals. *J. Clean. Prod.* 107, 836–853. doi: 10.1016/j.neuron.2020.06.003

Hartley, Z., and Dubinsky, J. M. (1993). Changes in intracellular pH associated with glutamate excitotoxicity. *J. Neurosci.* 13, 4690–4699. doi: 10.1523/jneurosci.13-11-04690.1993

Hirsch, D., and Zukowska, Z. (2012). NPY and stress 30 years later: The peripheral view. *Cell. Mol. Neurobiol.* 32, 645–659. doi: 10.1007/s10571-011-9793-z

Hoogstraaten, R. I., van Keimpema, L., Toonen, R. F., and Verhage, M. (2020). Tetanus insensitive VAMP2 differentially restores synaptic and dense core vesicle fusion in tetanus neurotoxin treated neurons. *Sci. Rep.* 10:10913. doi: 10.1038/s41598-020-67988-2

Irwin, R. P., Lin, S. Z., Long, R. T., and Paul, S. M. (1994). N-methyl-D-aspartate induces a rapid, reversible, and calcium-dependent intracellular acidosis in cultured fetal rat hippocampal neurons. *J. Neurosci.* 14(3 Pt 1), 1352–1357. doi: 10.1523/jneurosci.14-03-01352.1994

Jing, M., Zhang, Y., Wang, H., and Li, Y. (2019). G-protein-coupled receptor-based sensors for imaging neurochemicals with high sensitivity and specificity. *J. Neurochem.* 151, 279–288. doi: 10.1111/jnc.14855

Kendrick, K. M. (1990). Microdialysis measurement of in vivo neuropeptide release. *J. Neurosci. Methods* 34, 35–46. doi: 10.1016/0165-0270(90)90040-m

Kennedy, R. T. (2013). Emerging trends in in vivo neurochemical monitoring by microdialysis. *Curr. Opin. Chem. Biol.* 17, 860–867. doi: 10.1016/j.cbpa.2013.06.012

Kostyuk, A. I., Demidovich, A. D., Kotova, D. A., Belousov, V. V., and Bilan, D. S. (2019). Circularly permuted fluorescent protein-based indicators: History, principles, and classification. *Int. J. Mol. Sci.* 20:4200. doi: 10.3390/ijms20174200

Kristensen, K., Henriksen, J. R., and Andresen, T. L. (2015). Adsorption of cationic peptides to solid surfaces of glass and plastic. *PLoS One* 10:e0122419. doi: 10.1371/journal.pone.0122419

Lambert, P. D., Wilding, J. P., Turton, M. D., Ghatei, M. A., and Bloom, S. R. (1994). Effect of food deprivation and streptozotocin-induced diabetes on hypothalamic neuropeptide Y release as measured by a radioimmunoassay-linked microdialysis procedure. *Brain Res.* 656, 135–140. doi: 10.1016/0006-8993(94)91374-9

Larhammar, D., and Salaneck, E. (2004). Molecular evolution of NPY receptor subtypes. *Neuropeptides* 38, 141–151. doi: 10.1016/j.npep.2004.06.002

Li, Q., Bartley, A. F., and Dobrunz, L. E. (2017). Endogenously released neuropeptide Y suppresses hippocampal short-term facilitation and is impaired by stress-induced anxiety. *J. Neurosci.* 37, 23–37. doi: 10.1523/jneurosci.2599-16.2016

Lin, S., Boey, D., and Herzog, H. (2004). NPY and Y receptors: Lessons from transgenic and knockout models. *Neuropeptides* 38, 189–200. doi: 10.1016/j.npep.2004.05.005

Nasu, Y., Shen, Y., Kramer, L., and Campbell, R. E. (2021). Structure- and mechanism-guided design of single fluorescent protein-based biosensors. *Nat. Chem. Biol.* 17, 509–518. doi: 10.1038/s41589-020-00718-x

Nusbaum, M. P., Blitz, D. M., and Marder, E. (2017). Functional consequences of neuropeptide and small-molecule co-transmission. *Nat. Rev. Neurosci.* 18, 389–403. doi: 10.1038/nrn.2017.56

Patriarchi, T., Cho, J. R., Merten, K., Howe, M. W., Marley, A., Xiong, W. H., et al. (2018). Ultrafast neuronal imaging of dopamine dynamics with designed genetically encoded sensors. *Science* 360:eaat4422. doi: 10.1126/science.aat4422

Qian, J., Colmers, W. F., and Saggau, P. (1997). Inhibition of synaptic transmission by neuropeptide Y in rat hippocampal area CA1: Modulation of presynaptic Ca2+ entry. *J. Neurosci.* 17, 8169–8177. doi: 10.1523/jneurosci.17-21-08169.1997

Raimondo, J. V., Irkle, A., Wefelmeyer, W., Newey, S. E., and Akerman, C. J. (2012). Genetically encoded proton sensors reveal activity-dependent pH changes in neurons. *Front. Mol. Neurosci.* 5:68. doi: 10.3389/fnmol.2012.00068

Shiozaki, K., Kawabe, M., Karasuyama, K., Kurachi, T., Hayashi, A., Ataka, K., et al. (2020). Neuropeptide Y deficiency induces anxiety-like behaviours in zebrafish (*Danio rerio*). *Sci. Rep.* 10:5913. doi: 10.1038/s41598-020-62699-0

Siesjö, B. K., von Hanwehr, R., Nergelius, G., Nevander, G., and Ingvar, M. (1985). Extra- and intracellular pH in the brain during seizures and in the recovery period following the arrest of seizure activity. *J. Cereb. Blood Flow Metab.* 5, 47–57. doi: 10.1038/jcbfm.1985.7

Sørensen, A. T., Kanter-Schlifke, I., Lin, E. J., During, M. J., and Kokaia, M. (2008). Activity-dependent volume transmission by transgene NPY attenuates glutamate release and LTP in the subiculum. *Mol. Cell. Neurosci.* 39, 229–237. doi: 10.1016/j.mcn.2008.06.014

Soud, K., Jørgensen, S. H., Woldbye, D. P. D., and Sørensen, A. T. (2019). The C-terminal flanking peptide of neuropeptide Y (NPY) is not essential for seizure-suppressant actions of prepro-NPY overexpression in male rats. *J. Neurosci. Res.* 97, 362–372. doi: 10.1002/jnr.24350

Sperk, G., Hamilton, T., and Colmers, W. F. (2007). Neuropeptide Y in the dentate gyrus. *Prog. Brain Res.* 163, 285–297. doi: 10.1016/s0079-6123(07)63017-9

Südhof, T. C. (2017). Molecular neuroscience in the 21st century: A personal perspective. *Neuron* 96, 536–541. doi: 10.1016/j.neuron.2017.10.005

Sun, F., Zhou, J., Dai, B., Qian, T., Zeng, J., Li, X., et al. (2020). Next-generation GRAB sensors for monitoring dopaminergic activity in vivo. *Nat. Methods* 17, 1156–1166. doi: 10.1038/s41592-020-00981-9

Svichar, N., Esquenazi, S., Chen, H. Y., and Chesler, M. (2011). Preemptive regulation of intracellular pH in hippocampal neurons by a dual mechanism of depolarization-induced alkalinization. *J. Neurosci.* 31, 6997–7004. doi: 10.1523/jneurosci.6088-10.2011

Tasan, R. O., Verma, D., Wood, J., Lach, G., Hörmer, B., de Lima, T. C. M., et al. (2016). The role of Neuropeptide Y in fear conditioning and extinction. *Neuropeptides* 55, 111–126. doi: 10.1016/j.npep.2015.09.007

Tatemoto, K., Carlquist, M., and Mutt, V. (1982). Neuropeptide Y—a novel brain peptide with structural similarities to peptide YY and pancreatic polypeptide. *Nature* 296, 659–660. doi: 10.1038/296659a0

Tian, L., Akerboom, J., Schreiter, E. R., and Looger, L. L. (2012). Neural activity imaging with genetically encoded calcium indicators. *Prog. Brain Res.* 196, 79–94. doi: 10.1016/b978-0-444-59426-6.00005-7

Tu, B., Timofeeva, O., Jiao, Y., and Nadler, J. V. (2005). Spontaneous release of neuropeptide Y tonically inhibits recurrent mossy fiber synaptic transmission in epileptic brain. *J. Neurosci.* 25, 1718–1729. doi: 10.1523/jneurosci.4835-04.2005

van den Pol, A. N. (2012). Neuropeptide transmission in brain circuits. *Neuron* 76, 98–115. doi: 10.1016/j.neuron.2012.09.014

Wang, H., Qian, T., Zhao, Y., Zhuo, Y., Wu, C., Osakada, T., et al. (2022). A toolkit of highly selective and sensitive genetically encoded neuropeptide sensors. *bioRxiv* [preprint]. doi: 10.1101/2022.03.26.485911

Wu, Z., Lin, D., and Li, Y. (2022b). Pushing the frontiers: Tools for monitoring neurotransmitters and neuromodulators. *Nat. Rev. Neurosci.* 23, 257–274. doi: 10.1038/s41583-022-00577-6

Wu, Z., He, K., Chen, Y., Li, H., Pan, S., Li, B., et al. (2022a). A sensitive GRAB sensor for detecting extracellular ATP in vitro and in vivo. *Neuron* 110, 770–782.e775. doi: 10.1016/j.neuron.2021.11.027

Xiong, Z. Q., Saggau, P., and Stringer, J. L. (2000). Activity-dependent intracellular acidification correlates with the duration of seizure activity. *J. Neurosci.* 20, 1290–1296. doi: 10.1523/jneurosci.20-04-01290.2000

Zhan, R. Z., Fujiwara, N., Tanaka, E., and Shimoji, K. (1998). Intracellular acidification induced by membrane depolarization in rat hippocampal slices: Roles of intracellular Ca2+ and glycolysis. *Brain Res.* 780, 86–94. doi: 10.1016/s0006-8993(97)01149-9

frontiers | Frontiers in Cellular Neuroscience

TYPE Methods
PUBLISHED 23 August 2023
DOI 10.3389/fncel.2023.1217368

OPEN ACCESS

EDITED BY
Jacopo Lamanna,
Vita-Salute San Raffaele University, Italy

REVIEWED BY
Arpad Mike,
Institute of Experimental Medicine (MTA), Hungary
Srdjan D. Antic,
University of Connecticut Health Center, United States

*CORRESPONDENCE
Takashi Tominaga
✉ tominagat@kph.bunri-u.ac.jp

RECEIVED 05 May 2023
ACCEPTED 09 August 2023
PUBLISHED 23 August 2023

CITATION
Utsumi Y, Taketoshi M, Miwa M, Tominaga Y and Tominaga T (2023) Assessing seizure liability *in vitro* with voltage-sensitive dye imaging in mouse hippocampal slices. *Front. Cell. Neurosci.* 17:1217368. doi: 10.3389/fncel.2023.1217368

Assessing seizure liability *in vitro* with voltage-sensitive dye imaging in mouse hippocampal slices

Yuichi Utsumi[1,2], Makiko Taketoshi[2], Michiko Miwa[3], Yoko Tominaga[2] and Takashi Tominaga[1,2,3]*

[1]Graduate School of Pharmaceutical Sciences, Tokushima Bunri University, Sanuki, Japan, [2]Institute of Neuroscience, Tokushima Bunri University, Sanuki, Japan, [3]Kagawa School of Pharmaceutical Sciences, Tokushima Bunri University, Sanuki, Japan

Non-clinical toxicology is a major cause of drug candidate attrition during development. In particular, drug-induced seizures are the most common finding in central nervous system (CNS) toxicity. Current safety pharmacology tests for assessing CNS functions are often inadequate in detecting seizure-inducing compounds early in drug development, leading to significant delays. This paper presents an *in vitro* seizure liability assay using voltage-sensitive dye (VSD) imaging techniques in hippocampal brain slices, offering a powerful alternative to traditional electrophysiological methods. Hippocampal slices were isolated from mice, and VSD optical responses evoked by stimulating the Schaffer collateral pathway were recorded and analyzed in the stratum radiatum (SR) and stratum pyramidale (SP). VSDs allow for the comprehensive visualization of neuronal action potentials and postsynaptic potentials on a millisecond timescale. By employing this approach, we investigated the *in vitro* drug-induced seizure liability of representative pro-convulsant compounds. Picrotoxin (PiTX; 1–100 μM), gabazine (GZ; 0.1–10 μM), and 4-aminopyridine (4AP; 10–100 μM) exhibited seizure-like responses in the hippocampus, but pilocarpine hydrochloride (Pilo; 10–100 μM) did not. Our findings demonstrate the potential of VSD-based assays in identifying seizurogenic compounds during early drug discovery, thereby reducing delays in drug development and providing insights into the mechanisms underlying seizure induction and the associated risks of pro-convulsant compounds.

KEYWORDS

voltage-sensitive dye, hippocampus, seizure liability, optical recording, stratum radiatum, stratum pyramidale, drug-induced seizures, toxicology

1. Introduction

Non-clinical toxicity is a leading cause of drug candidate attrition during drug development (Waring et al., 2015). To address this issue, regulatory agencies, such as the International Council for Harmonisation (ICH), have developed guidelines for safety pharmacology testing that require the evaluation of cardiovascular, respiratory, and central nervous system (CNS) functions prior to human administration. Specifically, the ICH guideline S7A mandates safety pharmacology tests including those that evaluate

CNS function. The Irwin test (Irwin, 1968) and functional observational battery (Moser et al., 1995) have been frequently used in preclinical safety studies to detect the potential toxicity of drugs on the CNS. Of the potential CNS toxicities detected through these tests, the most common finding is drug-induced seizures (Authier et al., 2016a). Although electroencephalogram (EEG) analysis can also detect seizures in laboratory animals, pre- or post-dose non-invasive EEG assessments are not commonly included in these studies (Authier et al., 2016b). As a result, drug-induced seizures are often not identified until later stages of drug development, which can cause significant delays and negatively impact the timeline of drug development. Therefore, an *in vitro* seizure liability assay developed and implemented in early drug discovery could help identify potential seizure-inducing compounds and reduce delays in drug development.

A seizure is a complex process involving multiple cellular mechanisms and therefore multiple pharmacological targets. *In vitro* brain slices, which retain many of the neural circuits and signaling pathways present in the brain, have been used as a model system for CNS activity in early drug development and safety studies (Easter et al., 2007, 2009; Accardi et al., 2016). The hippocampus, in particular, is known to play a crucial role in seizure induction (Schwartzkroin, 1994). Recently, seizure liability assessments using hippocampal brain slices from different animal species, such as rats, dogs, monkeys, and mini-pigs, have been performed and found to be sensitive to pro- and anti-convulsant agents (Accardi et al., 2018). Currently, besides whole animal behavior tests, hippocampal brain slice electrophysiology tests are considered the standard for seizure-liability testing (Easter et al., 2007; Accardi et al., 2018; Zhai et al., 2021).

Traditional electrophysiological techniques are limited by their inability to increase the number of electrodes and measure individual cell activity, leading to challenges in comprehensively monitoring neural activity. However, voltage-sensitive dyes (VSDs) can be incorporated into nerve cell membranes to produce optical signals in response to changes in nerve membrane potential, providing a valuable alternative to traditional electrophysiological techniques (Cohen et al., 1978; Cohen and Salzberg, 1978; Tominaga et al., 2000, 2013, 2023; Grinvald and Hildesheim, 2004; Peterka et al., 2011). VSDs allow for the optical measurement of membrane potential changes in milliseconds, providing a comprehensive visualization of neuronal action potentials and synaptic potentials. Recent advances in VSD imaging methods have enabled the measurement of subtle changes in neural circuit function, including those associated with gene-manipulated animals (Tanemura et al., 2002; Suh et al., 2011), developmental modifications induced by drugs (Juliandi et al., 2015; Ishihara et al., 2022), and diseases (Mann et al., 2005; Hayase et al., 2020). In this study, we demonstrated that the use of VSD-based assays to quantify and visualize neural circuit function in hippocampal slices is critical for assessing the *in vitro* drug-induced seizure liability of representative pro-convulsant compounds, such as picrotoxin (PiTX), gabazine (GZ), 4-aminopyridine (4AP), and pilocarpine hydrochloride (Pilo). Our results indicate that VSD methods can discriminate layer-specific effects of modulation by these compounds, as evidenced by contrasting the signal from the cell layer (stratum pyramidale) with that from the dendritic membrane potential response (stratum radiatum). Moreover, the manner in which dendritic membrane potential signals vary depends on the pharmacological effects of the compounds on membrane potential modulation. These results highlight the potential advantages of VSD spatial resolution and population intracellular signal over conventional field potential recordings.

2. Materials and methods

2.1. Slice preparation and staining with VSD

All animal experiments were performed according to protocols approved by the Animal Care and Use Committee of Tokushima Bunri University. Hippocampal slices (350 μm thick) were prepared from 4- to 7-week-old male mice (C57BL6) who were decapitated under deep isoflurane anesthesia. The preparation and staining of the VSD are the same as that in the method published by Tominaga et al. (2019). Briefly, the brains were rapidly cooled in ice-cold artificial cerebrospinal fluid (ACSF) containing 124 mM NaCl, 2.5 mM KCl, 2 mM $CaCl_2$, 2 mM MgSO4, 1.25 mM NaH_2PO_4, 26 mM $NaHCO_3$, and 10 mM glucose, at a pH of 7.4, equilibrated with 95%/5% O_2/CO_2 mixed gas. After cooling for 5 min, the hippocampus was dissected along with the surrounding cortex, and the entire hippocampal structure was placed on an agar block. The ventral side of the hippocampus was cut vertically, and this side was attached to a vibratome (VT-1000 and VT-1200S, Leica) with cyanoacrylate glue. Transverse sections (350 μm thick) containing the hippocampus were cut, and each slice was transferred to a fine mesh membrane filter (Omnipore, JHWP01300, 0.45 μm pores, Merck Millipore Ltd., MA, USA) and fixed with a plexiglass ring (11 mm i.d, 15 mm o.d., and 1–2 mm thick). It was then transferred to a moist chamber, whose atmosphere was maintained by 95%/5% O_2/CO_2 mixed gas continuously bubbling through the ACSF. The temperature of the chamber was maintained at 28°C for 25 min and then allowed to return to room temperature. After 1 h of incubation, the slices were stained for 20 min with 100–110 μL of VSD staining solution [0.1 mM Di-4-ANEPPS (D-1199, Thermo Fisher Scientific Inc., MA, USA), 2.7% ethanol, 0.13% Cremophor EL (Sigma-Aldrich Co.), 50% fetal bovine serum (Sigma-Aldrich Co.), and 50% ACSF]. Slices were incubated for at least 1 h at room temperature with protection from light prior to recording.

2.2. Stimulation and electrophysiological recordings

Hippocampal slices were transferred to a submerged chamber using the plexiglass ring and continuously perfused with ACSF at a rate of 1 mL/min, heated to 31°C, and bubbled with 95%/5% O_2/CO_2 mixed gas. Glass electrodes filled with ACSF and inserted with Ag/AgCl wire were used as stimulating and recording electrodes to measure field excitatory postsynaptic potential (fEPSP) in the Schaffer collateral (SC) pathway and the stratum radiatum (SR) of cornu ammonis 1 (CA1). Electrical artifacts were removed from the traces as shown in the results. The stimulation frequency of 0.05 Hz was maintained throughout the experiment. The stimulation intensity was altered using an

electrical stimulator (ESTM-8, Brainvision, Inc., Tokyo, Japan) and the IgorPro (WaveMetrics Inc., OR, USA) macro program. Field potential recordings were obtained using a differential amplifier (model 3000; AM Systems, WA, USA; low-pass filtered at 3 kHz, high-pass filter at 0.1 Hz, gain × 100), and digitized by analog inputs of ESTM-8 at 10 kHz sampling (an AD converter of 16 bits) and fed into a computer. The analysis of electrophysiological data was done for these recordings. The electrophysiological and optical recordings did not interfere with one another.

2.3. Optical recording with VSD signals

Optical recording of VSD signals was performed concurrently with electrophysiological recordings. Epifluorescence optics consisting of a focus length = 20 mm objective lens (numerical aperture = 0.35; Brainvision Inc., Tokyo, Japan), a × 1.0 Leica Microsystems (as a projection lens), a dichroic mirror (575 nm), and excitation (530 ± 30 nm) and emission (>590 nm) filters were mounted above the slice. Fluorescence was measured and projected onto a CMOS camera (MiCAM02, Brainvision Inc., Tokyo, Japan). The ratio of the fractional change in VSD fluorescence to the initial amount of fluorescence (ΔF/F) was used as the optical signal. The frame rate was 0.6 ms/frame on the MiCAM02 camera (12 bit ADC, 4.5×10^5 well depth, 70 dB). The optical signals presented in the following sections were spatially and temporally filtered twice with a Gaussian kernel of 5 × 5 × 3 (horizontal × vertical × temporal; $\sigma \approx 1$). The analysis of the optical signals was performed using Igor Pro software (WaveMetrics Inc., OR, USA). Field potential recordings were also captured with an analog input in the MiCAM02 system, and the time correlation of the electrophysiological data and optical signals was continually confirmed.

2.4. Drugs and solutions

The reference compounds used in this study were PiTX, SR95531 (GZ), 4AP, and Pilo (Table 1), which were obtained from Sigma-Aldrich Co. and Tocris. Stock solutions (1000 ×) of each compound were prepared in their respective solvents, aliquoted, and frozen at −20°C. They were then diluted in oxygenated ACSF immediately prior to use. Other reagents used were obtained from distributors in Japan.

2.5. Data and statistical analysis

During electrophysiological recordings, field potentials were obtained every 30 s (total 204 times) through electrodes placed in the SR, and the fEPSP slope was calculated (Figures 1A, B). Simultaneously, VSD optical data were recorded every 30 s (0.6 ms/frame × 512 frames, total 307.2 ms) to obtain response waveforms of the SR and stratum pyramidale (SP) (Figures 1A, C). Optical and electrophysiological signals were analyzed concurrently using custom macros developed in Igor Pro software (WaveMetrics Inc., OR, USA). All data are presented as means ± standard error of the mean (SEM), with n representing the number of slices. Statistical analyses were performed using the R statistical software package (4.1.2; R Core Team, 2021). Statistical significance was determined by one-way analysis of variance followed by Dunnett's test, with a p-value less than 0.05 considered significant ($^*p < 0.05$, $^{**}p < 0.01$, and $^{***}p < 0.001$).

3. Results

3.1. Effects of the seizurogenic compounds on the fEPSP slope

We investigated the effects of four reference compounds, namely PiTX, GZ, 4AP, and Pilo, on fEPSP slope and VSD optical signals in hippocampal slices (Figure 1) by testing three concentrations of each compound. fEPSP is essential as a direct synaptic response to neuronal inputs. In this study, it was used for monitoring the physiological response of the area CA1. The experimental sequence began with a 20 min baseline period in normal ACSF, followed by a test of the stimulus-response (S-R) relationship. Next, the solution was changed to ACSF containing vehicle medium for 20 min, followed by a second S-R test. Three different concentrations of each compound (Table 1) were then tested for 20 min (Figures 2Ai–Di), with concurrent optical recordings made throughout. The VSD optical signals were acquired every 30 s. Therefore, 204 recordings of 307.2 ms were acquired from the same brain slice.

We calculated the mean fEPSP slope from the average of 10 data points of fEPSP slope before the S-R relationship for each treatment, with ACSF as 100% relative to vehicle or each concentration (Figures 2Aii–Dii). PiTX significantly reduced the fEPSP slope at high concentrations (100 μM) (68.63 ± 1.39%, $p < 0.001$), as did GZ at middle concentrations (≥1 μM) (80.39 ± 2.43%, $p < 0.05$; 40.94 ± 2.46%, $p < 0.001$). Pilo strongly reduced the fEPSP slope at low concentrations (≥10 μM) (26.80 ± 1.47%, 21.02 ± 1.66%, 19.70 ± 1.43%, $p < 0.001$), while 4AP significantly raised the fEPSP slope at the middle concentrations (40 μM) (133.16 ± 2.39%, $p < 0.05$), it tended to raise its slope at high concentrations (100 μM).

3.2. Effect of seizurogenic compounds on VSD imaging in hippocampal slice

We used VSD imaging to observe the spread pattern of neuronal activity in response to Schaffer collateral pathway stimulation. A bright field view of the brain slice in the observation area is shown in Figure 3A. PiTX induced expanded neuronal activity area in the CA1 region and prolonged propagation at the middle concentration (10 μM), with marked effects at high concentrations (100 μM) (Figure 3B, upper left). Similarly, GZ induced significantly expanded neuronal activity area in the CA1 region with prolonged propagation and propagation to the CA3 area at middle concentrations (≥1 μM) (Figure 3B, upper right). 4AP also induced significantly expanded neuronal activity area in the CA1 region with prolonged propagation and propagation to the CA3 area at middle concentrations (≥40 μM) (Figure 3B, lower left). In contrast, Pilo caused a marked reduction in the

TABLE 1 Compound reference set including solvent used and reported mode(s) of action.

Compound	Solvent	Description	Concentration (μM)	References
Picrotoxin	Ethanol	$GABA_A$ receptor antagonist, used in research to induce seizures	1, 10, 100	Mackenzie et al., 2002
Gabazine	Water	SR95531 is $GABA_A$ receptor antagonist, used in research to induce seizures	0.1, 1, 10	Lindquist et al., 2005; Johnston, 2013
4-Aminopyridine	DMSO	Potassium channel blocker, used to induce seizures in *in vivo* experiments	10, 40, 100	Peña and Tapia, 2000
Pilocarpine hydrochloride	Water	Muscarinic acetylcholine (ACh) receptor agonist, used as *in vivo* model for epilepsy	10, 30, 100	Zimmerman, 1981; Marchi et al., 2007

GABA, gamma-aminobutyric acid.

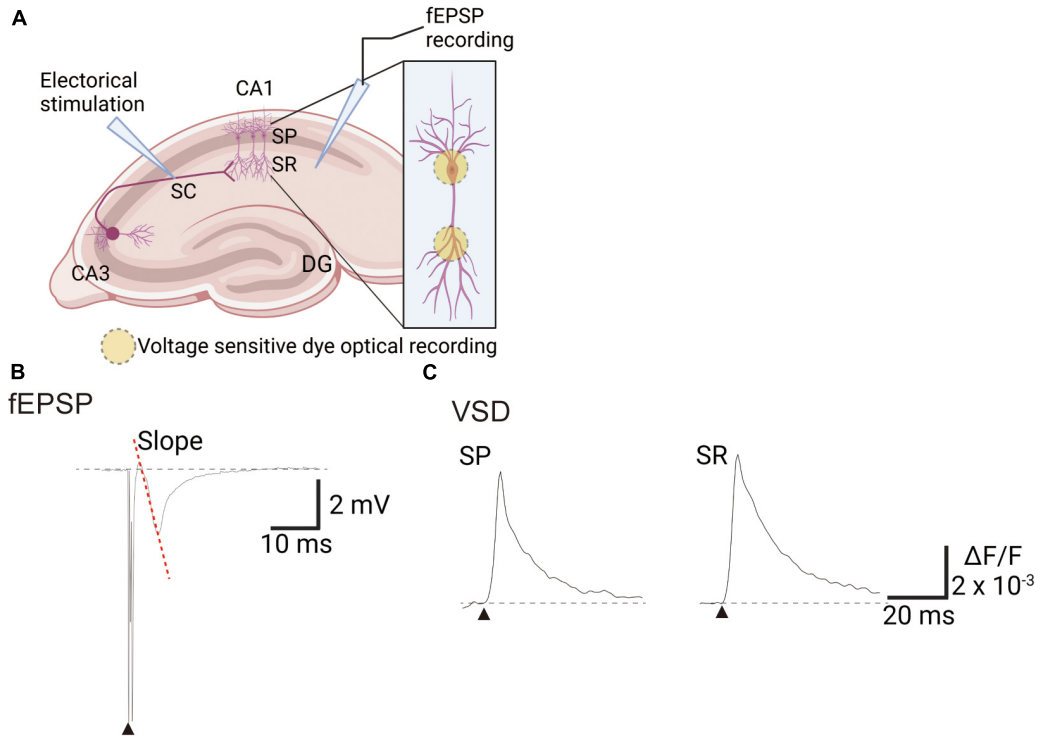

FIGURE 1
Experimental scheme of recording voltage sensitive dye (VSD) and electrophysiological signals in mice hippocampal slices. **(A)** An illustration showing the arrangement of recording optical and electrophysiological signals. **(B)** Trace of field excitatory postsynaptic potentials (fEPSPs) recorded with the field electrode in the SR. **(C)** Trace of VSD optical signals in the SP or SR. Filled black triangles indicate electrical stimulation. Image created on BioRender.com. DG, dentate gyrus; SC, Schaffer collateral; SP, stratum pyramidale; SR, stratum radiatum; ΔF/F, ratio of the fractional change in VSD fluorescence to the initial amount of fluorescence.

propagation area in the CA1 region and shortened propagation at low concentrations (≥10 μM) (Figure 3B, lower right).

3.3. Effect of seizurogenic compounds on VSD optical response

To further analyze the VSD signal, we compared waveforms of the optical signal at the middle of the SR to examine the effects of each compound. Figure 4A illustrates the arrangement of recording optical signals. All compounds caused changes in the waveform. PiTX at high concentrations (100 μM) and GZ at middle and high concentrations (1 and 10 μM) showed an increase in sustained response (Figures 4Bi, Ci). 4AP showed a clear increase in the immediate peak value at high concentrations (100 μM), and an increase in sustained response at middle or higher concentrations (≥40 μM) (Figure 4Di). However, Pilo showed a distinct decrease in the amplitude of the immediate peak (Figure 4Ei).

3.4. Comparison of defined parameters in VSD optical response

To elucidate the mechanisms underlying the effects of reference compounds, we further analyzed the optical traces by evaluating

10.3389/fncel.2023.1217368

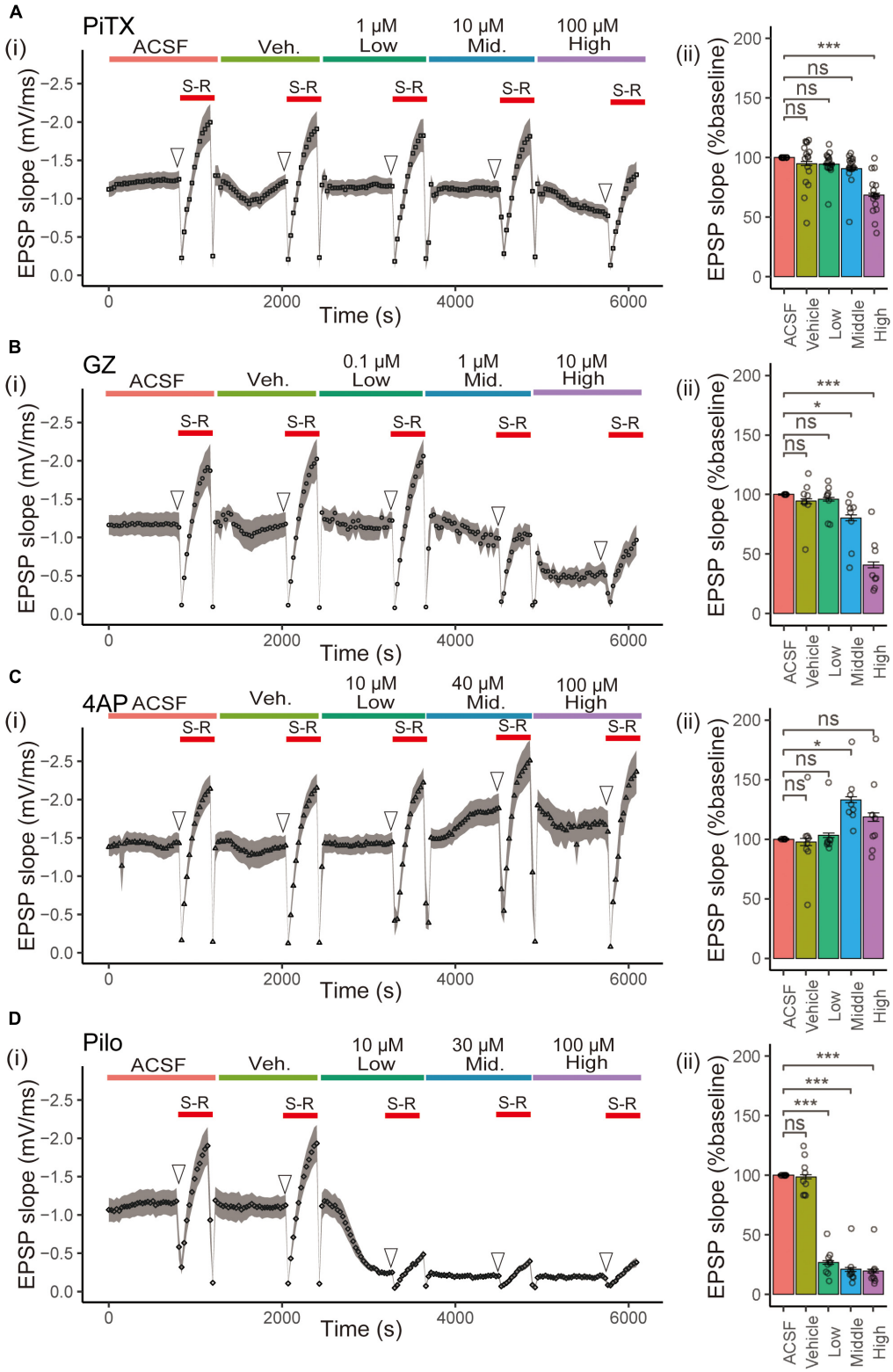

FIGURE 2
Effect of seizurogenic compounds on fEPSP slope in stratum radiatum. (i) The time courses of the slope of the fEPSP after application of ACSF, vehicle (Veh), and each compound [**(A)** picrotoxin (PiTX), **(B)** gabazine (GZ), **(C)** 4-amino pyridine (4AP), and **(D)** pilocarpine (Pilo)] over a series of three ascending concentrations [Low, Mid (middle), High] for a period of 20 min per concentration. The stimulus -response S, R relationship was done in each concentration of the test compound (red solid line). (ii) Mean data summary of compound effects on EPSP slopes. The mean fEPSP slopes were determined for 10 data points of the fEPSP slopes (open arrowhead) before (S-R) relationship. All error bars, ± SEM from n = 8 to 16 slices. *$p < 0.05$; ***$p < 0.001$; ns, not significant (Dunnett's test). fEPSPs, field excitatory postsynaptic potentials; EPSP, excitatory postsynaptic potentials; Mid., middle.

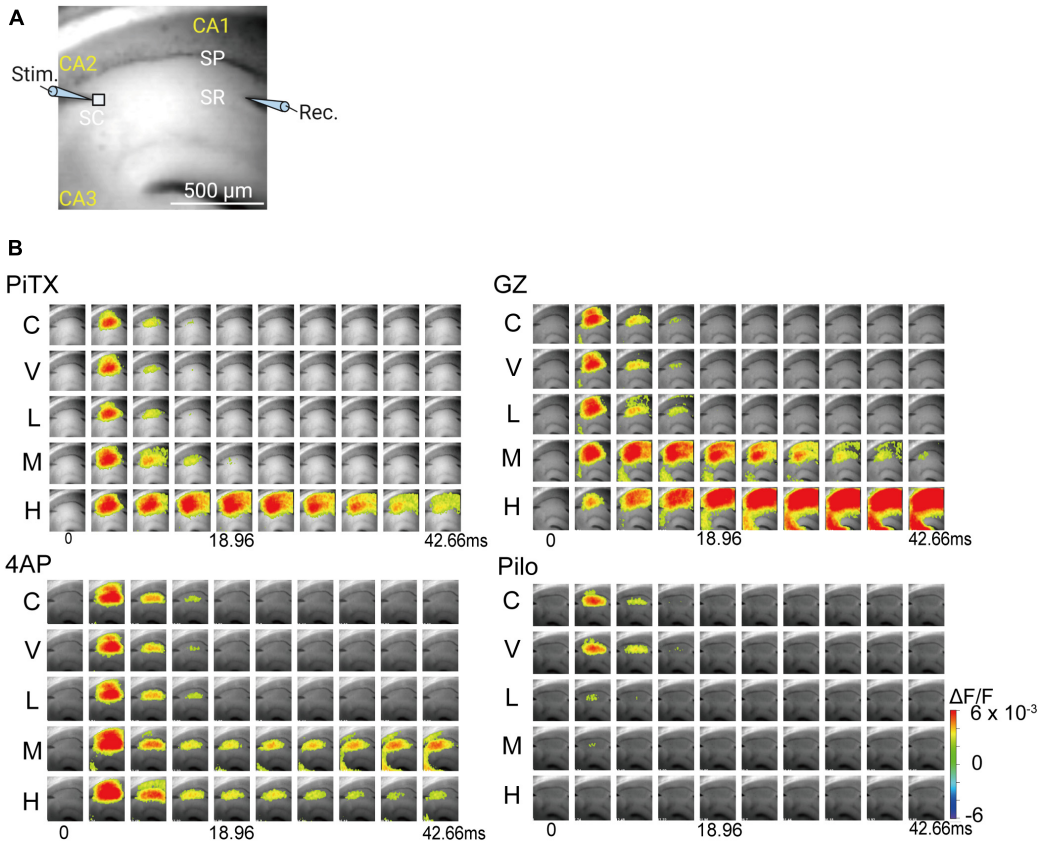

FIGURE 3
Spread of neural activity upon single stimulation of hippocampus under seizurogenic compounds treatment. **(A)** Fluorescent image of mouse hippocampal slices captured with 90 × 80 pixels high speed camera system. **(B)** Typical spread pattern of evoked neural activity following electrical stimulation. The sequence of images are the neural activity map after stimulation with: PiTX (upper left), GZ (upper right), 4AP (lower left), and Pilo (lower right). Depolarization was measured as fractional changes in fluorescence in each pixel; this value is encoded in pseudocolor as indicated in the scale and superimposed on a fluorescent image of the slice. PiTX, picrotoxin; GZ, gabazine; 4AP, 4-amino pyridine; Pilo, pilocarpine; C, control; V, vehicle; L, low; M, middle; H, high; ΔF/F, ratio of the fractional change in voltage-sensitive dye fluorescence to the initial amount of fluorescence.

three parameters: the immediate peak value, which corresponds to the excitatory postsynaptic potential (EPSP); the post-immediate peak value, defined as the signal size between 50 and 100 ms, where the feedback inhibitory response typically appears; and the sustained response, corresponding to the signal size after 150 ms from stimulation, which reflects the sustained response characteristic induced by the reference compounds (Figures 4Bi–Ei).

We calculated the maximum values for the immediate peak, post-immediate peak, and sustained responses (Figures 4Bii–Eii) for quantitative analysis of waveform data (averaging 10 waveforms following 20 min exposure to the drugs). PiTX did not impact the immediate peak but increased the sustained peak (6.65 ± 0.97, $p < 0.001$) at a high concentration (100 μM). GZ reduced the immediate peak (3.97 ± 0.15, $p < 0.001$) and elevated the sustained peak (7.47 ± 1.24, $p < 0.001$) at a high concentration (10 μM). 4AP also increased the immediate peak (6.36 ± 0.24, $p < 0.05$) at a high concentration (100 μM) and elevated the sustained peak at both middle and high concentrations (40 and 100 μM) (3.17 ± 0.28, 3.91 ± 0.33, respectively; $p < 0.001$ each). In contrast, Pilo decreased the immediate peak at low, middle, and high concentrations (10 to 100 μM) (2.32 ± 0.15, 1.90 ± 0.14, 1.65 ± 0.14, respectively; $p < 0.001$ each) but did not affect the sustained peak value.

Moreover, we calculated the difference between the maximum sustained response value and the maximum post-immediate peak value as ΔSPi (sustained response value minus post-immediate peak value) (Figures 4Bii–Eii). Neither PiTX nor Pilo influenced ΔSPi, while GZ reduced ΔSPi (−1.87 ± 0.32, $p < 0.05$) at a middle concentration (1 μM) and increased ΔSPi (0.86 ± 0.62, $p < 0.01$) at a high concentration (10 μM). 4AP also elevated ΔSPi at middle and high concentrations (40 and 100 μM) (0.93 ± 0.23, 1.40 ± 0.18, respectively; $p < 0.001$ each).

3.5. Effect of seizurogenic compounds on the ratio of VSD optical response between stratum pyramidale and SR (PR-ratio)

Waveforms of the VSD optical response in the SR and SP were obtained as described in section "3.1. Effects of the seizurogenic compounds on the fEPSP slope." The optical signal in the SR is dependent on EPSP, while that in the SR is dependent on spike

10.3389/fncel.2023.1217368

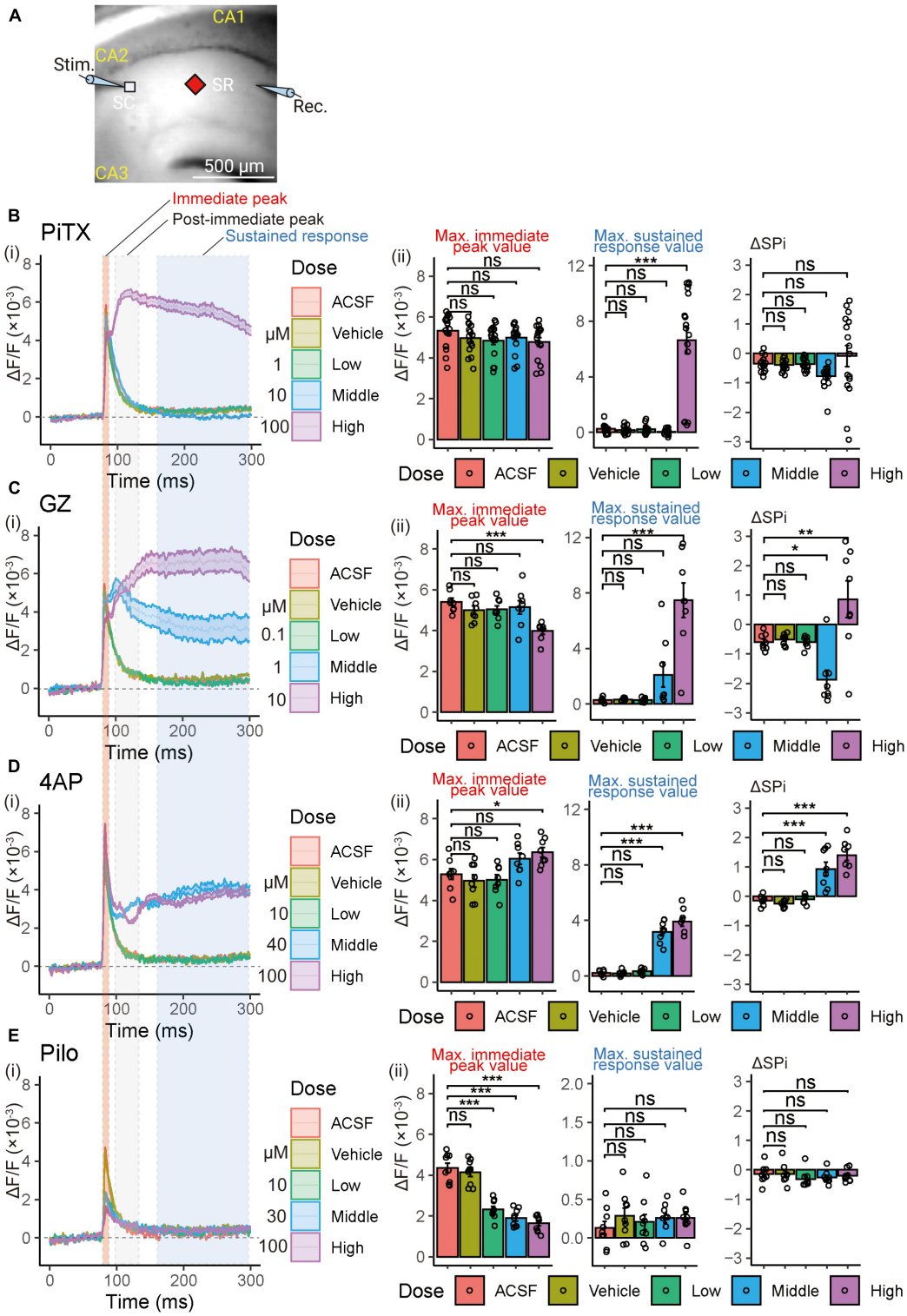

FIGURE 4
Voltage-sensitive dye (VSD) optical response waveforms analysis following single stimulation in SR. **(A)** Illustration of the recording setup for optical signal detection (Captured 90 × 80 pixels high speed camera system). Maximum values of 3 parameter (immediate peak, post-immediate peak, and sustained response) were utilized for the analysis. Figure created using BioRender.com. **(B–E)** (i) Comparison of alterations in VSD optical response waveforms. Solid lines and corresponding shaded areas represent mean ± SEM, derived from n = 8 to 16 slices. (ii) Comparison of the maximum immediate peak values of the VSD optical response in the presence of increasing compound concentrations (left panel). Comparison of the maximum sustained response values of the VSD optical response in the presence of increasing compound concentrations (center panel). Comparison of the delta maximum values of the VSD optical response (sustained response value—post-immediate peak value; ΔSPi) in the presence of increasing compound concentrations (right panel). Effects are depicted as ΔF/F ± SEM from n = 8 to 16 slices. *$p < 0.05$; **$p < 0.01$; ***$p < 0.001$; ns, not significant (Dunnett's test). ACSF, artificial cerebrospinal fluid; PiTX, picrotoxin; GZ, gabazine; 4AP, 4-amino pyridine; Pilo, pilocarpine; VSD, voltage-sensitive dye; SC, Schaffer collateral; SP, stratum pyramidale; SR, stratum radiatum.

occurrence (Tominaga et al., 2009). Consequently, the ratio of immediate peak values in the SR and SP indicates the excitation-spike (E-S) firing relationship. Therefore, we employed the ratio of the SP response to the SR response (PR-ratio) as a measure of the E-S relationship's strength. Maximum peak values were calculated from the VSD optical response data of the stimulus-response relationship (**Figures 2Ai–Di**, **5A**; red solid line) for each concentration of treatment. The concentration and treatment of each compound were consistent with those in section "3.1. Effects of the seizurogenic compounds on the fEPSP slope." Representative VSD optical response waveforms (10- and 55-volt stimulation) of each compound are shown in **Figure 5Aii**. These waveforms showed similar changes to those in **Figures 4Bi–Ei**.

The PR-ratio is a measure of the excitatory-inhibitory ratio and is sensitive to the inhibitory input to the soma, particularly at weak stimulation levels (Tominaga et al., 2009). **Figures 5Bi–Ei** show the changes in the maximum immediate peak value of SP and SR, which is necessary for the calculation of PR-ratio, by each concentration and stimulus intensity. The maximum values in SP and SR of PiTX and GZ did not change with increasing concentration (**Figures 5Bi, Ci**). 4AP produced a concentration-dependent increase in the maximum values of SP and SR (**Figure 5Di**), while Pilo caused a concentration-dependent decrease (**Figure 5Ei**). The PR-ratio for the optical signal was calculated as the ratio of the maximum immediate peak value of SP and that of SR in each measurement point (**Figure 5Ai**, filled red diamond). **Figures 5Bii–5Eii** represent the comparison of the PR-ratio, calculated for weak (10 V) and saturation (55 V) stimuli, respectively. PiTX showed a significant increase in the average PR-ratio at middle or higher concentrations ($\geq$10 μM) for both 10- and 55-V stimuli (**Figure 5Bii**). Similarly, GZ displayed a tendency to elevate the average PR-ratio at middle or higher concentrations ($\geq$1 μM), with a significant difference observed only at 55-V stimulation (**Figure 5Cii**). These findings suggest a reduction in inhibitory action at the soma caused by PiTX and GZ. In contrast, 4AP exhibited an increase in the average PR-ratio at middle or higher concentrations ($\geq$40 μM), but this effect was limited to 10-V stimulation (**Figure 5Dii**), indicating minimal impact on the E-S relationship. On the other hand, Pilo demonstrated a decreasing trend in the average PR-ratio at middle and low or higher concentrations (30 and $\geq$10 μM) for weak and saturation stimuli, respectively. However, no significant differences were observed at either 10- or 55-V stimuli (**Figure 5Eii**). Therefore, PiTX and GZ exhibited a clear reduction in inhibitory action at the soma, leading to a noticeable increase in the PR-ratio. Meanwhile, 4AP had only a modest effect on the E-S relationship, and Pilo had little influence on the PR-ratio and did not show statistical significance for the chosen stimuli.

4. Discussion

In vitro brain slice assays, such as electrophysiological assays using hippocampal slices for seizure liability evaluation, have been employed in early safety pharmacology assessments (Easter et al., 2009; Accardi et al., 2016). Despite the relatively high predictive rate of 89% for this assay (Easter et al., 2009), differences in responses have been observed between rodents and humans (Löscher, 2009; Bankstahl et al., 2012; Nagayama, 2015). However, VSD-based assays can measure membrane potential changes in milliseconds, enabling comprehensive visualization of neuronal action potentials and synaptic receptive potentials (Tominaga et al., 2009). Leveraging this capability, our study examined the effects of four compounds known to induce seizures in animal models and humans on electrophysiological parameters (fEPSP slope) and VSD optical response. To the best of our knowledge, this study represents the first application of seizure liability assessment using a VSD-based assay *in vitro*.

4.1. Consideration of throughput compared to published *in vitro* brain slice experiments

In drug discovery, the throughput performance of screening assays is of utmost importance. In this context, assays using cell lines with multielectrode array (MEA) measurements (Zhai et al., 2021) offer certain advantages. This method is also applicable to induced pluripotent stem (iPS) cells (Tukker et al., 2018, 2020). However, given the complex nature of seizure initiation, whole animal studies remain necessary. Brain slice experiments represent a step forward in increasing the throughput of seizure liability assays. More importantly, this method can improve our mechanistic understanding of seizures because the slice preparation provides access to the functioning of the neural network.

The throughput of brain slice experiments (Easter et al., 2007; Accardi et al., 2018; Zhai et al., 2021) is determined by the experimental procedures used to collect viable physiological tissue from the brain of a single animal. The time required to collect data is relatively consistent across experimental procedures. For example, in the study by Easter et al. (2007), it took approximately 70 min to collect data for a single compound (5 concentrations, 2 stimulus-response relationships), compared to 100 min in the present study, which included the stimulus-response relationship recordings. The VSD assay can visualize the range and extent of change in stimulus propagation, allowing quantitative analysis at any part of the recorded image field of view.

The active concentration ranges of the positive compound used in this study were compared with the active concentration ranges at which seizure liability assays (electrophysiology and MEA) using brain slices detected a seizurogenic response (**Table 2**). The concentrations of PiTX, GZ, and 4AP were considered to be within the range of existing assays. Pilo was not detected by the VSD-based assay, a point discussed further in section "4.3. Visualization of neural activity by VSD imaging."

4.2. fEPSP for monitoring the physiological response of the CA1 cortex

In the present study, we utilized fEPSP to monitor the slices' physiological activity, as this method directly reflects synaptic activity. Seizure activity may be caused by various physiological processes in both presynaptic and postsynaptic systems. The changes induced by seizurogenic drugs should reflect alterations in synaptic causes, in addition to modifications in postsynaptic

10.3389/fncel.2023.1217368

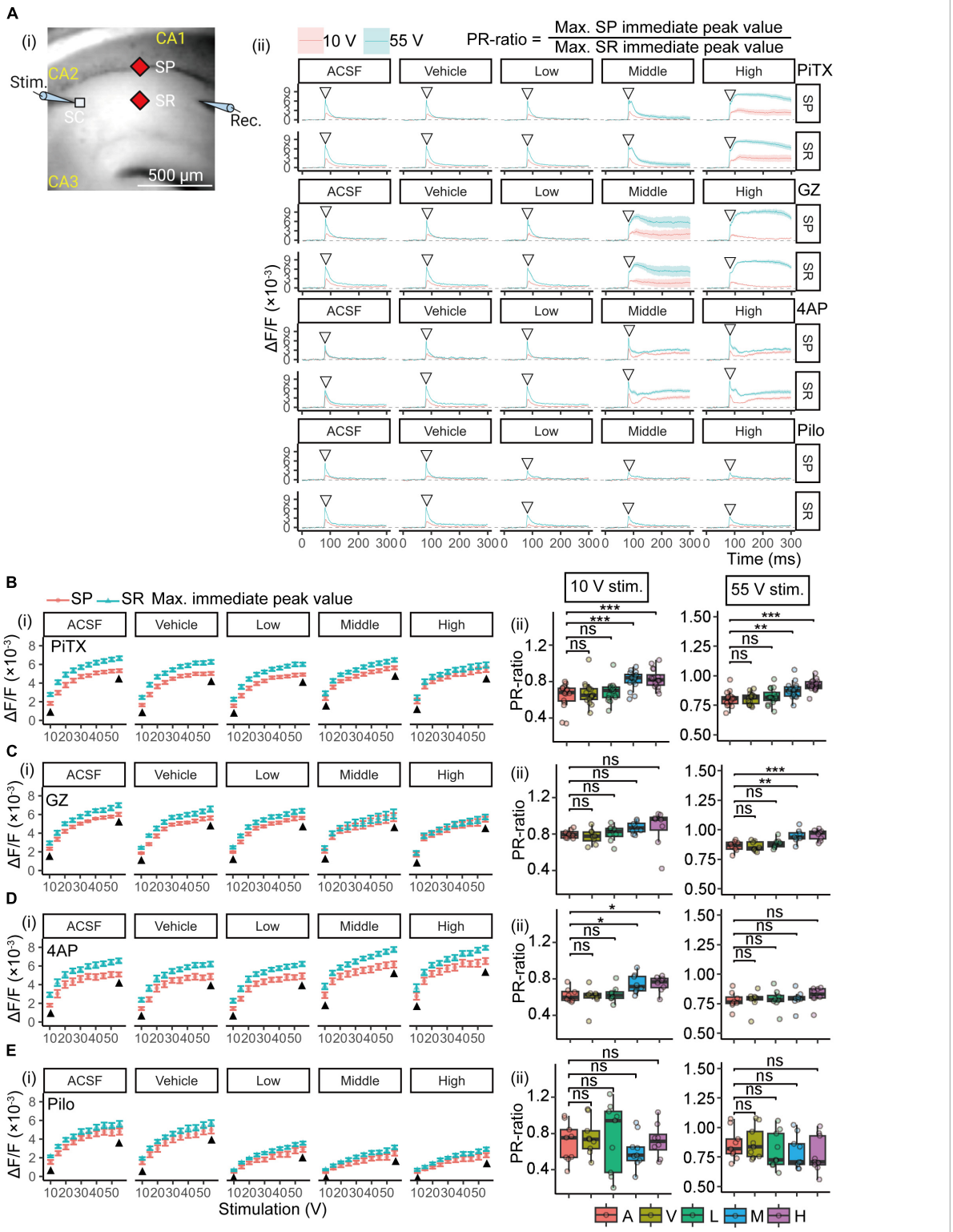

FIGURE 5
Voltage-sensitive dye (VSD) optical response analysis for E-S coupling. **(A)** An illustration demonstrating the arrangement for recording optical signals with increment stimulation of 10- to 55-volt. Measurement points of optical signals were shown filled red diamond in the **(A)** (i) image. The maximum values of SP and SR immediate peaks [open invert-triangles in the image of **(A)** (ii)] are represented. The PR-ratio is defined as the ratio of its values of SP and SR immediate peaks [**(A)** (ii), right]. **(B–E)** (i) Changes in the maximum immediate peak value of SP and SR are shown at each concentration and stimulus intensity. Black filled triangles indicate maximum immediate peak values of 10- and 55-volt. Plots are illustrated as mean ± SEM from n = 8 to 16 slices. (ii) Comparison of the PR-ratio in weak (10-volt) and saturated (55-volt) stimulation. Boxplot of PR-ratios are illustrated from n = 8 to 16 slices. *$p < 0.05$; **$p < 0.01$; ***$p < 0.001$; ns, not significant (Dunnett's test). VSD, voltage-sensitivity dye; PiTX, picrotoxin; GZ, gabazine; 4AP, 4-amino pyridine; Pilo, pilocarpine; ΔF/F, ratio of the fractional change in voltage-sensitive dye fluorescence to the initial amount of fluorescence; SR, stratum radiatum; SP, stratum pyramidale; C, control; V, vehicle; L, low; M, middle; H, high.

TABLE 2 Comparison with published *in vitro* seizure liability assay using brain slices.

Compound	Active concentration range (μM)		
	This study (VSD-based assay)	Published (assay method)	References
Picrotoxin	10–100	10–300 (PS number and PS area in EP)	Easter et al., 2007
		3–300 (PS number and PS area in EP)	Zhai et al., 2021
		0.2–100 (MEA)	Bradley et al., 2018
		10–100 (MEA)	Gao et al., 2017; Fan et al., 2019
Gabazine	1–10	1–10 (MEA)	Bradley et al., 2018
		0.3–3 (MEA)	Fan et al., 2019
4-aminopyridine	40–100	10–100 (PS number and PS area in EP)	Easter et al., 2007
		1–300 (PS number and PS area in EP)	Zhai et al., 2021
		11–100 (MEA)	Bradley et al., 2018
		10–100 (MEA)	Fan et al., 2019
Pilocarpine	ND	10–1000 (PS number and PS area in EP)	Zhai et al., 2021
		NEG (MEA)	Fan et al., 2019

EP, electrophysiology; MEA, multiwell microelectrode arrays or multi-electrode array; ND, not determined; NEG, negative for seizure liability.

cells. In the electrophysiological assay, decreases in fEPSP slope were observed with gamma-aminobutyric acid type A ($GABA_A$) receptor antagonists PiTX and GZ (**Figures 2Aii, Bii**), likely due to the intermission of a presynaptic GABAA receptor-mediated tonic facilitation of glutamatergic transmission (Jang et al., 2005). This may indicate the complex pathways of hippocampal disinhibition associated with $GABA_A$ receptor antagonists (Bast et al., 2017). An increase in the fEPSP slope was observed with 4AP at a middle concentration (40 μM), as previously reported (Barish et al., 1996). However, 4AP showed no significant difference at a high concentration (100 μM) in contrast to a previous report (Wheeler et al., 1996). Although an increasing trend was observed at a high concentration (100 μM) of 4AP (**Figure 2Cii**), the cumulative increase of 4-AP dose concentration from low to high might explain this discrepancy. Additionally, a concentration-dependent decrease in fEPSP slope was observed with Pilo, whereas in a rat model of Pilo-induced temporal lobe epilepsy, a decrease in fEPSP slope was observed in the hippocampal slice after the onset of status epilepticus (Postnikova et al., 2021).

These observations highlight the synaptic changes caused by seizurogenic drugs. However, VSD imaging can provide access not only to the EPSP components at the stratum radiatum, along with the output function of principal cells at the stratum pyramidale (**Figure 3**), but also to the input-output function as the P-R ratio (**Figure 5**) and changes in different time windows (**Figure 4**: Immediate—Post-Immediate—Sustained ratios). This may reveal different mechanisms by which individual compounds induce seizures.

4.3. Visualization of neural activity by VSD imaging

Picrotoxin, GZ, and 4AP showed an expansion of the spread of neuronal activity in hippocampal slices and prolonged propagation time (**Figure 3B**), suggesting that a seizure-like response could be detected. The seizurogenic response of Pilo was not detected in this assay, nor could it be detected by multiwell microelectrode arrays (MEAs) using rat cortical neurons (Bradley et al., 2018). Similarly, MEAs using human induced pluripotent stem cell (hiPSC)-derived neuronal cells and rodent primary cortical cells did not detect dose-dependent and clear seizurogenic responses of Pilo (Tukker et al., 2020). Thus, detection of seizurogenic responses to Pilo could be challenging. However, VSD imaging using hippocampal slices from an animal model of Pilo-induced seizure demonstrated marked activation of the temporoammonic pathway (Ang et al., 2006). This suggests that depending on the drug, multiple pathways may need to be analyzed.

4.4. Exploiting the direct pharmacological impact on neuronal function using VSD assay parameters

In this study, we defined three parameters for the VSD response waveform: immediate peak, post-immediate peak, and sustained response (**Figure 4**). The VSD response waveform in the SR demonstrated an increase in sustained response, confirming a seizurogenic response for all compounds except Pilo (**Figure 4E**). For antagonists of the $GABA_A$ receptor, increased sustained responses were observed with PiTX at high concentrations (100 μM) and GZ at middle or more concentrations (≥10 μM). The half-maximal inhibitory concentration (IC_{50}) of PiTX for the $GABA_A$ receptor is 1.15 μM (Ng et al., 2017), and that of GZ is 0.2 μM (Ueno et al., 1997). The difference in the active concentrations of seizurogenic responses was considered to be related to the difference in IC_{50} of the receptors. 4AP showed an increase in sustained response and ΔSPi (**Figures 4Di, ii**) at middle or high concentrations (≥40 μM). The application of 4-AP caused delayed depolarization following the initial synaptic response (Barish et al., 1996; **Figure 4Di**), whereas PiTX and GZ induced a prolonged depolarizing response (**Figures 4Bi, Ci**). This phenomenon is thought to be due to the inhibition of potassium current, a pharmacological effect of 4AP, and a similar phenomenon has been observed in rat brain slices (Barish et al., 1996).

We utilized the PR-ratio for evaluating the effects of PiTX, GZ, and 4AP. The PR-ratio reflects the E-S firing relationship and is calculated as the ratio of the amplitude at the SP to the SR (Tominaga et al., 2009). PiTX and GZ resulted in an increased PR-ratio (**Figures 5Bii, Cii**), suggesting that these compounds may induce a seizure response by reducing the shunting action

of GABA receptors and lowering the threshold for spike firing (Mann and Paulsen, 2007). Similarly, 4AP exhibited an increased PR-ratio at low stimulation voltages (**Figure 5Dii**), indicating that it may also lower the threshold for spike firing and induce a seizure response. 4AP is known to inhibit D-type potassium conductance at low (<40 μM) concentrations (Storm, 1988) and inhibit A-type potassium conductance at higher concentrations (Gutman et al., 2005). These effects on potassium channels may affect the E-S firing function of the pyramidale cells and contribute to the modification of the PR-ratio. However, the PR-ratio of 4AP showed no significant change at 55-volt stimulation (**Figure 5Dii**), suggesting that delayed repolarization (**Figures 4Di, ii**) may induce a seizure response.

Overall, the parameters of the VSD assay, which directly reflect membrane potential responses, were useful in investigating the mode of action of unknown seizurogenic compounds by capturing their direct pharmacological impact on neuronal function. Our findings demonstrate the potential of VSD-based assays in identifying seizurogenic compounds during early drug discovery, thereby reducing delays in drug development and providing insights into the mechanisms underlying seizure induction and the associated risks of pro-convulsant compounds.

Data availability statement

The original contributions presented in this study are included in the article/supplementary material, further inquiries can be directed to the corresponding author.

Ethics statement

All animal experiments were performed according to protocols approved by the Animal Care and Use Committee of Tokushima Bunri University. The study was conducted in accordance with the local legislation and institutional requirements.

Author contributions

YU and TT designed the research, analyzed the data, and wrote the manuscript. YU, MT, MM, YT, and TT performed the research. YT and TT developed the software. All authors contributed to the article and approved the final submitted version.

Funding

This work was supported by JSPS KAKENHI Grant Numbers JP23K18485, JP23H03488, JP22H05698, JP21H03606, JP21K06702, JP21H03532, JP21H00447, JP20H04341, JP19H01142, JP19K 12190, and JP16H06532 to TT, and JP21K15247 to YT.

Acknowledgments

We would like to thank Editage (www.editage.com) for their writing support on the manuscript.

Conflict of interest

The authors declare that the research was conducted in the absence of any commercial or financial relationships that could be construed as a potential conflict of interest.

Publisher's note

References

Accardi, M. V., Huang, H., and Authier, S. (2018). Seizure liability assessments using the hippocampal tissue slice: Comparison of non-clinical species. *J. Pharmacol. Toxicol. Methods* 93, 59–68. doi: 10.1016/j.vascn.2017.11.003

Accardi, M. V., Pugsley, M. K., Forster, R., Troncy, E., Huang, H., and Authier, S. (2016). The emerging role of in vitro electrophysiological methods in CNS safety pharmacology. *J. Pharmacol. Toxicol. Methods* 81, 47–59. doi: 10.1016/j.vascn.2016.03.008

Ang, C. W., Carlson, G. C., and Coulter, D. A. (2006). Massive and specific dysregulation of direct cortical input to the hippocampus in temporal lobe epilepsy. *J. Neurosci.* 26, 11850–11856. doi: 10.1523/JNEUROSCI.2354-06.2006

Authier, S., Arezzo, J., Delatte, M. S., Kallman, M.-J., Markgraf, C., Paquette, D., et al. (2016a). Safety pharmacology investigations on the nervous system: An industry survey. *J. Pharmacol. Toxicol. Methods* 81, 37–46. doi: 10.1016/j.vascn.2016.06.001

Authier, S., Delatte, M. S., Kallman, M.-J., Stevens, J., and Markgraf, C. (2016b). EEG in non-clinical drug safety assessments: Current and emerging considerations. *J. Pharmacol. Toxicol. Methods* 81, 274–285. doi: 10.1016/j.vascn.2016.03.002

Bankstahl, M., Bankstahl, J. P., Bloms-Funke, P., and Löscher, W. (2012). Striking differences in proconvulsant-induced alterations of seizure threshold in two rat models. *NeuroToxicology* 33, 127–137. doi: 10.1016/j.neuro.2011.12.011

Barish, M. E., Ichikawa, M., Tominaga, T., Matsumoto, G., and Iijima, T. (1996). Enhanced fast synaptic transmission and a delayed depolarization induced by transient potassium current blockade in rat hippocampal slice as studied by optical recording. *J. Neurosci.* 16, 5672–5687. doi: 10.1523/JNEUROSCI.16-18-05672.1996

Bast, T., Pezze, M., and McGarrity, S. (2017). Cognitive deficits caused by prefrontal cortical and hippocampal neural disinhibition. *Br. J. Pharmacol.* 174, 3211–3225. doi: 10.1111/bph.13850

Bradley, J. A., Luithardt, H. H., Metea, M. R., and Strock, C. J. (2018). In vitro screening for seizure liability using microelectrode array technology. *Toxicol. Sci.* 163, 240–253. doi: 10.1093/toxsci/kfy029

Cohen, L. B., and Salzberg, B. M. (1978). "Optical measurement of membrane potential," in *Reviews of physiology, biochemistry and pharmacology*, Vol. 86, eds R. H. Adrian, E. Helmreich, H. Holzer, R. Jung, O. Krayer, R. J. Linden, et al. (Berlin: Springer Berlin Heidelberg), 35–88. doi: 10.1007/3-540-08907-1_2

Cohen, L. B., Salzberg, B. M., and Grinvald, A. (1978). Optical methods for monitoring neuron activity. *Annu. Rev. Neurosci.* 1, 171–182. doi: 10.1146/annurev.ne.01.030178.001131

Easter, A., Bell, M. E., Damewood, J. R., Redfern, W. S., Valentin, J.-P., Winter, M. J., et al. (2009). Approaches to seizure risk assessment in preclinical drug discovery. *Drug Discov. Today* 14, 876–884. doi: 10.1016/j.drudis.2009.06.003

Easter, A., Sharp, T. H., Valentin, J.-P., and Pollard, C. E. (2007). Pharmacological validation of a semi-automated in vitro hippocampal brain slice assay for assessment of seizure liability. *J. Pharmacol. Toxicol. Methods* 56, 223–233. doi: 10.1016/j.vascn.2007.04.008

Fan, J., Thalody, G., Kwagh, J., Burnett, E., Shi, H., Lewen, G., et al. (2019). Assessing seizure liability using multi-electrode arrays (MEA). *Toxicol. In Vitro* 55, 93–100. doi: 10.1016/j.tiv.2018.12.001

Gao, M., Igata, H., Takeuchi, A., Sato, K., and Ikegaya, Y. (2017). Machine learning-based prediction of adverse drug effects: An example of seizure-inducing compounds. *J. Pharmacol. Sci.* 133, 70–78. doi: 10.1016/j.jphs.2017.01.003

Grinvald, A., and Hildesheim, R. (2004). VSDI: A new era in functional imaging of cortical dynamics. *Nat. Rev. Neurosci.* 5, 874–885. doi: 10.1038/nrn1536

Gutman, G. A., Chandy, K. G., Grissmer, S., Lazdunski, M., McKinnon, D., Pardo, L. A., et al. (2005). International Union of Pharmacology. LIII. Nomenclature and molecular relationships of voltage-gated potassium channels. *Pharmacol. Rev.* 57, 473–508. doi: 10.1124/pr.57.4.10

Hayase, Y., Amano, S., Hashizume, K., Tominaga, T., Miyamoto, H., Kanno, Y., et al. (2020). Down syndrome cell adhesion molecule like-1 (DSCAML1) links the GABA system and seizure susceptibility. *Acta Neuropathol. Commun.* 8:206. doi: 10.1186/s40478-020-01082-6

Irwin, S. (1968). Comprehensive observational assessment: Ia. A systematic, quantitative procedure for assessing the behavioral and physiologic state of the mouse. *Psychopharmacologia* 13, 222–257. doi: 10.1007/BF00401402

Ishihara, Y., Honda, T., Ishihara, N., Namba, K., Taketoshi, M., Tominaga, Y., et al. (2022). A CCR5 antagonist, maraviroc, alleviates neural circuit dysfunction and behavioral disorders induced by prenatal valproate exposure. *J. Neuroinflammation* 19:195. doi: 10.1186/s12974-022-02559-y

Jang, I.-S., Ito, Y., and Akaike, N. (2005). Feed-forward facilitation of glutamate release by presynaptic GABA(A) receptors. *Neuroscience* 135, 737–748. doi: 10.1016/j.neuroscience.2005.06.030

Johnston, G. A. R. (2013). Advantages of an antagonist: Bicuculline and other GABA antagonists. *Br. J. Pharmacol.* 169, 328–336. doi: 10.1111/bph.12127

Juliandi, B., Tanemura, K., Igarashi, K., Tominaga, T., Furukawa, Y., Otsuka, M., et al. (2015). Reduced adult hippocampal neurogenesis and cognitive impairments following prenatal treatment of the antiepileptic drug valproic acid. *Stem Cell Rep.* 5, 996–1009. doi: 10.1016/j.stemcr.2015.10.012

Lindquist, C. E. L., Laver, D. R., and Birnir, B. (2005). The mechanism of SR95531 inhibition at GABA receptors examined in human alpha1beta1 and alpha1beta1gamma2S receptors. *J. Neurochem.* 94, 491–501. doi: 10.1111/j.1471-4159.2005.03240.x

Löscher, W. (2009). Preclinical assessment of proconvulsant drug activity and its relevance for predicting adverse events in humans. *Eur. J. Pharmacol.* 610, 1–11. doi: 10.1016/j.ejphar.2009.03.025

Mackenzie, L., Medvedev, A., Hiscock, J. J., Pope, K. J., and Willoughby, J. O. (2002). Picrotoxin-induced generalised convulsive seizure in rat: Changes in regional distribution and frequency of the power of electroencephalogram rhythms. *Clin. Neurophysiol. Off. J. Int. Fed. Clin. Neurophysiol.* 113, 586–596. doi: 10.1016/s1388-2457(02)00040-8

Mann, E. O., and Paulsen, O. (2007). Role of GABAergic inhibition in hippocampal network oscillations. *Trends Neurosci.* 30, 343–349. doi: 10.1016/j.tins.2007.05.003

Mann, E. O., Tominaga, T., Ichikawa, M., and Greenfield, S. A. (2005). Cholinergic modulation of the spatiotemporal pattern of hippocampal activity in vitro. *Neuropharmacology* 48, 118–133. doi: 10.1016/j.neuropharm.2004.08.022

Marchi, N., Oby, E., Batra, A., Uva, L., De Curtis, M., Hernandez, N., et al. (2007). In vivo and in vitro effects of pilocarpine: Relevance to ictogenesis. *Epilepsia* 48, 1934–1946. doi: 10.1111/j.1528-1167.2007.01185.x

Moser, V. C., Cheek, B. M., and MacPhail, R. C. (1995). A multidisciplinary approach to toxicological screening: III. Neurobehavioral toxicity. *J. Toxicol. Environ. Health* 45, 173–210. doi: 10.1080/15287399509531988

Nagayama, T. (2015). Adverse drug reactions for medicine newly approved in Japan from 1999 to 2013: Syncope/loss of consciousness and seizures/convulsions. *Regul. Toxicol. Pharmacol.* 72, 572–577. doi: 10.1016/j.yrtph.2015.05.030

Ng, C. C., Duke, R. K., Hinton, T., and Johnston, G. A. R. (2017). Effects of bilobalide, ginkgolide B and picrotoxinin on GABAA receptor modulation by structurally diverse positive modulators. *Eur. J. Pharmacol.* 806, 83–90. doi: 10.1016/j.ejphar.2017.04.019

Peña, F., and Tapia, R. (2000). Seizures and neurodegeneration induced by 4-aminopyridine in rat hippocampus in vivo: Role of glutamate- and GABA-mediated neurotransmission and of ion channels. *Neuroscience* 101, 547–561. doi: 10.1016/s0306-4522(00)00400-0

Peterka, D. S., Takahashi, H., and Yuste, R. (2011). Imaging voltage in neurons. *Neuron* 69, 9–21. doi: 10.1016/j.neuron.2010.12.010

Postnikova, T. Y., Diespirov, G. P., Amakhin, D. V., Vylekzhanina, E. N., Soboleva, E. B., and Zaitsev, A. V. (2021). Impairments of long-term synaptic plasticity in the hippocampus of young rats during the latent phase of the lithium-pilocarpine model of temporal lobe epilepsy. *Int. J. Mol. Sci.* 22:13355. doi: 10.3390/ijms222413355

R Core Team (2021). *R: A language and environment for statistical computing*. Vienna: R Foundation for Statistical Computing. Available online at: https://www.R-project.org/

Schwartzkroin, P. A. (1994). Role of the hippocampus in epilepsy. *Hippocampus* 4, 239–242. doi: 10.1002/hipo.450040302

Storm, J. F. (1988). Temporal integration by a slowly inactivating K+ current in hippocampal neurons. *Nature* 336, 379–381. doi: 10.1038/336379a0

Suh, J., Rivest, A. J., Nakashiba, T., Tominaga, T., and Tonegawa, S. (2011). Entorhinal cortex layer III input to the hippocampus is crucial for temporal association memory. *Science* 334, 1415–1420. doi: 10.1126/science.1210125

Tanemura, K., Murayama, M., Akagi, T., Hashikawa, T., Tominaga, T., Ichikawa, M., et al. (2002). Neurodegeneration with Tau accumulation in a transgenic mouse expressing V337M human Tau. *J. Neurosci.* 22, 133–141. doi: 10.1523/JNEUROSCI.22-01-00133.2002

Tominaga, T., Kajiwara, R., and Tominaga, Y. (2013). VSD imaging method of ex vivo brain preparation. *J. Neurosci. Neuroengineering* 2, 211–219. doi: 10.1166/jnsne.2013.1051

Tominaga, T., Kajiwara, R., and Tominaga, Y. (2023). Stable wide-field voltage imaging for observing neuronal plasticity at the neuronal network level. *Biophys. Physicobiol.* 20:e200015. doi: 10.2142/biophysico.bppb-v20.0015

Tominaga, T., Tominaga, Y., Yamada, H., Matsumoto, G., and Ichikawa, M. (2000). Quantification of optical signals with electrophysiological signals in neural activities of Di-4-ANEPPS stained rat hippocampal slices. *J. Neurosci. Methods* 102, 11–23. doi: 10.1016/s0165-0270(00)00270-3

Tominaga, Y., Ichikawa, M., and Tominaga, T. (2009). Membrane potential response profiles of CA1 pyramidal cells probed with voltage-sensitive dye optical imaging in rat hippocampal slices reveal the impact of GABA(A)-mediated feed-forward inhibition in signal propagation. *Neurosci. Res.* 64, 152–161. doi: 10.1016/j.neures.2009.02.007

Tominaga, Y., Taketoshi, M., Maeda, N., and Tominaga, T. (2019). Wide-field single-photon optical recording in brain slices using voltage-sensitive dye. *J. Vis. Exp.* 20:59692. doi: 10.3791/59692

Tukker, A. M., Wijnolts, F. M. J., de Groot, A., and Westerink, R. H. S. (2018). Human iPSC-derived neuronal models for in vitro neurotoxicity assessment. *Neurotoxicology* 67, 215–225. doi: 10.1016/j.neuro.2018.06.007

Tukker, A. M., Wijnolts, F. M. J., de Groot, A., and Westerink, R. H. S. (2020). Applicability of hiPSC-derived neuronal cocultures and rodent primary cortical cultures for in vitro seizure liability assessment. *Toxicol. Sci.* 178, 71–87. doi: 10.1093/toxsci/kfaa136

Ueno, S., Bracamontes, J., Zorumski, C., Weiss, D. S., and Steinbach, J. H. (1997). Bicuculline and gabazine are allosteric inhibitors of channel opening of the GABAA receptor. *J. Neurosci. Off. J. Soc. Neurosci.* 17, 625–634. doi: 10.1523/JNEUROSCI.17-02-00625.1997

Waring, M. J., Arrowsmith, J., Leach, A. R., Leeson, P. D., Mandrell, S., Owen, R. M., et al. (2015). An analysis of the attrition of drug candidates from four major pharmaceutical companies. *Nat. Rev. Drug Discov.* 14, 475–486. doi: 10.1038/nrd4609

Wheeler, D. B., Randall, A., and Tsien, R. W. (1996). Changes in action potential duration alter reliance of excitatory synaptic transmission on multiple types of Ca^{2+} channels in rat hippocampus. *J. Neurosci. Off. J. Soc. Neurosci.* 16, 2226–2237. doi: 10.1523/JNEUROSCI.16-07-02226.1996

Zhai, J., Zhou, Y.-Y., and Lagrutta, A. (2021). Sensitivity, specificity and limitation of in vitro hippocampal slice and neuron-based assays for assessment of drug-induced seizure liability. *Toxicol. Appl. Pharmacol.* 430:115725. doi: 10.1016/j.taap.2021.115725

Zimmerman, T. J. (1981). Pilocarpine. *Ophthalmology* 88, 85–88. doi: 10.1016/s0161-6420(81)35072-6

Frontiers in
Cellular Neuroscience

Leading research in cellular mechanisms underlying brain function and development

Part of the world's most cited neuroscience journal series that advances our understanding of the cellular mechanisms underlying cell function in the nervous system across all species.

Discover the latest Research Topics

See more →

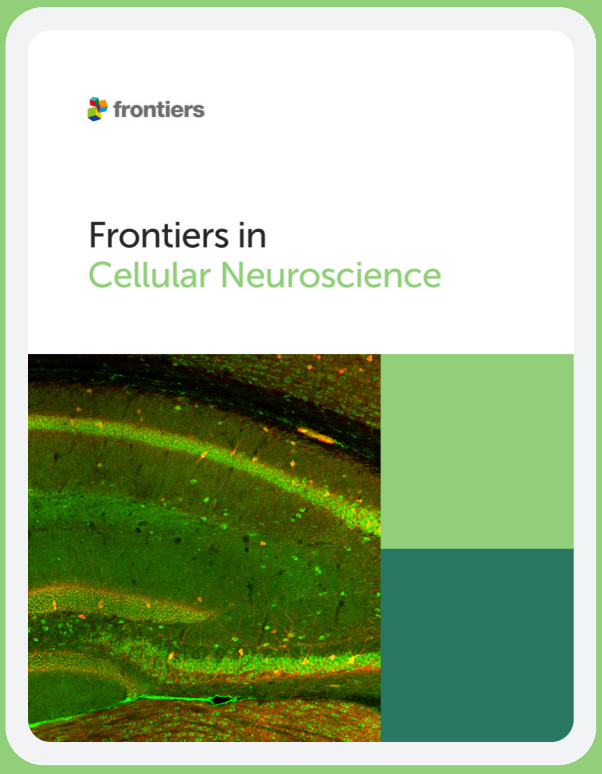

Frontiers

Avenue du Tribunal-Fédéral 34
1005 Lausanne, Switzerland
frontiersin.org

Contact us

+41 (0)21 510 17 00
frontiersin.org/about/contact